Assimilation of 3D Polarimetric Microphysical Retrievals with an Ensemble Kalman Filter in Germany

DISSERTATION

ZUR

ERLANGUNG DES DOKTORGRADES (DR. RER. NAT.)

DER

MATHEMATISCH-NATURWISSENSCHAFTLICHEN FAKULTÄT

DER

RHEINISCHEN FRIEDRICH-WILHELMS-UNIVERSITÄT BONN

vorgelegt von

Lucas Reimann

aus

Peine, Niedersachsen

Bonn, Juni 2023

Angefertigt mit Genehmigung der Mathematisch-Naturwissenschaftlichen
Fakultät der Rheinischen Friedrich-Wilhelms-Universität Bonn

Erster Gutachter:	Prof. Dr. Clemens Simmer
Zweite Gutachterin:	PD Dr. Silke Trömel
Tag der Promotion:	13. Oktober 2023
Erscheinungsjahr:	2023

Abstract

Accurate quantitative precipitation forecasts (QPF) by numerical weather prediction (NWP) models are and remain of high societal interest, especially in times of global warming, which causes an increasing frequency and intensity of heavy precipitation events across the earth. The assimilation of weather radar observations in convective-scale NWP systems has been proven highly beneficial for improving short-term QPF, but research has so far mostly focused on the assimilation of non-polarimetric radar quantities such as horizontal radar reflectivity Z_H and radar radial wind observations. Polarimetric radar data carry more independent information about cloud-precipitation microphysics than Z_H observations do and thus have the potential to further improve short-term QPF. However, assimilation of polarimetric data is still in its infancy.

In this study, polarimetric information from the C-band radar network operated by the German meteorological service (DWD, Deutscher Wetterdienst) are assimilated in DWD's operational convective-scale ensemble-based NWP system for the first time. The polarimetric observations are assimilated using 3D microphysical retrievals of liquid and ice water content (LWC and IWC) below and above the melting layer, respectively, and the impact on short-term QPF compared to the assimilation of Z_H observations alone is investigated. For this purpose, this thesis develops an LWC estimator based on a large German disdrometer data set and C-band T-matrix scattering calculations. It is designed to exploit and mitigate the respective advantages and shortcomings of the different polarimetric radar moments known for different precipitation characteristics in a hybrid way. When applied to German C-band radar observations of four stratiform and five convective warm-season events, the adapted hybrid LWC estimator yields an encouraging close-to-zero bias and better correlations than all tested non-hybrid new and existing estimators from the scientific literature.

With optimized data assimilation settings, the assimilation of the new hybrid LWC estimator below the melting layer mostly improves deterministic and ensemble first-guess QPF over the assimilation of Z_H observations alone for two intense stratiform cases in the summers of 2017 and 2021 and an intense convective case in the summer of 2021. Assimilation of polarimetric data above the melting layer using a hybrid state-of-the-art IWC retrieval from the scientific literature mostly degrades the first guess, especially for convective precipitation, likely because of a lower quality of the estimator in these situations. However, first-guess QPF quality is improved notably for the 2021 stratiform case, for which the estimation of specific differential phase profits from a higher radial radar resolution compared to the other cases. Overall, the best first guess is achieved when Z_H, LWC, and IWC are assimilated together.

The assimilation of 3D LWC or IWC estimates on average slightly improves nine-hour QPF for most forecast hours compared to the assimilation of Z_H observations alone, in particular when LWC estimates are assimilated for the 2017 convective case and when IWC estimates are assimilated for the 2021 stratiform case. Nonetheless, the IWC assimilation degrades deterministic nine-hour QPF again for convective precipitation, which suggests the need for the development of convection-adjusted IWC retrievals for future assimilation studies with polarimetric ice microphysical retrievals. Overall, the best QPF over the first six forecast hours is yielded when Z_H, LWC, and IWC are assimilated together.

Contents

Chapter 1

Introduction

The Sixth Assessment Report of the Intergovernmental Panel on Climate Change (IPCC, 2021) has drawn attention to the alarming effects of global warming on precipitation patterns across the earth. The report indicates that with high confidence the frequency and intensity of heavy precipitation events have increased since the 1950s for most land areas with sufficient observational data for trend analysis. Furthermore, the report emphasizes that these extreme weather events are likely to become even more frequent and intense in most regions as global warming continues. E.g., extreme daily precipitation events are projected to strengthen globally by about 7 % for each K of additional global temperature rise. Heavy precipitation events can threaten lives, livelihoods, property, and economic structures, not only in regions frequently affected by tropical cyclones or monsoon-related precipitation, etc., but also in mid-latitude regions such as Central Europe. Extreme stratiform precipitation in western parts of Germany and its neighboring countries associated with a slow-moving low-pressure system in July 2021 led to devastating floods, e.g., in the Ahr valley in Rhineland-Palatinate, with more than 180 deaths and an insured loss of more than 30 billion euros in Germany alone[1]. Reducing the impact of such dangerous precipitation events on the public is therefore highly desirable and will become even more important in the future with further ongoing climate change.

Quantitative precipitation forecasts (QPF) by numerical weather prediction (NWP) models can play a key role in providing early warnings of hazardous precipitation to the public. However, the accurate prediction of quantitative precipitation by NWP models has been a long-standing goal and challenge for weather forecasters, especially during the summer season when the majority of heavy precipitation occurs (Olson et al., 1995). Significant improvements in QPF quality have been achieved in recent years, primarily due to the increased resolution of operational NWP models as a result of increased computing power at national meteorological forecast centers. Operational NWP models now have horizontal resolutions of only a few kilometers and are thus able to explicitly resolve moist-convective atmospheric processes. They are often referred to as “convective-scale” NWP models. In order for these high-resolution NWP models to provide the best possible weather forecasts, high-resolution convective-scale atmospheric observations that capture the details of moist-convective processes are needed to

[1] *https://www.theguardian.com/world/2022/jul/13/floods-then-and-now-photographs-germany-ahr-valley-flooding-disaster-july-2021 (last accessed 18 June 2023).*

determine appropriate model initial conditions. This so-called “initialization” of operational NWP models is typically done by statistically combining atmospheric observations and short-term weather forecasts (also known as the first guess), taking into account the respective uncertainties of the available sources of information, in order to obtain the best possible estimate of the true state of the atmosphere (also known as the analysis). This process is commonly referred to as “data assimilation” (DA; e.g., Talagrand, 1997). Proper initialization of convective-scale NWP models is particularly challenging because the uncertainties in convective processes are difficult to estimate and observations resolving moist-convective atmospheric processes are required. Weather surveillance radars can provide these observations at uniquely high spatial and temporal resolution and have therefore become an indispensable source of information for convective-scale NWP systems.

The first successful initialization of an NWP model with weather radar observations was presented by Lin et al. (1993), who directly inserted wind and thermodynamic fields derived from multiple-Doppler radar observations, i.e., observations of the same atmospheric spot from several different radars, into their NWP model. They were able to show similarities between a predicted convective storm and the corresponding observed storm for a short period of time. Since then, intensive research has been carried out on the assimilation of weather radar observations into NWP models, and several DA techniques have been tested for their ability to produce accurate convective-scale weather analyses and forecasts. Besides the direct insertion of radar retrieved fields into NWP models, empirical approaches and statistical interpolation schemes have been used for model initialization. The former comprise the successive corrections method (SCM; e.g., Bergthörsson and Döös, 1955) and Newtonian nudging or relaxation (e.g., Hoke and Anthes, 1976). The latter include the 3D and 4D variational (3DVar and 4DVar; e.g., Lewis and Derber, 1985; Le Dimet and Talagrand, 1986; Courtier et al., 1998) schemes. Over roughly the past two decades, radar DA based on the Ensemble Kalman Filter (EnKF; Evensen, 1994, 2003) – a Monte Carlo approximation of the original Kalman Filter (KF; Kalman, 1960; Kalman and Bucy, 1961) – has become increasingly popular because of its ability to estimate the highly flow-dependent forecast uncertainty (the forecast error covariance matrix) at the convective scale using an ensemble of model forecasts (e.g., Snyder and Zhang, 2003; Tong and Xue, 2005; Aksoy et al., 2009; Dowell et al., 2011; Tanamachi et al., 2013; Wheatley et al., 2015; Bick et al., 2016; Gastaldo et al., 2021). An additional advantage of the EnKF is that it does not require the formulation of tangent linear and adjoint microphysical models and observation operators (e.g., Houtekamer and Mitchell, 1998) like in variational approaches. However, running a forecast ensemble of sufficient size to robustly estimate the forecast error covariance matrix is not feasible in operational forecast routines due to high computational cost. Too small ensemble sizes can lead to sampling errors that may cause filter divergence and spurious long-range correlations in the model domain (e.g., Houtekamer and Mitchell, 1998; Hamill et al., 2001). A common approach to mitigate this problem is observation localization (Ott et al., 2004), which restricts the

radius of observations affecting the analysis. The Local Ensemble Transform Kalman Filter (LETKF; Hunt et al., 2007) – a manifestation of the EnKF approach in which observation localization is a key feature and in which analyses are computed independently at all grid points allowing for easy parallelization – is currently very popular in the (radar) DA community. It is used for research purposes at the Japan Meteorological Agency (JMA; e.g., Miyoshi et al., 2010) and the European Centre for Medium-Range Weather Forecasts (ECMWF; e.g., Hamrud et al., 2015) and has been implemented in operational weather forecasting routines at the Italian operational center for meteorology (COMET; Bonavita et al., 2010) and at the national meteorological services of Germany (Deutscher Wetterdienst, DWD) and Switzerland (Federal Office of Meteorology and Climatology MeteoSwiss). Several studies showed that the assimilation of 3D radar observations with the LETKF has a positive impact on short-term QPF (e.g., Bick et al., 2016; Gastaldo et al., 2021). Since spring 2021, 3D radar data have been assimilated in DWD's operational LETKF-based convective-scale NWP system comprising the DA framework KENDA (Kilometre-scale Ensemble Data Assimilation; Schraff et al. 2016) and the limited-area setup of the global ICON (Icosahedral Nonhydrostatic) model (Zängl et al., 2015) covering Germany and adjacent countries ICON-D2.

Assimilation of weather radar observations has mostly focused on the horizontal radar reflectivity factor (hereafter simply reflectivity) Z_H and the Doppler radial wind V_r, with only Z_H providing direct information on microphysical processes in clouds and precipitation. Dual-polarization (i.e., linear orthogonal polarization diversity; Seliga and Bringi, 1976, 1978; hereafter referred to as polarimetric) radar observations provide additional independent information on clouds and precipitation, such as the size, shape, orientation, and composition of hydrometeors compared to Z_H observations alone (e.g., Zrnic and Ryzhkov, 1999). Therefore, polarimetric radar observations may be valuable for improving the representation of cloud-precipitation microphysics in NWP models, weather analyses, and consequently short-term QPF through evaluation of NWP models and microphysical parameterizations, microphysical parameterization development, and DA (e.g., Kumjian, 2013a; Zhang et al., 2019). While polarimetric radar observations have already been used to improve attenuation correction (e.g., Bringi et al., 1990; Testud et al., 2000; Snyder et al., 2010), quantitative precipitation estimation (QPE; e.g., Zrnic and Ryzhkov, 1996; Ryzhkov et al., 2005a; Tabary et al., 2011; Chen et al., 2021), severe weather observation and detection (e.g., Ryzhkov et al., 2005b; Bodine et al., 2013), hydrometeor classification (e.g., Park et al., 2009; Dolan et al., 2013), and model validation (e.g., Jung et al., 2012; Putnam et al., 2014, 2017), their assimilation in NWP models is still in its infancy. This is partly due to the remaining uncertainties in the relationships between the polarimetric radar moments and model microphysical state variables needed for DA. Another reason for this is the fact that polarimetric upgrades of national weather radar networks just finished within the past decade. E.g., the upgrade was completed in the USA in 2013 and in Germany in 2015.

Polarimetric radar moments can be linked to model microphysical state variables for DA using either radar forward operators or retrieval algorithms. Radar forward operators simulate synthetic radar observations based, e.g., on model-simulated parameterized particle size distributions that can be compared to the real radar observations. Retrievals estimate model microphysical state variables from the real radar observations prior to DA in order to establish the link to the model. Both approaches can be challenging. The direct approach via forward operators can be difficult because, e.g., the shape, size and orientation distributions of hydrometeors, all of which influence (polarimetric) radar observations, are still rather rudimentarily represented in NWP models (e.g., Schinagl et al., 2019). The indirect approach via retrievals circumvents these model deficiencies but suffers from uncertainties within the retrieval algorithms. A few case studies from the USA, Japan, and China have attempted the direct assimilation of polarimetric radar observations with some success using the EnKF approach (e.g., Jung et al., 2008b; Jung et al., 2010b; Putnam et al., 2019, 2021; Zhu et al., 2020) or the 3DVar method (e.g., Li et al., 2017; Du et al., 2021). Other studies have assimilated polarimetric data indirectly via retrieved hydrometeor mixing ratios using the 4DVar approach (e.g., Wu et al., 2000), the 3DVar approach (e.g., Li and Mecikalski, 2010, 2012), or the EnKF method (e.g., Yokota et al., 2016). Furthermore, polarimetric radar observations have been used to modify cloud analysis schemes based on polarimetric signatures in convective storms (Carlin et al., 2017) or by improving hydrometeor classification (Ding et al., 2022). To the author's knowledge, there is no published study assimilating polarimetric weather radar observations in Central Europe. The non-polarimetric radar forward operator EMVORADO (Efficient Modular Volume-scanning Radar Forward Operator; Zeng et al., 2016), which is in operational use at DWD for the KENDA-ICON-D2 system, is currently being upgraded to polarimetry in preparation for the direct assimilation of polarimetric observations in Germany in the near future. However, the polarimetric version of the EMVORADO radar forward operator is still in a test phase. For indirect assimilation of polarimetric data, polarimetric microphysical retrieval algorithms for liquid water content (LWC) and ice water content (IWC) have been proposed in the scientific literature (e.g., Ryzhkov et al., 1998; Bringi and Chandrasekar, 2001; Doviak and Zrnic, 2006; Carlin et al., 2016; Ryzhkov and Zrnic, 2019; Bukovcic et al., 2018, 2020; Carlin et al., 2021), but most of these estimators were developed with a focus on S-band radars in the USA. The applicability of these retrieval algorithms for Germany, with its national C-band radar network and different precipitation climatology, may thus be limited.

As part of the research project RealPEP (Near-Realtime Quantitative Precipitation Estimation and Prediction) funded by DFG (Deutsche Forschungsgemeinschaft), this study assimilates polarimetric information from the German national C-band radar network into DWD's LETKF-based convective-scale KENDA-ICON-D2 NWP system for the first time and evaluates the assimilation impact on short-term QPF compared to the assimilation of Z_H observations alone (submitted for publication, Reimann et al., 2023). The assimilation of polarimetric data is performed indirectly

using microphysical retrievals of LWC and IWC below and above the melting layer, respectively, also because the finalization of DWD's polarimetric EMVORADO radar forward operator is not yet completed. To this end, this thesis develops a polarimetric LWC estimator (published in Reimann et al., 2021) for the indirect assimilation of polarimetric radar observations below the melting layer, which is adapted to the German C-band radar network and precipitation climatology by being based on a large German pure-rain disdrometer data set and C-band T-matrix scattering calculations. It is designed to exploit and mitigate the respective advantages and disadvantages of the different polarimetric radar moments known for different precipitation characteristics in a hybrid way. To address these central objectives, this thesis aims to answer the following research questions:

Q1: What is the best-performing polarimetric LWC retrieval for application to the German C-band radar network?

Q2: Does the assimilation of polarimetric microphysical retrievals into the KENDA-ICON-D2 system of DWD improve short-term QPF compared to the assimilation of Z_H observations alone?

Together with this introduction, this thesis is divided into six chapters. Chapter 2 introduces the basics of polarimetric weather radar observations, including a brief introduction to electromagnetic scattering theory and the definition of the polarimetric radar moments used. It also describes the German national polarimetric C-band radar network, from which observations are used in Chapters 3 and 5 for the evaluation of LWC estimators and the assimilation of polarimetric information. Chapter 3 develops new polarimetric LWC retrievals adapted to the German C-band radar network and precipitation climatology based on a large pure-rain disdrometer data set and C-band T-matrix scattering calculations, and formulates a hybrid combination of these new relations. It also evaluates the new and existing LWC estimators from the literature with real radar observations from nine precipitation events in the summers of 2016 to 2019. Chapter 4 reviews the key methods and achievements of assimilation of (polarimetric) radar observations into NWP models with a focus on the EnKF approach, in particular the LETKF. In Chapter 5, the performed DA experiments with polarimetric microphysical retrievals in DWD's KENDA-ICON-D2 system are described. These include the identification of suitable DA settings for LWC and IWC based on first-guess quality and the evaluation of the assimilation impact on nine-hour QPF compared to the assimilation of Z_H observations alone. Thereby, the focus is on three intense precipitation periods in the summers of 2017 and 2021. Final conclusions and an outlook are given in Chapter 6.

Chapter 2

Polarimetric Radar Observations and Microphysical Retrievals

In this study, polarimetric information from the German national C-band radar network is assimilated into DWD's convective-scale KENDA-ICON-D2 NWP system for the first time. The assimilation is performed using polarimetric microphysical retrievals of LWC and IWC below and above the melting layer, respectively. For improving understanding of the approaches, findings, as well as conclusions presented in this thesis, Section 2.1 of the present chapter gives a brief introduction to the physical principle behind polarimetric weather radars, including an introduction to electromagnetic scattering theory and the derivation of the basic polarimetric radar moments considered. Furthermore, the German national polarimetric C-band radar network operated by DWD is described, from which polarimetric observations are used for the evaluation of LWC estimators in Chapter 3 and for the DA experiments performed in Chapter 5. Section 2.2 subsequently reviews the existing LWC estimators for C-band radars from the scientific literature potentially usable for polarimetric DA purposes in Germany.

2.1 Polarimetric Weather Radar

Weather radars are active remote sensing instruments that emit pulsed and directed electromagnetic radiation at microwave frequencies (e.g., about 4 to 8 GHz or wavelengths of 75 to 37.5 mm for C-band radars) into the surrounding atmosphere and receive the echoes from atmospheric targets such as raindrops, snowflakes, and hail or graupel. The detected echoes contain information about the bulk properties of the illuminated hydrometeors in clouds and precipitation, such as their size, shape, physical composition, and orientation, which can be used to improve the understanding of microphysical cloud-precipitation processes, hazard detection, hydrometeor classification, and weather forecasting through DA. The type of weather radar used (e.g., single- or dual-polarization) thereby determines the amount of independent microphysical information provided.

An electromagnetic wave is a coupled vibration of electric and magnetic forces propagating through free space or a medium, and the electromagnetic waves transmitted by weather radars can be considered sinusoidal (Ryzhkov and Zrnic,

2019). Far away from the radar antenna, the electric and magnetic field vectors oscillate orthogonally to each other in the polarization plane that is perpendicular to the direction of wave propagation (Ryzhkov and Zrnic, 2019). The polarization plane is defined by the two orthogonal unit vectors $\vec{e}_H$ and $\vec{e}_V$ (hereafter, vectors are indicated by rightwards arrows) with the indices H and V denoting the horizontal (parallel to the local earth surface) and vertical directions (Zhang, 2016; Ryzhkov and Zrnic, 2019). An important property of electromagnetic waves used by common weather radars is the polarization state of the transmitted and received electromagnetic waves. The polarization state of an electromagnetic wave is defined by the shape that the locus of the electric field vector tip forms in the polarization plane as time proceeds (Zhang, 2016). The electric field vector $\vec{E}$ of a polarized, sinusoidal, and plane electromagnetic wave propagating through a vacuum or an isotropic medium can be written in complex notation as the sum of its horizontally and vertically polarized components $\vec{E}_H$ and $\vec{E}_V$ as

$$\vec{E}(r,t) = \vec{E}_H(r,t) + \vec{E}_V(r,t)$$
$$= E_H^0 \exp[j(2\pi ft - kr - \varphi_H)]\vec{e}_H + E_V^0 \exp[j(2\pi ft - kr - \varphi_V)]\vec{e}_V \quad (2.1)$$

with $E_{H/V}^0$ the amplitudes of the horizontal/vertical components, j the complex solution to the equation $j^2 = -1$, f the wave frequency in Hz, k the wave number in m^{-1}, and $\varphi_{H/V}$ the start phases of the horizontal/vertical components (Zhang, 2016; Ryzhkov and Zrnic, 2019). The real part of the complex vector $\vec{E}$ in Eq. (2.1) $\mathrm{Re}(\vec{E})$ refers to the physical electric field vector (Ryzhkov and Zrnic, 2019). If the phase difference $\Delta\varphi$ between the real parts of the horizontally and vertically polarized components $\mathrm{Re}(\vec{E}_H)$ and $\mathrm{Re}(\vec{E}_V)$ is 0 or π, the orthogonal wave components are in or out of phase and the locus of $\mathrm{Re}(\vec{E})$ in the polarization plane forms a straight line. In this case, the electromagnetic wave is called linearly polarized. Otherwise, the locus of $\mathrm{Re}(\vec{E})$ forms an ellipse, and consequently the polarization of the electromagnetic wave is called elliptical (Zhang, 2016; Ryzhkov and Zrnic, 2019). A special case of elliptical polarization is the circular polarization characterized by a phase difference $\Delta\varphi = \pm\frac{\pi}{2}$ and equal orthogonal component amplitudes $E_H^0 = E_V^0$.

A polarimetric radar emits linearly polarized electromagnetic waves in both the horizontal and vertical directions and detects the linearly polarized components of the echoed signals in both polarization channels (e.g., Kumjian, 2013a). Polarimetric radars that transmit and receive electromagnetic radiation in the horizontal and vertical polarization channels at the same time are most commonly used in national polarimetric radar networks and are referred to as operating in "simultaneous transmission/reception" mode or simply SHV-mode (Ryzhkov and Zrnic, 2019). The polarimetric variables obtained by polarimetric radars operating in SHV-mode are in focus in this thesis and can be derived from electromagnetic scattering theory.

2.1.1 Electromagnetic Scattering Theory

Consider a plane sinusoidal electromagnetic wave propagating in a vacuum or another non-attenuating isotropic medium incident on a single hydrometeor like a raindrop. The incident electric field $\vec{E}_i$ produces electromagnetic currents inside the illuminated hydrometeor, which result in secondary radiation being scattered radially in all directions (Zhang, 2016). At a far distance from the particle, the scattered electric field $\vec{E}_s$ behaves like a spherical wave, and both $\vec{E}_i$ and $\vec{E}_s$ can be related via the scattering equation

$$\vec{E}_s = \frac{\exp[-jkr]}{r}\boldsymbol{S}\vec{E}_i \tag{2.2}$$

with r the distance between the hydrometeor and the observation point of $\vec{E}_s$, $k = 2\pi/\lambda$ the wave number in the background medium with the wavelength λ, and $\boldsymbol{S}$ the complex scattering matrix (e.g., Zhang, 2016; Ryzhkov and Zrnic, 2019; hereafter, matrices are indicated by bold capital letters). In Eq. (2.2) and below, the time-varying factors are neglected so that $\vec{E}_i$ and $\vec{E}_s$ represent complex amplitudes or so-called phasors (e.g., Ryzhkov and Zrnic, 2019). For polarimetric weather radar applications, the scattering matrix $\boldsymbol{S}$ is defined in the coordinate system based on the horizontal and vertical directions by

$$\boldsymbol{S} = \begin{bmatrix} s_{HH} & s_{HV} \\ s_{VH} & s_{VV} \end{bmatrix} \tag{2.3}$$

with the complex scattering amplitudes s_{XY}, which magnitudes quantify the fraction of the incident wave field in X-polarization scattered to Y-polarization and their phases quantify the corresponding phase shift with respect to the incident wave field (Ryzhkov and Zrnic, 2019). The cases $X = Y$ and $X \neq Y$ refer to the co- and cross-polar scattering amplitudes, respectively. Equation (2.2) can be rewritten in matrix form as

$$\begin{bmatrix} E_{s,H} \\ E_{s,V} \end{bmatrix} = \frac{\exp[-jkr]}{r}\begin{bmatrix} s_{HH}(\vec{k}_i, \vec{k}_s) & s_{HV}(\vec{k}_i, \vec{k}_s) \\ s_{VH}(\vec{k}_i, \vec{k}_s) & s_{VV}(\vec{k}_i, \vec{k}_s) \end{bmatrix}\begin{bmatrix} E_{i,H} \\ E_{i,V} \end{bmatrix} \tag{2.4}$$

with $\vec{k}_i$ and $\vec{k}_s$ the unit vectors in the propagation direction of the incident and scattered waves, respectively (Ryzhkov and Zrnic, 2019). Meteorologists are typically interested in the portion of the incident wave scattered back to the radar antenna that contains information about the illuminated hydrometeors in the probed atmospheric volume (Ryzhkov and Zrnic, 2019). For the wave field scattered back to the radar, $\vec{k}_s = -\vec{k}_i$, and the corresponding scattering matrix is called backscattering

matrix (Ryzhkov and Zrnic, 2019). In the following, the focus will thus be on the backscattering matrix, hereafter simply referred to as the scattering matrix $\boldsymbol{S}$.

Calculating $\boldsymbol{S}$ for arbitrary particles can be challenging, but closed-form solutions exist for scattering hydrometeors that are spheroidal in shape and small compared to the radar wavelength (Rayleigh approximation; Ryzhkov and Zrnic, 2019). For C-band radars, the Rayleigh approximation is mostly valid for raindrops, small snowflakes, small hail, graupel, and ice crystals, and the spheroid approximation is especially suitable for raindrops, which flatten in response to air drag when falling (Ryzhkov and Zrnic, 2019). As is common in the literature, the spheroid model is used here. A spheroid is described by two axes a and b, where axis a connects the poles of the spheroid and axis b connects two points on its equator by cutting through its center. Hydrometeors tumble as they fall, which affects the scattering of incident electromagnetic waves, and thus makes it necessary to consider particle canting (Ryzhkov and Zrnic, 2019). A spheroid projected onto the polarization plane of an electromagnetic wave can be rotated by two angles χ and ψ referring to the angles between axis a and the vertical direction in the polarization plane and between axis a and the direction of wave propagation. The matrix $\boldsymbol{S}$ defined in the horizontal-vertical system of the incident wave like in Eq. (2.3) depends on the complex scattering amplitudes s_a and s_b along the axes a and b of the spheroid and its canting angles χ and ψ as

$$\boldsymbol{S} = \begin{bmatrix} (s_a - s_b)\sin^2(\psi)\sin^2(\chi) + s_b & (s_a - s_b)\sin^2(\psi)\sin(\chi)\cos(\chi) \\ (s_a - s_b)\sin^2(\psi)\,\sin(\chi)\,\cos(\chi) & (s_a - s_b)\sin^2(\psi)\cos^2(\chi) + s_b \end{bmatrix} \tag{2.5}$$

(Ryzhkov and Zrnic, 2019). Note that Eq. (2.5) was derived based on the "backscatter rule", which describes the dependencies of s_a and s_b on the angle ψ in the Rayleigh approximation (Holt and Shepherd, 1979).

The hydrometeors in a radar resolution volume have different sizes and orientations and all of them contribute to the backscattered signal. The size distribution in an atmospheric radar volume is characterized by the particle size distribution $N(D)$ with D the particle diameter, and integrals over $N(D)$ are denoted in the following by angular brackets

$$\langle \dots \rangle = \int N(D) \dots dD. \tag{2.6}$$

Note that in the literature the angular brackets in Eq. (2.6) are often referred to as an "ensemble average" rather than as an integral (e.g., in Ryzhkov and Zrnic, 2019), which can be misleading. The second-order backscattering moments are

$$\langle |s_{HH}|^2 \rangle = \langle |s_b|^2 \rangle - 2\mathrm{Re}(\langle s_b^*(s_b - s_a) \rangle) M_2 + \langle |(s_b - s_a)|^2 \rangle M_4, \tag{2.7}$$

$$\langle |s_{VV}|^2 \rangle = \langle |s_b|^2 \rangle - 2\mathrm{Re}(\langle s_b^*(s_b - s_a) \rangle) M_1 + \langle |(s_b - s_a)|^2 \rangle M_3, \tag{2.8}$$

$$\langle |s_{HV}|^2 \rangle = \langle |s_{VH}|^2 \rangle = \langle |(s_b - s_a)|^2 \rangle M_5, \tag{2.9}$$

and

$$\langle s_{HH}^* s_{VV} \rangle = \langle |s_b|^2 \rangle + \langle |(s_b - s_a)|^2 \rangle M_5 - \langle s_b^* (s_b - s_a) \rangle M_1 - \langle s_b (s_b^* - s_a^*) \rangle M_2 \tag{2.10}$$

(Ryzhkov and Zrnic, 2019) with $\mathrm{Re}(c)$ the real part and c^* the complex conjugate of a complex number c. When the backscattered and forward scattered waves are equal, i.e., $\vec{k}_s = \vec{k}_i$, which is the case for Rayleigh scatterers, the first-order forward scattering moments are

$$\langle s_{HH}^{(0)} \rangle = \langle s_b^{(0)} \rangle - \langle s_b^{(0)} - s_a^{(0)} \rangle M_2 \tag{2.11}$$

and

$$\langle s_{VV}^{(0)} \rangle = \langle s_b^{(0)} \rangle - \langle s_b^{(0)} - s_a^{(0)} \rangle M_1 \tag{2.12}$$

with the superscript "(0)" indicating forward scattering (Ryzhkov and Zrnic, 2019). In Eqs. (2.7) through (2.12), M_{1-5} are the angular moments

$$M_1 = \langle \sin^2(\psi) \cos^2(\chi) \rangle, \tag{2.13}$$

$$M_2 = \langle \sin^2(\psi) \sin^2(\chi) \rangle, \tag{2.14}$$

$$M_3 = \langle \sin^4(\psi) \cos^4(\chi) \rangle, \tag{2.15}$$

$$M_4 = \langle \sin^4(\psi) \sin^4(\chi) \rangle, \tag{2.16}$$

and

$$M_5 = \langle \sin^4(\psi) \cos^2(\chi) \sin^2(\chi) \rangle \tag{2.17}$$

(Ryzhkov and Zrnic, 2019). Assuming the distributions of particle orientations described by the angles ψ and χ being characterized by a 2D axisymmetric angular Gaussian distribution with mean angles $\langle \psi \rangle \approx \frac{\pi}{2}$ and $\langle \chi \rangle \approx 0$ and corresponding standard deviations σ_ψ and $\sigma_\chi = \sigma_\psi / \sin(\psi)$, the angular moments can be formulated following Ryzhkov et al. (2011) as

$$M_1 = \frac{1}{4}(1 + r_\psi)^2, \tag{2.18}$$

$$M_2 = \frac{1}{4}(1 - r_\psi^2), \tag{2.19}$$

$$M_3 = (\tfrac{3}{8} + \tfrac{1}{2} r_\psi + \tfrac{1}{8} r_\psi^4)^2, \tag{2.20}$$

$$M_4 = (\tfrac{3}{8} - \tfrac{1}{2} r_\psi + \tfrac{1}{8} r_\psi^4)(\tfrac{3}{8} + \tfrac{1}{2} r_\psi + \tfrac{1}{8} r_\psi^4), \tag{2.21}$$

and

$$M_5 = \tfrac{1}{8}(\tfrac{3}{8} + \tfrac{1}{2} r_\psi + \tfrac{1}{8} r_\psi^4)(1 - r_\psi^4) \tag{2.22}$$

with $r_\psi = \exp[-2\sigma_\psi^2]$ and σ_ψ in radians.

When considering electromagnetic waves emitted by a weather radar in precipitation, propagation effects due to atmospheric gases and hydrometeors on the propagation path of the electromagnetic waves must also be considered. These effects include accumulation of phase shift with respect to the theoretical propagation of the electromagnetic waves in a vacuum, reduction of wave amplitude due to absorption and scattering, also known as attenuation, and depolarization in the presence of canted hydrometeors. The changes in an electromagnetic wave traveling from a position 0 to a position r through an atmospheric volume filled with hydrometeors can be calculated using the transmission matrix $\boldsymbol{T}$ as

$$\begin{bmatrix} E_H(r) \\ E_V(r) \end{bmatrix} = \boldsymbol{T} \begin{bmatrix} E_H(0) \\ E_V(0) \end{bmatrix} = \begin{bmatrix} T_{HH} & T_{HV} \\ T_{VH} & T_{VV} \end{bmatrix} \begin{bmatrix} E_H(0) \\ E_V(0) \end{bmatrix} \tag{2.23}$$

(Zhang, 2016; Ryzhkov and Zrnic, 2019). For simplicity, assume that the mean canting angles of hydrometeors are zero, which results in zero depolarization of the electromagnetic wave as it propagates due to statistical symmetry and in zero off-diagonal elements of $\boldsymbol{T}$ as

$$\begin{bmatrix} E_H(r) \\ E_V(r) \end{bmatrix} = \begin{bmatrix} T_{HH} & 0 \\ 0 & T_{VV} \end{bmatrix} \begin{bmatrix} E_H(0) \\ E_V(0) \end{bmatrix}$$

$$= \begin{bmatrix} \exp[-j \int_0^r K_H dl] & 0 \\ 0 & \exp[-j \int_0^r K_V dl] \end{bmatrix} \begin{bmatrix} E_H(0) \\ E_V(0) \end{bmatrix} \tag{2.24}$$

with the effective propagation constants K_H and K_V defined by

$$K_H = k + \frac{2\pi}{k} \langle s_{HH}^{(0)} \rangle \tag{2.25}$$

and

$$K_V = k + \frac{2\pi}{k} \langle s_{VV}^{(0)} \rangle \tag{2.26}$$

(Zhang, 2016). Radar measurements contain information about both the scattering and propagation of electromagnetic waves. These two principles have been introduced separately above. To obtain a formulation of first-order multiple scattering by combining both schemes, the transmission-included scattering matrix $\boldsymbol{S}'$ is used to relate the radar-transmitted electromagnetic wave field $\vec{E}_t$ with the radar-received electromagnetic wave field $\vec{E}_r$ as

$$\begin{bmatrix} E_{r,H} \\ E_{r,V} \end{bmatrix} = \frac{1}{r}\boldsymbol{S}' \begin{bmatrix} E_{t,H} \\ E_{t,V} \end{bmatrix} \tag{2.27}$$

with $\boldsymbol{S}'$ including propagation effects from the radar antenna to the scatterers, wave scattering, and propagation effects from the scatterers back to the radar, and given by

$$\boldsymbol{S}' = \boldsymbol{TST} = \begin{bmatrix} s_{HH}\exp[-2j\int_0^r K_H dl] & s_{HV}\exp[-j\int_0^r (K_H + K_V) dl] \\ s_{VH}\exp[-j\int_0^r (K_H + K_V) dl] & s_{VV}\exp[-2j\int_0^r K_V dl] \end{bmatrix} \tag{2.28}$$

with $\boldsymbol{T}$ and $\boldsymbol{S}$ the transmission and scattering matrices, respectively (Zhang, 2016). Cross-polar components (off-diagonal elements) of $\boldsymbol{S}'$ in the case of zero depolarization upon wave propagation are only induced by scattering. The transmission-included scattering matrix $\boldsymbol{S}'$ can be used to calculate radar variables influenced by propagation effects such as phase shift and attenuation (Zhang, 2016). More detailed overviews of the topic can be found, e.g., in the books of Bringi and Chandrasekar (2001), Zhang (2016) and Ryzhkov and Zrnic (2019).

2.1.2 Polarimetric Radar Moments

Perhaps the most basic quantity provided by polarimetric weather radars is the radar equivalent reflectivity factor, or simply reflectivity, at horizontal polarization

$$z_H = \frac{4\lambda^4}{\pi^4 |K_w|^2} \langle |s_{HH}|^2 \rangle \tag{2.29}$$

(given in $\mathrm{mm}^6\,\mathrm{m}^{-3}$) with λ the radar wavelength in mm and $|K_w| = \frac{\varepsilon_w - 1}{\varepsilon_w + 2}$ with ε_w the dielectric constant of water (e.g., Zhang, 2016; Ryzhkov and Zrnic, 2019), which is related to the refractive index of water n_w via $\varepsilon_w = n_w^2$ (e.g., Kumjian, 2013a). Since z_H covers a wide range of possible values, it is typically expressed in logarithmic units by $Z_H = 10\log(z_H)$ in dBZ. A polarimetric radar can also measure reflectivity at vertical polarization Z_V. Both Z_H and Z_V depend on the raindrop size and number concentration in the radar resolution volume, and in the Rayleigh regime, $Z_H > Z_V$ due to oblate shapes of raindrops, and both Z_H and Z_V increase continuously with the

hydrometeor size, such that $Z_{H/V} \sim D^6$ (Ryzhkov and Zrnic, 2019). Moreover, Z_H and Z_V depend on the dielectric constant of the hydrometeors, which is a function of their physical composition, including their density and temperature, and the wavelength of the incident electromagnetic waves (Kumjian, 2013a). E.g., the dielectric constant of ice is much smaller than that of liquid water, so that the reflectivity of an ice hydrometeor with the same shape as a liquid hydrometeor will be much lower (e.g., Kumjian, 2013a; Ryzhkov and Zrnic, 2019). The quality of $Z_{H/V}$ measurements can be degraded by partial beam blockage, radar miscalibration, attenuation, non-uniform beam filling, resonance scattering, and noise bias, but they are mostly not affected by depolarization effects (Kumjian, 2013a).

The deviation of hydrometeor shapes from the sphere model results in differences in the received powers in the horizontal and vertical polarization channels. This effect can be quantified with the ratio of the horizontal and vertical reflectivities

$$Z_{DR} = 10 \log\left(\frac{z_H}{z_V}\right) = 10 \log\left(\frac{\langle |s_{HH}|^2 \rangle}{\langle |s_{VV}|^2 \rangle}\right) \tag{2.30}$$

with z_V in mm^6 m^{-3} known as the differential reflectivity (given in dB; e.g., Ryzhkov and Zrnic, 2019) and first introduced by Seliga and Bringi (1976). Z_{DR} round 0 dB corresponds to spherical or randomly oriented hydrometeors in the radar resolution volume, such as drizzle rain or dry tumbling hail. For Rayleigh scatterers, positive values of Z_{DR} indicate that the hydrometeors have, on average, a larger extent in the horizontal than in the vertical direction, which is the case, as mentioned before, for falling raindrops. Thus, Z_{DR} can be used as an indirect measure of raindrop size, as the oblateness of raindrops increases with increasing size. Negative Z_{DR} can also be observed, e.g., in the presence of vertically oriented ice needles in a strong electric field or conical graupel, and also due to resonance effects (e.g., Kumjian, 2013a). Thus, Z_{DR} also depends on the average orientation of probed particles. It also depends on the particle's dielectric constant, thus it will be smaller for an ice hydrometeor of the same shape as a liquid hydrometeor, but unlike $Z_{H/V}$, Z_{DR} does not depend on the hydrometeor number concentration or on absolute miscalibration of the radar transmitter or receiver (Kumjian, 2013a). However, Z_{DR} can be negatively affected by biases introduced in the radar hardware, biases due to anisotropic beam blockage, noise bias, partial beam blockage, non-uniform beam filling, resonance scattering, depolarization, and differential attenuation (Kumjian, 2013a).

The co-polar cross-correlation coefficient ρ_{HV} is another polarimetric radar moment that can be used to characterize the synchrony of backscattered signals in horizontal and vertical polarizations, and is thus a measure of the diversity of hydrometeor types, shapes, and orientations in a radar resolution volume (e.g., Kumjian, 2013a; Ryzhkov and Zrnic, 2019). It was introduced by Sachidananda and Zrnic (1985) and Jameson and Mueller (1985) and combines the three second-order moments $\langle |s_{HH}|^2 \rangle$, $\langle |s_{VV}|^2 \rangle$, and $\langle s_{HH}^* s_{VV} \rangle$ in Eqs. (2.7), (2.8), and (2.10) to

$$\rho_{HV} = \frac{\langle s_{HH}^* s_{VV} \rangle}{(\langle |s_{HH}|^2 \rangle \langle |s_{VV}|^2 \rangle)^{1/2}} \tag{2.31}$$

(e.g., Ryzhkov and Zrnic, 2019). The variable ρ_{HV} will be equal to one if the Rayleigh scatterers in a radar volume differ only in size, and the shapes, orientations, and types of hydrometeors are uniform. As this uniformity decreases, i.e., as the diversity of types, shapes, and orientations increases, ρ_{HV} will decrease. Moreover, ρ_{HV} is strongly reduced in the presence of non-Rayleigh and non-meteorological scatterers. Thus, ρ_{HV} can be used to identify and filter out non-meteorological echoes and is therefore a valuable tool for data quality assurance. Furthermore, ρ_{HV} is immune to (differential) attenuation effects, partial beam blockage, depolarization, and radar miscalibration, and does not depend on the number concentration of hydrometeors, but it can be affected by non-uniform beam filling and noise bias (Kumjian, 2013a).

In addition to the polarimetric radar moments based on the second-order moments of the backscattered signal (i.e., $Z_{H/V}$, Z_{DR}, and ρ_{HV}), information about hydrometeors in a radar resolution volume is also provided by phase differences of the received signals in the horizontal and vertical polarization channels. The total differential phase Φ_{DP} is defined by

$$\Phi_{DP} = \delta + \varphi_{DP} = \delta + 2\int_0^r K_{DP}(l)dl \tag{2.32}$$

with $\delta = \arg(\langle s_{HH}^* s_{VV} \rangle)$ the backscatter differential phase and φ_{DP} the propagation differential phase (e.g., Trömel et al., 2014; Ryzhkov and Zrnic, 2019). In real applications, a third contribution φ_{DP}^{sys} must be considered to account for the phase offset caused by the radar system. According to Eq. (2.32), φ_{DP} is twice the range integral from the radar ($l = 0$) to the measurement location ($l = r$) of the specific differential phase K_{DP} defined by the real parts of the effective propagation constants K_H and K_V in Eqs. (2.25) and (2.26) as

$$K_{DP} = \mathrm{Re}(K_H - K_V) = \lambda \mathrm{Re}(\langle s_{HH}^{(0)} \rangle - \langle s_{VV}^{(0)} \rangle) \tag{2.33}$$

and can be written as

$$K_{DP} = \frac{180\lambda}{\pi}(M_1 - M_2)\langle s_b^{(0)} - s_a^{(0)} \rangle * 10^{-3} \tag{2.34}$$

and is given in deg km^{-1}. Equation (2.34) was derived assuming a 2D axisymmetric Gaussian distribution of hydrometeor canting angles (Ryzhkov and Zrnic, 2019) and $s_{a,b}^{(0)}$ are the forward scattering amplitudes along the axes a and b of a spheroid. However, the forward scattering of electromagnetic waves is not measurable with a usual polarimetric monostatic (i.e., the same radar transmits and receives the signals)

weather radar. Another way to determine K_{DP} is to express it as half the range-derivative of the measurable total differential phase Φ_{DP}

$$K_{DP} = \frac{1}{2}\frac{d\Phi_{DP}}{dr} \tag{2.35}$$

(e.g., Bringi and Chandrasekar, 2001). Note that Eq. (2.35) is only applicable if the backscatter differential phase δ can be neglected such that $\Phi_{DP} \approx \varphi_{DP}$. K_{DP} shows values close to zero for spherical or randomly oriented particles and increases for Rayleigh scatterers with increasing oblateness of hydrometeors similar to Z_{DR}, thus K_{DP} is affected by variability in the particle size distribution (Kumjian, 2013a), but to a lesser extend (in rain $K_{DP} \sim D^{4.24}$; Sachidananda and Zrnic, 1986) compared to $Z_{H/V}$ (recall $Z_{H/V} \sim D^6$; Ryzhkov and Zrnic, 2019). In addition, K_{DP} is proportional to the hydrometeor number concentration, increases with the density of the particles, and increases with increasing LWC, while being relatively immune to dry tumbling hail, making it particularly useful for estimating LWC in rain-hail mixtures (e.g., Balakrishnan and Zrnic, 1990; Giangrande and Ryzhkov, 2008). As a phase-based quantity, K_{DP} is also unaffected by attenuation, partial beam blockage, and radar miscalibration, and is not affected by noise bias (Kumjian, 2013a). However, proper estimation of K_{DP} can be challenging in light rain due to noise in the underlying total differential phase Φ_{DP} and in the presence of non-Rayleigh scatterers or non-uniform beam filling (Ryzhkov and Zrnic, 1998; Gosset, 2004; Kumjian, 2013a). Like in dry tumbling hail, the intrinsic K_{DP} in large dry snow aggregates is close to zero and K_{DP} estimates can be very noisy (Kumjian, 2013a), but K_{DP} can be enhanced in the presence of pristine ice crystals with values > 0.5 deg km^{-1} (e.g., Kennedy and Rutledge, 2011) and strongly enhanced in melting snow or hail (Kumjian, 2013a).

As an electromagnetic wave emitted by a weather radar travels through the atmosphere filled with hydrometeors, it loses amplitude due to absorption and scattering of the transmitted energy by atmospheric gases and hydrometeors. The specific attenuation at horizontal polarization A_H (given in dB km^{-1}) quantifies this loss of energy in the horizontal polarization channel and is defined by

$$A_H = -8.686\lambda * \mathrm{Im}(\langle s_{HH}^{(0)} \rangle) \tag{2.36}$$

with $\mathrm{Im}(c)$ the imaginary part of a complex number c (likewise, the specific attenuation in the vertical channel A_V can be defined; Ryzhkov and Zrnic, 2019). Analogue to Eq. (2.34), Eq. (2.36) can be written as

$$A_H = -8.686\lambda * \left\{ \mathrm{Im}(\langle s_b^{(0)} \rangle) - M_2 \mathrm{Im}(\langle s_b^{(0)} - s_a^{(0)} \rangle) \right\} \tag{2.37}$$

(Ryzhkov and Zrnic, 2019). A_H depends on the physical composition of hydrometeors (e.g., size and dielectric constant) in a radar resolution volume, the

temperature, and is inversely related to the radar wavelength, so that radar measurements at shorter wavelengths (e.g., X- or C-band) are subject to larger attenuation compared to longer wavelengths (e.g., S-band; Kumjian, 2013b). In addition, A_H also depends on the particle size distribution, but is a lower-order moment of the size distribution in rain ($A_H \sim D^{3+\eta}$ with η between 0.5 and 0.8; Ryzhkov and Zrnic, 2019) compared to $Z_{H/V}$ and also K_{DP}, which has made it particularly interesting for QPE in the past years (Ryzhkov et al., 2014; Diederich et al., 2015). Like K_{DP}, A_H cannot be calculated in practice from Eq. (2.37), because forward scattering from hydrometeors cannot be measured by monostatic weather radars. However, a relationship between K_{DP} and A_H is obtained by considering the linear attenuation correction proposed by Bringi et al. (1990)

$$\Delta Z_H = \alpha \Phi_{DP} = 2\alpha \int_0^r K_{DP}(l) dl \tag{2.38}$$

with ΔZ_H the reduction in horizontal reflectivity by attenuation, α the attenuation parameter in dB deg^{-1}, and assuming the two-way path-integrated attenuation PIA

$$\mathrm{PIA} = 2 \int_0^r A_H(l) dl \tag{2.39}$$

given in dB to be equal to ΔZ_H and the parameter α to be constant, which is

$$A_H = \alpha K_{DP}. \tag{2.40}$$

The attenuation parameter α is sensitive to temperature and variations in the drop size distribution (DSD), and for C-band radars, a climatological value for rain of 0.08 dB deg^{-1} is suggested, while for the correction of differential attenuation a climatological differential attenuation parameter β of 0.02 dB deg^{-1} is commonly used (e.g., Ryzhkov and Zrnic, 2019).

A more sophisticated approach to estimate A_H is the ZPHI-method following Testud et al. (2000), which estimates A_H from attenuated (measured) reflectivity $z_{H,att}$ using PIA (see Eq. (2.39)) as a constraint by

$$A_H(r) = \frac{\left[z_{H,att}(r)\right]^{b_{ZPHI}} C(b_{ZPHI}, \mathrm{PIA})}{I(r_1, r_2) + C(b_{ZPHI}, \mathrm{PIA}) I(r, r_2)} \tag{2.41}$$

with

$$C(b_{ZPHI}, \mathrm{PIA}) = \exp[0.23 b_{ZPHI} \mathrm{PIA}(r_1, r_2)] - 1, \tag{2.42}$$

$$I(r_1, r_2) = 0.46 b_{ZPHI} \int_{r_1}^{r_2} \left[z_{H,att}(l)\right]^{b_{ZPHI}} dl, \tag{2.43}$$

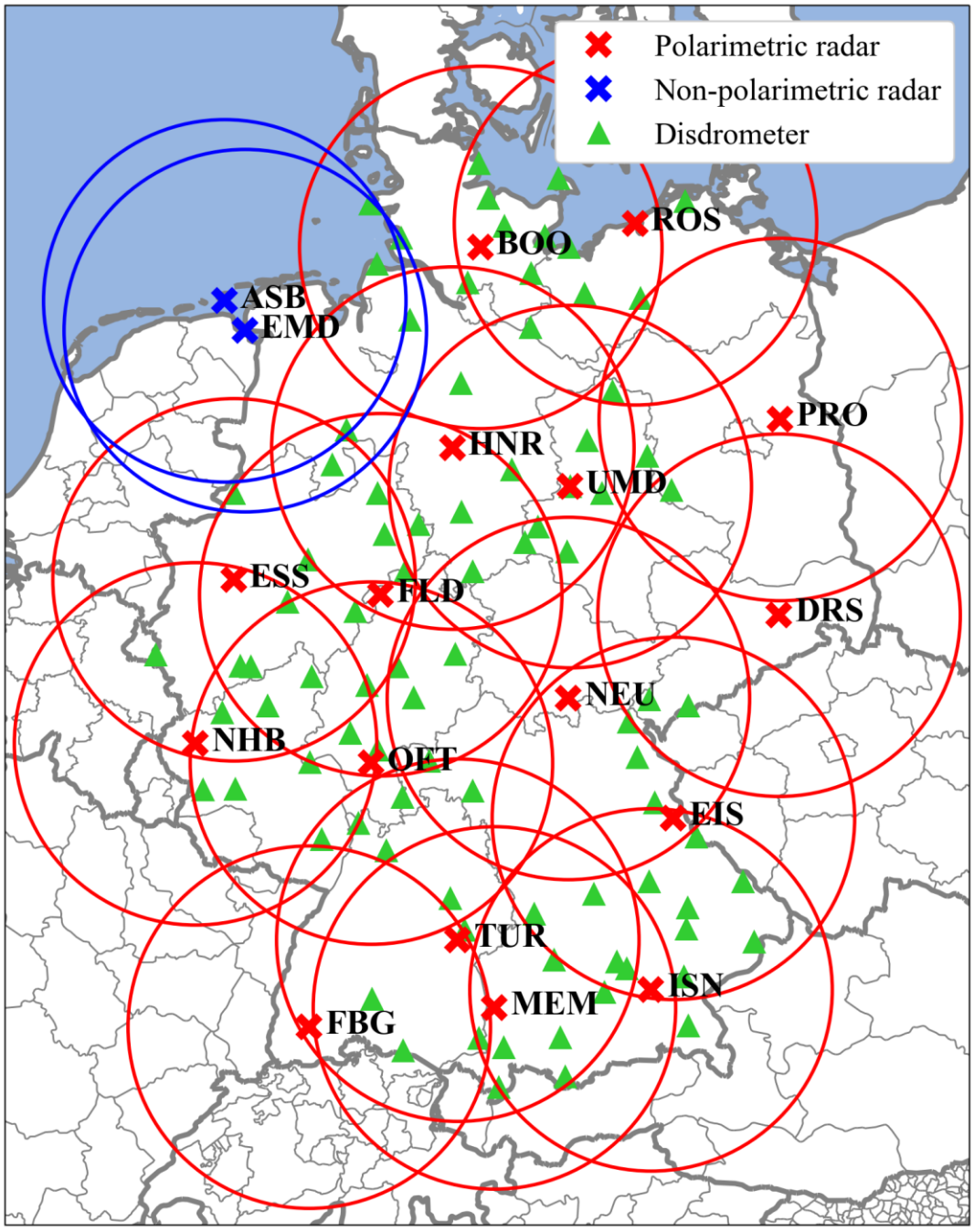

FIGURE 2.1: Stereographic projection of the area covered by the German national C-band weather radar network operated by DWD with polarimetric radars (indicated by red crosses; red circles indicate the approximate 150 km ranges around the radars) in Rostock (ROS), Boostedt (BOO), Prötzel (PRO), Hannover (HNR), Ummendorf (UMD), Essen (ESS), Flechtdorf (FLD), Dresden (DRS), Neuhaus (NEU), Neuheilenbach (NHB), Offenthal (OFT), on Eisberg (EIS), in Türkheim (TUR), Isen (ISN), Memmingen (MEM), and on Feldberg (FBG), and non-polarimetric radars (indicated by blue crosses and circles) in Emden (EMD) and on the island Borkum (ASB). The ASB radar is used only in case of system failure of the EMD radar. Green triangles indicate locations of the DWD/University-of-Bonn surface-based Thies-disdrometers from which observations are used for the development and evaluation of LWC estimators in Chapter 3.

and

$$I(r, r_2) = 0.46 b_{ZPHI} \int_r^{r_2} \left[z_{H,att}(l) \right]^{b_{ZPHI}} dl. \quad (2.44)$$

In Eqs. (2.41) through (2.44), b_{ZPHI} is the exponent of an empirical power-law relation between unattenuated reflectivity z_H and specific attenuation A_H (Ryzhkov et al., 2013) and r_1 and r_2 are the lower and upper limits of the range window between which A_H at the range r is to be calculated (Testud et al., 2000; Ryzhkov et al., 2013).

2.1.3 The German National C-Band Radar Network

DWD operates a network of 18 C-band (approximate wavelength of 53 mm) Doppler weather surveillance radars covering the whole of Germany (Fig. 2.1). Sixteen of these radars have polarimetric capabilities (red radars in Fig. 2.1) and measure in SHV-mode. The remaining two radars are non-polarimetric radars (blue radars in Fig. 2.1) of which the radar on the island of Borkum (ASB radar in Fig. 2.1) is only used for system failure of the radar in Emden (EMD). The radar moments provided by the polarimetric radars include Z_H and Z_V, Z_{DR}, ρ_{HV}, Φ_{DP}, and V_r, while the two non-polarimetric radars only provide Z_H and V_r. All radars follow a scan schedule that is repeated every 5 min and starts with a so-called "precipitation-scan" at low and terrain-following radar elevation angles with an azimuthal resolution of 1 deg and a range resolution of 0.25 km with a maximum slant range of about 150 km. The precipitation-scan is followed by so-called "volume-scans" consisting of the plan position indicators (PPI) monitored at the 10 elevation angles 0.5, 1.5, 2.5, 3.5, 4.5, 5.5, 8.0, 12.0, 17.0, and 25.0 deg. The volume-scan PPIs have an azimuthal resolution of also 1 deg like the precipitation-scan PPIs and a range resolution of only 1 km. In March 2021, the radial resolution was increased to 0.25 km at DWD. The maximum slant range is 180 km for radar elevation angles from 0.5 to 5.5 deg, 124 km for 8.0 deg, and 60 km for the higher elevation angles. The scan routine is completed with a vertical scan, which is used for radar calibration. A more detailed description of the scanning routine at DWD can be found in Helmert et al. (2014).

2.2 Existing Microphysical Retrievals for C-Band Radars

This section reviews the existing LWC and IWC estimators for C-band radars proposed in the literature potentially usable for polarimetric DA in Germany.

2.2.1 Liquid Water Content

One of the first LWC retrievals (hereafter, LWC is always in units of g m^{-3}) based on horizontal reflectivity Z_H was proposed by Greene and Clark (1972) as

$$\mathrm{LWC}(z_H) = 3.44 * 10^{-3} * z_H^{0.57} \tag{2.45}$$

with z_H the linear horizontal reflectivity given in $\mathrm{mm}^6\,\mathrm{m}^{-3}$. Equation (2.45) was developed based on theoretical considerations with the assumption of rain DSDs following the well-known Marshall-Palmer distribution (Marshall and Palmer, 1948) and has been used to estimate the horizontal distribution of the liquid water path – the vertically integrated LWC – of mesoscale convective systems, and is still a commonly used tool to quantify storm intensity and the potential of storms to produce hail (Ryzhkov and Zrnic, 2019).

More recently, Carlin et al. (2016) introduced the empirical relation

$$\mathrm{LWC}(z_H) = 1.59 * 10^{-3} * z_H^{0.657} \tag{2.46}$$

developed based on a large disdrometer data set (about 47,000 unique DSDs) from Oklahoma, including stratiform and convective rainfall data, and warm-rain T-matrix scattering calculations at a C-band radar wavelength (53 mm). A very similar estimator, also based on a large disdrometer data set from Oklahoma and scattering calculations at C-band, was later proposed in the book of Ryzhkov and Zrnic (2019) and is given by

$$\mathrm{LWC}(z_H) = 1.58 * 10^{-3} * z_H^{0.659}. \tag{2.47}$$

Carlin et al. (2016) also proposed $\mathrm{LWC}(Z_H)$ estimators adapted to precipitation type using the normalized number concentration of raindrops N_w (given in $\mathrm{m}^{-3}\,\mathrm{mm}^{-1}$)

$$N_w = \frac{\frac{4^4}{\pi\rho_w} * \mathrm{LWC}}{D_m^4} \tag{2.48}$$

with ρ_w the density of water, D_m the mean volume diameter of raindrops defined as the ratio between the third and the fourth DSD moments given in mm (Testud et al. 2001). N_w can be interpreted as the y-axis intercept of an exponential DSD with the same D_m and LWC values like the real DSD (Carlin et al., 2016). The proposed parameterized relation for C-band is

$$\mathrm{LWC}(z_H, N_w) = 1.51 * 10^{-4} * z_H^{0.572} N_w^{0.363}. \tag{2.49}$$

Another approach undertaken by Carlin et al. (2016) to improve their $\mathrm{LWC}(Z_H)$ relation by parameterizing it with additional information about precipitation is the empirical bivariate power-law relation

$$\mathrm{LWC}(z_H, z_{DR}) = 1.29 * 10^{-3} * z_H^{0.701} z_{DR}^{-0.790} \tag{2.50}$$

with z_{DR} linear and unitless. Also Bringi and Chandrasekar (2001) proposed a $\mathrm{LWC}(z_H, z_{DR})$ relation based on physical considerations and scattering calculations for C-band radars given by

$$\mathrm{LWC}(z_H, z_{DR}) = 0.6 * 10^{-3} * z_H^{0.85} z_{DR}^{-2.36}. \tag{2.51}$$

The specific attenuation at horizontal polarization A_H has been identified to be strongly beneficial for QPE (Ryzhkov et al., 2014; Diederich et al., 2015) and may thus also favor the estimation of LWC. A univariate $\mathrm{LWC}(A_H)$ relation was proposed by Carlin et al. (2016) and is given by

$$\mathrm{LWC}(A_H) = 11.0 A_H^{0.777} \tag{2.52}$$

with A_H in dB deg^{-1}. The corresponding $\mathrm{LWC}(A_H)$ relation proposed by Ryzhkov and Zrnic (2019) is again very similar to the one introduced by Carlin et al. (2016) in Eq. (2.52) and is given by

$$\mathrm{LWC}(A_H) = 11.6 A_H^{0.794}. \tag{2.53}$$

Univariate LWC retrievals based on specific differential phase K_{DP} have also been proposed in the literature. Carlin et al. (2016) suggested the relation

$$\mathrm{LWC}(K_{DP}) = 1.27 K_{DP}^{0.714} \tag{2.54}$$

with K_{DP} given in deg km^{-1}. Again, a very similar estimator was presented by Ryzhkov and Zrnic (2019) given by

$$\mathrm{LWC}(K_{DP}) = 1.28 K_{DP}^{0.713}. \tag{2.55}$$

In the books of Bringi and Chandrasekar (2001) and Doviak and Zrnic (2006), power-law $\mathrm{LWC}(K_{DP})$ relations developed based on physical considerations and scattering calculations were proposed. They can be written in a generalized form following Ryzhkov and Zrnic (2019) as

$$\mathrm{LWC}(K_{DP}) = c_1 (K_{DP} \lambda * 10)^{c_2} \tag{2.56}$$

with $c_1 = 0.26$ and $c_2 = 0.77$ in Bringi and Chandrasekar (2001) and $c_1 = 0.34$ and $c_2 = 0.702$ in Doviak and Zrnic (2006), and λ the radar wavelength in mm.

In addition, a bivariate power-law LWC estimator combining K_{DP} and Z_{DR} has been proposed by Bringi and Chandrasekar (2001) for C-band as

$$\mathrm{LWC}(K_{DP}, z_{DR}) = 2.32 K_{DP}^{0.83} z_{DR}^{-1.11}. \tag{2.57}$$

2.2.2 Ice Water Content

A number of studies in the literature proposed power-law IWC(Z_H) relations (e.g., Sekhon and Srivastava, 1970; Sassen, 1987; Atlas et al., 1995; Liu and Illingworth, 2000; Hogan et al., 2006; Delanoe et al., 2014; Heymsfield et al., 2016). The inherent uncertainty in these proposed reflectivity-based IWC estimators is primarily due to the variability in the ice/snow particle size distribution, but also, to a lesser extent, due to the variability in the density of frozen hydrometeors (Ryzhkov and Zrnic, 2019). Under the assumption of an exponential particle size distribution and a power-law relationship between particle density and particle diameter, Ryzhkov and Zrnic (2019) derived the analytical expression

$$\mathrm{IWC}(z_H, N_{0s}, \kappa) = 3.81 * 10^{-4} \kappa^{-0.2} N_{0s}^{0.4} z_H^{0.6} \tag{2.58}$$

with N_{0s} the y-axis intercept of an exponential particle size distribution and κ a factor related to the degree of riming. Ryzhkov and Zrnic (2019) further stated that the considerable differences between the IWC(Z_H) relations proposed in the literature can be explained by the large variability in the observable N_{0s}, which has been shown to vary by four orders of magnitude for snow in Oklahoma (Bukovcic et al., 2018).

Also some IWC retrievals using phase-based polarimetric variables have been proposed in the literature. A first relation between IWC and K_{DP} was proposed by Vivekanandan et al. (1994), who used K_{DP} and Z_{DR} to estimate IWC in ice clouds consisting of pristine ice crystals. Later, Ryzhkov et al. (1998) proposed another relation using K_{DP} and Z_{DR} based on physical considerations applicable to pristine or lightly to moderately aggregated ice crystals, which is given by

$$\mathrm{IWC}(K_{DP}, z_{DR}) = 4.46 * 10^{-3} \frac{K_{DP} \lambda}{1 - z_{DR}^{-1}}. \tag{2.59}$$

The estimator in Eq. (2.59) is largely insensitive to the ice particle shape and orientation, because the nominator and denominator are proportionally affected by both (Ryzhkov and Zrnic, 2019). However, Eq. (2.59) is sensitive to the particle density and thus to the degree of riming, and is negatively affected by errors due to Z_{DR} bias, especially in areas of low Z_{DR}, such as in aggregated snow (Carlin et al., 2021). Equation (2.59) was used with a slightly modified prefactor in Carlin et al. (2021) as

$$\mathrm{IWC}(K_{DP}, z_{DR}) = 4.0 * 10^{-3} \frac{K_{DP}\lambda}{1 - z_{DR}^{-1}} \tag{2.60}$$

in combination with the $\mathrm{IWC}(K_{DP}, z_H)$ relation of Bukovcic et al. (2018, 2020)

$$\mathrm{IWC}(K_{DP}, z_H) = 3.3 * 10^{-2} (K_{DP}\lambda)^{0.67} z_H^{0.33}. \tag{2.61}$$

Carlin et al. (2021) notes that the estimator in Eq. (2.61) is immune to Z_{DR} miscalibration and affected by particle orientations, shapes, and densities. They combined Eqs. (2.60) and (2.61) considering their respective advantages and disadvantages: Eq. (2.61) is used when Z_{DR} < 0.4 dB and Eq. (2.60) is used when $Z_{DR} \geq 0.4$ dB. The high accuracy of this hybrid estimator (Pearson correlation coefficient PCC of 0.96 and root mean square deviation RMSD of 0.19 g m^{-3}) was demonstrated by Blanke et al. (2023) in an evaluation study with airplane in-situ observations on the west coast of the USA. Both parts of the hybrid IWC estimator in Eqs. (2.60) and (2.61), however, have been adjusted for snowfall – their derivations are based on an inversely proportional relationship between particle density and diameter, which usually does not hold for hail and graupel. Therefore, its applicability to hail and graupel, which is likely present in intense convective summer precipitation in Germany, may be limited.

Chapter 3

A Hybrid Liquid Water Content Retrieval for C-Band Radars

Most of the polarimetric LWC and IWC retrievals for C-band radars proposed in the literature (see a review in Section 2.2) were developed for utilization in the USA with its different precipitation climatology compared to Germany. Thus, their suitability for the indirect assimilation of polarimetric radar observations in Germany may be limited. In Section 3.2, the applicability of the existing LWC retrievals to German C-band radar network in rain is evaluated using a large pure-rain disdrometer data set from Germany and T-matrix scattering calculations at C-band (the data used and their processing are detailed in Section 3.1). Based on different (sets of) T-matrix simulated polarimetric radar variables, new LWC relations are developed and subsequently combined in a hybrid way taking into account the respective advantages and disadvantages of the different used polarimetric variables known for different precipitation characteristics. In Section 3.3, the new (hybrid) LWC relations and the existing LWC retrievals for C-band radars are evaluated with observations from the German C-band radar network. The approaches and results presented in this chapter follow those published in Reimann et al. (2021) and any deviations in this thesis are shown and discussed.

A comparable evaluation of the existing IWC relations from the literature (also reviewed in Section 2.2) and the development of new IWC algorithms adapted to Germany are not performed. One reason is that measurements in the ice phase by the DWD disdrometers are too limited due to the rather rare occurrence of snow on the ground in Germany. Another reason is the limitation of the widely used instruments to accurately measure particle size distributions in snow and ice (e.g., Battaglia et al., 2010). More suitable instruments, such as the 2DVD-disdrometers or the Multi-Angle Snowflake Camera (e.g., Praz et al., 2017), are not yet widely used by DWD.

3.1 Data Sets and Processing

First, the German disdrometer data and their processing, including T-matrix scattering calculations at C-band (53 mm), used to develop and evaluate new and existing LWC relations based on simulations are detailed. In a second step, the polarimetric observations from the German C-band radar network used for the

evaluation of the new and existing LWC retrievals in a real-world application including their processing are presented.

3.1.1 Disdrometer Observations

For the evaluation and development of LWC retrievals in this thesis, a large DSD data set obtained from 89 surface-based Thies-disdrometers (see respective locations as green triangles in Fig. 2.1), 88 from the DWD observation network and one further from the University of Bonn, from the years 2015 to 2019 is used. The provided data include measurements of the diameters and fall velocities of individual particles averaged over 1 min and are structured in 22 diameter classes from 0.125 to 8.0 mm and 20 velocity classes from zero to 11 m s^{-1} in 2D matrices $\boldsymbol{M}_{DSD}$ (the sum of $\boldsymbol{M}_{DSD}$ over all times and stations is shown in Fig. 3.1). The equivalent-volume spherical diameter D (in mm) and the terminal fall velocity v_t (in m s^{-1}) of raindrops are related according to Brandes et al. (2002) by the polynomial function

$$v_t(D) = -0.1021 + 4.932D - 0.9551D^2 + 0.07934D^3 - 0.002362D^4. \tag{3.1}$$

Individual particles with measured fall velocities less than 50 % or greater than 150 % of the corresponding value expected from the relation in Eq. (3.1) (black solid and dotted curves in Fig. 3.1) and all 2D matrices $\boldsymbol{M}_{DSD}$ corresponding to a non-zero intensity of solid precipitation as identified by the Thies-disdrometer software are excluded from the data set to avoid contamination by, e.g., frozen particles or insects. Frozen particles are further excluded by removing all data corresponding to an outside temperature measured by the Thies-disdrometers below the freezing level. Data contaminated by, e.g., insects in situations without significant rainfall (less than 10 particles in total) are further excluded, leaving approximately 818,000 individual 2D DSD matrices $\boldsymbol{M}_{DSD}$ for analysis.

Raindrop size distributions $N(D)$ given in $m^{-3}\,mm^{-1}$ are determined by sums of $\boldsymbol{M}_{DSD}$ over all velocity classes $\boldsymbol{M}_{DSD,d}$ via

$$N(D) = \boldsymbol{M}_{DSD,d}(D) * (A_{Thies} * \Delta\tau_{DSD} * v_t(D) * \mathrm{DCW}(D))^{-1} \tag{3.2}$$

with A_{Thies} the detection area of the Thies-disdrometers in m^2, $\Delta\tau_{DSD}$ the considered time interval (given in s), v_t the terminal fall velocity of raindrops in m s^{-1} following Brandes et al. (2002) in Eq. (3.1), and DCW the widths of the diameter classes of the disdrometers in mm. LWC can be calculated with the third moment of the DSDs by

$$\mathrm{LWC} = 10^{-9}\frac{\rho_w \pi}{6}\int_0^\infty D^3 N(D) dD \tag{3.3}$$

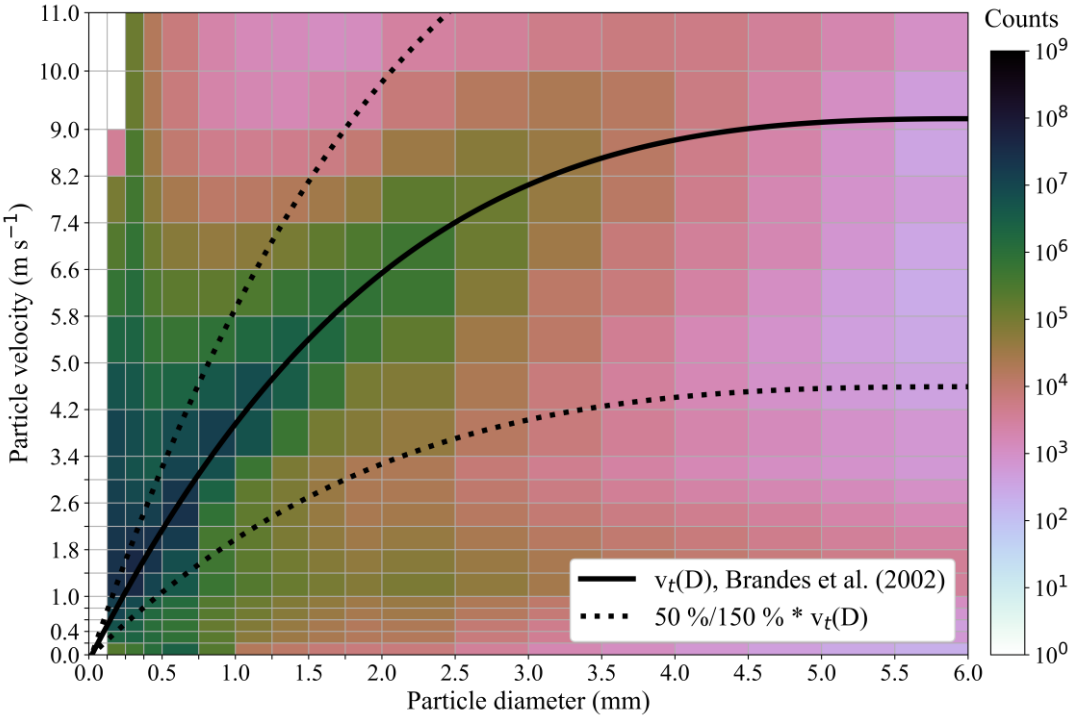

FIGURE 3.1: Total counts of 1 min average particle numbers observed in different Thies-disdrometer particle diameter (in mm) and particle fall velocity (in m s^{-1}) classes in the raw large surface-based Thies-disdrometer data set obtained from DWD surface stations and the University of Bonn (locations of used disdrometers as green triangles in Fig. 2.1). The black solid curve shows the relationship between raindrop diameter and terminal fall velocity proposed by Brandes et al. (2002) in Eq. (3.1) and the upper and lower dotted black curves show 150 % and 50 % of this expected relationship, respectively.

with ρ_w the density of liquid water in g m^{-3} (e.g., Carlin et al., 2016). Furthermore, the T-matrix algorithms[1] of Leinonen (2014) are used to simulate synthetic polarimetric radar variables for each DSD at C-band (53 mm). The simulations are based on a maximum raindrop diameter of 8 mm, a Gaussian-shaped raindrop canting angle distribution with a width of 10 deg and a mean of 0 deg, the axis-ratio relation according to Brandes et al. (2002), and a complex refractive index calculated as a function of the exterior temperature measured by the Thies-disdrometers. The simulated polarimetric radar moments are Z_H, Z_{DR}, K_{DP}, and A_H.

3.1.2 Polarimetric Observations

The polarimetric data from the C-band radar network of DWD used in this chapter for the evaluation of existing and new LWC retrieval algorithms in a real-world application include observations of Z_H, Z_{DR}, ρ_{HV}, and Φ_{DP}. The data are from the 10

[1] *Used open source T-matrix algorithms for Python by Leinonen (2014) available under https://github.com/jleinonen/pytmatrix (last accessed 25 May 2019).*

polarimetric radars in Boostedt (BOO), Rostock (ROS), Essen (ESS), Ummendorf (UMD), Flechtdorf (FLD), Neuheilenbach (NHB), Offenthal (OFT), Memmingen (MEM), Isen (ISN), and on Eisberg (EIS; see red stations in Fig. 2.1). PPIs at only the two lowest radar elevation angles of 0.5 and 1.5 deg of the volume-scans performed at DWD are used, because data below the melting layer at higher elevations are mostly too limited. The focus is on nine summer precipitation events to ensure a sufficiently high melting layer and thus a sufficient amount of data usable for evaluation. The first four events considered on 20 June 2016, and 24, 25, and 26 July 2017 were dominated by stratiform precipitation. Another five events considered on 19 July 2017, 28 July 2018, 9 August 2018, 20 July 2019, and 29 August 2019 were dominated by convective rainfall. The data have a temporal, radial, and azimuthal resolution of 5 min, 1 km, and 1 deg, respectively, with maximum slant ranges of about 180 km (see Section 2.1.3).

The data are restricted to pure rain below the melting layer, the height of which is determined by Quasi-Vertical Profiles (QVP), i.e., azimuthal medians of PPIs at sufficiently high elevation angles transferred to a time-height display (e.g., Trömel et al., 2014; Ryzhkov et al., 2016), of ρ_{HV} and Z_{DR}, as performed here at a radar elevation angle of 5.5 deg, or by means of the height of the freezing level (the height of the 273.15 K isotherm) measured by the closest operational radio sounding of DWD. The latter approach is used when it is difficult to determine the height of the melting layer using QVPs, such as in convective situations with strong vertical mixing and thus no clear bright band. The use of measurements from the DWD lidar ceilometer network may have the potential to improve the detection of the melting layer height (e.g., Sassen and Chen, 1995), but this approach is not followed in this study due to limited data access. Kumjian (2013a) notes that pure rain can be associated with ρ_{HV} values between 0.95 and 1.01 at S-band. The lower value of 0.95 is used here as quality threshold for the radar data below the melting layer by assuming its validity also at C-band. Unlike in Reimann et al. (2021), a noise correction of ρ_{HV} following Ryzhkov and Zrnic (2019) is performed before application of the ρ_{HV} threshold. This approach retains more data for evaluation, especially at greater distances from the radar station and at the boundaries of precipitation systems (not shown). The slight differences in the results due to this modification compared to Reimann et al. (2021) are highlighted and discussed. Furthermore, as in Reimann et al. (2021), data from ranges below 5 km are excluded from the analysis to reduce contamination by ground clutter.

The horizontal specific attenuation A_H is estimated by using the filtered and smoothed total differential phase Φ_{DP} below the melting layer and the measured (attenuated) horizontal reflectivity z_{att} using the ZPHI-method (see Eqs. (2.41) to (2.44); Testud et al., 2000). Different from Reimann et al. (2021), the used total increment in Φ_{DP} along a ray below the melting layer $\Delta\Phi_{DP}$ is determined by subtracting the mean of the last five values of Φ_{DP} from the mean of the first five values of Φ_{DP} instead of using only single values. This modification reduces noise in the $\Delta\Phi_{DP}$ estimate and consequently in the A_H estimates, especially in weaker

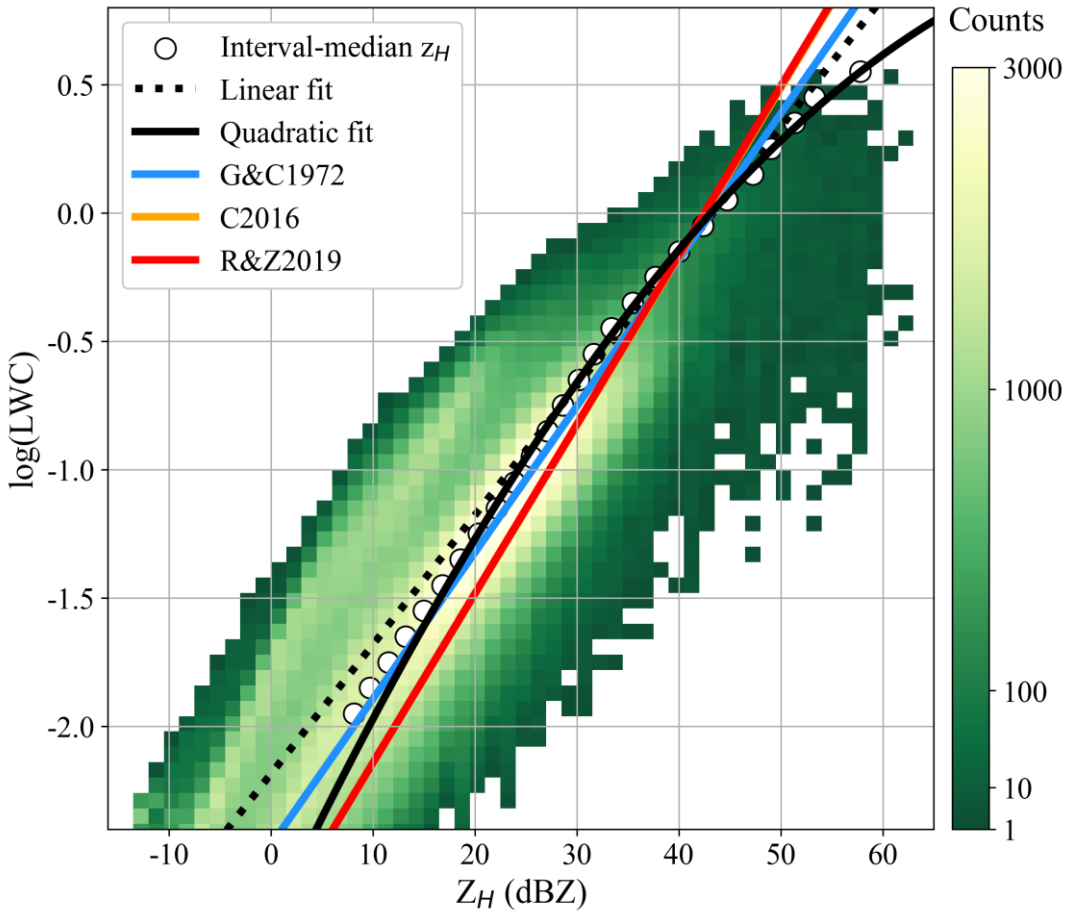

FIGURE 3.2: 2D histogram of pairs of T-matrix calculated Z_H and log(LWC) computed using Eq. (3.3) based on the large, filtered disdrometer data set of 1 min average pure-rain DSDs (about 818,000). White dots represent pairs of log(LWC)-interval centers (0.1-intervals from -2.0 to 0.6) and corresponding interval-median z_H values used to determine weighted fits to the data following the technique of Carlin et al. (2016) and Ryzhkov and Zrnic (2019). The black dotted and solid curves are weighted linear and quadratic fits to the data (Eqs. (3.6) and (3.7)), the blue curve depicts the LWC(Z_H) relation of Greene and Clark (1972; Eq. (2.45); "G&C1972"), and the orange and red curves show the relations of Carlin et al. (2016; Eq. (2.46); "C2016") and Ryzhkov and Zrnic (2019; Eq. (2.47); "R&Z2019"). The red curve mostly covers the orange curve due to similar relationships.

precipitation. The attenuation parameter α (the ratio between A and K_{DP} given in dB deg^{-1}, see Eq. (2.40)) is optimized for each radar ray below the melting layer using the self-consistency method of Bringi et al. (2001): for a ray with $\Delta\Phi_{DP} > 20$ deg, the α value is used that minimizes the difference between Φ_{DP} and the recalculated total differential phase obtained with the ZPHI-method; if no optimal α value is found in a certain range of allowed values (here 0.02 to 0.14 dB deg^{-1}) or if $\Delta\Phi_{DP} \leq 20$ deg, the climatological value for α of 0.08 dB deg^{-1} (Ryzhkov and Zrnic, 2019) is used. Proper estimation of the optimal α value can be challenging with the coarse radial resolution of the radar data used (1 km; recall that the used data is from before March 2021 when DWD increased the radial volume scan resolution from 1 to 0.25 km, see

Section 2.1.3) combined with the limited data available below the melting layer. The optimization of α may also be favored by determining $\Delta\Phi_{DP}$ from averages over five values instead of using only single values, as described above.

The specific differential phase K_{DP} is estimated from Φ_{DP} following the method of Vulpiani et al. (2012) with a fixed window size of 9 km. This rather large value is required to obtained relatively stable K_{DP} estimates and to keep noise rather low due to the coarse 1 km radial resolution of the analyzed PPIs. In regions of non-monotonically increasing Φ_{DP}, especially in weak rain, the few values contributing to the K_{DP} estimation with a 9 km window and the 1 km radial resolution (nine values) can lead to negative K_{DP} estimates. Using even larger window sizes to incorporate more radar pixels would average out local features in the precipitation fields too much, especially in convective cores. Later in this chapter, different approaches are tested to avoid the problems arising from negative K_{DP} values.

Measured Z_H and Z_{DR} values suffer from (differential) attenuation. Thus, both quantities must be corrected for (differential) attenuation before use in the evaluation of LWC algorithms. The correction is done following Ryzhkov and Zrnic (2019) by

$$Z_H = Z_{H,att} + \alpha\Phi_{DP} \tag{3.4}$$

and

$$Z_{DR} = Z_{DR,att} + \beta\Phi_{DP} \tag{3.5}$$

with $Z_{H,att}$ and $Z_{DR,att}$ the attenuated (measured) values of Z_H and Z_{DR}, α the climatological or, if available, optimized attenuation parameter, and the climatological differential attenuation parameter β for C-band of 0.02 dB deg^{-1}.

3.2 Retrieval Development and Evaluation with Simulations

In this section, new LWC retrievals adapted to the German C-band radar network are developed and both the new and the existing relations for C-band radars (reviewed in Section 2.2.1) are evaluated based on the described German DSD data set and the T-matrix scattering calculations performed. The bivariate LWC(K_{DP}, Z_{DR}) relation proposed by Bringi and Chandrasekar (2001) in Eq. (2.57) is not considered, because problems of the estimator in heavy rain due to negative effects of differential attenuation on Z_{DR} and in light rain because of noise in the K_{DP} estimates due to low signal-to-noise ratios (SNRs) in the underlying Φ_{DP} can be expected.

The quality of new and existing LWC retrievals is quantified by the root-mean-square deviation (RMSD), the Pearson correlation coefficient (PCC), and the mean-bias deviation (MBD) between the LWC calculated from the observed DSDs via Eq. (3.3) and the retrieval-estimated LWC using the DSD-based simulated polarimetric radar variables. New estimators are derived following the technique of

Carlin et al. (2016) and Ryzhkov and Zrnic (2019) of producing weighted least-squares fits of the logarithm of LWC, log(LWC), against the logarithm of the median simulated polarimetric radar variables calculated for 0.1-intervals of log(LWC). The intervals range from values of -2.0 (corresponding to $0.01\,\mathrm{g\,m^{-3}}$) and 0.6 (corresponding to about $4.0\,\mathrm{g\,m^{-3}}$) representing the approximate maximum log(LWC) in the DSD data. The weighting is done with respect to the number of observations in the log(LWC) intervals multiplied with the corresponding squared interval-center LWC values. This approach increases the weight also for the highest LWC values, which are only little represented in the DSD data set, but are especially important for the accuracy of the developed LWC retrievals even in stronger rain.

The retrieval development is performed after removing the circa 25,000 DSDs (about 3.1 % of the total DSD data set) that contribute to the retrieval evaluation with real C-band radar observations in Section 3.3 to allow for an independent evaluation. In Reimann et al. (2021), only about 21,000 DSDs were removed from the same total DSD data set, which is because in this thesis, unlike in Reimann et al. (2021), ρ_{HV} is corrected for noise before filtering (see Section 3.1.2), which retains more radar data for comparison with the disdrometer observations. Thus, less DSDs are used for the development and evaluation of retrieval relations with simulated radar data while more DSDs are used for evaluation with real radar observations in Section 3.3 compared to Reimann et al. (2021).

The LWC relations proposed in most other studies (e.g., Greene and Clark, 1972; Doviak and Zrnic, 2006; Carlin et al., 2016) are rather simple linear functions in the logarithmic scale (i.e., power-law relationships in the linear scale) between the logarithm of the polarimetric variables and log(LWC). In this thesis, higher-order polynomial fits like quadratic, cubic, or quartic functions (in the logarithmic scale) are also considered, while those fits with a non-zero y-axis intercept in the linear scale are excluded from the analysis.

3.2.1 Z_H-Based Retrievals

Starting with the development of $\mathrm{LWC}(Z_H)$ retrievals adjusted for use with German C-band radars, the linear and quadratic relations (black dotted and solid lines in Fig. 3.2) fitted to Z_H-log(LWC) pairs in the DSD data set

$$\log(\mathrm{LWC}(Z_H)) = 0.050 Z_H - 2.18 \tag{3.6}$$

and

$$\log(\mathrm{LWC}(Z_H)) = -0.0005 Z_H^2 + 0.084 Z_H - 2.77 \tag{3.7}$$

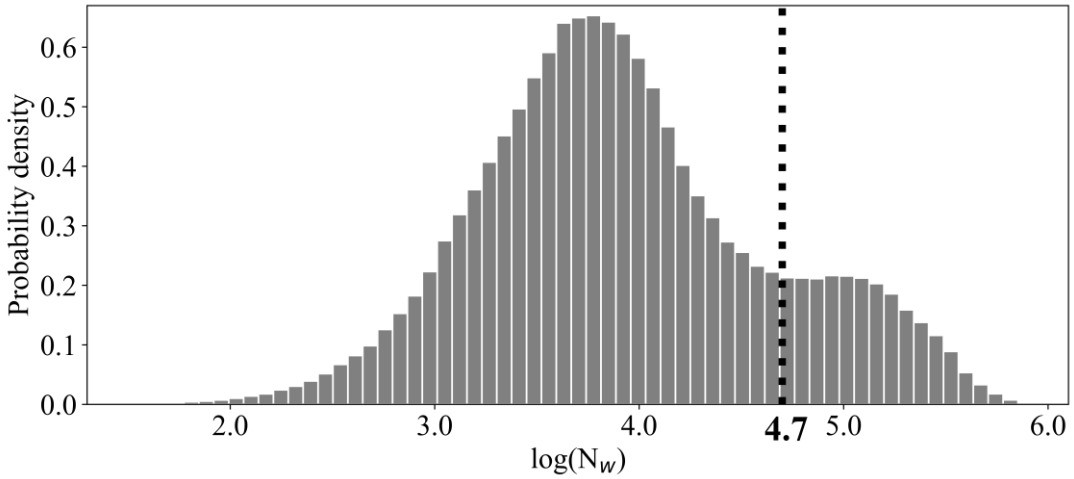

FIGURE 3.3: Probability density distribution of $\log(N_w)$ values (see Eq. (2.48)) in the large, filtered disdrometer data set of 1 min average pure-rain DSDs (about 818,000) used in this thesis for the development and evaluation of LWC estimators (grey bars). The black dotted vertical line indicates the position at which the DSD data set is separated for the retrieval development based on the different $\log(N_w)$ regimes corresponding to the primary and secondary maxima of the $\log(N_w)$ distribution.

with Z_H as before in dBZ and LWC in g m^{-3}. The comparison of the LWC retrieved from the simulated Z_H data via the linear and quadratic fits (Eqs. (3.6) and (3.7)) with the LWC calculated from the DSDs using Eq. (3.3) yields RMSDs of 0.12 and 0.10 g m^{-3}, PCCs of 0.75 and 0.79, and MBDs for both relations of 0.01 g m^{-3} (see all RMSD, PCC, and MBD values as black numbers in Table 3.1). Slight differences between some of the quality values and the corresponding values listed in Reimann et al. (2021) are due to the smaller number of DSDs for evaluation used in this thesis (quality values listed in Reimann et al. (2021) are shown as grey italicized numbers in Table 3.1 where they differ from this thesis). Cubic and quartic fits were also tested, but showed non-zero y-axis intercepts on the linear scale and were therefore excluded from the analysis. In this thesis, a given new LWC retrieval is considered to outperform another relation if at least two of the quality measures RMSD, PCC, and MBD considered are better. Thus, the quadratic fit in Eq. (3.7) is the preferred relation among the polynomial fits tested.

The existing LWC(Z_H) retrievals proposed by Greene and Clark (1972; see Eq. (2.45); blue curve in Fig. 3.2), Carlin et al. (2016; see Eq. (2.46); orange curve), and by Ryzhkov and Zrnic (2019; see Eq. (2.47); red curve) lead to worse RMSDs (0.14, 0.19, and 0.20 g m^{-3}), worse PCCs (0.69, 0.60, and 0.60), and similarly low MBDs (0.00, -0.01, and -0.01 g m^{-3}; see all quality values for the existing relations as black numbers also in Table 3.1) compared to the found quadratic relation adjusted to the German DSDs (0.10 g m^{-3}, 0.79, and 0.01 g m^{-3}). Again, there are slight changes in the quality values compared to those listed Reimann et al. (2021) due the

LWC Retrieval Input	Specification	RMSD (g m^{-3})	PCC	MBD (g m^{-3})
Z_H	G&C1972 (Eq. (2.45))	0.14	0.69	**0.00**
	C2016 (Eq. (2.46))	0.19 *0.20*	0.60	-0.01
	R&Z2019 (Eq. (2.47))	0.20	0.60	-0.01
	Linear fit (Eq. (3.6))	0.12 *0.11*	0.75	0.01
	Quadratic fit (Eq. (3.7))	**0.10**	**0.79** *0.80*	0.01
Z_H, Z_{DR}	B&C2001 (Eq. (2.51))	0.08	0.86	**-0.01**
	C2016 (Eq. (2.50))	0.09	0.79	**-0.01**
	Linear fit (Eq. (3.11))	**0.06**	**0.88**	**0.01**
A_H	C2016 (Eq. (2.52))	0.13	0.82	0.02
	R&Z2019 (Eq. (2.53))	0.14	0.81	0.02
	Linear fit (Eq. (3.12))	0.07	0.88	0.02
	Quadratic fit (Eq. (3.13))	**0.06**	**0.91**	**0.01**
	Cubic fit (Eq. (3.14))	**0.06**	**0.91**	**0.01**
K_{DP}	B&C2001 (Eq. (2.56))	0.07	0.83	-0.03
	D&Z2006 (Eq. (2.56))	**0.06**	0.85	-0.02 *0.01*
	C2016 (Eq. (2.54))	0.07	0.85	-0.01
	R&Z2019 (Eq. (2.55))	0.07	0.85	-0.01
	Linear fit (Eq. (3.15))	**0.06**	**0.87**	0.01
	Quadratic fit (Eq. (3.16))	0.07	**0.87**	**0.00**
	Cubic fit (Eq. (3.17))	0.07	**0.87**	**0.00**

TABLE 3.1: Comparison of the quality of the different tested existing and newly developed LWC(Z_H), LWC(Z_H, Z_{DR}), LWC(A_H), and LWC(K_{DP}) estimators in terms of RMSD (in g m^{-3}), PCC, and MBD (in g m^{-3}). The quality measures are determined from pairs of calculated LWC (in g m^{-3}) using Eq. (3.3) and the LWC retrieved from DSD-based T-matrix simulated polarimetric variables via the tested retrievals. The evaluated existing retrievals are those proposed by Greene and Clark (1972; "G&C1972"), Carlin et al. (2016; "C2016"), Bringi and Chandrasekar (2001; "B&C2001"), Ryzhkov and Zrnic (2019; "R&Z2019"), and Doviak and Zrnic (2006; "D&Z2006"). The quality values for the respective new fits to the DSD data are also shown. The best quality measures for specific retrieval types are printed in bold, the best among all tested retrievals are underlined. Grey italicized values indicate the corresponding values listed in Reimann et al. (2021) where they differ from this thesis.

differences in the evaluation data set. However, the new quadratic relation in this thesis still clearly outperforms all the existing relations in terms of RMSD and PCC.

The normalized number concentration N_w (see Eq. (2.48); Testud et al., 2001) is calculated for each DSD and its distribution shows a bimodal structure on the logarithmic scale (grey bars in Fig. 3.3). This bimodality can also be seen in the Z_H-log(LWC) histogram (see Fig. 3.2). Most DSDs can be associated with the primary maximum of the $\log(N_w)$ distribution (Fig. 3.3) at a value of about 3.7 – approximately followed by the tested LWC(Z_H) estimators (see Fig. 3.2). The secondary maximum of the $\log(N_w)$ distribution at a value of about 5.0 produces the secondary peak below 25 dBZ in the Z_H-log(LWC) histogram (see Fig. 3.2), which can be associated with DSDs dominated by very small raindrops, such as in drizzle

rain. Therefore, the use of different $\mathrm{LWC}(Z_H)$ estimators adapted to the different $\log(N_w)$ regimes may have the potential to improve the quality of LWC estimation. The DSD data corresponding to the primary $\log(N_w)$ maximum are here roughly separated from the DSDs corresponding to the secondary $\log(N_w)$ maximum at a $\log(N_w)$ value of 4.7 (see black dotted vertical line in Fig. 3.3). Polynomial fits are derived for both sub-data sets: the best $\mathrm{LWC}(Z_H)$ estimator for the low $\log(N_w)$ region (primary maximum in Fig. 3.3) is, like for the total DSD data set, a quadratic relation given by

$$\log\big(\mathrm{LWC}(Z_H)\big) = -0.0004 Z_H^2 + 0.084 Z_H - 2.87, \tag{3.8}$$

and for the secondary maximum in Fig. 3.3 a linear relation given by

$$\log\big(\mathrm{LWC}(Z_H)\big) = 0.050 Z_H - 1.70. \tag{3.9}$$

The similarity of the quadratic relation in Eq. (3.8) to that based on the full DSD data set in Eq. (3.7) emphasizes the dominance of the fits to the full data set by the data corresponding to the primary $\log(N_w)$ maximum. The combination of both relations (Eqs. (3.8) and (3.9)) gives an RMSD of 0.09 g m^{-3}, an PCC of 0.82, and an MBD of 0.01 g m^{-3} (values not shown in Table 3.1), which values are indeed slightly better than those of the found quadratic fit to the full data set (Eq. (3.7); 0.10 g m^{-3}, 0.79, and 0.01 g m^{-3}).

Another approach to include information from N_w in the estimation of LWC is the parameterization of $\mathrm{LWC}(Z_H)$ relations with N_w as suggested by, e.g., Carlin et al. (2016) noted in Eq. (2.49). Their parameterized relation yields, applied to the German DSD data set, further improved quality values (RMSD of 0.05 g m^{-3}, PCC of 0.94, and a zero MBD; values also not shown in Table 3.1). An alternative parameterized relation derived from the German DSDs is

$$\log\big(\mathrm{LWC}(Z_H, \log(N_w))\big) = 0.056 Z_H + 0.439 \log(N_w) - 4.09, \tag{3.10}$$

which, as expected, yields even better quality values (0.03 g m^{-3}, 0.97, and a zero MBD; values also not shown in Table 3.1). However, an application of Eqs. (3.8) through (3.10) to observations from the German C-band radar network showed much larger errors in the LWC estimation compared to the quadratic fit to the full DSD data set in Eq. (3.7) (not shown). One reason may be that proper estimation of N_w from real radar data, e.g., using the "ZZDR" algorithm of Illingworth and Thompson (2005) and Tabary et al. (2011) is challenging because it requires intrinsic (non-attenuated) high-quality values of Z_H and Z_{DR}, which is often difficult at shorter radar wavelengths (e.g., C- or X-band). In addition, the low radial resolution of the radar data used (1 km) may be a hindrance.

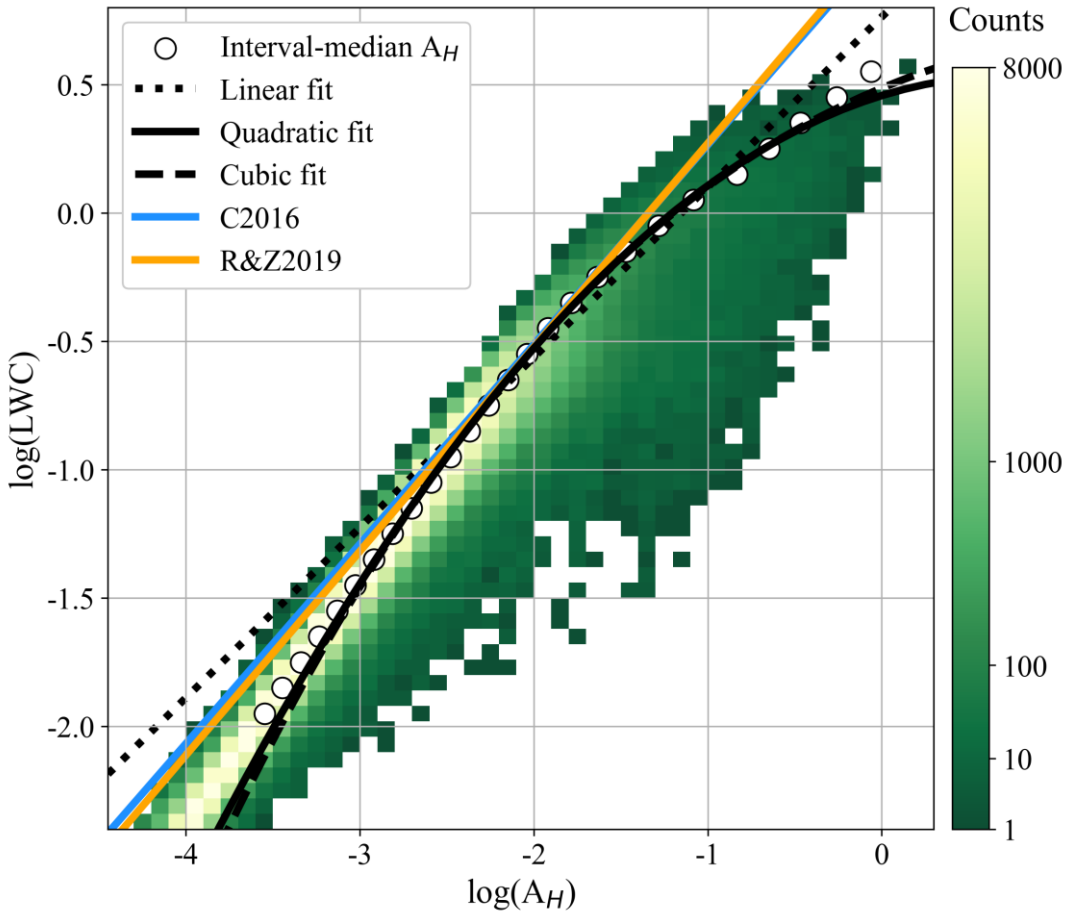

FIGURE 3.4: As Fig. 3.2, but with DSD-based pairs of T-matrix-calculated $\log(A_H)$ and log(LWC) computed using Eq. (3.3). White dots represent pairs of log(LWC)-interval centers (0.1-intervals from -2.0 to 0.6) and corresponding interval-median A_H used to determine weighted fits to the data. The black dotted, solid, and dashed curves are weighted linear, quadratic, and cubic fits to the DSD data (Eqs. (3.12) through (3.14)), the blue curve depicts the LWC(A_H) relation of Carlin et al. (2016; Eq. (2.52); "C2016"), and the orange curve draws the relation of Ryzhkov and Zrnic (2019; Eq. (2.53); "R&Z2019").

3.2.2 Z_H-Z_{DR}-Based Retrievals

A new LWC(Z_H) retrieval parameterized with the differential reflectivity Z_{DR} in the form of a bivariate linear fit derived from the German DSD data set is

$$\log\big(\mathrm{LWC}(Z_H, Z_{DR})\big) = 0.058Z_H - 0.118Z_{DR} - 2.36 \qquad (3.11)$$

with Z_{DR} as usual in dB. The relation in Eq. (3.11) results in an RMSD of 0.06 g m^{-3}, an PCC of 0.88, and an MBD of 0.01 g m^{-3}, and thus in clearly improved RMSDs and PCCs compared to the new quadratic LWC(Z_H) relation (Eq. (3.7); 0.10 g m^{-3} and 0.79). Bivariate polynomial fits and relations based on fitting the logarithmic ratio between LWC and Z_H as a polynomial function of Z_{DR} (personal communication

Alexander Ryzhkov, The University of Oklahoma) were also tested. These approaches only partially resulted in improved quality measures when applied to the simulated radar data (the fitting method suggested by Alexander Ryzhkov was tested with a third-order polynomial relation, which resulted in a worse RMSD of 0.08 g m^{-3}, a better PCC of 0.93, and a similar MBD compared to the new bivariate linear fit in Eq. (3.11); values not shown in Table 3.1), but led to strongly enhanced errors when applied to real observations from the German C-band radar network (not shown). Therefore, only the found bivariate linear fit in Eq. (3.11) is considered in this thesis.

The bivariate structure of the data seen in the $\log(N_w)$ distribution (Fig. 3.3) and in the Z_H-log(LWC) histogram in Fig. 3.2 is also evident in the 3D Z_H-Z_{DR}-log(LWC) histogram (not shown), which suggests that the development of separate relations for the two main N_w regimes potentially further improves the LWC(Z_H, Z_{DR}) retrieval quality. Although the adapted relations again gave better quality values compared to the bivariate linear relation fitted to the whole DSD data set in Eq. (3.11) when applied to the simulated data (RMSD of 0.05 g m^{-3}, PCC of 0.92, and MBD of 0.01 g m^{-3}; values not shown in Table 3.1), their application to real radar observations again resulted in clearly enhanced errors in the LWC estimation (not shown).

The LWC(Z_H, Z_{DR}) estimators proposed by Bringi and Chandrasekar (2001; Eq. (2.51)) and by Carlin et al. (2016; Eq. (2.50)) result in clearly worse RMSDs and PCCs (0.08 and 0.09 g m^{-3} and 0.86 and 0.79, see Table 3.1) compared to the new LWC(Z_H, Z_{DR}) relation (RMSD of 0.06 g m^{-3} and PCC of 0.88).

3.2.3 A_H-Based Retrievals

New LWC estimators based on A_H adapted to Germany are also derived in this thesis. The respective linear, quadratic, and cubic fits (drawn as dotted, solid, and dashed black curves in Fig. 3.4) are given by

$$\log\big(\mathrm{LWC}(A_H)\big) = 0.663\log(A_H) + 0.76, \tag{3.12}$$

$$\log\big(\mathrm{LWC}(A_H)\big) = -0.1415\log(A_H)^2 + 0.209\log(A_H) + 0.46, \tag{3.13}$$

and

$$\log\big(\mathrm{LWC}(A_H)\big) = 0.00985\log(A_H)^3 - 0.0924\log(A_H)^2 + 0.281\log(A_H) + 0.49. \tag{3.14}$$

The quadratic and cubic fits (Eqs. (3.13) and (3.14)) perform best with the same RMSDs, PCCs, and MBDs of 0.06 g m^{-3}, 0.91, and 0.01 g m^{-3}; thus, the quadratic fit in Eq. (3.13) is the preferred choice. A quartic fit was also tested, but resulted in a non-zero y-axis intercept at the linear scale and is therefore not considered.

The bimodal distribution previously identified in the $\log(N_w)$ data (see Fig. 3.3) can also be identified for the $\log(A_H)$-log(LWC) data pairs, although the secondary

maximum is very close to the primary maximum and therefore not clearly visible in Fig. 3.4. This finding emphasizes the lower sensitivity of the specific attenuation A_H to DSD variations compared to Z_H (see Section 2.1.2). As expected, the development of separate estimators for the two main N_w regimes did not lead to clear improvements over the quadratic relation fitted to the full data set.

The quite similar LWC(A_H) relations proposed by Carlin et al. (2016; Eq. (2.52)) and Ryzhkov and Zrnic (2019; Eq. (2.53)) result in similar and clearly worse quality measures RMSD (0.13 and 0.14 g m^{-3}), PCC (0.82 and 0.81), and MBD (both 0.02 g m^{-3}) compared to the new adjusted relation (Eq. (3.13); 0.06 g m^{-3}, 0.91, and 0.01 g m^{-3}) when applied to the simulated radar data.

3.2.4 K_{DP}-Based Retrievals

Finally, new univariate LWC estimators based on the specific differential phase K_{DP} are developed. Linear, quadratic, and cubic fits to the German DSD data set are

$$\log\big(\mathrm{LWC}(K_{DP})\big) = 0.568\log(K_{DP}) + 0.06, \tag{3.15}$$

$$\log\big(\mathrm{LWC}(K_{DP})\big) = -0.0315\log(K_{DP})^2 + 0.520\log(K_{DP}) + 0.05, \tag{3.16}$$

and

$$\log\big(\mathrm{LWC}(K_{DP})\big) = 0.00045\log(K_{DP})^3 - 0.0303\log(K_{DP})^2 + 0.521\log(K_{DP}) + 0.05. \tag{3.17}$$

The linear relation in Eq. (3.15) is the most suitable fit with an RMSD of 0.06 g m^{-3}, an PCC of 0.87, and an MBD of 0.01 g m^{-3} among the tested relations. Again, a quartic fit was also tested, but resulted in a non-zero y-axis intercept on the linear scale.

The $\log(K_{DP})$-log(LWC) data pairs in the German DSDs also show a clear bimodal structure as seen for $\log(N_w)$ in Fig. 3.3 with a secondary maximum located below $\log(K_{DP})$ values of -2.0 (see Fig. 3.5). Separated estimators adapted to the two main N_w regimes again resulted in better performance when applied to the simulated radar data (RMSD of 0.05 g m^{-3}, PCC of 0.92, and MBD of 0.01 g m^{-3}; values again not included in Table 3.1) compared to the new linear fit adjusted to the full DSD data set (Eq. (3.15); 0.06 g m^{-3}, 0.87, and 0.01 g m^{-3}); again, clearly enhanced LWC errors were obtained in the application to real radar observations (not shown).

The LWC(K_{DP}) relations proposed by Bringi and Chandrasekar (2001) and Doviak and Zrnic (2006; both Eq. (2.56) with corresponding coefficients), by Carlin et al. (2016; Eq. (2.54)), and in the book of Ryzhkov and Zrnic (2019; Eq. (2.55)) yield similar to slightly worse RMSDs (0.07, 0.06, 0.07, and 0.07 g m^{-3}) and MBDs (-0.03, -0.02, -0.01, and -0.01 g m^{-3}), and worse PCCs (0.83, 0.85, 0.85, and 0.85) compared to the new linear fit (Eq. (3.15); 0.06 g m^{-3}, 0.01 g m^{-3}, and 0.87). Note that the small

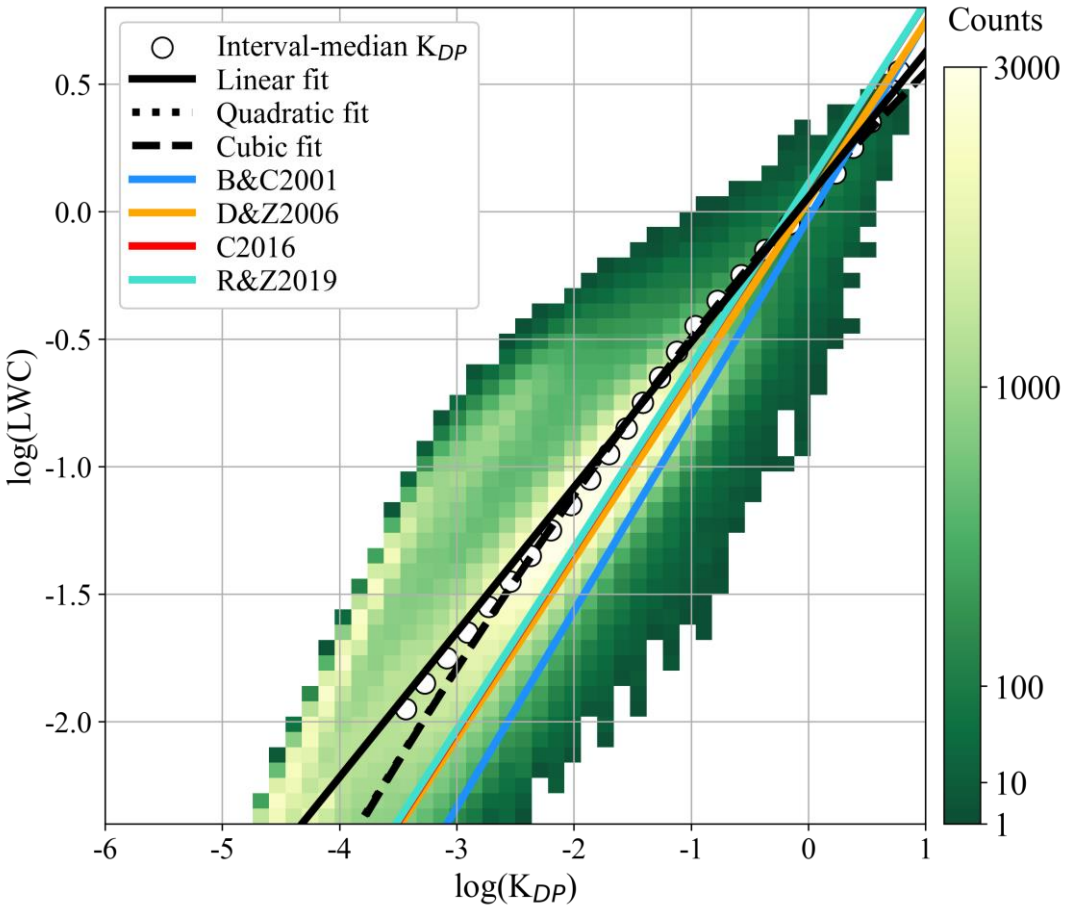

FIGURE 3.5: As in Figs. 3.2 and 3.4, but with DSD-based pairs of T-matrix-calculated $\log(K_{DP})$ and log(LWC) computed using Eq. (3.3). White dots represent pairs of log(LWC)-interval centers (0.1-intervals from -2.0 to 0.6) and corresponding interval-median K_{DP} values used to determine weighted fits to the data. Black solid, dotted, and dashed curves are weighted linear, quadratic, and cubic fits (Eqs. (3.15) through (3.17)), the blue, orange, red, and turquoise curves show the LWC(K_{DP}) relations of Bringi and Chandrasekar (2001; Eq. (2.56); "B&C2001"), Doviak and Zrnic (2006; Eq. (2.56); "D&Z2006"), Carlin et al. (2016; Eq. (2.54); "C2016"), and Ryzhkov and Zrnic (2019; Eq. (2.55); "R&Z2019").

difference in the MBD of the relation of Doviak and Zrnic (2006) compared to the value listed in Reimann et al. (2021) is again due to the changed evaluation data set.

3.2.5 A Hybrid Retrieval

The above analysis suggests that the combined use of the horizontal reflectivity Z_H and the differential reflectivity Z_{DR} for estimating LWC using the new bivariate linear relation in Eq. (3.11) is superior to estimating LWC from Z_H alone using the corresponding adjusted quadratic relation in Eq. (3.7) in terms of RMSD and PCC (see Table 3.1 and Fig. 3.6a,b). The results also show that the new quadratic LWC(A_H) relation in Eq. (3.13) further improves the quality of LWC estimation compared to the new LWC(Z_H, Z_{DR}) retrieval in terms of PCC, while the RMSDs and MBDs are

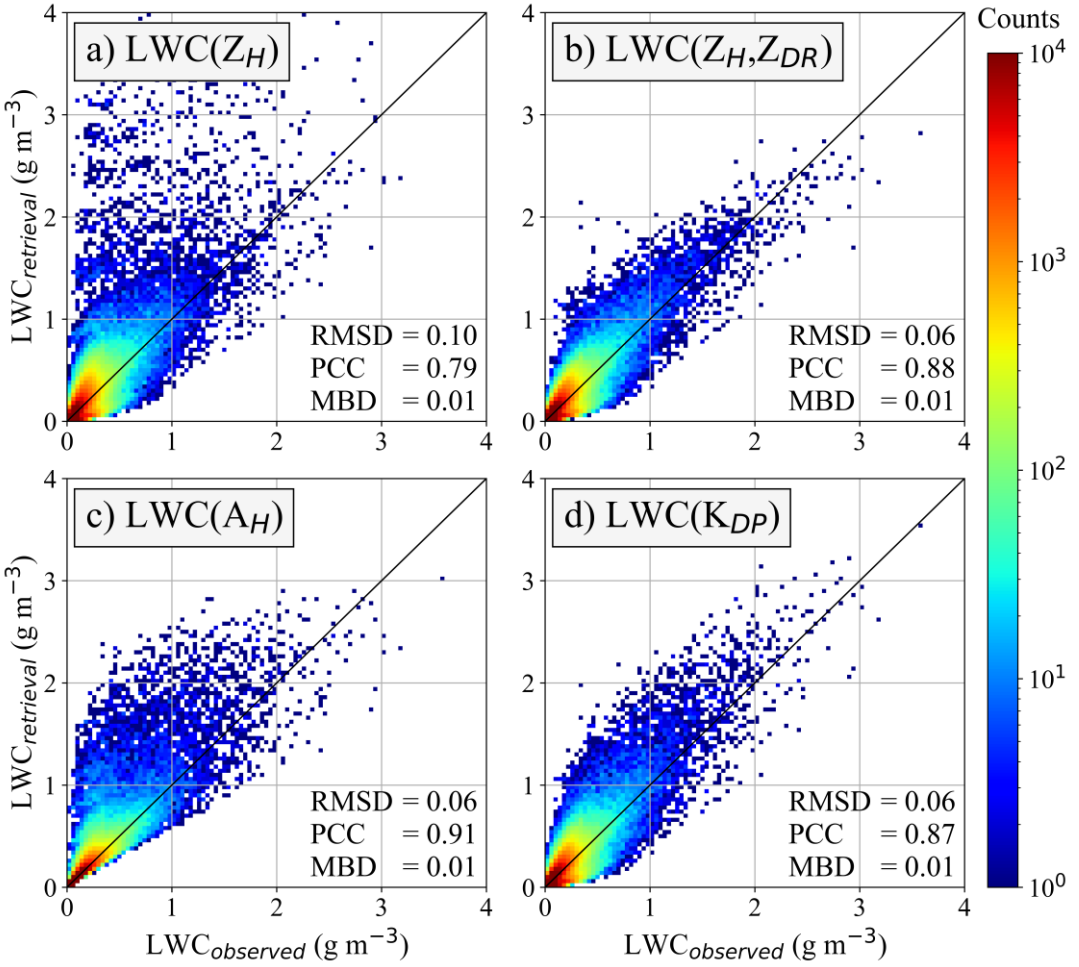

FIGURE 3.6: 2D histograms of DSD-based pairs of LWC (given in g m^{-3}) computed using Eq. (3.3) (LWC$_{observed}$) and LWC retrieved from T-matrix simulated radar variables (LWC$_{retrieval}$) via the new a) LWC(Z_H), b) LWC(Z_H, Z_{DR}), c) LWC(A_H), and d) LWC(K_{DP}) estimators (Eqs. (3.7), (3.11), (3.13), and (3.15)). Each subplot shows the respective quality values RMSD (given in g m^{-3}), PCC, and MBD (given in g m^{-3}).

comparable (Fig. 3.6b,c). The new linear LWC(K_{DP}) estimator in Eq. (3.15) also gives clearly better PCCs and RMSDs than the new LWC(Z_H) estimator in Eq. (3.7), while the PCC is slightly lower compared to the new LWC(Z_H, Z_{DR}) and LWC(A_H) estimators (see Table 3.1 and Fig. 3.6). However, for LWC above about 1.0 g m^{-3}, the new LWC(K_{DP}) estimator seems to perform best (see Fig. 3.6d).

The good performance of the new LWC(A_H) and LWC(K_{DP}) estimators is promising, because the polarimetric radar variables A_H and K_{DP}, as phase-based quantities, do not suffer from radar observation deficiencies such as (differential) attenuation, radar miscalibration, and partial beam-blockage (see Section 2.1.2). In practice, estimating LWC from real radar observations using A_H and K_{DP} can be challenging because the underlying Φ_{DP} suffers more from low SNRs at lower LWC. Conversely, the use of Z_H and Z_{DR} for the estimation of LWC can be challenging in regions of high LWC due to potential (differential) attenuation effects. Therefore, it

is desirable to combine the newly developed LWC retrievals (Eqs. (3.7), (3.11), (3.13), and (3.15)), so that the respective advantages and disadvantages of the different employed polarimetric radar moments known in different precipitation situations are taken into account. Such a hybrid LWC estimator is expected to retrieve LWC more accurately compared to the pure estimators and thus to favor the indirect assimilation of polarimetric information as performed in Chapter 5.

The total increment in total differential phase $\Delta\Phi_{DP}$ below the melting layer is a crucial measure for potential negative effects of (differential) attenuation on the data along a radar ray. If $\Delta\Phi_{DP}$ is less than 5 deg, the effects of (differential) attenuation on Z_H and Z_{DR} can be assumed to be small and the new LWC(Z_H) or LWC(Z_H, Z_{DR}) estimators can be applied along the entire radar ray below the melting layer. Since the adjusted LWC(Z_H, Z_{DR}) estimator was found to clearly outperform the new LWC(Z_H) estimator in terms of RMSD and PCC (see Table 3.1), the new LWC(Z_H, Z_{DR}) relation in Eq. (3.11) is used for the hybrid LWC retrieval in regions with low precipitation intensity. For radar rays with stronger rain and correspondingly stronger negative effects of (differential) attenuation on Z_H and Z_{DR}, as characterized by $\Delta\Phi_{DP} \geq 5$ deg, the new phase-based LWC(A_H) and LWC(K_{DP}) relations in Eqs. (3.13) and (3.15) are used. However, the LWC(A_H) estimator is less reliable in the presence of hail, requiring either an appropriate Z_H threshold or the prior use of a hydrometeor classification algorithm (e.g., Park et al., 2009; Dolan et al., 2013). For simplicity, a Z_H threshold of 45 dBZ as listed by Kumjian (2013a) as the lowest typical Z_H for hail at S-band is used by assuming its validity also at C-band. Accordingly, the new LWC(A_H) relation is applied if $\Delta\Phi_{DP} \geq 5$ deg and if $Z_H < 45$ dBZ. Otherwise, if $\Delta\Phi_{DP} \geq 5$ deg and $Z_H \geq 45$ dBZ, the new LWC(K_{DP}) retrieval is used, because K_{DP} is less affected by hail than A_H (e.g., Kumjian, 2013a). In summary, this thesis proposes the following hybrid LWC estimator for the indirect assimilation of polarimetric C-band radar observations in Germany:

$$\mathrm{LWC}(Z_H, Z_{DR}) \quad \text{for} \quad \Delta\Phi_{DP} < 5 \text{ deg}, \tag{3.18}$$

$$\mathrm{LWC}(A_H) \quad \text{for} \quad \Delta\Phi_{DP} \geq 5 \text{ deg} \quad \text{and} \quad Z_H < 45 \text{ dBZ}, \tag{3.19}$$

and

$$\mathrm{LWC}(K_{DP}) \quad \text{for} \quad \Delta\Phi_{DP} \geq 5 \text{ deg} \quad \textit{and} \quad Z_H \geq 45 \text{ dBZ}. \tag{3.20}$$

3.3 Retrieval Evaluation with Radar Observations

The LWC retrievals in the previous section were developed and evaluated with synthetic radar data obtained from DSD-based T-matrix scattering calculations. For use in real applications in Germany, the newly developed LWC relations including the new hybrid retrieval (Eqs. (3.18) through (3.20)) must also be evaluated with radar observations from DWD's C-band radar network. For this purpose, PPIs of

LWC at the radar elevation angles of 0.5 and 1.5 deg are retrieved from the polarimetric data described in Section 3.1 using the LWC algorithms assessed in Section 3.2. The radar-estimated LWC values are then compared with the ground-based disdrometer observations that did not contribute to the assessment in Section 3.2 (about 25,000 1 min average DSDs). For each disdrometer site considered (see green triangles in Fig. 2.1), the corresponding radar range-azimuth bins within a radius of 1500 m are averaged. The averaging is only performed if at least 50 % of the radar pixels in the radius considered have valid values but at least two valid radar pixels are included, which is especially relevant for disdrometers far from the radar site, where the respective radar pixels correspond to larger radar resolution volumes compared to those closer to the radars. Radar pixels may have invalid values due to the applied ρ_{HV} threshold (see Section 3.1), which removes data from beyond pure rain or with a low overall quality.

Despite the applied data filtering and averaging, there are several sources of error in this radar-ground LWC comparison. One is the inherent uncertainties in the radar and disdrometer observations. Another is the considerable difference in the spatial and temporal extent of the radar and disdrometer measurements: the disdrometer measurements are ground-based point observations averaged over 1 min (in their raw format, see Section 3.1), while the radar measurements represent snapshots of 3D spatial averages of comparatively much larger observation volumes in several 100 to 1,000 m height. These different observation heights introduce another error source: DSDs are likely to change as rain falls over long distances through the atmosphere due to microphysical processes such as raindrop breakup or coalescence. The influence of these error sources on the comparison results is here partially compensated for by not only comparing 1 min averaged disdrometer data with the corresponding radar snapshots, but also by performing the evaluation with temporal averages of up to 6 h. However, the consideration of even longer time periods resulted in too small data sets for a reasonable evaluation, since continuous time series of both the disdrometer and radar data are required.

The quality of the different tested LWC retrievals when applied to real radar data is quantified, like for the evaluation with simulated data, by means of RMSD, PCC, and MBD. To test whether the PCC of a given LWC retrieval is statistically significantly different compared to another given algorithm or not, an F-test is performed. The corresponding test statistic considered is

$$F_{test} = \frac{\mathrm{PCC}_A}{\mathrm{PCC}_B} \tag{3.21}$$

with the Pearson correlation coefficient $\mathrm{PCC}_{A/B}$ of the estimator A/B assumed to be a χ^2-distributed random variable following an F-distribution $F[n_A - 1 - d_A, n_B - 1 - d_B]$ under the null hypothesis of H_0: $\mathrm{PCC}_A \leq \mathrm{PCC}_B$ with $n_{A/B}$ the sample size and $d_{A/B}$ the degrees of freedom of the retrieval A/B. The different time periods considered for the radar-disdrometer comparison 1 (instantaneous), 20, 60, 180, and

360 min (1, 4, 12, 36, and 72 consecutive radar snapshots) lead to the different sample sizes of 39,926, 8,052, 1,981, 371, and 90 individual LWC retrieval-observation pairs, respectively. The different existing and newly developed LWC estimators evaluated in this section exhibit two (all univariate power-law relations on the linear scale; e.g., Eqs. (2.45), (3.6), and (3.15)) or three (all bivariate power-law relations on the linear scale or the quadratic functions on the logarithmic scale; e.g., Eqs. (2.51), (3.7), and (3.11)) degrees of freedom. The resulting PCC thresholds that must be exceeded to identify two retrievals as statistically significantly different (with a significance level of 5 %) are thus 0.01, 0.02, 0.05, 0.11, and 0.22 for the 1, 20, 60, 180, and 360 min comparisons. Note that in Reimann et al. (2021) the numbers of comparison pairs were generally lower due to the ρ_{HV} noise correction applied in this thesis (see Section 3.1.2) leading to a different PCC threshold for statistical significance for the 180 min comparison of 0.14 in Reimann et al. (2021) instead of 0.11 in this thesis, and the 360 min comparison was not performed in Reimann et al. (2021).

3.3.1 New Retrievals

First, the focus is on the new LWC estimators developed in Section 3.2 and hourly comparisons (Fig. 3.7). The PCC of the new LWC(Z_H, Z_{DR}) estimator in Eq. (3.11) is 0.67 (all quality values shown as black numbers in Table 3.2) and thus slightly higher than that yielded by the new LWC(Z_H) estimator in Eq. (3.7) of 0.66 (see Fig. 3.7a,b). This difference is not significant according to the F-test performed (recall that 0.05 must be exceeded). Both PCC values are slightly higher than those listed in Reimann et al. (2021) of 0.66 and 0.65 (values differing in this thesis from those listed in Reimann et al. (2021) are shown in grey italics in Table 3.2). These differences are again caused by the changed evaluation DSD data set (see Section 3.1.2). The new LWC(A_H) estimator in Eq. (3.13) and the new LWC(Z_H) estimator give comparable PCCs (both 0.66, see Fig. 3.7a,c), thus also no significant difference. The new LWC(K_{DP}) estimator in Eq. (3.15) results (with negative K_{DP} values in weak precipitation replaced by zero) in a worse PCC compared to the LWC(Z_H) retrieval and an even significantly worse PCC compared to the LWC(Z_H, Z_{DR}) estimator of 0.61. Note that a significant difference in PCC between the new LWC(K_{DP}) and LWC(Z_H, Z_{DR}) relations was not found in Reimann et al. (2021), possibly due to the inclusion of additional noise in the K_{DP} estimates by the ρ_{HV} noise correction applied here (see Section 3.1.2). The performance of the retrievals based on A_H and K_{DP} was expected to be clearly better in terms of PCC compared to the LWC(Z_H) estimator based on the simulations (see Fig. 3.6a,c,d). A likely reason are low SNRs of Φ_{DP} in weak precipitation, which also favor negative K_{DP} estimates, especially with the low radial resolution of the radar data used (1 km), as discussed before. The correlation for the LWC(K_{DP}) retrieval improves when negative K_{DP} estimates are replaced with a $K_{DP}(Z_H)$ relation derived from the German DSD data set given by

$$\log\big(K_{DP}(Z_H)\big) = -0.0006 Z_H^2 + 0.125 Z_H - 4.52 \tag{3.22}$$

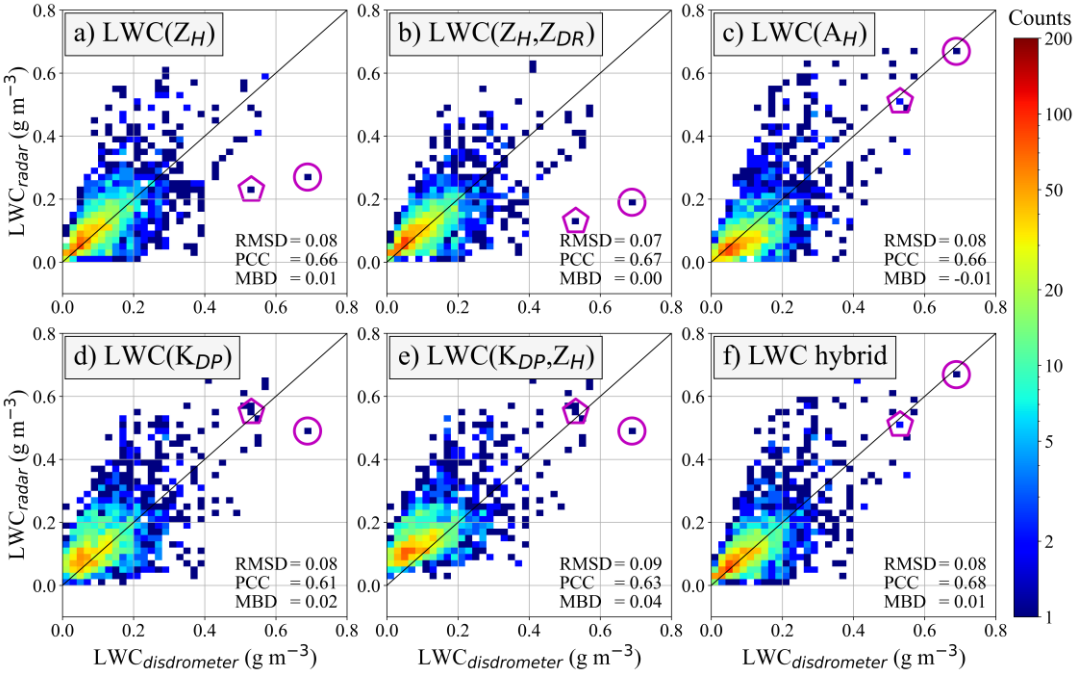

FIGURE 3.7: 2D histograms of hourly averaged pairs of disdrometer-measured LWC and the LWC retrieved from polarimetric radar observations from Germany using the new a) $LWC(Z_H)$, b) LWC(Z_H, Z_{DR}), and c) LWC(A_H) retrievals in Eqs. (3.7), (3.11), and (3.13). In d), the new LWC(K_{DP}) estimator (Eq. (3.15)) is used with negative K_{DP} replaced by zero. In e), the same new LWC(K_{DP}) relation is used with negative K_{DP} substituted using the empirical $K_{DP}(Z_H)$ relation in Eq. (3.22) derived from the German DSD data set. In f), the hybrid LWC estimator (Eqs. (3.18) to (3.20)) is applied. Also shown are the respective quality measures RMSD (given in g m^{-3}), PCC, and MBD (given in g m^{-3}). Pixels marked by violet circle and pentagon shapes are discussed in Section 3.3.1.

to 0.63 (see quality values for the LWC(K_{DP}, Z_H) estimator in Table 3.2). Note that the quadratic relation in Eq. (3.22), when applied to the simulated radar data, gives much better performance in terms of RMSD and PCC than the linear $K_{DP}(Z_H)$ relation proposed and used in Reimann et al. (2021; not shown). Also note that a direct comparison of the results for the LWC(K_{DP}, Z_H) estimator using Eq. (3.22) with the corresponding results shown in Reimann et al. (2021) is not meaningful due to an error in the computer code used: the $K_{DP}(Z_H)$ relation was used for all comparison pairs in Reimann et al. (2021), so that no Φ_{DP}-based K_{DP} was employed, which made their LWC(K_{DP}, Z_H) relation effectively an LWC$(K_{DP}(Z_H))$ estimator.

The new LWC(Z_H, Z_{DR}) estimator gives an RMSD of 0.07 g m^{-3} (Fig. 3.7b), which is slightly lower than the corresponding value of the new LWC(Z_H) relation (0.08 g m^{-3}, Fig. 3.7a). The new LWC(A_H) and LWC(K_{DP}) estimators (Fig. 3.7c,d) give RMSDs comparable to that of the LWC(Z_H) relation (all 0.08 g m^{-3}), and the LWC(K_{DP}, Z_H) estimator (negative K_{DP} substituted using Eq. (3.22); Fig. 3.7e) gives an even slightly higher RMSD (0.09 g m^{-3}). Thus, the LWC(A_H) and LWC(K_{DP}) estimators, against the expectations from the simulations (Fig. 3.6a,c,d), do also not

LWC Retrieval		RMSD (g m^{-3}) minutes					PCC minutes					MBD (g m^{-3}) minutes				
Input	**Specification**	**1**	**20**	**60**	**180**	**360**	**1**	**20**	**60**	**180**	**360**	**1**	**20**	**60**	**180**	**360**
$\mathbf{Z_H}$	Quadr. fit (Eq. (3.7))	0.13 *0.14*	0.10 *0.11*	0.08	0.05 *0.06*	0.04	0.57 *0.56*	0.65 *0.63*	0.66 *0.65*	0.65 *0.63*	0.65	0.02 *0.03*	0.02	0.01 *0.02*	0.00	0.00
	G&C1972 (Eq. (2.45))	0.13 *0.14*	0.09 *0.10*	0.07 *0.08*	0.05 *0.06*	0.05	0.56 *0.54*	0.63 *0.62*	0.65 *0.64*	0.64 *0.62*	0.65	0.00 *0.01*	0.00	-0.01	-0.02	-0.02
	C2016 (Eq. (2.46))	0.14 *0.16*	0.10 *0.11*	0.08	0.06 *0.07*	0.06	0.53 *0.52*	0.61	0.63	0.63 *0.61*	0.66	-0.01 *-0.01*	-0.02 *-0.01*	-0.03 *-0.02*	-0.04	-0.04
	R&Z2019 (Eq. (2.47))	0.15	0.10	0.08	0.06	0.06	0.53	0.61	0.63	0.63	0.66	-0.01	-0.02	-0.02	-0.03	-0.04
$\mathbf{Z_H}$, $\mathbf{Z_{DR}}$	Linear fit (Eq. (3.11))	0.14 *0.15*	0.09 *0.10*	0.07	0.05	0.05	0.54 *0.52*	0.65 *0.63*	0.67 *0.66*	0.65 *0.62*	0.63	0.01 *0.02*	0.01	0.00 *0.01*	-0.01	-0.01
	B&C2001 (Eq. (2.51))	1.65	0.15	0.09	0.07	0.07	0.08	0.49	0.59	0.64	0.65	0.00	-0.02	-0.03	-0.04	-0.05
	C2016 (Eq. (2.50))	0.14 *0.15*	0.10	0.08	0.06 *0.07*	0.06	0.54 *0.52*	0.62 *0.61*	0.65 *0.64*	0.64 *0.62*	0.66	-0.02	-0.02	-0.03	-0.04	-0.05
$\mathbf{A_H}$	Quadr. fit (Eq. (3.13))	0.15 *0.17*	0.11 *0.12*	0.08 *0.09*	0.06	0.05	0.54 *0.50*	0.63 *0.62*	0.66	0.66 *0.67*	0.70	0.01 *0.02*	0.00 *0.01*	-0.01 *0.00*	-0.02	-0.03
	C2016 (Eq. (2.52))	0.26 *0.38*	0.16 *0.25*	0.10 *0.11*	0.06 *0.07*	0.05	0.40 *0.32*	0.54 *0.43*	0.64 *0.65*	0.65 *0.66*	0.69	0.03 *0.05*	0.02 *0.04*	0.01 *0.02*	-0.01 *0.00*	-0.01
	R&Z2019 (Eq. (2.53))	0.25	0.15	0.10	0.06	0.05	0.42	0.53	0.64	0.65	0.68	0.03	0.02	0.00	-0.01	-0.01
$\mathbf{K_{DP}}$	Linear fit (Eq. (3.15))	0.15	0.11	0.08 *0.09*	0.06	0.05	0.49 *0.51*	0.60 *0.61*	0.61 *0.63*	0.59 *0.61*	0.53	0.03	0.03	0.02	0.01 *0.00*	0.01
	B&C2001 (Eq. (2.56))	0.13	0.09 *0.10*	0.08 *0.09*	0.08 *0.09*	0.08	0.51 *0.52*	0.60 *0.61*	0.61 *0.62*	0.58 *0.61*	0.55	-0.04	-0.04 *-0.05*	-0.05 *-0.06*	-0.06 *-0.07*	-0.06
	D&Z2006 (Eq. (2.56))	0.13	0.09 *0.10*	0.08	0.06 *0.07*	0.06	0.51 *0.52*	0.60 *0.61*	0.61 *0.63*	0.59 *0.61*	0.54	-0.01 *-0.02*	-0.01 *-0.02*	-0.02 *-0.03*	-0.03 *-0.04*	-0.04
	C2016 (Eq. (2.54))	0.14	0.10	0.08	0.06	0.06	0.51 *0.52*	0.60 *0.61*	0.61 *0.62*	0.59 *0.61*	0.55	0.00	0.00 *-0.01*	-0.01	-0.02 *-0.03*	-0.03
	R&Z2019 (Eq. (2.55))	0.14	0.10	0.08	0.06	0.06	0.51	0.60	0.61	0.59	0.55	0.00	0.00	-0.01	-0.02	-0.03
$\mathbf{K_{DP}}$, $\mathbf{Z_H}$	Linear fit (Eq. (3.15))	0.14 *0.13*	0.11 *0.09*	0.09 *0.07*	0.06 *0.05*	0.05	0.52 *0.55*	0.62 *0.63*	0.63 *0.65*	0.61 *0.62*	0.57	0.05 *0.01*	0.05 *0.00*	0.04 *0.00*	0.03 *-0.02*	0.02
hybrid Eqs. (3.11), (3.13), (3.15)		0.14 *0.16*	0.10 *0.11*	0.08	0.05 *0.06*	0.04	0.55 *0.52*	0.65 *0.63*	0.68 *0.69*	0.69	0.72	0.02 *0.03*	0.02 *0.03*	0.01 *0.02*	0.00	-0.01

TABLE 3.2: Comparison of RMSD (in g m^{-3}), PCC, and MBD (in g m^{-3}) values between disdrometer-measured LWC and radar-estimated LWC via the new and existing LWC(Z_H), LWC(Z_H, Z_{DR}), LWC(A_H), and LWC(K_{DP}) relations proposed by Greene and Clark (1972; "G&C1972"), Carlin et al. (2016; "C2016"), Bringi and Chandrasekar (2001; "B&C2001"), Ryzhkov and Zrnic (2019; "R&Z2019"), and Doviak and Zrnic (2006; "D&Z2006") for time intervals from 1 to 360 min for nine warm-season rainfall events. In the LWC(K_{DP}) estimator, negative K_{DP} is substituted by zero. Also shown are the results for the new LWC(K_{DP}) estimator with negative K_{DP} replaced using an empirical $K_{DP}(Z_H)$ relation (Eq. (3.22); LWC(K_{DP}, Z_H) estimator), and for the new hybrid estimator (hybrid). Grey italicized values show values listed in Reimann et al. (2021) where different from this thesis.

outperform the LWC(Z_H) relation in terms of RMSD, possibly again because of low SNRs of Φ_{DP} in weak rain. However, the MBDs of all the new LWC(Z_H), LWC(Z_H, Z_{DR}), LWC(A_H), and LWC(K_{DP}) estimators are generally low (0.01, 0.00, -0.01, and 0.02 g m^{-3}), except for the LWC(K_{DP}, Z_H) estimator (0.04 g m^{-3}).

Next, the new hybrid LWC retrieval, which uses the new LWC(Z_H, Z_{DR}), LWC(A_H), and LWC(K_{DP}) estimators depending on the rainfall characteristic (Eqs. (3.18) through (3.20)), is also evaluated with observations from the German C-band radar network (Fig. 3.7f). It yields the highest PCC of 0.68 among all new LWC retrievals in the hourly comparison (see Table 3.2). This PCC value is not significantly better than the PCC values of the pure new LWC(Z_H), LWC(Z_H, Z_{DR}), and LWC(A_H) relations, but is statistically significantly better than that of the new LWC(K_{DP}) estimator (with negative K_{DP} substituted by zero). In contrast, the RMSD of the hybrid estimator is comparable to that of all the other relations (0.08 g m^{-3}), and the MBD is small (0.01 g m^{-3}) like it is the case for all the individual new relations, which is an encouraging result for the application of the new hybrid LWC estimator to the indirect assimilation of polarimetric information in Chapter 5.

The benefit of using phase-based polarimetric variables in the hybrid LWC estimator is emphasized by the much better performance of LWC estimation using the hybrid compared to the single LWC(Z_H) and LWC(Z_H, Z_{DR}) retrievals in certain situations. E.g., the highest hourly-averaged disdrometer-measured LWC values contributing to the ground-radar comparison (histogram pixel marked by violet circles in Fig. 3.7) is underestimated by more than 50 % using the LWC(Z_H) and LWC(Z_H, Z_{DR}) retrievals (Fig. 3.7a,b). In contrast, the Φ_{DP}-based LWC(A_H) and LWC(K_{DP}) estimators and the new hybrid retrieval show much better performance in that comparison (Fig. 3.7c,d,f). Investigation shows that the respective hourly LWC value is measured by the DWD disdrometer in Braunlage in the Harz mountains in central Germany (see black crosses in Fig. 3.8a-d), while observations from the DWD radar in Ummendorf (radar UMD, see Fig. 2.1; black circles in Fig. 3.8) at an elevation angle of 0.5 deg were used for the radar-retrieved LWC. The histograms in Figs. 3.7c and 3.7f suggest that the LWC(A_H) retrieval was used in the hybrid retrieval for the data point considered. The rays corresponding to the disdrometer location (all within the radius of 1500 m) have $\Delta\Phi_{DP} > 5$ deg and $Z_H < 45$ dBZ (see hourly averaged Z_H and Φ_{DP} in Fig. 3.8a and b) for all time steps in the hour considered (not shown), thus the hybrid estimator indeed uses the LWC(A_H) estimator for all aggregated values (see Eq. (3.19)). The inferior performance of the Z_H-based estimators (Fig. 3.7a,b) is most likely due to partial beam blockage by the Harz mountain rise behind which the Braunlage disdrometer is located along the radar ray (see Fig. 3.8c,d). As phase-based polarimetric radar variables, A_H and K_{DP} are not affected by partial beam blockage (see Section 2.1.2), which may be responsible for the found better performance of the LWC(A_H), LWC(K_{DP}), and hybrid LWC estimators (Fig. 3.7c,d,f) compared to the Z_H-based retrievals (Fig. 3.7a,b). A similar picture is obtained for another distinct and analyzed data point (pixels marked by

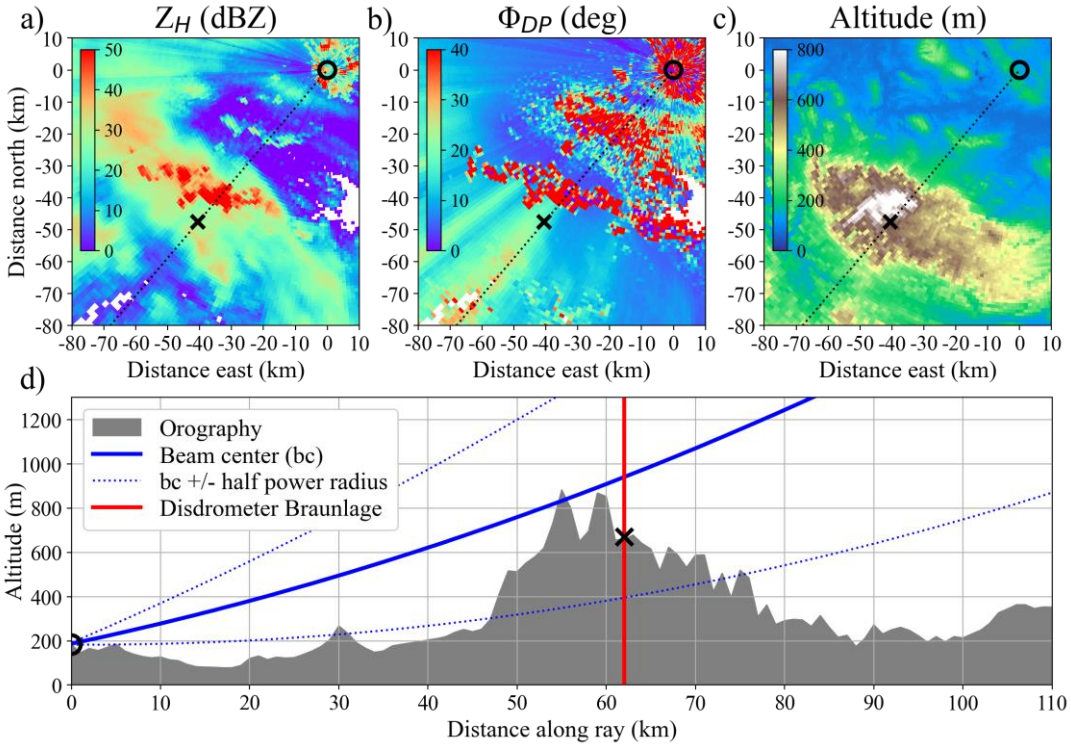

FIGURE 3.8: Investigation of the histogram pixel marked in Fig. 3.7 by violet circles. The hourly mean a) Z_H and b) Φ_{DP} PPIs measured at 0.5 deg elevation angle by the DWD radar station Ummendorf (radar location marked by black circles in a)-d); see radar UMD in Fig. 2.1) in the area of the investigated DWD surface disdrometer in Braunlage (black crosses; red line in d)). In c), the orography of the earth's surface is shown. In d), the orographic profile along the connection line between the radar and the disdrometer (black dotted lines in a)-c)) is depicted and the approximate radar beam center (blue solid curve) and the half power beam radius is illustrated (blue dotted curves).

violet pentagons in Fig. 3.7): radar rays from the UMD radar at the 0.5 deg elevation angle in the direction of the DWD disdrometer in Braunschweig, Lower Saxony are partially (about 50 %) blocked by the orography (not shown), which possibly again leads to the worse performance of the LWC(Z_H) and LWC(Z_H, Z_{DR}) estimators compared to the LWC(A_H), LWC(K_{DP}), and hybrid LWC estimators.

As expected, the instantaneous comparison yields the largest RMSDs and the lowest PCCs for the new LWC(Z_H), LWC(Z_H, Z_{DR}), LWC(A_H), and LWC(K_{DP}) estimators and also for the new hybrid estimator (RMSDs of 0.13, 0.14, 0.15, 0.15, and 0.14 g m^{-3}, PCCs of 0.57, 0.54, 0.54, 0.49, and 0.55; see Table 3.2) among all the comparison time periods considered (1, 20, 60, 180, and 360 min averages). The LWC(Z_H) estimator performs significantly better in terms of PCC than all other new relations including the hybrid estimator (recall that for the instantaneous comparison a difference in PCC of 0.01 must be exceeded). Unlike in Reimann et al. (2021), the LWC(Z_H, Z_{DR}) estimator is not significantly better than the LWC(A_H) estimator, and the LWC(A_H) and LWC(K_{DP}) estimators differ significantly, which again are results

New LWC Retrievals	RMSD (g m^{-3})					PCC					MBD (g m^{-3})				
	minutes					minutes					minutes				
	1	20	60	180	360	1	20	60	180	360	1	20	60	180	360
LWC(Z_H) (Eq. (3.7))	0.09	0.07	0.06	0.05	0.04	0.62	0.67	0.66	0.65	0.65	0.00	0.00	0.00	0.00	0.00
	0.26	*0.20*	*0.17*	-	-	*0.56*	*0.68*	*0.71*	-	-	*0.12*	*0.13*	*0.14*	-	-
LWC(Z_H, Z_{DR}) (Eq. (3.11))	0.10	0.07	0.06	0.05	0.05	0.54	0.68	0.66	0.64	0.63	0.00	-0.01	-0.01	-0.01	-0.01
	0.24	*0.17*	*0.13*	-	-	*0.54*	*0.67*	*0.71*	-	-	*0.09*	*0.10*	*0.09*	-	-
LWC(A_H) (Eq. (3.13))	0.10	0.08	0.07	0.06	0.05	0.56	0.62	0.65	0.65	0.70	-0.02	-0.02	-0.02	0.03	-0.03
	0.28	*0.20*	*0.17*	-	-	*0.54*	*0.70*	*0.74*	-	-	*0.12*	*0.13*	*0.13*	-	-
LWC(K_{DP}) (Eq. (3.15))	0.12	0.09	0.07	0.05	0.05	0.42	0.53	0.55	0.58	0.53	0.02	0.01	0.01	0.01	0.01
	0.25	*0.19*	*0.17*	-	-	*0.58*	*0.75*	*0.82*	-	-	*0.13*	*0.14*	*0.15*	-	-
LWC(K_{DP}, Z_H) (Eq. (3.15))	0.11	0.09	0.07	0.06	0.05	0.47	0.57	0.60	0.62	0.58	0.04	0.04	0.03	0.03	0.02
	0.25	*0.20*	*0.18*	-	-	*0.60*	*0.76*	*0.82*	-	-	*0.15*	*0.16*	*0.16*	-	-
hybrid (Eqs. (3.11), (3.13), (3.15))	0.09	0.07	0.06	0.05	0.04	0.61	0.67	0.69	0.69	0.72	0.00	0.00	0.00	0.00	-0.01
	0.28	*0.20*	*0.17*	-	-	*0.53*	*0.69*	*0.73*	-	-	*0.12*	*0.13*	*0.13*	-	-

TABLE 3.3: Comparison of RMSD (in g m^{-3}), PCC, and MBD (in g m^{-3}) values between disdrometer-measured LWC and radar-estimated LWC via the new LWC(Z_H), LWC(Z_H, Z_{DR}), LWC(A_H), and LWC(K_{DP}) estimators for time intervals from 1 to 360 min for four stratiform (black numbers) and five convective (grey italic numbers) warm-season rainfall events. The RMSDs, PCCs, and MBDs are calculated for at least 10 comparison pairs. In the LWC(K_{DP}) estimator, negative K_{DP} is substituted by zero. Also shown are the results for the new LWC(K_{DP}) estimator with negative K_{DP} substituted using an empirical $K_{DP}(Z_H)$ relation (Eq. (3.22); LWC(K_{DP}, Z_H) estimator), and for the new hybrid estimator (hybrid).

of the larger evaluation DSD data set and/or the modified $\Delta\Phi_{DP}$ estimation procedure for the A_H derivation, which leads to less noisy A_H estimates (see Section 3.1.2). Averaging of the data pairs over 20, 60, 180, and 360 min always decreases the RMSDs for all new LWC(Z_H), LWC(Z_H, Z_{DR}), LWC(A_H), and LWC(K_{DP}) estimators and the hybrid relation (see Table 3.2). The PCCs systematically increase up to the 60 min comparison and decrease again for longer averaging times, except for the LWC(A_H) and the hybrid LWC algorithm, for which the PCCs are highest for the 360 min comparison (0.70 and 0.72; however, not significantly higher than for the other new relations). The PCC of the hybrid LWC estimator is always (although statistically insignificantly) higher than that of the other new pure LWC relations for time periods longer than 20 min. Interestingly, the MBDs for all new individual and the hybrid LWC estimators continuously decrease from the instantaneous to the 360 min comparisons (see again Table 3.2). Separating the analysis for rainfall dominated by convective (five events) and stratiform (four events) precipitation shows that the MBDs for stratiform rainfall are generally lower compared to the convective events (compare black with grey italic numbers in Table 3.3). Note that about 83 % of the observations considered are from stratiform rainfall, and with increasing time intervals considered, the stratiform cases, which usually lead to longer lasting rainfall at a given location compared to the convective cases, are better represented in the data set than the convective events: for the instantaneous, 20, 60, 180, and 360 min comparisons there are 33,199 and 6,727, 6,957 and 1,095, 1,803 and 178, 364/7, as well as 90 and zero data pairs available for comparison for the

stratiform and convective cases, respectively. Thus, the MBDs of the entire data set (stratiform and convective events together) approximate those of the stratiform events with increasing time intervals considered. Also note that the better performance of the stratiform events with respect to MBD compared to the convective events may be because the retrieval development in Section 3.2 was based on a DSD data set also dominated by stratiform rainfall. Adjusting LWC retrievals to different N_w regimes (see Section 3.2) may potentially result in a better representation of stratiform and convective rainfall, but, as noted earlier in this chapter, the performance of the LWC estimation generally suffered when radar-estimated N_w was used (not shown).

3.3.2 Existing Retrievals

The quality of the existing LWC estimators from the literature when applied to real radar observation is also examined for comparison. The PCCs are always better for the new LWC(Z_H), LWC(Z_H, Z_{DR}), and LWC(A_H) estimators than for the respective existing counterparts, except for the 360 min comparison for the LWC(Z_H) and LWC(Z_H, Z_{DR}) estimators (see also the quality values of the existing relations as black numbers in Table 3.2). The new LWC(Z_H) relation is even significantly better in terms of PCC compared to the respective relations of Carlin et al. (2016; Eq. (2.46)) and Ryzhkov and Zrnic (2019; Eq. (2.47)) in the instantaneous and 20 min comparisons. The new LWC(Z_H, Z_{DR}) relation yields a significantly better PCC than the corresponding relation proposed by Bringi and Chandrasekar (2001; Eq. (2.51)) for the 1, 20, and 60 min comparisons, and significantly better than the relation of Carlin et al. (2016; Eq. (2.50)) in the 20 min comparison. The PCC of the new LWC(A_H) estimator is also significantly better than that of the existing counterparts by Carlin et al. (2016; Eq. (2.52)) and Ryzhkov and Zrnic (2019; Eq. (2.53)) in the instantaneous and 20 min comparisons. However, the new LWC(K_{DP}) estimator mostly gives similar or even lower PCCs compared to the respective existing relations from the literature (Eqs. (2.54), (2.55), and (2.56)) and the respective PCC is even significantly lower than that of the existing relations in the instantaneous comparison.

The RMSD of the new LWC(Z_H) estimator is generally lower than for the respective relations of Carlin et al. (2016) and Ryzhkov and Zrnic (2019) and similar or also slightly lower than for the relation of Greene and Clark (1972). The new LWC(Z_H, Z_{DR}) relation generally also gives a lower RMSD than the respective existing relations. This also holds for the new LWC(A_H) relation, while the corresponding relation of Carlin et al. (2016) performs similarly well for the 180 and 360 min comparisons. The new LWC(K_{DP}) estimator generally gives similar to even larger RMSDs compared to the existing relations, except for the 360 min comparison, where the new algorithm slightly outperforms the existing ones.

In terms of bias, the existing LWC(Z_H) and LWC(Z_H, Z_{DR}) relations yield similar MBDs like the new fits for the instantaneous and 20 min comparisons, but the (absolute) MBDs for the existing relations tend to increase with increasing time intervals. MBDs of the existing LWC(A_H) relations are generally similar to those of

the new relation and low. The MBDs of the existing LWC(K_{DP}) relations are highest for the relations of Bringi and Chandrasekar (2001) and Doviak and Zrnic (2006), and those of the other existing LWC(K_{DP}) relations of Carlin et al. (2016) and of Ryzhkov and Zrnic (2019) are generally comparable to that of the new LWC(K_{DP}) relation and also low.

The new hybrid estimator always gives higher PCCs compared to all existing retrievals, except for the LWC(Z_H) retrieval of Greene and Clark (1972) in the instantaneous comparison. Yielded RMSDs are generally lower compared to all existing relations, especially for time intervals greater than 60 min, where also MBDs are better compared to all existing relations (see Table 3.2).

3.4 Summary and Conclusions

In this chapter, new LWC(Z_H), LWC(Z_H, Z_{DR}), LWC(A_H), and LWC(K_{DP}) retrievals applicable to C-band radars in Germany were developed and evaluated together with respective existing LWC estimators from the literature based on a large German surface-based disdrometer data set and T-matrix scattering calculations at C-band. Quadratic relations (on the logarithmic scale) were found most suitable for the LWC(Z_H) and LWC(A_H) estimators in terms of root-mean-square deviation (RMSD), Pearson correlation coefficient (PCC), and mean-bias deviation (MBD) when applied to simulated radar data, while a linear function and a bivariate linear function (also on the logarithmic scale) were found best for the LWC(K_{DP}) and LWC(Z_H, Z_{DR}) retrievals. When evaluated with the synthetic radar data, the newly developed retrievals mostly gave much better PCCs and RMSDs compared to their respective existing counterparts, while biases (MBD) were similar and generally low.

The adapted and existing LWC relations were then evaluated with real radar observations from the German C-band radar network of four summertime stratiform and five summertime convective rainfall events for time periods up to 6 h. The new retrievals yielded overall satisfactory results in terms of generally low biases, but the differences in RMSDs and PCCs between the new LWC(Z_H, Z_{DR}) and LWC(A_H) estimators and the new LWC(Z_H) estimator were less pronounced than expected from the simulations. The LWC(K_{DP}) estimator mostly resulted in even worse RMSDs and PCCs compared to the new LWC(Z_H) relation. Although the new LWC retrievals mostly outperformed the respective existing counterparts, the differences in the RMSDs and PCCs between the new and the existing retrievals were also smaller than expected from their application to the synthetic radar data. It remains to be explored to what extent these smaller-than-expected improvements of the new LWC(Z_H), LWC(Z_H, Z_{DR}) and LWC(A_H) retrievals and the mostly even worse performance of the new LWC(K_{DP}) estimator are caused by errors in the comparison of in-situ with remotely sensed observations, and to what extent low SNRs of the C-band radar products, spatial degradation of K_{DP}, and radar calibration problems are responsible.

The new LWC(Z_H, Z_{DR}), LWC(A_H), and LWC(K_{DP}) estimators were combined to exploit and mitigate the respective strengths and shortcomings of the used polarimetric variables Z_H, Z_{DR}, A_H, and K_{DP} known for different precipitation characteristics in a hybrid way. For light rain as characterized by a total differential phase increment below the melting layer smaller than 5 deg, where the negative effect of (differential) attenuation on Z_H and Z_{DR} can be expected small, and A_H and K_{DP} are potentially noisy due to low SNRs of Φ_{DP}, the new LWC(Z_H, Z_{DR}) estimator is used, which showed a better performance than the new LWC(Z_H) relation in terms of RMSD and PCC when applied to the simulated radar data. The new LWC(A_H) and LWC(K_{DP}) estimators are used for stronger rain as characterized by total differential phase increments larger than 5 deg, where the negative effect of (differential) attenuation on Z_H and Z_{DR} is more pronounced, and A_H and K_{DP} are potentially less affected by low SNRs of Φ_{DP}. LWC(K_{DP}) is used for radar pixels with potential hail contamination as characterized by $Z_H \geq 45$ dBZ and LWC(A_H) is used elsewhere, because K_{DP} is less affected by hail than A_H is. Application of the hybrid LWC estimator to observations from the German C-band radar network gave the overall best PCCs among the new retrievals for time intervals longer than 20 min, while RMSDs and MBDs were comparable to the pure new estimators. The hybrid estimator generally also outperformed the existing retrievals from the literature.

Chapter 4

Assimilation of Polarimetric Radar Data: State of the Art

The assimilation of polarimetric radar observations in NWP models is still in its infancy. While one reason is the lack of widespread polarimetric observations from national weather radar networks in the past, another reason is the remaining uncertainties in the relationships between polarimetric radar moments and the microphysical state variables of the NWP models. However, first successful attempts of assimilating simulated or real polarimetric radar observations directly using polarimetric radar forward operators or indirectly using, e.g., hydrometeor mixing ratios as surrogates for polarimetric radar moments have been made in the past about two decades (see Section 4.1.4). The rather novel field of assimilating polarimetric radar observations in NWP models is fundamentally based on the findings, approaches, and achievements in the assimilation of non-polarimetric radar data, such as Z_H and V_r observations, which in contrast has been studied extensively over the past three to four decades. Therefore, Section 4.1 first provides an overview of the key approaches and achievements in radar data assimilation in general and subsequently the assimilation of polarimetric radar data is considered. Section 4.2 then describes the operational assimilation of (non-polarimetric) radar observations in Germany, including a description of the convective-scale NWP model ICON-D2 and the DA framework KENDA, in preparation of the assimilation experiments presented later in this thesis (Chapter 5).

4.1 Key Approaches and Achievements

This section provides a general overview of the key approaches and achievements of radar DA in NWP models to date. The review begins with a brief description of the earliest attempts to diagnose wind, microphysical, and thermodynamic fields from dual- or single-Doppler radar observations and to use these fields directly to initialize NWP models. In a second step, empirical DA methods that have been used for the assimilation of radar observations, such as those based on successive corrections or Newtonian relaxation or nudging, are briefly considered. Most of the research on radar data assimilation in recent decades has been devoted to statistical interpolation methods, including variational DA methods, sequential DA methods based on the EnKF approach, hybrid ensemble-variational fusions of both methods, or attempts

based on the particle filter. These methods and the corresponding achievements in radar DA are presented here with a focus on the EnKF method, in particular the LETKF, which is included in the KENDA suite at DWD and is used in this thesis for the assimilation of polarimetric radar data (Chapter 5). Finally, an overview of the state of the art in polarimetric radar DA in NWP models is provided.

4.1.1 Doppler Retrievals

Towards the end of the 20th century, researchers began to use Doppler radar observations to initialize NWP models, with a focus on convective storm forecasting (e.g., Lin et al., 1993). A key challenge in radar DA has been to establish an appropriate link between the radar observations and model state variables. Therefore, in the late 1970s and 1980s, techniques to retrieve thermodynamic and microphysical fields from 3D winds derived from multiple-Doppler radar observations (i.e., observations of the same atmospheric spot by two or more different Doppler radars) were developed (e.g., Gal-Chen, 1978; Roux, 1985; Ziegler, 1985). Lin et al. (1993) were the first to initialize a convective-scale NWP model with such Doppler-radar retrieved fields. They used radar-derived wind speeds merged with the horizontal environmental wind determined from a radio sounding, temperature and pressure perturbations retrieved following Hane and Ray (1985), and specified water substance fields, to initialize the Colorado State University Regional Atmospheric Modelling System model. They showed that the model initialization by direct insertion of the retrievals resulted in a good agreement of the ensuing predicted convective storm with its observed counterpart for less than 15 min.

However, the use of multiple-Doppler observations for the initialization of operational NWP models is generally not suitable because multiple-Doppler coverage is mostly not provided by operational Doppler-radar networks due to the large distances between the individual radar stations. It quickly became apparent that techniques for retrieving wind fields also from single-Doppler observations needed to be developed. Several techniques for doing so emerged, including the so-called simple adjoint method (e.g., Qiu and Xu, 1992; Xu and Qiu, 1994) and the two-scalar method (Shapiro et al., 1995). Most of these approaches have shown reasonable accuracy in retrieving low-level winds compared to multiple-Doppler wind retrievals. Weygandt et al. (2002) conducted a similar study like Lin et al. (1993), but they initialized their NWP model with single- instead of multiple-Doppler observations using the wind retrieval of Shapiro et al. (1995) and then retrieved thermodynamic fields from the derived winds following Gal-Chen (1978). Their simulated convective storm agreed well with the observed one for about 35 min.

The use of wind as well as thermodynamic and microphysical fields retrieved from Doppler radar observations for the initialization of NWP models by direct insertion is advantageous due to the relatively low computational costs required. In the case of only single-Doppler coverage, as common for operational NWP, a multi-step procedure is required, as performed by Weygandt et al. (2002), including a wind

retrieval and an ensuing thermodynamical retrieval procedure. However, Hu et al. (2006a) argue that the inclusion of several consecutive steps and the use of retrieved rather than direct observations make it difficult to achieve optimal analyses.

4.1.2 Empirical Approaches

This section provides a brief overview of the empirical approaches that have been used to initialize NWP models with radar data and the respective main achievements, starting with the successive corrections method (SCM). Then, the empirical approaches based on Newtonian relaxation or nudging are briefly outlined.

4.1.2.1 Successive Corrections Method

The SCM is an empirical method that has been successfully used to initialize NWP models with radar observations and was originally proposed by Bergthörsson and Döös (1955) in Sweden and by Cressman (1959) at the US Weather Service. In the SCM approach, the background (or first-guess) gridded field determined, e.g., from a previous short-range model forecast, represents the first gridded field estimate. Consecutive field estimations are then obtained by "successive corrections" towards the observations using specifically defined weighting factors, which can be defined in different ways. E.g., Cressman (1959) defined the weights empirically as functions of the distance between an observation and a given field grid point with a maximum radius of influence R_{scm} which can be changed over the iterations.

Barnes (1964) introduced another empirical version of the SCM that has been widely used to produce analyses in the absence of background fields such as for radar observations. In this SCM version, the squared radius of influence R_{scm}^2 changes iteration-wise by a factor γ_{scm}, such that $\gamma_{scm} = 1$ corresponds to the case that only the large scales are captured and that $\gamma_{scm} < 1$ corresponds to the case that the analysis converges towards the smaller scales with the successive iterations. The Barnes (1964) SCM version was implemented in the Local Analysis and Prediction System (LAPS; Albers, 1995) of the National Oceanic and Atmospheric Administration Forecast Systems Laboratory to produce high-resolution analyses including gridded V_r observations used in the second iteration pass with a smaller radius of influence R_{scm} to preserve smaller-scale features captured in the radar data.

Another version of the SCM approach was proposed by Bratseth (1986). It is not based on empirical formulations of the weighting coefficients, but uses appropriately chosen weights that make the scheme converge towards a proper statistical interpolation (Kalnay, 2003). This method allows accounting for background errors and errors in each individual observation source, and results in a relatively low sensitivity to fluctuations in data density (Sun, 2005b). The scheme is used at the Center for Analysis and Prediction of Storms at the University of Oklahoma for the Advanced Regional Prediction System's (ARPS; Xue et al., 2003) Data Assimilation System (ADAS; Brewster, 1996), which also assimilates V_r observations.

Albers et al. (1996) developed a "cloud analysis" that was implemented in LAPS. A cloud analysis was also implemented for ADAS using the LAPS cloud analysis algorithms in a customized, enhanced, and refined version (Zhang et al., 1998). The cloud analysis uses Z_H, satellite, and surface-based cloud observations to derive 3D precipitation and cloud fields, and can be used for moisture initialization of ARPS. The gridded variables include 3D cloud cover and cloud type, precipitation type, cloud liquid, cloud ice, rain, snow, and hail mixing ratios, and cloud base, top, and ceiling information. The cloud analysis also applies an in-cloud temperature adjustment through either a latent heat or a moist-adiabatic scheme (e.g., Hu et al., 2006a), which is particularly important for maintaining existing convection in the numerical model (Hu and Xue, 2007). The cloud analysis scheme with ADAS has proven to be advantageous, e.g., for QPF in Spain (e.g., Souto et al., 2003). The cloud analysis scheme has also attracted attention for its ease of implementation and computational efficiency (e.g., for rapid update cycling) while being disadvantageous in terms of being based on semi-empirical relationships and sensitive to the tuning and configuration of the DA settings (Hu and Xue, 2007).

4.1.2.2 Newtonian Relaxation or Nudging

Radar observations have also been successfully assimilated into NWP models via the empirical approaches of Newtonian relaxation or nudging (e.g., Hoke and Anthes, 1976), where prognostic model variables are dynamically relaxed towards observations within an empirically defined time window by modifying the tendency equation of a particular prognostic model variable. An early application of Newtonian nudging to radar DA was, e.g., performed by Xu et al. (2004), who assimilated 3D rain water mixing ratios derived from gridded Z_H observations over the north-east USA using a nudging scheme into the Fifth-Generation Pennsylvania State University–National Center for Atmospheric Research Mesoscale Model (MM5). They introduced an additional source term in the prognostic model equation for rainwater that accounted for the difference between the pseudo-observed and forecasted rain mixing ratios. The nudging-based assimilation of Z_H observations had a positive impact on the forecast of a case-study winter storm. Furthermore, they noted a positive effect of nudging latent heat information derived from the difference between observed and forecasted rain water.

The nudging of latent heat increments derived from near-surface precipitation rates derived from Z_H observations is a widely used and successful method of assimilating radar observations and is known as Latent Heat Nudging (LHN). LHN was first formulated by Wang and Warner (1988) and is described in detail by Jones and Macpherson (1997). It is based on the assumption that the near-surface rain rate RR is proportional to the latent heat released through condensation integrated over the atmospheric column above it. Thus, RR is assumed to be proportional to a given temperature change within this vertical column. The ratio between the observed rain rate RR_{obs} and the modeled rain rate RR_{mod}

$$\alpha_{LHN} = \frac{RR_{obs}}{RR_{mod}} \tag{4.1}$$

is used to determine the incremental temperature profile ΔT_{LHN} via

$$\Delta T_{LHN}(h) = (\alpha_{LHN} - 1)\Delta T_{LH,mod}(h) \tag{4.2}$$

with h the vertical coordinate and $\Delta T_{LH,mod}$ the vertical profile of modelled temperature change by latent heating (Schraff et al., 2016). The temperature profile used for scaling can also be predefined, but using the modeled latent heating profile $\Delta T_{LH,mod}$ allows for consistency with the model's parameterization scheme and for temporal evolution of the vertical profile (Jones and Macpherson, 1997). Equations 4.1 and 4.2 show that the increment ΔT_{LHN} is positive (negative) if the observed rain rate RR_{obs} is higher (lower) than the background rain rate RR_{mod}. The determined temperature increment is then used to apply Newtonian nudging with the thermodynamic prognostic model equations over a defined time interval. Positive increments lead to heating and upward air motion in the model leading to condensation and precipitation generation (Schraff et al., 2016). In addition, a specific humidity increment is often added to avoid and immediate decrease in relative humidity and connected cloud dissipation in the model (Schraff et al., 2016).

Several studies have shown that the assimilation of Z_H observations with LHN has a positive impact on QPF (e.g., Leuenberger and Rossa, 2007; Stephan et al., 2008; Schraff et al., 2016; Jacques et al., 2018; Jacques and Michelson, 2022). These encouraging results led to the operational implementation of LHN at several national meteorological services including the MetOffice (Jones and Macpherson, 1997; Macpherson, 2001), MeteoSwiss (Leuenberger and Rossa, 2007), and at DWD (Schraff et al., 2016). However, a clear drawback of the Newtonian relaxation or nudging approach is the fact that it can only be used to assimilate prognostic model variables, which limits its applicability to exploit, e.g., the full 3D structure of (polarimetric) radar observations in DA.

4.1.3 Statistical Interpolation Schemes

Over the past decades, the emphasis for initializing NWP models with radar observations has been on statistical interpolation methods. This section details the main statistical DA schemes that have been used for radar DA. These methods include variational DA schemes and sequential DA methods based on the EnKF (Evensen, 1994, 2003). First, the 3DVar method (Courtier et al., 1998) is derived, and the considerations and derivations made subsequently hand over to the formulations of the 4DVar method (e.g., Lewis and Derber, 1985; Le Dimet and Talagrand, 1986) – a generalization of the 3DVar method in terms of the inclusion of the time dimension of the observations – and the EnKF methods. The focus here is on the EnKF, in particular the LETKF (Hunt et al., 2007), which currently enjoys

great popularity in the (radar) DA community and is used in this thesis to assimilate polarimetric data from the German national C-band radar network (Chapter 5). In addition, first attempts to also use hybrid DA schemes and the particle filter are shortly described.

4.1.3.1 The 3DVar Method

The general objective of statistical DA schemes is to produce the best estimate of the true state of the atmospheric flow represented on the model grid (the analysis) in a least-squares sense by statistically combining meteorological observations and typically a prior model estimate in the form of a short-range model forecast (the background or first guess) considering their respective uncertainties (Talagrand, 1997; Kalnay, 2003). The background model state can be expressed as an N-dimensional vector $\vec{x}_b$ consisting of the arrayed prognostic model fields with N the number of model grid points times the number of prognostic model variables, which is on the order of 10^7 for modern operational NWP models (Kalnay, 2003). The observations can be described by an O-dimensional vector $\vec{y}_o$, where O is usually much smaller (about 10^4) than N. The uncertainties associated with the background and observation vectors $\vec{x}_b$ and $\vec{y}_o$ can be expressed through the $N \times N$ and $O \times O$ covariance matrices of their respective (unknown) errors $\vec{\varepsilon}_b$ and $\vec{\varepsilon}_o$

$$\boldsymbol{B} = \mathrm{E}[\vec{\varepsilon}_b \vec{\varepsilon}_b^T] \tag{4.3}$$

and

$$\boldsymbol{R} = \mathrm{E}[\vec{\varepsilon}_o \vec{\varepsilon}_o^T] \tag{4.4}$$

with $\vec{v}^T$ indicating the transpose of a vector $\vec{v}$ and $\mathrm{E}[x]$ is the expected value of a random variable x. The length of the vectors $\vec{\varepsilon}_b$ and $\vec{\varepsilon}_o$ is N and O, respectively, and

$$\vec{\varepsilon}_b = \vec{x}_b - \vec{x}_t \tag{4.5}$$

and

$$\vec{\varepsilon}_o = \vec{y}_o - \mathcal{H}(\vec{x}_t) \tag{4.6}$$

with $\mathcal{H}$ a (non-linear) observation operator, which maps a state vector $\vec{x}$ from model space (model grid points and variables) to observation space (observation locations and variables), e.g., using spatial interpolations or/and physical laws (Kalnay, 2003), and $\vec{x}_t$ the (of course unknown) true atmospheric state represented on the model grid with dimension N. The background and observation errors $\vec{\varepsilon}_b$ and $\vec{\varepsilon}_o$ are assumed to be unbiased and uncorrelated.

The true state $\vec{x}_t$ is treated as random variable described by a probability density function, which is attempted to be determined using Bayesian probabilistic arguments (e.g., Lorenc, 1986). According to Bayes' rule, the *a posteriori* probability of the occurrence of an event A, given that an event B is known to have occurred, is proportional to the *prior* probability of the occurrence of the event A multiplied by the probability of the occurrence of the event B, given that the event A has occurred. This can be formulated mathematically by

$$P(\mathrm{A}|\mathrm{B}) \propto P(\mathrm{B}|\mathrm{A})P(\mathrm{A}) \tag{4.7}$$

(Lorenc, 1986). Applied to DA, the prior probability $P(\mathrm{A})$ is the probability that a random model state $\vec{x}$ is equal to the true atmospheric state $\vec{x}_t$, $P(\mathrm{B}|\mathrm{A})$ is the conditional probability of the occurrence of the observation vector $\vec{y}_o$ given the occurrence of $\vec{x}$, and the a posteriori probability $P(\mathrm{A}|\mathrm{B})$ is the probability that $\vec{x}$ is equal to $\vec{x}_t$ given the observations $\vec{y}_o$, such that

$$P(\vec{x}|\vec{y}_o) \propto P(\vec{y}_o|\vec{x})P(\vec{x}) \tag{4.8}$$

(Lorenc, 1986). The Bayesian estimate of $\vec{x}_t$ is the vector $\vec{x}$ that maximizes the a posteriori probability $P(\vec{x}|\vec{y}_o)$ (Lorenc, 1986). Both the prior probability $P(\vec{x})$ and the conditional probability $P(\vec{y}_o|\vec{x})$ must be known to solve this problem.

In the 3DVar method (and the 4DVar and EnKF methods), both probabilities $P(\vec{x})$ and $P(\vec{y}_o|\vec{x})$ from Eq. (4.8) are assumed to be Gaussian distributed as

$$P(\vec{x}) = [(2\pi)^{\frac{N}{2}}|\boldsymbol{B}|^{\frac{1}{2}}]^{-1}\exp[-\tfrac{1}{2}(\vec{x}_b - \vec{x})^T\boldsymbol{B}^{-1}(\vec{x}_b - \vec{x})] \tag{4.9}$$

and

$$P(\vec{y}_o|\vec{x}) = [(2\pi)^{\frac{O}{2}}|\boldsymbol{R}|^{\frac{1}{2}}]^{-1}\exp[-\tfrac{1}{2}\big(\vec{y}_o - \mathcal{H}(\vec{x})\big)^T\boldsymbol{R}^{-1}\big(\vec{y}_o - \mathcal{H}(\vec{x})\big)] \tag{4.10}$$

(Kalnay, 2003). The prior distribution $P(\vec{x})$ in Eq. (4.9) is the only source of information about the truth before the observations are considered, and thus the model state $\vec{x}$ that is most likely $\vec{x}_t$ is given by $\vec{x} = \vec{x}_b$. Equation (4.8) can be written as

$$P(\vec{x}|\vec{y}_o) \propto \exp[-\left\{\tfrac{1}{2}(\vec{x} - \vec{x}_b)^T\boldsymbol{B}^{-1}(\vec{x} - \vec{x}_b) + \tfrac{1}{2}\big(\vec{y}_o - \mathcal{H}(\vec{x})\big)^T\boldsymbol{R}^{-1}\big(\vec{y}_o - \mathcal{H}(\vec{x})\big)\right\}] \tag{4.11}$$

and the maximum a posteriori probability is obtained when the exponent

$$J(\vec{x}) = \underbrace{\frac{1}{2}(\vec{x} - \vec{x}_b)^T \boldsymbol{B}^{-1}(\vec{x} - \vec{x}_b)}_{J_b(\vec{x})} + \underbrace{\frac{1}{2}\left(\vec{y}_o - \mathcal{H}(\vec{x})\right)^T \boldsymbol{R}^{-1}\left(\vec{y}_o - \mathcal{H}(\vec{x})\right)}_{J_o(\vec{x})} \quad (4.12)$$

is minimized (Lorenc, 1986; Kalnay, 2003). The term $J_b(\vec{x})$ measures the misfit between the background and $\vec{x}$ weighted by $\boldsymbol{B}$, while $J_o(\vec{x})$ quantifies the misfit between the observations and the background in observation space weighted by $\boldsymbol{R}$. By linearizing the observation operator $\mathcal{H}$ in Eq. (4.12) around the background state $\vec{x}_b$ one may obtain the gradient of the cost function J in Eq. (4.12) with respect to $\vec{x}$

$$\nabla J(\vec{x}) = \boldsymbol{B}^{-1}(\vec{x} - \vec{x}_b) + \boldsymbol{H}^T \boldsymbol{R}^{-1} \boldsymbol{H}(\vec{x} - \vec{x}_b) - \boldsymbol{H}^T \boldsymbol{R}^{-1}(\vec{y}_o - \mathcal{H}(\vec{x})) \quad (4.13)$$

(Kalnay, 2003) with $\boldsymbol{H}^T$ the adjoint of a linearization $\boldsymbol{H}$ of the nonlinear observation operator $\mathcal{H}$.

The 3DVar method attempts to minimize the cost function in Eq. (4.12), i.e., finding that $\vec{x}$, for which the gradient of the cost function vanishes, which is the N-dimensional analysis vector $\vec{x}_a$, such that

$$\nabla J(\vec{x}_a) = 0. \quad (4.14)$$

Combination of Eqs. (4.13) and (4.14) finally results in

$$\vec{x}_a = \vec{x}_b + (\boldsymbol{B}^{-1} + \boldsymbol{H}^T \boldsymbol{R}^{-1} \boldsymbol{H})^{-1} \boldsymbol{H}^T \boldsymbol{R}^{-1}(\vec{y}_o - \mathcal{H}(\vec{x}_b)), \quad (4.15)$$

so that the analysis state $\vec{x}_a$ is equal to the background state $\vec{x}_b$ plus the observation increment (or innovation) $\vec{d} = \vec{y}_o - \mathcal{H}(\vec{x}_b)$ weighted by a weighting matrix $(\boldsymbol{B}^{-1} + \boldsymbol{H}^T \boldsymbol{R}^{-1} \boldsymbol{H})^{-1} \boldsymbol{H}^T \boldsymbol{R}^{-1}$. Equation (4.15) is the formal solution of the 3DVar problem.

In practice, iterative approaches such as the steepest descent and conjugate gradient or quasi-Newton (Navon and Legler, 1987) methods are used to find the minimum of the cost function J in Eq. (4.12) using its gradient in Eq. (4.13) (Kalnay, 2003). In addition, the observation and background error covariance matrices $\boldsymbol{R}$ and $\boldsymbol{B}$ must be estimated, since the exact error statistics of the observations and the background model field are never fully known. The matrix $\boldsymbol{R}$ is typically assumed to be diagonal (e.g., Gao et al., 2004; Hu et al., 2006a), so that correlations between individual observations are neglected. The matrix $\boldsymbol{B}$ filters the observations and defines how analysis increments are distributed over the model domain (e.g., Kalnay, 2003). For operational weather forecasting, $\boldsymbol{B}$ typically contains more than 10^{10} elements (N^2), which must be determined from the innovation vectors $\vec{d}$ corresponding to about 10^7 to 10^8 observations per year (Courtier et al., 1998). Therefore, it is difficult to determine reasonably stable background statistics from

observations, which are instead inferred using statistical models, such as the NMC (National Meteorological Center) method (Parrish and Derber, 1992). This leads to a lack of appropriate balances between the model variables (e.g., Ge et al., 2012), which is a major drawback of 3DVar. Another drawback is the use of static background error covariance matrices (Kalnay, 2003; Gustafsson et al., 2018), especially at the convective scale. The ability to assimilate indirect observations and to solve the analysis problem globally are advantages of 3DVar (Kalnay, 2003; Sun, 2005b).

Assimilation of Doppler radar observations with the 3DVar method resulted in improved QPF. E.g., Xiao et al. (2005) demonstrated positive effects of assimilating V_r observations with 3DVar on heavy rainfall prediction over South Korea. They used preconditioned control variables, i.e., the variables with respect to which the cost function minimization is performed. Such preconditioning is a common approach to achieve faster convergence by a more "spherical" 3DVar cost function (e.g., Parrish and Derber, 1992; Kalnay, 2003). Hu et al. (2006b), Hu and Xue (2007), and Schenkman et al. (2011a,b) also presented positive impacts of assimilating V_r data using 3DVar in combination with a cloud analysis for assimilating Z_H observations on convective storm forecasts. More recently, Simonin et al. (2014) also showed positive impacts of assimilating V_r data on the forecasts of rain and wind by the MetOffice Unified Model for a few hours.

However, the direct assimilation of Z_H observations with 3DVar posed a greater challenge to the research community because appropriate background error statistics for hydrometeor variables such as rain mixing ratios are particularly difficult to obtain, e.g., via the NMC-method (Xiao et al., 2007). A technique to overcome this problem was developed by Xiao et al. (2007) for the MM5 3DVar DA system, in which they used the model total liquid water mixing ratio as the control variable instead of the rain-water mixing ratio, and partitioned the moisture and hydrometeor increments using a warm-rain microphysical process, its linear, and its adjoint. They then used the partitioned rain-water mixing ratio to enable direct assimilation of Z_H data, which together with the assimilation of V_r data, resulted in an improved short-range QPF for a typhoon at landfall in South Korea. Routray et al. (2010) used this technique to investigate the impact of V_r and Z_H data on the forecasts of Indian monsoon depressions using the Weather Research and Forecasting (WRF) model and its 3DVar system and showed positive effects of the radar DA on QPF. Sugimoto et al. (2009) presented improved QPF when using the technique of Xiao et al. (2005, 2007) for the assimilation of Doppler radar observations in convective situations. To avoid potential problems due to the linearization of the Z_H operator in the 3DVar analysis, Wang et al. (2013a) assimilated Z_H data indirectly using an in-cloud water vapor estimator and showed significantly improved QPF up to seven hours.

Work has also been done to improve the balance between model state variables in the 3DVar analysis by including weak constraints in the 3DVar cost function that allow the distribution of observational information also to model state variables that are not directly observed. This can be done by adding a "penalty-term" J_c to the 3DVar cost function in Eq. (4.12), which, e.g., incorporates a mass continuity

constraint (e.g., Gao et al., 2004; Hu et al., 2006b) also taken into account in the minimization process. Gao and Stensrud (2012) used the technique of Gao et al. (2004) within the ARPS 3DVar system, applied a Z_H forward operator that included a simple hydrometeor classification based on the model background temperature fields and reported an improved analysis and a dramatic improvement in the model spin-up for a convective storm. Another approach was taken by Vendrasco et al. (2016) to address the problem of spurious precipitation in the model domain and large errors in precipitation location and amount, in which they constrained the cost function in the WRF 3DVar system through a large-scale analysis at coarser resolution and found improved forecast skill. Similarly, Tong et al. (2016) used a divergence constraint in WRF 3DVar system and found reduced spurious precipitation and improved QPF.

The found positive effects on short-term QPF, its ability to directly assimilate radar observations, and its overall computational efficiency, which makes real-time applications relatively practical (Ge et al., 2012), led to the use of the 3DVar method for assimilation of Doppler radar observations also in operational settings, e.g., in the French Application of Research to Operations at Mesoscale model and at the Korean Meteorological Administration. However, the use of static background error covariances, especially at the convective scale, and the need for the development of tangent linear radar forward operators and respective adjoints (see Eq. (4.13)) overall limit the usability of the 3DVar method to directly assimilate radar observations.

4.1.3.2 The 4DVar Method

The 4DVar DA method is a generalization of the 3DVar method, which was introduced to meteorology in the mid 1980s (e.g., Lewis and Derber, 1985; Le Dimet and Talagrand, 1986; Talagrand and Courtier, 1987) and saw its first operational implementation at the ECMWF (e.g., Rabier et al., 2000). The 4DVar method, unlike 3DVar, considers the time dimension of observations distributed over an assimilation time window and also attempts to minimize a cost function (Kalnay, 2003)

$$J\big(\vec{x}(t_0)\big) = J_b(\vec{x}(t_0)) + J_o(\vec{x}(t_0)) \tag{4.16}$$

with

$$J_b\big(\vec{x}(t_0)\big) = \tfrac{1}{2}(\vec{x}(t_0) - \vec{x}_b(t_0))^T \boldsymbol{B}_0^{-1}(\vec{x}(t_0) - \vec{x}_b(t_0)) \tag{4.17}$$

and

$$J_o\big(\vec{x}(t_0)\big) = \tfrac{1}{2}\sum_{i=0}^{T}\big(\mathcal{H}(\vec{x}_i) - \vec{y}_{o,i}\big)^T \boldsymbol{R}_i^{-1}(\mathcal{H}(\vec{x}_i) - \vec{y}_{o,i}). \tag{4.18}$$

Unlike 3DVar, in the 4DVar cost function in Eqs. (4.16) to (4.18), the control variable is the model state at the beginning of the assimilation time window $\vec{x}(t_0)$. The term J_b in Eq. (4.17) measures the misfit between the variable initial model state $\vec{x}(t_0)$ and the background state $\vec{x}_b$ (at the initial time) weighted by the background error covariance matrix at the initial time $\boldsymbol{B}_0$. The term J_o (Eq. (4.18)) is a time summation of all observation increments weighted by the observation error covariance matrix at the ith of $\mathcal{T}$ observation times $\boldsymbol{R}_i$ and is computed from the model state at the ith observation time $\vec{x}_i$, which is obtained from the initial state $\vec{x}(t_0)$ by integration of the forecast model to the ith observation time. The analysis at the end of the assimilation window is obtained by integration of the model from time t_0 to the end time $t_{\mathcal{T}}$ with the initial model state $\vec{x}(t_0)$ that minimizes the cost function in Eq. (4.16) (Kalnay, 2003). In other words, the 4DVar method attempts to find an initial model state, which leads to a model forecast over the assimilation window that best fits the observations distributed over it. Therefore, the forecast model is a strong constraint on the 4DVar analysis solution (Sasaki, 1970; Kalnay, 2003).

In practice, iterative minimization algorithms like the steepest decent method and the conjugate gradient or quasi-Newton (Navon and Legler, 1987) are utilized to solve the 4DVar problem like for 3DVar. To this end, the gradient of the cost function J in Eq. (4.16) with respect to $\vec{x}(t_0)$ is required, which can be expressed as

$$\nabla J_b\big(\vec{x}(t_0)\big) = \boldsymbol{B}_0^{-1}(\vec{x}(t_0) - \vec{x}_b(t_0)) \tag{4.19}$$

for the background term and

$$\nabla J_o\big(\vec{x}(t_0)\big) = \sum_{i=0}^{\mathcal{T}} \boldsymbol{L}(t_i, t_0)^T \boldsymbol{H}_i^T \boldsymbol{R}_i^{-1}(\mathcal{H}(\vec{x}_i) - \vec{y}_{o,i}) \tag{4.20}$$

for the observation term (Kalnay, 2003). In Eq. (4.20), $\boldsymbol{L}(t_i, t_0)^T$ is the adjoint linear tangent forecast model operator (consisting of the product of the adjoint linear model operators at all observation times from t_i to t_0), which propagates the observation information backward from time t_i to the initial time t_0, and $\boldsymbol{H}_i^T$ is the adjoint linearized observation operator in the vicinity of the model state at the ith observation time $\vec{x}_i$ obtained from the incipient model forward integration. The integrations of the adjoint forecast model backward to the initial time in Eq. (4.20) are common for multiple time intervals. Thus, the calculation of the gradient of J can be made more feasible by rewriting Eq. (4.20) as

$$\nabla J_o\big(\vec{x}(t_0)\big) = \dot{\vec{d}}_0 + \boldsymbol{L}_0^T(\dot{\vec{d}}_1 + \boldsymbol{L}_1^T\left(\dot{\vec{d}}_2 + \cdots + \boldsymbol{L}_{\mathcal{T}-1}^T \dot{\vec{d}}_{\mathcal{T}}\right)) \tag{4.21}$$

with the negative observation increments weighted by $\boldsymbol{R}_i$ in model space

$$\dot{\vec{d}}_i = \boldsymbol{H}_i^T \boldsymbol{R}_i^{-1}(\mathcal{H}(\vec{x}_i) - \vec{y}_{o,i}) \tag{4.22}$$

and $\boldsymbol{L}_{i-1}^T$ the adjoint linear tangent forecast model in the vicinity of $\vec{x}_i$ propagating a state vector from time t_i to time t_{i-1} (Kalnay, 2003).

The 4DVar method has the advantage of being able, like 3DVar, to assimilate indirect observations such as radar observations with certain constraints. In contrast to 3DVar, if the forecast model was perfect and the background error covariance matrix at the in initial time $\boldsymbol{B}_0$ was exact, the 4DVar analysis at the end of the assimilation window was found to coincide with the analysis obtained with the extended KF (Lorenc, 1986), which uses the linearized forecast model to advance the background error covariance matrix and calculates the analysis error covariance matrix based on the Kalman gain (Kalnay, 2003). Thus, 4DVar is able to implicitly advance the background error covariance to the analysis time (Kalnay, 2003). However, the analysis error covariance matrix at the end of the assimilation window is not provided in 4DVar. Consequently, it must be assumed to be static as in 3DVar (Gustafsson et al., 2018). The perfect model assumption intrinsic in 4DVar is a drawback, since observations from the end of the assimilation window are weighted in the same way as those from the beginning, even though the newer observation information is integrated by the adjoint of the (non-perfect) model more often than the older information (Kalnay, 2003). In addition, the 4DVar method is computational expensive because the forecast model is used several times in the minimization process (Sun, 2005b). Finally, another advantage of 4DVar is that all the observations in the assimilation window are considered at their respective observation times and a global solution is sought for all observations simultaneously. Thus, the 4DVar analysis satisfies the model equations (Kalnay, 2003).

The 4DVar technique was first tested for radar observations by, e.g., Sun et al. (1991) and Kapitza (1991), who attempted, with some success, to retrieve unobserved velocity and temperature fields from single-Doppler radar data using high-resolution boundary layer models and their adjoints. Sun and Crook (1997) developed the frequently used 4DVar Doppler Radar Analysis System (VDRAS), which assimilated single- or multiple-Doppler radar observations into a cloud-scale NWP model with a warm-rain parameterization scheme. They showed that VDRAS was able to retrieve the detailed structure of the wind, thermodynamics, and microphysics from both single- and dual-Doppler radar data of a simulated convective storm. However, they also noted difficulties in minimizing the 4DVar cost function due to high nonlinearities in the parameterization scheme used. Indirect assimilation of synthetic Z_H data using rain-water mixing ratio estimators produced better results than their direct assimilation, which they attributed to the nonlinearity introduced into the cost function by the highly nonlinear reflectivity observation operator. Sun and Crook (1998) applied VDRAS to a real convective storm over Florida and found that the vertical velocity, buoyancy, and water-vapor mixing ratio fields could be retrieved well by assimilating V_r data and Z_H-based rain-water mixing ratios. Later, VDRAS

was also successfully applied in several studies for convective-scale storm analyses and forecasting (e.g., Sun, 2005a; Sun and Zhang, 2008; Sun et al., 2010).

Wang et al. (2013b) described the implementation of Doppler radar data assimilation in the WRF model 4DVar system. They modified the existing WRF 4DVar system by adding cloud water, rainwater, and vertical velocity as control variables, by modeling the respective error covariances, and incorporating the tangent-linear and adjoint models of a Kessler warm-rain microphysics scheme following Sun and Crook (1997) to allow for better minimization of the cost function. Moreover, they used a large ensemble to determine the background error covariance, and assimilated Z_H indirectly, similar to Sun and Crook (1997), following Wang et al. (2013a) to avoid a dry bias in the rainwater analysis. Their modifications resulted in successful convective-scale analyses and improved QPF. Kawabata et al. (2011) modified the 4DVar system of a nonhydrostatic convective-scale model to directly assimilate Z_H data using the full nonlinear forward model including ice microphysics, and a warm-rain-only adjoint model, which resulted in an improved prediction of heavy rainfall in the Tokyo, Japan, metropolitan area. More recently, Hawkness-Smith and Simonin (2021) investigated the direct assimilation of Z_H observations in the MetOffice Unified Model with an hourly 4DVar cycle. Only rainwater mixing ratios diagnosed from cloud water increments were updated in the 4DVar analysis, although the ice phase contributed to the Z_H forward operator.

The consideration of only warm-rain microphysical processes in the assimilation of radar observations with the 4DVar method, to the best of the author's knowledge, may be due to difficulties in formulating linear adjoints of highly complex ice microphysical processes, which may hamper the ability of the method to update NWP models with respect to the ice phase. Ice processes, however, play an important role not only in intense summertime convective situations, but especially also in winter ice-phase precipitation. For the assimilation of ice-phase radar data in these situations, the EnKF approach, detailed in the following section, is much more appropriate, because it estimates the highly flow-dependent forecast uncertainties at the convective scale from an ensemble of model forecasts and does not require the utilization of linearized models and operators and their adjoints.

4.1.3.3 The Ensemble Kalman Filter

The KF (Kalman, 1960; Kalman and Bucy, 1961) and 3DVar are formally similar approaches to determine the analysis. The former attempts to solve the analysis problem by computing the optimal weight (or gain) matrix, while the latter attempts to solve it by minimizing a cost function (Kalnay, 2003). A major difference between the two methods, however, is that the background error covariance matrix in the KF is advanced using the forecast model, while a static covariance matrix is used in the 3DVar method. For typical weather forecast models, the extended KF (EKF) is more appropriate, as it allows for nonlinear forecast models to advance the model state while a model linearization is used to advance the forecast error covariance matrix

(Ide et al., 1997; Kalnay, 2003). More specifically, the EKF forecast step evolves the analysis $\vec{x}_a$ and the analysis error covariance matrix $\boldsymbol{P}_a$ from time t_{i-1} to t_i as

$$\vec{x}_f(t_i) = \mathcal{M}_{i-1}(\vec{x}_a(t_{i-1})) \tag{4.23}$$

and

$$\boldsymbol{P}_f(t_i) = \boldsymbol{L}_{i-1}\boldsymbol{P}_a(t_{i-1})\boldsymbol{L}_{i-1}^T + \boldsymbol{Q}(t_{i-1}). \tag{4.24}$$

(Ide et al., 1997; Kalnay, 2003). In Eq. (4.23), $\vec{x}_f$ is the forecasted model state and $\mathcal{M}_{i-1}$ is the (non-linear) forward model operator used to evolve a model state from time t_{i-1} to t_i. In Eq. (4.24), $\boldsymbol{P}_f$ is the advanced forecast error covariance matrix, $\boldsymbol{L}_{i-1}$ is the linear tangent forecast model transforming a perturbation from time t_{i-1} to t_i (Lorenz, 1965), $\boldsymbol{L}_{i-1}^T$ is its adjoint, and $\boldsymbol{Q}$ is the covariance matrix of a zero-mean noise process representing subgrid-scale processes not resolved by the forecast model (Ide et al., 1997). The EKF analysis step then generates the new analysis state $\vec{x}_a$ and the new analysis error covariance matrix $\boldsymbol{P}_a$ at time t_i according to

$$\vec{x}_a(t_i) = \vec{x}_f(t_i) + \boldsymbol{K}_i[\vec{y}_{o,i} - \mathcal{H}_i\left(\vec{x}_f(t_i)\right)] \tag{4.25}$$

and

$$\boldsymbol{P}_a(t_i) = (\boldsymbol{I} - \boldsymbol{K}_i\boldsymbol{H}_i)\boldsymbol{P}_f(t_i) \tag{4.26}$$

with $\boldsymbol{I}$ the identity matrix and the Kalman gain (or weighting matrix)

$$\boldsymbol{K}_i = \boldsymbol{P}_f(t_i)\boldsymbol{H}_i^T[\boldsymbol{R}_i + \boldsymbol{H}_i\boldsymbol{P}_f(t_i)\boldsymbol{H}_i^T]^{-1} \tag{4.27}$$

equal to the weighting matrix in Eq. (4.15) in the case that $\boldsymbol{P}_f$ in Eq. (4.27) and $\boldsymbol{B}$ in Eq. (4.15) were identical (Ide et al., 1997; Kalnay, 2003). The EKF can provide the best (least-squares) linear unbiased estimate of the true state $\vec{x}_t$ and its associated error covariance matrix if the system under consideration is not too unstable and the observations are not too sparse in time (Miller et al., 1994). Unfortunately, the application of the EKF to meteorological DA problems is inappropriate, since the updating of the forecast error covariance matrix in the forecast step (Eq. (4.24)) requires computational expenses that are as high as performing N, the number of degrees of freedom of the model state (~10^7), model integrations (Kalnay, 2003).

The ensemble KF (EnKF), originally proposed by Evensen (1994) is a Monte Carlo approximation of the classical KF (Whitaker and Hamill, 2002). It uses an ensemble of short-term model forecasts to estimate the forecast error covariance

matrix at the analysis time required for the calculation of the Kalman gain, which is then used to generate the analysis ensemble. The ensemble means of the forecast and analysis ensembles $\overline{\vec{x}_f}$ and $\overline{\vec{x}_a}$ (ensemble means hereafter denoted by overbars) correspond to the states $\vec{x}_f$ and $\vec{x}_a$ in the EKF in Eqs. (4.23) and (4.25), respectively, while the spreads of the forecast and analysis ensembles $\vec{x}_f^m$ and $\vec{x}_a^m$ (ensemble members hereafter indicated by the superscript m) can be used to estimate the error covariance matrices $\boldsymbol{P}_f$ and $\boldsymbol{P}_a$ in Eqs. (4.24) and (4.26) (Houtekamer et al., 2005). The EnKF forecast and analysis step equations in Eqs. (4.23) to (4.26) can be written, dropping the time index for time t_i for clarity, as (Houtekamer and Mitchell, 2005):

$$\vec{x}_f^m = \mathcal{M}\left(\vec{x}_a^m(t_{i-1})\right) + \vec{q}^m \quad \text{with} \quad \vec{q}^m \sim \mathcal{N}(0, \boldsymbol{Q}), \tag{4.28}$$

$$\boldsymbol{P}_f\boldsymbol{H}^T = \frac{1}{M-1}\sum_{m=1}^{M}(\vec{x}_f^m - \overline{\vec{x}_f})(\mathcal{H}(\vec{x}_f^m) - \overline{\mathcal{H}(\vec{x}_f^m)})^T, \tag{4.29}$$

$$\boldsymbol{H}\boldsymbol{P}_f\boldsymbol{H}^T = \frac{1}{M-1}\sum_{m=1}^{M}(\mathcal{H}(\vec{x}_f^m) - \overline{\mathcal{H}(\vec{x}_f^m)})(\mathcal{H}(\vec{x}_f^m) - \overline{\mathcal{H}(\vec{x}_f^m)})^T, \tag{4.30}$$

$$\boldsymbol{K} = \boldsymbol{P}_f\boldsymbol{H}^T(\boldsymbol{R} + \boldsymbol{H}\boldsymbol{P}_f\boldsymbol{H}^T)^{-1}, \tag{4.31}$$

$$\vec{y}_o^m = \vec{y}_o + \vec{r}^m \quad \text{with} \quad \vec{r}^m \sim \mathcal{N}(0, \boldsymbol{R}), \tag{4.32}$$

and

$$\vec{x}_a^m = \vec{x}_f^m + \boldsymbol{K}(\vec{y}_o^m - \mathcal{H}(\vec{x}_f^m)). \tag{4.33}$$

To obtain the new forecast ensemble in Eq. (4.28) with the full nonlinear model $\mathcal{M}$, the noise process $\vec{q}^m$, which is normally distributed respecting the noise covariance matrix $\boldsymbol{Q}$, is added. The Kalman gain $\boldsymbol{K}$ in Eq. (4.31) can be calculated directly from the terms $\boldsymbol{P}_f\boldsymbol{H}^T$ in Eq. (4.29) and $\boldsymbol{H}\boldsymbol{P}_f\boldsymbol{H}^T$ in Eq. (4.30) determined from the forecast ensemble, with M the ensemble size, without the need for a linearization of the observation operator $\mathcal{H}$ or adjoints. Moreover, the very large forecast error covariance matrix $\boldsymbol{P}_f$ required for the calculation of $\boldsymbol{K}$ in Eq. (4.31) does not need to be computed, and thus only the ensemble members $\vec{x}_f^m$, but not $\boldsymbol{P}_f$, need to be stored. Finally, Eq. (4.33) shows the EnKF analysis step using observations normally perturbed by respecting the observation error covariance matrix $\boldsymbol{R}$ (see Eq. (4.32)).

Observation perturbation was not implemented in the original EnKF (Evensen, 1994). Burgers et al. (1998) stated that without the use of randomly perturbed observations for atmospheric applications, the error covariance matrix determined from the analysis ensemble is significantly underdetermined, potentially leading to filter divergence (Whitaker and Hamill, 2002). This point can be clarified writing the EnKF analysis step equation in Eq. (4.33) in terms of an update to the ensemble mean

$$\overline{\vec{x}_a} = \overline{\vec{x}_f} + \boldsymbol{K}(\overline{\vec{y}_o} - \mathcal{H}(\overline{\vec{x}_f})) \tag{4.34}$$

and an update of the deviations from the ensemble mean

$$\vec{x}_a^{m\prime} = \vec{x}_f^{m\prime} + \widetilde{\boldsymbol{K}}(\vec{y}_o^{m\prime} - \mathcal{H}(\vec{x}_f^{m\prime})) \tag{4.35}$$

with primes denoting deviations from the ensemble mean and $\boldsymbol{K}$ and $\widetilde{\boldsymbol{K}}$ the classical Kalman gain (see Eq. (4.31)) and the gain for updating the deviations from the ensemble mean (Whitaker and Hamill, 2002). The $\overline{\vec{y}_o}$ can be interpreted as the original observations, while the $\vec{y}_o^{m\prime}$ are the perturbations from $\overline{\vec{y}_o}$ respecting $\boldsymbol{R}$. The update of the analysis error covariance matrix $\boldsymbol{P}_a$ may be written as

$$\boldsymbol{P}_a = (\boldsymbol{I} - \boldsymbol{KH})\boldsymbol{P}_f = (\boldsymbol{I} - \boldsymbol{KH})\boldsymbol{P}_f(\boldsymbol{I} - \boldsymbol{KH})^T + \boldsymbol{KRK}^T \tag{4.36}$$

(Whitaker and Hamill, 2002). Burgers et al. (1998) noted that when $\boldsymbol{K} = \widetilde{\boldsymbol{K}}$, as in the original EnKF (Whitaker and Hamill, 2002), and no observation perturbations are used (i.e., $\vec{y}_o^{m\prime} = 0$), there is no analog to the term $\boldsymbol{KRK}^T$ in Eq. (4.36) in the analysis ensemble error covariance matrix (the same observations are used for all ensemble members), resulting in a systematic underestimation of $\boldsymbol{P}_a$.

There are various manifestations of the EnKF, most of which can be classified as either stochastic or deterministic in generating the analysis ensemble (Tippett et al., 2003; Meng and Zhang, 2011). The stochastic approaches use perturbed observations as described above to maintain spread in the analysis ensemble (Eqs. (4.28) to (4.33); e.g., Houtekamer and Mitchell, 1998), while the deterministic approaches use a deterministic transformation of the forecast to the analysis ensemble without the need for observation perturbations. The deterministic approaches, mostly in the form of ensemble square-root filters (EnSRF; for a review see Tippett et al., 2003), are justified by the argument that the perturbation of the observations, as done in the stochastic approaches, represents an additional source of sampling error, which, especially for smaller ensemble sizes, can reduce the accuracy of the analysis error covariances and increase the probability of their underestimation, potentially leading to filter divergence (Tippett et al., 2003; Houtekamer and Mitchell, 2005). Ensembles usable for atmospheric applications are typically severely limited in size due to computational constraints, so the deterministic EnKF approaches have been used more frequently overall. E.g., Whitaker and Hamill (2002) proposed a serial EnSRF that uses the traditional Kalman gain $\boldsymbol{K}$ to update the ensemble mean (as in Eq. (4.34)), but uses a modified gain $\widetilde{\boldsymbol{K}}$ to update the deviations from the ensemble mean, so that the resulting analysis ensemble satisfies Eq. (4.36) without applying observation perturbations. Their scheme has proven success in some mesoscale ensemble-based assimilation studies (e.g., Snyder and Zhang, 2003). Further deterministic EnKF approaches equivalent to the serial EnSRF of Whitaker and

Hamill (2002) in terms of functionality are, e.g., the ensemble adjustment KF (EAKF; Anderson, 2001) and the ensemble transform KF (ETKF; Bishop et al., 2001). Both methods generate the analysis ensemble mean using of the traditional Kalman gain $\boldsymbol{K}$ and both methods generate the updated deviations from the analysis ensemble mean with the constraint of satisfying Eq. (4.36). The EAKF utilizes a linear operator $\boldsymbol{A} = \boldsymbol{I} - \widetilde{\boldsymbol{K}}\boldsymbol{H}$ to generate an analysis ensemble with a sample covariance matrix that satisfies Eq. (4.36) by "adjusting" the background forecast ensemble. The ETKF uses an ensemble transformation and a normalized observation operator to obtain the analysis error covariances directly from the background error covariances in a low-dimensional space spanned by the ensemble perturbations.

Since forecast ensemble sizes are typically very limited in practice, non-zero uncertainty in the model state estimate can only be described in the subspace spanned by the ensemble (Hunt et al., 2007), i.e., the ensemble-estimated forecast error covariance matrix is severely rank deficient. In the case of a high-dimensional unstable system, such as a weather forecast model, forecast errors will grow in directions outside of the ensemble subspace and the analysis will not be able to make corrections for these errors (Hunt et al., 2007). As a result, the analysis ensemble spread tends to be significantly underestimated (Meng and Zhang, 2011), which can lead to filter divergence by giving too much credibility to the background state relative to new observations, i.e., the model trajectory decouples from the truth (Hunt et al., 2007). A common solution to avoid too small analysis ensemble spreads is covariance inflation, which artificially increases either the spread of the forecast ensemble or the spread of analysis ensemble. Inflating the background ensemble covariance can be interpreted as localizing observations in time, since the influence of past observations on the current analysis decays exponentially with increasing observation age by increasing the uncertainty in the background state (which contains information about the past observations) in each analysis cycle (Hunt et al., 2007). Especially in the presence of model errors (which is always the case), such temporal observation localization is advantageous, because the erroneous model is not able to reliably propagate past observation information over an unlimited time period (Hunt et al., 2007). Covariance inflation can be accomplished, e.g., by multiplicative covariance inflation (MCI; Anderson and Anderson, 1999), additive covariance inflation (ACI; e.g., Mitchell et al., 2002), or covariance relaxation to prior perturbations (CRPP; Zhang et al., 2004) or to prior spread (CRPS; Whitaker and Hamill, 2012). In MCI, all ensemble perturbations, i.e., the deviations of the ensemble members from the ensemble mean, either of the forecast or of the analysis ensemble, are multiplied by a factor slightly larger than one to increase the ensemble spread. ACI attempts to achieve a similar result by adding a small multiple of the identity matrix to either the background or the analysis ensemble covariance matrices. In CRPP, each analysis ensemble member is linked to a background ensemble member and the new analysis perturbation from the analysis ensemble mean is a weighted average of the former analysis perturbations and the corresponding background perturbations from their background ensemble means. Similarly, in CRPS the new

analysis ensemble spread is obtained as a weighted average of the actual analysis ensemble and the forecast ensemble spreads.

Another challenge posed by small ensemble sizes is sampling error. Erroneously large estimated correlations between model grid points that are far apart in the model domain can lead to spurious updates in the analysis step (Houtekamer and Mitchell, 1998; Hamill et al., 2001). Such spurious long-range correlations would result in random analysis increments if not suppressed (Hunt et al., 2007). Spatial observation localization is often used to overcome this problem, and there are two general ways to achieve this: explicit and implicit observation localization (Hunt et al., 2007). In the explicit approach, only observations within a certain radius around an analysis grid point are used for the analysis (e.g., Houtekamer and Mitchell, 1998; Ott et al., 2004), and all observations beyond this radius are neglected. In the implicit approach, the entries of the forecast error covariance matrix are multiplied by a function that continuously decays from one to zero as the observation location moves from the position of the analysis grid point to a certain distance from that grid point. For this purpose, a Schur or Hadamard (element-wise) product of the ensemble-estimated forecast error covariance matrix with a correlation function with local support is applied to produce the localized forecast error covariance matrix (e.g., Houtekamer and Mitchell, 2001; Hamill et al., 2001; Whitaker and Hamill, 2002). Typically, a fifth-order function of Gaspari and Cohn (1999) is used, which is similar to a Gaussian function but has compact support (i.e., the function has zero values beyond a certain distance). Covariance localization can be performed in both horizontal and vertical directions, and is not only advantageous for reducing the effects of spurious long-range correlations, but also for reducing computational costs and alleviating the problem of covariance matrix rank deficiency (Meng and Zhang, 2011). Covariance localization is a key element of the Local Ensemble KF (LEKF) introduced by Ott et al. (2004), which follows the idea that the forecast error vectors corresponding to local regions tend to lie in subspaces of the full model state space of much lower dimensionality. Thus, the LEKF uses observations only within local subspaces and, instead of processing the observations serially as in the ETKF, was designed to compute analyses at different model grid points in parallel.

The LETKF following Hunt et al. (2007) is closely related to the ETKF and the LEKF approaches. It uses a symmetric square root to generate the analysis ensemble from the forecast ensemble and thus is a deterministic EnKF approach. It was developed for being easily implemented and computationally efficient also for large spatiotemporally chaotic systems, and constructs the analysis ensemble from appropriate linear combinations of the forecast ensemble members simultaneously and independently for each analysis grid point via

$$\vec{x}_a^m = \overline{\vec{x}_b} + \boldsymbol{X}_b \vec{w}_a^m \tag{4.37}$$

(Hunt et al., 2007). In Eq. (4.37), $\vec{x}_a^m$ is the mth of M analysis ensemble members of dimension N, $\overline{\vec{x}_b}$ is the N-dimensional background ensemble mean, $\boldsymbol{X}_b$ is a $N \times M$ matrix of perturbation vectors of the background ensemble members from the background ensemble mean

$$\boldsymbol{X}_b = [\vec{x}_b^{m=1} - \overline{\vec{x}_b} \quad \cdots \quad \vec{x}_b^{m=M} - \overline{\vec{x}_b}] \tag{4.38}$$

with $\vec{x}_b^m$ the mth background ensemble member, and $\vec{w}_a^m$ is an M-dimensional weighting coefficient vector. The vector $\vec{w}_a^m$ can be decomposed into an ensemble mean $\overline{\vec{w}_a}$ and a perturbation $\boldsymbol{W}_a^m$ by

$$\vec{w}_a^m = \overline{\vec{w}_a} + \boldsymbol{W}_a^m \tag{4.39}$$

with all M columns $\boldsymbol{W}_a^m$ of the $M \times M$ weighting matrix $\boldsymbol{W}_a$. The LETKF attempts to determine appropriate vectors $\boldsymbol{w}_a^m$, which is done like in the 3DVar and 4DVar approaches by minimizing a cost function

$$J(\vec{x}) = \left(\vec{x} - \overline{\vec{x}_b}\right)^T \boldsymbol{P}_b^{-1}\left(\vec{x} - \overline{\vec{x}_b}\right) + \left(\vec{y}_o - \mathcal{H}(\vec{x})\right)^T \boldsymbol{R}^{-1}\left(\vec{y}_o - \mathcal{H}(\vec{x})\right) \tag{4.40}$$

with the background error covariance matrix $\boldsymbol{P}_b$ estimated from the forecast ensemble

$$\boldsymbol{P}_b = (M-1)^{-1}\boldsymbol{X}_b\boldsymbol{X}_b^T \tag{4.41}$$

to determine the analysis ensemble mean $\overline{\vec{x}_a}$. The estimation of $\boldsymbol{P}_b$ from an ensemble of size $M \ll N$ makes $\boldsymbol{P}_b$ to be severely rank deficient (rank at most $M-1$), thus $\boldsymbol{P}_b$ is not invertible and the cost function in Eq. (4.40) can not be minimized. However, $\boldsymbol{P}_b^{-1}$ is well-defined on the subspace $\mathcal{S}$ spanned by the ensemble perturbation vectors (the column space of $\boldsymbol{X}_b$), and the cost function can thus be minimized on $\mathcal{S}$ (Hunt et al., 2007). Performing the analysis for the ensemble mean on $\mathcal{S}$ is challenging, because the individual perturbation vectors representing the basis for $\mathcal{S}$ are linearly dependent by definition (see Eq. (4.38)). This problem can be avoided by considering another M-dimensional subspace $\tilde{\mathcal{S}}$ from which the perturbation matrix $\boldsymbol{X}_b$ transforms an M-dimensional vector $\vec{w}$ into the M-dimensional subspace $\mathcal{S}$ spanned by the ensemble perturbations (Hunt et al., 2007). A model state $\vec{x}$ can then be expressed by

$$\vec{x} = \overline{\vec{x}_b} + \boldsymbol{X}_b\vec{w}. \tag{4.42}$$

The cost function in Eq. (4.40) can then be reformulated for the subspace $\tilde{\mathcal{S}}$ with $\vec{w}$ as control variable regarded as a Gaussian random vector with zero mean and covariance matrix $(M-1)^{-1}\boldsymbol{I}$ to

$$\tilde{J}(\vec{w}) = (M-1)\vec{w}^T\vec{w} + [\vec{y}_o - \mathcal{H}(\overline{\vec{x}_b} + \boldsymbol{X}_b\vec{w})]^T\boldsymbol{R}^{-1}[\vec{y}_o - \mathcal{H}(\overline{\vec{x}_b} + \boldsymbol{X}_b\vec{w}) \tag{4.43}$$

(Hunt et al., 2007). It can be shown that if $\overline{\vec{w}_a}$ minimizes $\tilde{J}$ given by Eq. (4.43), then $\overline{\vec{x}_a} = \overline{\vec{x}_b} + \boldsymbol{X}_b\overline{\vec{w}_a}$ minimizes J given by Eq. (4.40) (Hunt et al., 2007). By applying the (non-linear) observation operator $\mathcal{H}$ to all background ensemble members, $\vec{y}_b^m = \mathcal{H}(\vec{x}_b^m)$, and calculating the corresponding ensemble mean in observation space, $\overline{\vec{y}_b} = \overline{\mathcal{H}(\vec{x}_b^m)}$, $\mathcal{H}$ can be "linearized" through interpolation between $\vec{y}_b^m$ and the corresponding ensemble mean $\overline{\vec{y}_b}$ using

$$\mathcal{H}(\overline{\vec{x}_b} + \boldsymbol{X}_b\vec{w}) \approx \overline{\vec{y}_b} - \boldsymbol{Y}_b\vec{w} \tag{4.44}$$

(Hunt et al., 2007). In Eq. (4.44), the $O \times M$ matrix $\boldsymbol{Y}_b$ comprises, similar to $\boldsymbol{X}_b$, the perturbations from the ensemble mean in observation space

$$\boldsymbol{Y}_b = [\vec{y}_b^{m=1} - \overline{\vec{y}_b} \quad \cdots \quad \vec{y}_b^{m=M} - \overline{\vec{y}_b}]. \tag{4.45}$$

Using Eq. (4.44) in the cost function in Eq. (4.53) yields

$$\tilde{J}^*(\vec{w}) = (M-1)\vec{w}^T\vec{w} + [\vec{y}_o - \overline{\vec{y}_b} - \boldsymbol{Y}_b\vec{w}]^T\boldsymbol{R}^{-1}[\vec{y}_o - \overline{\vec{y}_b} - \boldsymbol{Y}_b\vec{w}], \tag{4.46}$$

which formulation in the low-dimensional ensemble space $\tilde{\mathcal{S}}$ allows for the explicit calculation of its minimizer $\overline{\vec{w}_a}$, i.e., the weighting coefficient vector for the analysis ensemble mean, as

$$\overline{\vec{w}_a} = \widetilde{\boldsymbol{P}}_a\boldsymbol{Y}_b^T\boldsymbol{R}^{-1}(\vec{y}_o - \overline{\vec{y}_b}) \tag{4.47}$$

(Hunt et al., 2007; Schraff et al., 2016) and the corresponding analysis error covariance matrix in $\tilde{\mathcal{S}}$ as

$$\widetilde{\boldsymbol{P}}_a = [(M-1)\boldsymbol{I} + \boldsymbol{Y}_b^T\boldsymbol{R}^{-1}\boldsymbol{Y}_b]^{-1}. \tag{4.48}$$

Finally, the analysis ensemble mean in the full model space is given by

$$\overline{\vec{x}_a} = \overline{\vec{x}_b} + \boldsymbol{X}_b\overline{\vec{w}_a}, \tag{4.49}$$

and the analysis ensemble perturbations

$$\boldsymbol{X}_a = [\vec{x}_a^{m=1} - \overline{\vec{x}_a} \quad \cdots \quad \vec{x}_a^{m=M} - \overline{\vec{x}_a}] = \boldsymbol{X}_b\boldsymbol{W}_a \tag{4.50}$$

are constructed using a symmetric square-root

$$\boldsymbol{W}_a = [(M-1)\widetilde{\boldsymbol{P}}_a]^{1/2}, \tag{4.51}$$

which is applied to ensure that the sum of analysis ensemble perturbations from the analysis ensemble mean is zero and that the matrix $\boldsymbol{W}_a$ is a continuous function of the covariance matrix $\widetilde{\boldsymbol{P}}_a$ (Hunt et al., 2007; Schraff et al., 2016). The analysis ensemble can then be sampled using Eqs. (4.37) and (4.49). When observations are very frequent and irregularly distributed in time, the LETKF is best used in a 4D fashion (Hunt et al., 2007), which seeks linear combinations of the forecast ensemble trajectories over an assimilation time window that best fit the distributed observations rather than seeking optimal linear combinations of model states at particular times. Thus, the 4D version of the LETKF uses the ensemble-estimated 4D background covariance matrix at the times and locations of the observations to produce the analysis at the end of the DA window (Schraff et al., 2016).

The EnKF method has become increasingly popular in recent decades because of its ability to explicitly estimate and evolve the highly flow-dependent background error covariance matrix using an ensemble of forecasts (Schraff et al., 2016). The ensemble-estimated covariances are valuable for DA especially at the convective scale, because in principle all the variables of a model can be updated from any observation type, e.g., temperature or humidity fields can be updated by assimilating Z_H or V_r observations, even at model grid points far from the observation location (e.g., Snyder and Zhang, 2003; Snook et al., 2015). In addition, the EnKF does not require linearizations and adjoints of the forecast model (Hunt et al., 2007; Snook et al., 2011). This is a clear advantage over 3DVar and 4DVar and also allows the use of highly nonlinear observation operators, which is especially important for the direct assimilation of polarimetric radar observations (Putnam et al., 2019). Since linearizations and adjoints are not required, the use of the EnKF is relatively easy to implement and, most obviously for LETKF, to parallelize (Dowell et al., 2011). Furthermore, the EnKF analysis ensembles typically provide reasonable initial conditions for ensemble forecasts, which are considered valuable for weather prediction at the convective scale (Snook et al., 2015). However, compared to 3DVar, the EnKF has the disadvantage of much higher computational costs due to the need for forward integration of an ensemble of model states (e.g., Snook et al., 2015). The use of relatively small ensembles to reduce computational cost can lead to insufficient ensemble spreads and consequently filter divergence (e.g., Gao and Xue, 2008). Furthermore, uncertainty can only be quantified in the subspace spanned by the ensemble, which can be a strong constraint if the ensemble size is significantly smaller than the number of degrees of freedom of the model (Hunt et al., 2007). Another strong limitation of the EnKF, but also of 3DVar and 4DVar, is the assumption of Gaussian error statistics (Bick et al., 2016), especially at the convective scale. However, the strong advantages of the EnKF have led to its operational implementation in the form of the LETKF in Italy at COMET (Bonavita et al., 2010),

at DWD, and MeteoSwiss (Schraff et al., 2016), and for research purposes in Japan at JMA (Miyoshi et al., 2010) and at the ECMWF (Hamrud et al., 2015).

The application of the EnKF to radar DA was first tested by Snyder and Zhang (2003). They assimilated simulated single-Doppler V_r observations of a splitting supercell storm in a perfect model context into the cloud model of Sun and Crook (1997) and showed that the used EnSRF system of Whitaker and Hamill (2002) with observation localization using a 3D cutoff radius of four kilometers produced accurate analyses even of the unobserved model state variables after assimilation of about 30 minutes of data. Another such early observing system simulation experiment (OSSE) with simulated V_r observations of supercell storms was performed by Zhang et al. (2004) who used the same cloud model and also assimilated their data using the same EnSRF approach and a 3D cutoff radius of three kilometers for observation localization. Unlike Snyder and Zhang (2003), they used covariance relaxation to maintain sufficient spread in their 20-member ensemble. They evaluated the influence of more realistic initial fields and variations in the availability, resolution, and quality of the synthetic V_r observations on the analyses, and showed that the EnKF system performed well in these more realistic scenarios. Follow-up OSSE studies with EnKF systems also included the assimilation of synthetic Z observations. E.g., Caya et al. (2005) made a direct comparison between EnKF and 4DVar for the assimilation of simulated V_r and Z_H observations from a convective storm into the cloud model of Sun and Crook (1997) using the EnSRF system of Whitaker and Hamill (2002) with a 100-member ensemble and a Gaspari-Cohn correlation function for horizontal and vertical observation localization. They reported that the 4DVar scheme produced better analyses than the EnKF method when data from a very short period were assimilated while the result was reversed after several assimilation cycles, in part due to potential problems with proper ensemble initialization for the EnKF. Tong and Xue (2005) showed that by assimilating simulated V_r and Z_H data of a convective storm in the ARPS model, not only wind and thermodynamic fields were well analyzed, but also multiple ice species associated with a multi-class ice-microphysical scheme were successfully retrieved, confirming that the EnKF is able to spread information also to unobserved variables. They implemented the observation perturbation method following Burgers et al. (1998) and Houtekamer and Mitchell (1998), using a 100-member ensemble, and observation localization with a 3D Gaspari-Cohn correlation function. Best storm analyses were obtained by assimilating V_r and Z_H data together. Similarly, Xue et al. (2006) also studied the assimilation of simulated V_r and Z_H data from a supercell storm in the ARPS model including ice-microphysics, but they used the EnSRF approach of Whitaker and Hamill (2002) and, unlike the previous studies, the radar data were sampled at the radar PPIs instead of at the analysis grid points. They reported encouraging analyses despite the non-uniform resolution of the radar data in the radar PPIs. Sobash and Stensrud (2013) focused on the question how the choice of covariance localization affects the analysis of a mesoscale convective system assimilating synthetic V_r and Z_H data using the EAKF method. They found that increasing the horizontal

observation localization using a Gaspari-Cohn correlation function and decreasing the vertical localization generally improved analysis quality, but they noted that the proper choice of covariance localization depends on the choice of ensemble size and covariance inflation method. To reduce computational costs associated with the EnKF procedure while preserving its benefits, Gao and Xue (2008) successfully tested a dual-resolution approach with simulated V_r observations, in which they used the flow-dependent background error covariance matrix estimated from an ensemble at a lower-resolution grid to generate an analysis at a higher-resolution grid.

A first real-data study with radar observations using EnKF is Dowell et al. (2004). They used the warm-rain cloud model of Sun and Crook (1997) and assimilated real V_r and Z_H observations from a single Doppler radar of an isolated convective storm using an EnSRF with a 50-member ensemble, multiplicative covariance inflation, and covariance localization using a Gaspari-Cohn correlation function. By calculating background Z_H data via a rather simple reflectivity-rain water content relation and only updating model rain-water content from Z_H observations, the locations of the analyzed main storm updraft and the mesocyclone corresponded relatively well to the observations of another radar station, dual-Doppler wind syntheses, and in situ instrument tower measurements. Aksoy et al. (2009) presented another real-data study, in which they assimilated V_r and Z_H measurements from a single Doppler radar of different convective cases in the WRF model using the EAKF method, MCI, and a Gaspari-Cohn correlation function for covariance localization. They found that their EnKF method produced robust results for all convective cases and that the assimilation of Z_H data in "no-precipitation" areas, i.e. regions with Z_H low enough to be considered free of precipitation, following Tong and Xue (2005) could successfully suppress spurious precipitation in the ensemble members. Another real-world study focusing solely on analysis quality is Dowell and Wicker (2009). They developed an additive-noise method to maintain sufficient spread in the ensemble, in which model temperature, wind, and water vapor fields are locally perturbed where Z_H indicates precipitation. By using a simplified cloud model, V_r observations from a supercell storm in Oklahoma, the EnSRF approach of Whitaker and Hamill (2002), and, similar to many other studies, a Gaspari-Cohn correlation function for covariance localization, they were able to show that the additive-noise method, in addition to providing a generally good analysis of the considered storm, could reduce the number of spurious precipitation cell compared to previously used storm-scale ensemble methods. Snook et al. (2011) and Jung et al. (2012) presented further real-data assimilation studies with a focus on analyses using the EnSRF approach of Whitaker and Hamill (2002), the ARPS model, and V_r and Z_H observations from tornadic storms. Snook et al. (2011) demonstrated that their EnKF system was able to clearly improve storm analyses by incorporating radar observations from different radar networks and showed that the use of three different ice-microphysical schemes for the different ensemble members helped to increase the spread in the forecast ensemble. Polarimetric radar data from Oklahoma were used in Jung et al. (2012) to evaluate the quality of storm analyses based on non-polarimetric data from another

radar station and using single- and double-moment microphysical schemes in the ARPS model. They showed that V_r and Z_H were analyzed well with both schemes, however, the double-moment scheme yielded significantly better analyzed polarimetric signatures compared to the one-moment-scheme (more below).

Several studies also focused on the impact of assimilating real radar observations in an EnKF system on short-term QPF (e.g., Zhang et al., 2009; Aksoy et al., 2010; Dong and Xue, 2012; Chang et al., 2014; Snook et al., 2015; Johnson et al., 2015; Gao and Min, 2018). The effect of assimilating radar observations in an EnKF system on forecasts of Hurricanes was investigated by Zhang et al. (2009) and Dong and Xue (2012), where the former assimilated V_r observations from three radars along the Gulf coast in the WRF model and the latter also assimilated Z_H observations of two radars in the ARPS model using the EnSRF approach of Whitaker and Hamill (2002). Zhang et al. (2009) noted that the assimilation of V_r improved deterministic forecasts of the considered Hurricane with respect to the case that no radar data was assimilated or a 4DVar scheme was used with the same radar data. Dong and Xue (2012) also reported improved Hurricane forecasts, both deterministic and ensemble-based, for up to 12 hours forecast lead time with a larger effect attributable to the V_r observations compared to the Z_H data. Unlike most of the previous EnKF radar studies, Chang et al. (2014) considered, besides two convective summertime precipitation cases with squall-line and small-scale structures, also a case with widespread stratiform rainfall over the Montreal, Canada region. They examined the analysis and short-term forecasts resulting from the assimilation of V_r observations from these three cases using the stochastical EnKF method of Houtekamer and Mitchell (1998) in the Canadian Meteorological Center's Global Environmental Multiscale Limited-Area Model, and reported a clear impact on the update of unobserved variables through the background error covariance matrix estimated from an 80-member ensemble. Both Snook et al. (2015) and Johnson et al. (2015) reported improved QPF using the EnSRF method of Whitaker and Hamill (2002) for model initialization with V_r and Z_H observations. Snook et al. (2015) considered a mesoscale convective system simulated with the ARPS model and found substantially improved ensemble QPF through radar DA. Johnson et al. (2015) considered multiple diverse rainfall cases and directly compared analyses and ensuing QPF produced with EnKF and a 3DVar scheme after assimilation of observations from both meso- and synoptic-scale networks and radar data. Produced EnKF analyses resulted in a five times longer improvement in QPF due to the assimilation of radar data compared to the 3DVar approach, which they reason by better analyses of the meso-scale environment and convective-scale features with the EnKF method due to lack of flow-dependence in the static background error covariance matrix used in the 3DVar scheme.

More recently, using the LETKF scheme for the assimilation of radar observations into NWP models has gained popularity. One of the first studies using LETKF is Lange and Craig (2014), who assimilated simulated Z_H and V_r observations in a perfect model context into the COSMO (Consortium for Small-scale Modeling) model. They tested the influence of different assimilation length scales on analyses

and short-term forecasts of long-living convective systems in terms of observation localization length scale, the length scale of the observations modified by averaging the observations spatially to so-called superobservations ("superobbing"; Alpert and Kumar, 2007), the calculation of the LETKF analyses at reduced-resolution analysis grids (Yang et al., 2009), and the modification of the temporal analysis window length. The high-resolution LETKF settings were found to produce the best analyses with respect to RMSD and field-oriented measures after three hours of assimilation, and subsequent three-hour forecasts were found to be best when initiated with the high-resolution analysis up to the first hour, but to be comparable to the coarser schemes thereafter. They supposed that the more rapid error growth in the forecast associated with the high-resolution setting may likely be attributable to a smaller predictability of the small scales, gravity wave noise, and spurious convective precipitation. Another more recent application of the LETKF for the assimilation of real Z_H observations from Germany in the COSMO model is Bick et al. (2016). They assimilated 3D Z_H fields observed by the national German C-band weather radar network in combination with conventional observations for a case study using the KENDA assimilation system, an implementation of the LETKF scheme developed by DWD and its partners (more details on the KENDA system in Section 4.2). Background Z_H data were simulated using the EMVORADO radar forward operator on the radar PPIs, the radar observations and the background values were superobbed, no-precipitation information was assimilated like in Aksoy et al. (2009) setting all Z_H values below 5 dBZ to 5 dBZ, a fixed observation error standard deviation of 10 dBZ was assumed upon experimentation, the analysis grid was coarsened by a factor of three following Yang et al. (2009), and covariance inflation was performed using CRPS. In addition, covariance localization was performed using a Gaspari-Cohn correlation function. The direct assimilation of 3D Z_H data had a clear positive impact on the analysis and ensuing (ensemble) QPF for up to four hours. Taking into account a seven-day period of precipitation over Germany, the direct assimilation of 3D Z, although at the time still experimental, yielded results comparable to the operational LHN approach used at DWD. Gastaldo et al. (2018) also used the KENDA system for the assimilation of 3D Z_H observations from the Italian C-band weather radar network, also in combination with conventional observations, in the COSMO model for a four-day case study in February 2017. Superobbing was performed and no-precipitation areas were assimilated with a value of 5 dBZ like in Bick et al. (2016), but unlike this previous study, an observation error standard deviation of 5 dBZ estimated from observation-minus-first-guess and observation-minus-analysis residuals following Desroziers et al. (2005) was used. They performed sensitivity tests for the observations error by modifying it to values of 0.5 dBZ and 10 dBZ, and for the length of the assimilation window. QPF up to a few hours was improved through the 3D Z_H assimilation for both experiment variants using LHN or not. A more thorough investigation in Italy using the KENDA system and the convection-permitting limited-area version of the COSMO model over Italy COSMO-2I considering 37 precipitation days in 2018 was conducted by Gastaldo et al. (2021).

Their results showed that the assimilation of 3D Z_H data on average outperformed the already operational LHN method for up to seven hours lead time with improvements stronger for convective precipitation. Based on these encouraging results, a parallel preoperational framework was set up for the COSMO-2I model, in which LHN is replaced by the direct 3D Z_H assimilation using the KENDA assimilation framework. Finally, Vobig et al. (2021) attempted to resolve the problem of radar DA within the KENDA-ICON-D2 system at DWD at model grid points with a zero ensemble spread but radar-observed precipitation. They developed the "Targeted Covariance Inflation" method, which artificially enhances sensitivity through perturbations in the first-guesses to achieve background correlations between Z_H and humidity, and showed improved LETKF analyses and ensuing QPF in a case study.

4.1.3.4 Hybrid Schemes and the Particle Filter

The use of flow-dependent background error covariances estimated from ensembles of model states in the EnKF has been shown to be beneficial for analyses (e.g., Tong and Xue, 2005) and subsequent weather forecasts (e.g., Johnson et al., 2015). However, the EnKF approach is suboptimal, in part because the background uncertainty can only be represented in the subspace spanned by the ensemble perturbations, thus limiting the freedom of the analysis solution, and sampling errors can occur. In contrast, the variational approaches such as 3DVar are suboptimal because they use static and more unrealistic background error covariances, which are, however, more robust in a statistical sense compared to the ensemble-estimated covariances in EnKF (Bannister, 2017). Combining ensemble and variational methods into hybrid ensemble-variational (EnVar) schemes to complement their respective strengths may be done as described by Hamill and Snyder (2000) by solving the 3DVar cost function using a blended background error covariance matrix in terms of a weighted average of the static 3DVar covariance matrix and the ensemble-estimated flow-dependent covariance matrix. E.g., Lorenc (2003) developed this approach into the so-called extended control variable method, where the control variable – the variable with respect to which the cost function is minimized – is the sum of an analysis increment associated with the static 3DVar background error covariance matrix and an analysis increment produced from local linear combinations of the ensemble perturbations, i.e., an analysis increment associated with the flow-dependent covariances. Wang (2010) described the implementation of this EnVar method in the Gridpoint Statistical Interpolation (GSI; Wu et al., 2002) assimilation system. A different but mathematically equivalent (Wang et al., 2007) version of EnVar was later proposed by Buehner (2005).

EnVar schemes have mostly been applied to meso- or global-scale NWP models so far (e.g., Wang et al., 2008). Few studies have focused on storm-scale applications, including radar observations. One of the first studies to assimilate radar observations using a hybrid scheme is Li et al. (2012), who assimilated V_r observations of two coastal radars sampling a hurricane at the Gulf Coast in the WRF ensemble-3DVar scheme (Wang et al., 2008), which implements the extended control variable

approach of Lorenc (2003). They found that the hybrid method resulted in better wind forecasts, improved three-hour QPF, and a better track prediction of the hurricane compared to the pure 3DVar method. They stated that the improved forecast of the hurricane could be attributed to dynamically more consistent analyses produced by the hybrid approach using flow-dependent error covariances. Gao et al. (2013) described the development of a hybrid 3DVar-EnKF scheme following Buehner (2005) for the ARPS model, applied it to a case study of assimilating simulated Doppler radar data of a supercell storm, and compared the results with pure EnKF and pure 3DVar schemes. They reported that for the assimilation of data from a single radar, the pure EnKF method performed best for the analysis of dynamical variables, while the new hybrid approach performed best for the retrieval of variables related to hydrometeors, and the 3DVar method was generally worse in terms of RMSD. The spin-up time of the simulated storm was shortest for the hybrid approach. More recently, e.g., Wang and Wang (2017) proposed an approach to directly assimilate Z_H data in the GSI EnVar assimilation system, and Duda et al. (2019) made a comparison of the same system to a cloud analysis.

In contrast to the variational and EnKF approaches and the EnVar hybrid methods, which are all based on the assumption of linearity and Gaussian error statistics, nonlinear and non-Gaussian DA approaches, such as the particle filter (for a review, see van Leeuwen, 2009), have been developed. However, their application to storm-scale NWP models for the assimilation of radar observations is still in a more preliminary stage than the hybrid EnVar methods. One of the few investigations was conducted by Poterjoy et al. (2017), who used a localized version of the particle filter (Poterjoy, 2016) to assimilate simulated V_r and Z_H data of a squall line into the WRF model. They showed that, compared to EnKF, the particle filter was advantageous for probabilistic analyses of non-Gaussian variables such as hydrometeor mixing ratios, and that the particle filter yielded more accurate forecasts at the cost of higher posterior RMSD values. Based on their initial tests, they stated that in the future, the particle filter approach could be valuable for better assimilating remotely sensed observations that are nonlinearly related to the model state, such as radar reflectivities or satellite radiances.

4.1.4 Assimilation of Polarimetric Observations

The assimilation of polarimetric radar observations in NWP models is still at an early stage. Besides the lack of widespread polarimetric radar observations in the past, until national radar networks started to be upgraded to polarimetry in recent years, another reason is the difficulty in developing accurate polarimetric radar forward operators that produce realistic polarimetric variables from the variables of the model's microphysical schemes, which are under continuous development themselves. To avoid the problems associated with the inadequacies of the polarimetric radar forward operators, a few studies have assimilated polarimetric data indirectly by retrieving model state variables (mostly hydrometeor mixing ratios) from the polarimetric radar

data prior to assimilation. A first such approach with real radar data was made by Wu et al. (2000), who, besides V_r observations, assimilated rainwater and hail and graupel mixing ratios estimated from Z_H and Z_{DR} observations of a severe thunderstorm in the USA with a 4DVar scheme in the cloud model of Sun and Crook (1997). They extended its original warm-rain-only microphysics scheme to simple ice categories (cloud ice, hail, and graupel), and the results showed that the 4DVar method was generally able to analyze the storm well, but difficulties were reported in accurately tracking the storm's evolution. Shortcomings of the simple microphysical scheme or the cloud model used in representing the true nonlinear cloud-precipitation processes were suggested as reasons. Later, e.g., Li and Mecikalski (2010, 2012, 2013) and Yokota et al. (2016) also followed the indirect assimilation approach, but with different DA schemes. Li and Mecikalski (2010, 2012, 2013) assimilated real polarimetric observations from convective storms with 3DVar in the WRF model with a warm-rain single-moment bulk microphysics scheme. They used Z_H and Z_{DR} (Li and Mecikalski, 2010), and Z_H, Z_{DR}, and K_{DP} (Li and Mecikalski, 2012, 2013) observations to retrieve rainwater mixing ratios before assimilation and used the total water mixing ratio as the control variable in the 3DVar cost function. Storm-scale analyses and short-term forecasts were notably improved by the inclusion of the polarimetric data. Moreover, a sensitivity experiment performed by Li and Mecikalski (2013) showed that the choice of retrieval relation had a significant impact on the produced thermodynamic, kinematic, and microphysical fields of the storm while the general location and motion of the storms were largely unaffected. Yokota et al. (2016) used the indirect assimilation approach with the LETKF scheme. They investigated the impact of assimilating rainwater mixing ratios estimated from real Z_H and K_{DP} observations from four C-band radars in combination with surface network measurements in the JMA non-hydrostatic model on the prediction of a tornadic storm over Japan. Rainwater mixing ratios were estimated from Z_H for weaker rain, from K_{DP} for stronger rain, and a mixture of both in the transition zone due to enhanced noise in the K_{DP} estimate in weak precipitation. The prediction of a strong low-level mesocyclone near the observed tornado track was successfully predicted, and the exclusion of either the surface data or the radar data from the assimilation failed to produce this particular storm feature in the forecast. These recent indirect assimilation studies have all focused on warm-rain microphysics and neglected ice processes, which, however, are important, especially in convective situations. In addition, only single-moment bulk microphysics schemes were used, further limiting the ability of the models employed to realistically simulate microphysical processes in clouds and precipitation.

Another attempt to indirectly assimilate polarimetric radar data was made by Carlin et al. (2017), who made temperature and moisture adjustments to the ARPS cloud analysis based on observations of columns of enhanced Z_{DR} values above the melting layer as indicators of strong updrafts in convective storms (Z_{DR}-columns; Kumjian et al., 2014). With these modifications, the analyses and forecasts of two tornadic supercells in the USA improved in terms of updraft analyses, predicted Z

structures, a better agreement between predicted updraft helicity and radar-derived rotation tracks, and improved Z_H frequency biases and equitable threat scores. Recently, Ding et al. (2022) took a similar approach by modifying the GSI cloud analysis based on polarimetric radar measurements (Z_{DR}, ρ_{HV}, and K_{DP}) by employing a fuzzy-logic hydrometeor classification, an improved determination of liquid and ice phase regions, and a new hydrometeor number concentration retrieval. Tests with a squall-line case in China showed improved analyzed precipitation structures including polarimetric signatures and consistently improved QPF.

Polarimetric radar observations have also been directly assimilated through the use of polarimetric radar forward operators, which simulate radar observations from the variables provided by the model microphysical schemes. Such forward operators have been proposed by, e.g., by Jung et al. (2008a), Pfeifer et al. (2008), Jung et al. (2010a), Ryzhkov et al. (2011), Matsui et al. (2019), and Zhang et al. (2021). Jung et al. (2008b) developed a polarimetric radar simulator for a single-moment bulk microphysics scheme (i.e., typically only hydrometeor mixing ratios are simulated), including ice microphysics for Z_H, Z_{DR}, the reflectivity difference Z_{DP}, and K_{DP}. The operators used the hydrometeor axis ratio relation following Zhang et al. (2001), a simple melting model, and radar scattering amplitude functions fitted to T-matrix scattering calculations for the liquid phase and to the Rayleigh approximation for frozen particles. They showed that the new radar simulator produced polarimetric signatures such as the bright band and realistic spatial distributions of Z_{DR} and K_{DP} of simulated convective storms. This set of polarimetric forward operators was subsequently used in Jung et al. (2008b), which represents the first work in the literature to directly assimilate polarimetric radar observations in a storm-scale NWP model. They applied the EnSRF approach following Whitaker and Hamill (2002) to directly assimilate simulated Z_{DR}, Z_{DP}, and K_{DP} data, along with Z_H and V_r data, of a convective storm into the ARPS model with a single-moment microphysics scheme including ice processes. They reported improved storm analyses by assimilating the polarimetric observations, especially in the rainwater mixing ratio, vertical velocity, and water vapor fields, and found that Z_{DR} had the largest positive impact among the assimilated polarimetric variables. Jung et al. (2010a) proposed a more general set of polarimetric operators compared to that proposed by Jung et al. (2008a). It was developed to be applicable to the output of convective-scale models with not only single-moment, but also double- or triple-moment bulk microphysical schemes. In double-moment bulk microphysical schemes, the number concentration of hydrometeor classes is typically simulated along with the corresponding mixing ratios, and in triple-moment schemes, the corresponding Z_H is typically forecasted in addition. Their radar simulator was also developed to be usable with different radar wavelengths, included T-matrix scattering calculations also for frozen particles, and accounted for continuous melting processes. Applied to a convective storm simulated with a double-moment scheme, various characteristic polarimetric radar signatures could be realistically simulated. Direct comparison of the application of the simulator to the output of a single-moment microphysical scheme revealed that certain

polarimetric signatures could not be produced with the single-moment scheme, which they suggested was due to the fact that the single-moment scheme was not able to simulate shifts in the particle size distributions at constant mixing ratios, and stated that higher-moment schemes are required to adequately simulate crucial polarimetric fingerprints.

Putnam et al. (2019) were the first to assimilate real polarimetric radar observations into a storm-scale model using a multi-moment microphysical scheme including ice processes with an EnKF approach and an advanced polarimetric radar observation forward operator. The radar simulator used was the one proposed by Jung et al. (2010a), slightly modified for reasons of computational efficiency, while retaining most of its accuracy. The radar variables Z_H, V_r, and Z_{DR} were assimilated into the ARPS convective-scale model with the EnSRF method following Whitaker and Hamill (2002). The assimilation of Z_{DR} observations below the melting layer of a supercell storm in Oklahoma, USA clearly improved storm analyses in terms of polarimetric signatures such as the so called Z_{DR}-arc (arc of enhanced Z_{DR} values in the forward flank of supercell storms associated with size sorting due to storm-relative wind shear; Kumjian and Ryzhkov, 2008) and Z_{DR}-columns. In a follow-up study, Putnam et al. (2021) investigated the impact of assimilating real Z_{DR} observations of convective storms in Oklahoma with different assimilation window lengths (30, 45, and 60 min) in the same DA system like used in Putnam et al. (2019) on storm-scale ensemble forecasts. They found that Z_{DR} observations can improve storm predictions for smaller assimilation window lengths if the assimilation window covers the initial development and organization stages of the storms, where observed Z_{DR}-columns contribute to the storm analyses. Similar to Putnam et al. (2019), Zhu et al. (2020) investigated the impact of directly assimilating Z_{DR} data of a tornadic storm in an OSSE framework in the ARPS EnSRF system, including a double-moment microphysical scheme using the polarimetric radar simulator of Jung et al. (2010a). Errors in all analyzed state variables were reduced by the inclusion of Z_{DR}, the structure and intensity of the analyzed hydrometeor fields were improved, and polarimetric signatures such as Z_{DR}-columns and Z_{DR}-arcs were better reproduced. In addition, sensitivity experiments were conducted in which certain state variables were not updated from the Z_{DR} observations. When the hydrometeor number concentrations were not updated, the assimilation of the Z_{DR} data was largely ineffective, and the updating of the water vapor mixing ratio and the vertical wind velocity were also found to be important for the improvements found. Therefore, they concluded that the cross-variable covariances provided by the forecast ensemble in the EnKF were highly beneficial for their storm-scale analyses. Despite this clear advantage of the EnKF method for the direct polarimetric radar DA, studies have also investigated using the 3DVar method for this purpose. E.g., Li et al. (2017) assimilated real K_{DP} estimates in the WRF 3DVar system using a newly developed single-moment ice microphysical forward model and empirical relations between K_{DP} and mixing ratios as forward operators, and reported a positive effect of the K_{DP} estimates on the analysis of a mesoscale convective system in Alabama, USA.

4.2 Assimilation of Radar Observations in Germany

The assimilation of Z_H observations from the German C-band radar network at DWD started in 2007 with LHN (Stephan et al., 2008; Milan et al., 2008) in the, at that time, operational convective-scale NWP model covering Germany and parts of its neighboring states COSMO-DE (Baldauf et al., 2011). The COSMO-DE model was replaced at DWD by the now operational convective-scale NWP model ICON-D2 in 2021. The KENDA system, an implementation of the LETKF, is the DA framework currently used for the ICON-D2 model at DWD. LHN is still included in KENDA and recently also the direct assimilation of 3D Z_H and V_r observations from the German C-band radars was implemented operationally. This section describes the ICON-D2 model and the KENDA DA system, including the direct 3D Z_H and V_r DA technique used, which are used later in this thesis to assimilate for the first time polarimetric data in a convective-scale NWP system in Germany (Chapter 5).

4.2.1 The ICON-D2 Model

The ICON modeling framework (Zängl et al., 2015) is a global NWP and climate modeling system jointly developed by DWD and the Max Planck Institute for Meteorology in Hamburg, Germany. It became operational in the DWD forecast system in 2015. The convective-scale, limited-area setup of the ICON model ICON-D2 covers Germany and parts of its neighboring countries. It has an unstructured triangular grid with a horizontal resolution of about 2.2 km and 65 vertical levels, of which the near-ground levels are terrain-following and the higher ones gradually shift to constant heights with increasing altitude. Lateral boundary conditions are provided by the ICON-EU model, a nesting setup of the ICON model over Europe.

The ICON-D2 model provides prognostic variables including the 3D wind velocity components and the virtual potential temperature. The total density of the air-water mixture and the individual mass fractions of dry air, water vapor, cloud water, cloud ice, rain, snow, and graupel are further prognostic variables simulated through a coupled single-moment bulk microphysical scheme representing a two-component system of dry air and water that can occur in all three states of matter. A more detailed overview of the ICON model can be found in Prill et al. (2020).

4.2.2 The KENDA Suite

The KENDA system is the DA framework for the operational ICON-D2 model at DWD. It includes the LETKF scheme following Hunt et al. (2007) in a 4D manner, which is achieved by computing innovations using the observation operator during the model forward integration at each observation time (Schraff et al., 2016). In addition to the currently used 40-member ensemble, an additional deterministic analysis and forecast cycle is performed in KENDA (40+1 mode) by applying the LETKF Kalman gain for the ensemble mean

$$\boldsymbol{K} = \boldsymbol{X}_b \widetilde{\boldsymbol{P}}_a \boldsymbol{Y}_b^T \boldsymbol{R}^{-1} \tag{4.52}$$

to the innovations of the unperturbed deterministic run

$$\vec{x}_a^{det} = \vec{x}_b^{det} + \boldsymbol{K}(\vec{y}_o - \mathcal{H}(\vec{x}_b^{det})) \tag{4.53}$$

with $\vec{x}_a^{det}$ and $\vec{x}_b^{det}$ the deterministic analysis and background states, respectively. This allows for the use of the ensemble-estimated flow-dependent background error covariance matrix for the deterministic analysis (Schraff et al., 2016). To reduce computational cost, the analysis in ensemble space can be calculated on a coarsened grid, which is then interpolated to the full-resolution model grid before determining the analysis in model space (Yang et al., 2009). Since the analysis in ensemble space is the weights for linear combinations of the forecast ensemble members (see Eq. (4.47)), the final analysis in model space still captures the small-scale features (Schraff et al., 2016). Currently, KENDA uses a coarsening factor of three.

Furthermore, the KENDA suite includes various tools to address the problem of underestimation of background and analysis error covariances, which is typically observed in EnKF schemes and arises partly from sampling errors due to too small ensemble sizes and partly from inadequate representation of background and observation errors (Schraff et al., 2016). Horizontal and vertical observation localization is performed in KENDA by scaling the inverse observation error covariance matrix $\boldsymbol{R}^{-1}$ with a Gaspari-Cohn correlation function (Gaspari and Cohn, 1999). KENDA allows for adaptive horizontal observation localization so that the number of observations influencing an analysis grid point, which should be somewhat larger than the number of ensemble members, is kept constant (Schraff et al., 2016). Thus, the radius of influence is smaller in regions with dense data than in regions with sparse data. Adaptive horizontal localization is applied in KENDA within the limits of localization length-scales of 50 and 100 km corresponding to the radii of main observation influence of 100 and 200 km, respectively. The vertical observation localization length-scale increases gradually from the model surface to the model top from 0.075 to 0.5 in logarithm of pressure (ln(p)). KENDA also allows for the determination of background error variances and their adaptation following Desroziers et al. (2005). MCI (Anderson and Anderson, 1999), CRPP (Zhang et al., 2004), and CRPS (Whitaker and Hamill, 2012) are usable in KENDA, where MCI can be used also adaptively. Adaptive MCI with factors between 0.5 and 3.0, and CRPP with a weight for the background ensemble perturbations set to a value of 0.75 are currently used in KENDA, and CRPS is not applied.

4.2.3 Radar Data Assimilation with KENDA

As stated above, Z_H observations can be indirectly assimilated with LHN in KENDA, which is applicable to both the ensemble members and the deterministic run during model forward integration. KENDA allows for the parallel use of LHN and direct 3D

radar DA. For the direct radar DA, first-guess PPIs of Z_H and V_r at all 10 measured radar elevation angles between 0.5 and 25 deg for each of the 17 radar stations of DWD (see Fig. 2.1) and every 5 min in correspondence to the observations are calculated from the model states using the EMVORADO radar forward operator. The EMVORADO simulator considers various physical aspects of radar measurements, such as beam bending, broadening, and shielding, partially melted hydrometeors, reflectivity attenuation, reflectivity weighting, and particle fall velocity for Doppler radial wind, as well as the Rayleigh- or Mie-scattering theory, which are implemented in a modular way and can be optionally chosen based on the user's needs regarding the degree of approximation and computational cost (Zeng et al., 2016). E.g., Mie-scattering calculations are currently used in KENDA through efficient look-up tables, and particle size distributions are described by modified gamma distributions, which parameters are determined from the model hydrometeor fields and pre-definitions depending on the particular microphysical scheme used (personal communication Jana Mendrok, DWD).

For the direct 3D radar DA in KENDA, Z_H data of only the five radar elevation angles of 1.5, 3.5, 5.5, 8.0, and 12.0 deg are used as a compromise between observation impact and computational effort (personal communication Ulrich Blahak and Christian Welzbacher, DWD). Similarly, V_r observations are only assimilated for the radar elevation angles 0.5, 1.5, and 3.5 deg. Z_H and V_r observations from heights from below 600 and above 9,000 m are not used. The assimilation of the radar observations in their full PPI resolution may lead to a degradation of the model state in the analysis step due to the much coarser analysis grid especially for the data close to the radar stations (Liu and Rabier, 2002). Thus, radar observations are spatially averaged elevation-wise for each radar station to approximate the analysis grid resolution. This procedure known as superobbing (e.g., Alpert and Kumar, 2007; Bick et al., 2016) is performed in KENDA within the EMVORADO forward operator, is applied to both the observed and background radar data, and contains the following steps. First, a 2D horizontal Cartesian grid with a resolution of LC approximating the analysis grid used (LC is 10 km for the ICON-D2 model using a coarsening factor of three) is defined. In a second step, the azimuth-range radar bins are projected onto the Cartesian grid to find the closest radar bin for each Cartesian grid point, which become the centers of the averaging performed in the radar polar coordinates. The averaging is performed within azimuth-range intervals, where the number of radar bins contributing to the averaging decreases with the range: the width of the range interval is determined by $LC\sqrt{2}$ and the width of the azimuth interval is determined by $2\arctan\left\{\left(\frac{LC\sqrt{2}}{2}\right)/r_0\right\}$ with r_0 the range of the determined center radar bin. Averaging is performed on the linear scale and only if $r_0 \geq 0.75LC\sqrt{2}$ and if the number of range-azimuth bins with valid values within the superobbing window is at least three observations (Fig. 5.1 exemplifies superobbing).

The assimilation of Z_H data is also performed in regions without precipitation (no-precipitation areas), which has been found valuable in some studies to suppress

spurious precipitation (e.g., Tong and Xue, 2005; Aksoy et al., 2009; Bick et al., 2016). The observed Z_H can span a range from about -30 to 60 dBZ, of which the no-precipitation echoes can cover a significant fraction, possibly resulting in large differences between the observed no-precipitation Z_H and the corresponding model background Z_H values, which can lead to large and unphysical analysis increments (Bick et al., 2016). To alleviate this problem, no-precipitation data identified by a lower no-precipitation threshold is set to the selected threshold, keeping the weight of the no-precipitation data in the analysis step within reasonable limits. Currently, the lower threshold is 0 dBZ in KENDA and is applied to the observed and first-guess Z_H data before superobbing. The observational error standard deviation for Z_H is chosen to be fixed and 10 dBZ based on experiments (personal communication Klaus Stephan, DWD), while that for V_r is set to 2.5 m s^{-1}. The horizontal observation localization length-scales for Z_H and V_r data are set to a fixed value of 16 km, corresponding to a radius of main observation influence of 32 km. The vertical observation localization for V_r is set to a fixed value of 0.3 ln(p), while the one for the Z_H assimilation follows the height-dependent profile as for the other observations (gradually increasing from 0.075 to 0.5 ln(p) with height).

Chapter 5

Assimilation of 3D Microphysical Retrievals in Germany

In this chapter, polarimetric observations from the German national C-band radar network are assimilated in the operational convective-scale KENDA-ICON-D2 system of DWD for the first time. The assimilation is performed using 3D polarimetric microphysical retrievals of LWC and IWC below and above the melting layer, respectively. Their impact on short-term QPF in Germany in comparison to the assimilation of Z_H observations alone is evaluated. Section 5.1 describes the observational and model data sets used as well as their processing. Section 5.2 then describes the retrieval assimilation technique applied and the assimilation experiments performed. In the first part of the experiment, the impact of the 3D microphysical retrievals on first-guess QPF quality with different DA settings is investigated. In the second part of the experiment, nine-hour forecasts of the ICON-D2 model initiated with the most successful retrieval assimilation settings found are evaluated. Results are presented in Section 5.3, and finally, a summary and conclusions are given in Section 5.4. The assimilation approach and results presented in this chapter are submitted for publication in Reimann et al. (2023).

5.1 Data Sets and Processing

Heavy summer precipitation events can pose serious risks to society and the economy in Central Europe and are particularly difficult to predict (Olson et al., 1995). Therefore, this thesis focuses on three intense summer precipitation events in Germany. The first event considered covered a 1.5-day period from 19 to 20 July 2017 and was dominated by convective precipitation including a squall-line that crossed Germany in the evening hours of 19 July 2017 (case C2017). The second event covered a 3-day period from 24 to 26 July 2017 and was characterized by widespread intense and mostly stratiform precipitation (case S2017). It caused flooding, especially in Lower Saxony in the middle of Northern Germany along the Bode River catchment. The third event was dominated by heavy stratiform precipitation resulting from a slow-moving low-pressure system over Central Europe and covered a 2-day period from 13 to 14 July 2021 (case S2021). It caused devastating flooding, e.g., along the Ahr River in Rhineland-Palatinate in western

parts of Germany with more than 180 deaths and an insured loss of more than 30 billion euros in Germany alone[1].

5.1.1 Conventional Observations

Conventional observations taken from the DWD archive are assimilated as a baseline in this thesis. They include 10 m horizontal wind and pressure observations from surface weather stations, horizontal wind and temperature observations reported from commercial aircrafts, horizontal wind observations by pilot balloons and wind profilers, horizontal wind, relative humidity, and temperature observations from radiosondes, and sea-surface observations of, e.g., air pressure and horizontal wind.

5.1.2 Polarimetric Observations

For the direct assimilation of 3D Z_H observations employed in this study, Z_H observations already processed, including quality assurance and attenuation correction, from the DWD data archive are used. For the estimation of LWC and IWC, raw polarimetric radar moments are processed from scratch. The basic polarimetric moments used include horizontal reflectivity Z_H, differential reflectivity Z_{DR}, total differential phase Φ_{DP}, and co-polar cross-correlation coefficient ρ_{HV}. As performed in Chapter 3 for the evaluation of estimators with real radar observations, data below/above the melting layer are used for $\rho_{HV} > 0.95/0.85$ according to Kumjian (2013a) with ρ_{HV} corrected for noise before filtering following Ryzhkov and Zrnic (2019). QVPs of ρ_{HV} and Z_{DR}, as derived from PPIs at a 5.5 deg radar elevation angle, or the closest operational radio sounding of DWD, are used to estimate the height of the melting layer. In addition, only radar bins at ranges greater than 5 km are considered to reduce negative effects of ground clutter.

As in Chapter3, K_{DP} is estimated from the filtered and smoothed Φ_{DP} following Vulpiani et al. (2012) with a fixed window size of 9 km. This rather large window size is, as described before, needed because of the coarse radial resolution (1 km) of most of the PPIs considered to allow for proper K_{DP} estimation and to keep noise in the K_{DP} estimates rather low. Only one of the considered precipitation cases (S2021) has data with a radial resolution of 0.25 km (recall the increase of the radial resolution of the DWD volume-scan in March 2021, see Section 2.1.3). Nevertheless, K_{DP} is also estimated for the S2021 case with a 9 km window for reasons of comparability.

Also as in Chapter 3, the horizontal specific attenuation A_H is derived below the melting layer using the filtered and smoothed Φ_{DP} and the measured (attenuated) Z_H using the ZPHI-method (Testud et al., 2000). Thereby, the attenuation parameter α is optimized for each ray below the melting layer using the self-consistency method proposed by Bringi et al. (2001).

[1] *https://www.theguardian.com/world/2022/jul/13/floods-then-and-now-photographs-germany-ahr-valley-flooding-disaster-july-2021 (last accessed 18 June 2023).*

Finally, the raw Z_H and Z_{DR} observations are corrected for (differential) attenuation using the optimized or climatological (0.08 dB deg^{-1}) α values below or above the melting layer, respectively, and the climatological value for the differential attenuation parameter β for C-band of 0.02 dB deg^{-1} is used everywhere (see Eqs. (3.4) and (3.5) in Section 3.1.2, or Ryzhkov and Zrnic, 2019).

5.2 Setup of Assimilation Experiments

The hybrid LWC retrieval adapted to the German C-band radar network and developed in Chapter 3 (Eqs. (3.11), (3.13), (3.15), and (3.18) through (3.20)) and published in Reimann et al. (2021) is used to assimilate polarimetric radar observations below the melting layer into DWD's KENDA-ICON-D2 system. A recent study by Blanke et al. (2023) showed that the hybrid IWC estimator proposed by Carlin et al. (2021) noted in Eqs. (2.60) and (2.61) performed best in terms of RMSD (0.19 g m^{-3}) and also good in terms of PCC (0.96) when applied to X-band radar data over the west coast of the USA and evaluated with aircraft in-situ observations. These encouraging results, although obtained with an X-band radar over US terrain, motivate the use of that hybrid estimator for the assimilation of polarimetric radar observations from above the melting layer in this thesis. However, as stated before, the selected IWC estimator of Carlin et al. (2021) was developed based on assumptions valid for snowfall, but not, e.g., for hail and graupel, like an inversely proportional relationship between hydrometeor size and density. Thus, its applicability to especially hail and/or graupel bearing convective situations may be limited. The same holds for the newly developed LWC retrieval, which was derived from pure-rain disdrometer observations (see Chapter 3).

5.2.1 Retrieval Resolution

The LWC and IWC values are estimated on the radar PPIs and thus have the same resolution as the raw radar observations. As for the Z_H DA in KENDA, the LWC and IWC estimates require superobbing prior to assimilation to better match the analysis grid resolution in the analysis step. Superobbing of the LWC and IWC estimates is performed in the linear scale with a minimum number of valid values for averaging in the superobbing window MV of three observations (see an example of superobbing of LWC and IWC estimates in Fig. 5.1), like for the Z_H data in KENDA. Here, the superobbing window length LS (given in km), which is equal to the Cartesian grid resolution LC for the Z_H DA in KENDA (10 km for an analysis coarsening factor of three), is used to allow modifications of the superobbing window size for the LWC and IWC estimates independent of the selected analysis grid coarsening factor.

The microphysical estimates are assimilated with a lower limit LL according to the no-precipitation threshold of 0 dBZ used for the assimilation of 3D Z_H data in KENDA. However, the LWC and IWC retrievals in no-precipitation regions are mostly filtered out by the ρ_{HV} thresholds applied. The use of such a lower limit can

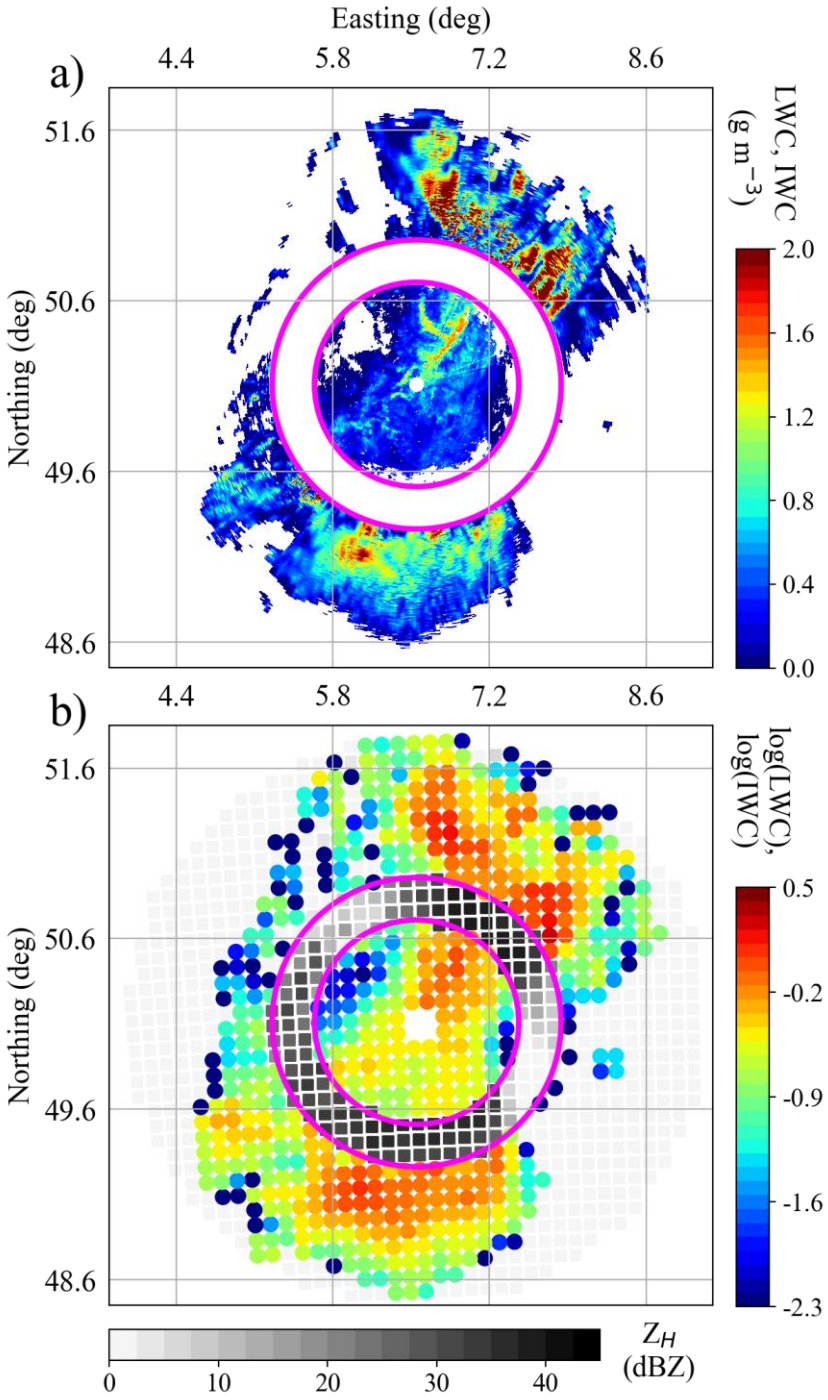

FIGURE 5.1: a) PPI at 1.5 deg elevation angle of the DWD radar in Neuheilenbach (NHB; see Fig. 2.1 of radar-estimated LWC (in g m^{-3}) using the hybrid estimator developed in Chapter 3 (Eqs. (3.11), (3.13), (3.15), and (3.18) to (3.20)) below the melting layer (upper and lower boundaries of the melting layer are marked by violet circles in both subplots) and of the radar-estimated IWC (in g m^{-3}) using the hybrid retrieval proposed by Carlin et al. (2021; Eqs. (3.60) and (3.61)) above the melting layer for the stratiform case on 14 July 2021 (S2021) at 16 UTC. b) Superobbed PPI data from subplot a) (colored cycles) on the logarithmic scale matching approximately the analysis grid resolution (10 km), and corresponding superobbed Z_H data (in dBZ) where no superobbed LWC and IWC estimates are available (grey/black squares), e.g., within the melting layer.

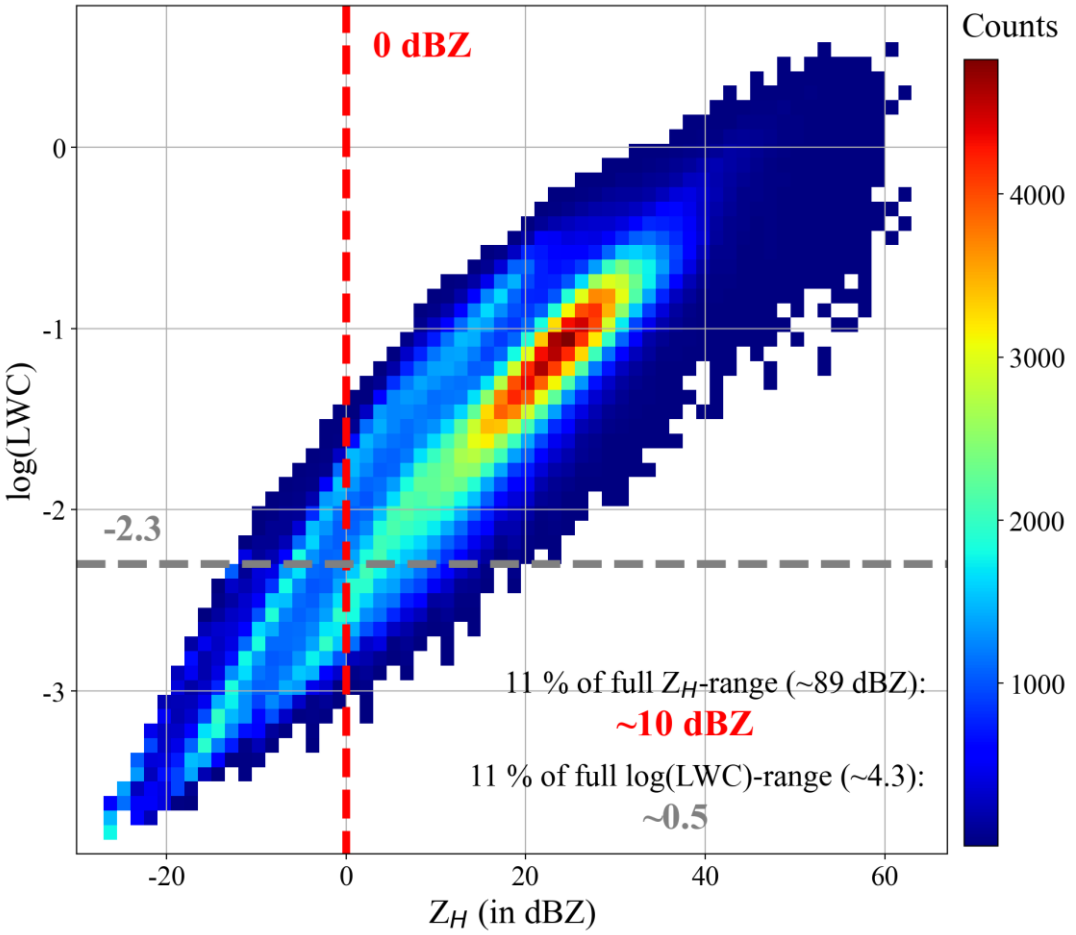

FIGURE 5.2: 2D histogram of DSD-based pairs of T-matrix calculated Z_H and log(LWC) computed using Eq. (3.3). The dashed red vertical line indicates the lower limit (LL) of 0 dBZ used in KENDA for the assimilation of Z_H data in no-precipitation regions, the dashed grey horizontal line indicates the approximately corresponding value for log(LWC) of -2.3. Also shown are the fraction that 10 dBZ (observation error standard deviation OE for the Z_H assimilation in KENDA) covers of the full range of Z_H in the DSD data set (about 89 dBZ or 11 %), and the corresponding 11 % fraction in the full range of log(LWC) data (about 4.3) of 0.5 used as pre-selected OE value for the log(LWC) assimilation.

still be beneficial to limit the variability of the LWC and IWC data and can also be used for tuning purposes (personal communication Ulrich Blahak, DWD). The comparison of measured log(LWC) and synthetic Z_H observations obtained from T-matrix scattering calculations at C-band in the large German pure-rain disdrometer data set used for the development and evaluation of the LWC retrievals in Chapter 3 indicates that the 0 dBZ no-precipitation threshold for the Z_H assimilation corresponds approximately to a log(LWC) value of -2.3 (see red and grey dashed lines in Fig. 5.2). The rare occurrence of snow at the surface in Germany and instrument restrictions mentioned in Chapter 3 make a similar analysis for the IWC estimates difficult. Thus, -2.3 is also used for LL for log(IWC).

Analogous to the assimilation of Z_H data in KENDA, PPIs of LWC and IWC estimates are assimilated at only the radar elevation angles of 1.5, 3.5, 5.5, 8.0, and 12.0 deg, and data from heights below 600 and above 9,000 m remain unconsidered. Using comparable DA settings allows for a better comparability of the assimilation impact of the Z_H observations and the microphysical LWC and IWC estimates. As with the Z_H assimilation in KENDA, the LWC and IWC retrievals are assimilated in the logarithmic scale, which leads to better results (not shown).

5.2.2 Assimilation Settings and First Guess

A fixed observation error standard deviation OE of 10 dBZ is currently used in KENDA for the direct assimilation of 3D Z_H observations. For the assimilation of 3D log(LWC) values, a fixed OE value of 0.5 is used, which is obtained statistically from the large German disdrometer data set used above for the evaluation and development of LWC retrievals in Chapter 3. A difference in log(LWC) of 0.5 covers a similar fraction of the full range of log(LWC) data (about 11 %) as 10 dBZ does of the full range of simulated Z_H data (about 89 dBZ, see Fig. 5.2). Again, the same OE value is also used for log(IWC). The horizontal and vertical observation localization length-scales LH and LV for the microphysical estimates are set to 16 km and to a height-dependent profile (i.e., increasing from 0.075 to 0.5 ln(p) with height), respectively, as in KENDA for the assimilation of 3D Z_H observations.

The model counterpart (first-guess) LWC and IWC data are calculated using a simple "forward operator" which uses the prognostic model variables total air density including liquid and solid water (ρ_{tot}, given in kg m^{-3}) and the rain and cloud water mixing ratios q_r and q_c for LWC as well as the snow, graupel, and cloud ice mixing ratios q_s, q_g, and q_i (all given in g m^{-3}) for IWC at the model grid points to compute

$$\mathrm{LWC} = 10^3 \rho_{tot}(q_r + q_c) \tag{5.1}$$

and

$$\mathrm{IWC} = 10^3 \rho_{tot}(q_s + q_g + q_i). \tag{5.2}$$

The first-guess LWC and IWC data at the model grid points are then projected with the nearest-neighbor method onto the polar PPI grid of the observed LWC and IWC data, followed by superobbing as with the observed estimates. The procedure is performed for each of the 40 ensemble members and the deterministic run.

5.2.3 Model Initial and Lateral Boundary Data

ICON-D2 model data in 40+1 mode from the DWD data archive for 22 UTC 12 July 2021, 00 UTC 23 July, and 00 UTC 18 July 2017 are used. These data are output from the regular ICON-D2 routine and thus do not require further "spin-up"

integrations to be used for the assimilation experiments performed in this thesis. Hourly assimilation cycles with the KENDA-ICON-D2 system with assimilation of conventional and 3D radar observations, including LHN as in the operational routine are performed to obtain model states for the initial times of the experiment periods 00 UTC 13 July 2021, 00 UTC 24 July 2017, and 11 UTC 19 July 2017. ICON-EU model data from the DWD archive serves as lateral boundary conditions.

5.2.4 Experiment Part A: Assimilation Configurations

Starting from the initial times (11 UTC 19 July 2017, 00 UTC 24 July 2017, and 00 UTC 13 July 2021) of the experiment periods (C2017, S2017, and S2021), 3D LWC and IWC estimates obtained from the polarimetric radars of the DWD radar network (see red radars in Fig. 2.1) are assimilated in hourly assimilation cycles instead of Z_H observations, where available. This procedure seek to avoid potential problems arising from assimilating the information from the Z_H data twice – first directly and second indirectly via the retrievals. This strategy also allows to study the differences in the assimilation impact of the Z_H data and the microphysical estimates. Thus, Z_H data are always assimilated within the melting layer and in precipitation-free regions, where the LWC and IWC estimates are not available due to the applied ρ_{HV} thresholds. The assimilation of 3D V_r observations and LHN are not performed in the hourly assimilation cycles in order to focus on the assimilation of microphysical information from the DWD radar network. The LWC and IWC estimates are assimilated separately to study their individual impact on the first guess, but also to find the best DA parameter (DAP; LH, LV, OE, LS, LL, and MV) sets for both quantities separately. Therefore, Z_H data are also assimilated above the melting layer when LWC is assimilated, and Z_H data are also assimilated below the melting layer if IWC is assimilated. The respective assimilation configurations also assimilate conventional observations as a baseline and are therefore referred to as the CNV+LWC/Z and CNV+IWC/Z configurations. The assimilation configurations assimilating only conventional observations and assimilating both conventional and 3D Z_H data are considered as references in this study (CNV and CNV+Z).

The impact of the 3D LWC and IWC assimilation on the first-guess deterministic and ensemble QPF is quantified by the Fractions Skill Score (FSS; Roberts and Lean, 2008) and the Brier Skill Score (BSS; following Wilks, 2019) using the RADOLAN (Radar Online Aneichung) QPE product of DWD as verification data. The RADOLAN data used[1], the so-called "RW" product, are hourly precipitation accumulations obtained from Z_H observations and adjusted to surface-network rain gauges in an equidistant grid covering Germany and parts of its neighboring states with a resolution of 1 km in a polar-stereographic projection. The FSS is calculated

[1]*The open source RADOLAN data of DWD used, the "RW" product (hourly accumulations), were downloaded from https://opendata.dwd.de/climate_environment/CDC/grids_germany /hourly/radolan/historical/asc/ (last accessed 17 May 2022).*

after projection of the forecasted and observed precipitation accumulations onto the chosen verification grid, namely the RADOLAN grid reduced to 3 km resolution, to better fit the model data of about 2.2 km horizontal resolution. The RADOLAN data are averaged over nine grid points in the original RADOLAN grid, while the model data are selected by the nearest-neighbor method. The projected fields of observations P_O and model first-guess P_M are converted to binary fields I_O and I_M for the chosen precipitation accumulation thresholds q_{th} as

$$I_{O,(q_{th})} = \begin{cases} 1 & for\ P_O \geq q_{th} \\ 0 & for\ P_O < q_{th} \end{cases} \tag{5.3}$$

and

$$I_{M,(q_{th})} = \begin{cases} 1 & for\ P_M \geq q_{th} \\ 0 & for\ P_M < q_{th} \end{cases} \tag{5.4}$$

(Roberts and Lean, 2008). Fractions of surrounding points within squares of $n_{FSS} \times n_{FSS}$ data points in the binary fields $I_{O,(q_{th})}$ and $I_{M,(q_{th})}$, $F_{O,(n_{FSS},q_{th})}$ and $F_{M,(n_{FSS},q_{th})}$, that have a value of one are calculated for each verification grid point. The FSS for a window size n_{FSS} and a precipitation threshold q_{th} then is

$$\mathrm{FSS}_{(n_{FSS},q_{th})} = 1 - \frac{\mathrm{MSD}_{(n_{FSS},q_{th})}}{\mathrm{MSD}_{(n_{FSS},q_{th}),ref}} \tag{5.5}$$

with the mean squared deviation (MSD) for the observed and forecasted fractions

$$\mathrm{MSD}_{(n_{FSS},q_{th})} = \frac{1}{V}\sum_{i=1}^{V}\left[F_{O,(n_{FSS},q_{th}),i} - F_{M,(n_{FSS},q_{th}),i}\right]^2 \tag{5.6}$$

and the total number V of verification grid points (Roberts and Lean, 2008). The reference MSD given by

$$\mathrm{MSD}_{(n_{FSS},q_{th}),ref} = \frac{1}{V}\sum_{i=1}^{V} F^2_{O,(n_{FSS},q_{th})i} + F^2_{M,(n_{FSS},q_{th})i} \tag{5.7}$$

represents the largest possible MSD from the observation and forecast fractions (Roberts and Lean, 2008). The FSS shows values between zero and one with the higher values the better. A value for n_{FSS} of five (like used in Bick et al., 2016) corresponding to a 15 km window is used in this thesis.

The Brier Score (BS; Wilks, 2019) is a measure for the accuracy of probabilistic forecasts and takes the forecast ensemble into account via

DAP values	LH (km)	LV (ln(p))	OE	LS (km)	LL	MV
Pre-selected (S-pre)	16	h.d.	0.50	10	-2.30	3
Variation 1	8	0.2	0.25	5	-1.15	25 %
Variation 2	32	0.5	1.00	20	-4.60	50 %

TABLE 5.1: Pre-selected values for the DAPs LH and LV (horizontal and vertical observation localization length-scales in km and ln(p), with "h.d." for LV standing for "height-dependent" from 0.075 to 0.5 ln(p)), OE (observation error standard deviation), LS (superobbing window size in km), LL (lower limit of data applied before superobbing), and MV (the minimum required number of valid observations for superobbing), and two variations considered each.

$$\mathrm{BS}_{(q_{th})} = \frac{1}{V}\sum_{i=1}^{V}\left[p_{(q_{th}),i} - I_{O,(q_{th}),i}\right]^2 \tag{5.8}$$

with $p_{(q_{th}),i}$ the fraction of ensemble members within the ensemble exceeding the threshold q_{th} at the i$^{\mathrm{th}}$ verification grid point. The BSS for a threshold q_{th} then is calculated by

$$\mathrm{BSS}_{(q_{th})} = 1 - \frac{\mathrm{BS}}{\mathrm{BS}_{ref}}, \tag{5.9}$$

(e.g., Bick et al., 2016) with BS_{ref} the Brier score of a reference ensemble forecast (here forecasts resulting from the CNV configuration). The BSS shows positive/negative values if the probabilistic QPF fits the observations better/worse compared to the probabilistic reference QPF.

Using Latin Hypercube Sampling (LHS), a near-random sample of DAP settings is generated (DAP settings S1-01 through S1-12 in Table 5.2) by modifying the DAP values from their pre-selected values (pre-selected and varied values in Table 5.1): the pre-selected values for the DAPs LH, OE, LS, and LL are doubled or halved; for LV, fixed values of 0.2 and 0.5 ln(p) instead of the height-dependent profile are used as variations; MV is modified from an absolute value of three valid observations required for superobbing to the fractions 25 or 50 % of valid values in the superobbing window required for averaging. The DAP configurations/values are compared with each other in terms of first-guess deterministic and ensemble QPF quality by considering a single univariate measure – the joint quality score (JQS)

$$\begin{aligned}\mathrm{JQS}_{c/v} = {} & \mathrm{median}_w(\Delta_{CNV+Z}\mathrm{FSS}_{norm}[\mathrm{CNV}+\therefore/\mathrm{Z}]) \\ & +\mathrm{median}_w(\Delta_{CNV+Z}\mathrm{BSS}_{norm}[\mathrm{CNV}+\therefore/\mathrm{Z}]).\end{aligned} \tag{5.10}$$

DAP settings	LH (km)	LV (ln(p))	OE	LS (km)	LL	MV
S1-01	16	h.d.	1.00	5	-2.30	50 %
S1-02	8	0.5	0.25	10	-1.15	50 %
S1-03	8	0.5	0.25	20	-1.15	3
S1-04	32	0.5	0.50	5	-2.30	25 %
S1-05	8	0.2	0.25	10	-4.60	50 %
S1-06	16	h.d.	0.50	20	-1.15	25 %
S1-07	32	0.2	1.00	5	-1.15	3
S1-08	8	0.2	0.50	20	-2.30	3
S1-09	32	0.5	0.50	5	-4.60	25 %
S1-10	16	h.d.	1.00	10	-4.60	25 %
S1-11	32	h.d.	1.00	20	-4.60	3
S1-12	16	0.2	0.25	10	-2.30	50 %
S2-01	16	0.2	1.00	20	-1.15	50 %
S2-02	16	0.2	0.25	10	-2.30	3
S2-03	8	h.d.	1.00	20	-1.15	3
S2-04	16	0.2	1.00	20	-2.30	50 %
S2-05	16	h.d.	0.25	10	-2.30	50 %
S2-06	8	0.2	0.25	20	-1.15	3
S2-07	8	0.2	1.00	10	-1.15	3
S2-08	8	h.d.	0.25	10	-1.15	50 %
S2-09	8	h.d.	1.00	20	-2.30	50 %
S2-10	16	h.d.	0.25	10	-2.30	3

TABLE 5.2: Near-random sample of DAP settings from the pre-selected and varied DAP values in Table 5.1 generated with Latin Hypercube Sampling (LHS). The first sample S1-01 to S1-12 is generated based on all DAP values in Table 5.1. The second sample S2-01 to S2-10 is generated with a reduced number of DAP values from Table 5.1 with the reduction of DAP values performed by consideration of the univariate measure JQS_v defined in Eq. (5.10) determined from the first DAP setting sample (S1-01 to S1-12).

In Eq. (5.10), Δ_{CNV+Z} indicates differences with respect to the CNV+Z assimilation configuration, "$\therefore$" is either LWC or IWC, the index "norm" denotes normalization with the means of Δ_{CNV}FSS[CNV+Z] or BSS[CNV+Z] over all considered precipitation accumulation thresholds (0.5, 1.0, 2.0, and 4.0 mm h^{-1}) and cases (C2017, S2017, and S2021), and $\mathrm{median}_w(\ldots)$ indicates a weighted median. Medians are used instead of means to reduce the effect of outliers in FSS and BSS. The weights are determined by the fractions of threshold exceedances for a given time and threshold in the total number of exceedances in all thresholds and cases considered in the RADOLAN data (see fractions in Fig. 5.3). Thus, the number threshold exceedances is taken into account by JQS, and lower (more frequently exceeded) accumulation thresholds generally have a larger influence on the result compared to higher (less frequently exceeded) thresholds. Weighted medians over all cases and thresholds are calculated to compare first-guess QPF quality between different DAP configurations (JQS_c), and medians are additionally calculated over all DAP settings with the same DAP values to compare individual DAP *values* (JQS_v).

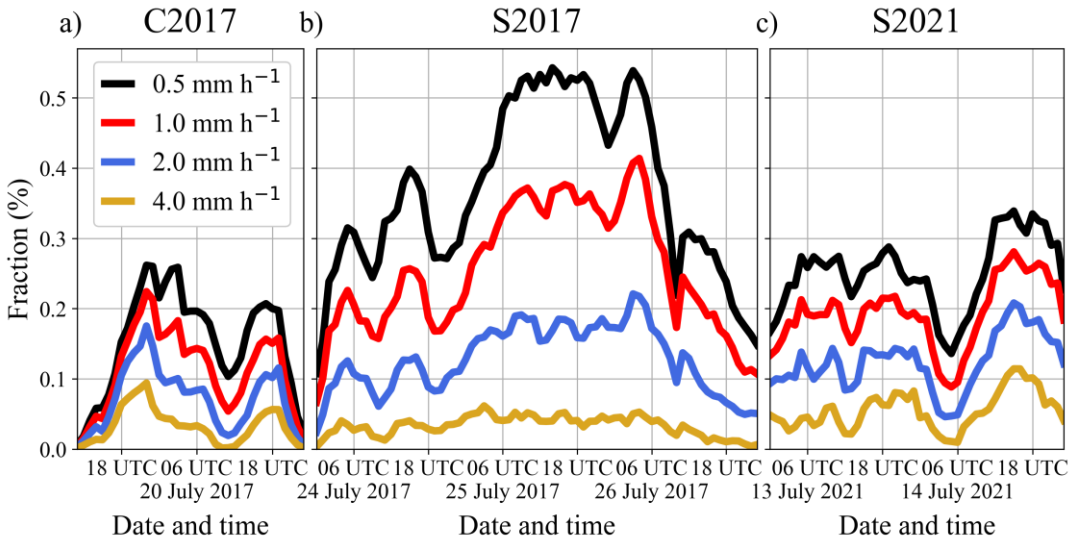

FIGURE 5.3: Time series of the fractions of the number of precipitation accumulation threshold exceedances in the RADOLAN QPE data of DWD ("RW"-product, hourly accumulations) in the thresholds 0.5, 1.0, 2.0, and 4.0 mm h^{-1} (black, red, blue, and golden curves) for a) the 2017 convective case C2017, b) the 2017 stratiform case S2017, and c) the 2021 stratiform case S2021 of the total number of threshold exceedances in all thresholds and precipitation cases in the DWD RADOLAN data. Fractions are used to calculate weighted median FSS/BSS values and the univariate measure JQS defined in Eq. (5.10).

Besides best-performing DAP settings for LWC and IWC, this thesis also attempts to find best-performing combinations of the radar data sets considered (i.e., LWC, IWC, and Z_H). For this purpose, the parallel assimilations of LWC or IWC and Z_H (CNV+LWC+Z or CNV+IWC/Z, respectively), the combined assimilation of LWC and IWC instead of Z_H, where available (CNV+[LWC+IWC]/Z), or in parallel to Z_H (CNV+LWC+IWC+Z) are also evaluated with respect to first-guess deterministic and ensemble QPF quality quantified by the univariate measure JQS_c.

5.2.5 Experiment Part B: Nine-Hour Forecasts

In the second and final step, the impact of assimilating the 3D polarimetric LWC and IWC retrievals with KENDA on deterministic forecasts of the ICON-D2 model with lead times greater than one hour is evaluated. The 3D microphysical estimates are assimilated in hourly assimilation cycles using the identified best-performing DAP settings and radar data set configurations from the previous experiment part and subsequently nine-hour forecasts of the ICON-D2 model are initiated every third hour from the produced analyses. The quality of deterministic QPF is evaluated, as before, by considering the FSS and also the Frequency Bias (FBI) defined by

$$\mathrm{FBI}_{(q_{th})} = \frac{a_{(q_{th})}+b_{(q_{th})}}{a_{(q_{th})}+c_{(q_{th})}} \tag{5.11}$$

(e.g., Bick et al., 2016) with $a_{(q_{th})}$ the total number of verification grid points that exceed the threshold q_{th} in P_O and P_M, $b_{(q_{th})}$ the total number of points where q_{th} is exceeded in P_M but not in P_O, and $c_{(q_{th})}$ the total number of points for which the threshold q_{th} is not exceeded in P_M, but in P_O. The FBI shows values below/above one in the case of underforecasted/overforecasted number of threshold exceedances. Ensemble forecasts remain unconsidered here due to data storage restrictions.

5.3 Numerical Results

5.3.1 Experiment Part A: Assimilation Configurations

The assimilation of 3D LWC estimates as alternatives to Z_H observations, where possible (CNV+LWC/Z), yields different FSS and BSS values for the 12 different DAP settings (S1-01 through S1-12 in Table 5.2) and three different precipitation cases (C2017, S2017, and S2021) considered (Fig. 5.4a,c). Improvements in FSS and BSS over the assimilation of Z_H data alone (CNV+Z) considering all precipitation cases together are obtained, e.g., with the DAP sets S1-01 through S1-03, S1-06, or S1-08 (see Fig. 5.4a4,c4). These best-performing DAP settings are characterized by small horizontal observation localization length-scales (LH of 8 and 16 km) and rather high lower limits of the microphysical estimates (LL of -2.30 and -1.15). Thus best first-guess QPF quality is obtained when the influence of the microphysical retrievals on the model state is rather small, probably because of discrepancies between true and model microphysics. The assimilation of IWC instead of Z_H data, where possible (CNV+IWC/Z), also yields different FSS and BSS values for the different DAP settings and precipitation cases (Fig. 5.4b,d). Improvements in first-guesses over the CNV+Z configuration are mostly limited to the stratiform S2021 case, e.g., DAP settings S1-02 or S1-05 (Fig. 5.4b3,d3), while the first-guess QPF quality is always degraded for the convective C2017 case (Fig. 5.4b1,d1).

In order to identify the best-performing DAP sets for LWC and IWC while taking into account all three precipitation cases C2017, S2017, and S2021, the univariate measure JQS_v (introduced in Section 5.2.4 and Eq. (5.10)), which is based on the first-guess FSS and BSS values, is used. The DAP values that yield the worst (and negative) JQS_v values among the tested DAP values in Table 5.1 for each DAP calculated from the DAP sample S1-01 to S1-12 in Table 5.2 are 32 km, 0.5 ln(p), 0.5, 5 km, -4.6, and 25 % (i.e., 25 % of the radar pixels in the superobbing window must have valid values for superobbing) for the DAPs LH, LV, OE, LS, LL, and MV, respectively, for both LWC and IWC (black and grey bars in Fig. 5.5a). Another 10 DAP settings are sampled with LHS in the vicinity of the better performing ones (S2-01 through S2-10 in Table 5.2). Using the new DAP settings for LWC and IWC again yields different first-guess FSS and BSS values for the different new DAP settings and considered precipitation cases (Fig. 5.4e-h). Improvements in the first-guess FSS and BSS values compared to the assimilation of Z_H data alone (CNV+Z) are again evident for the

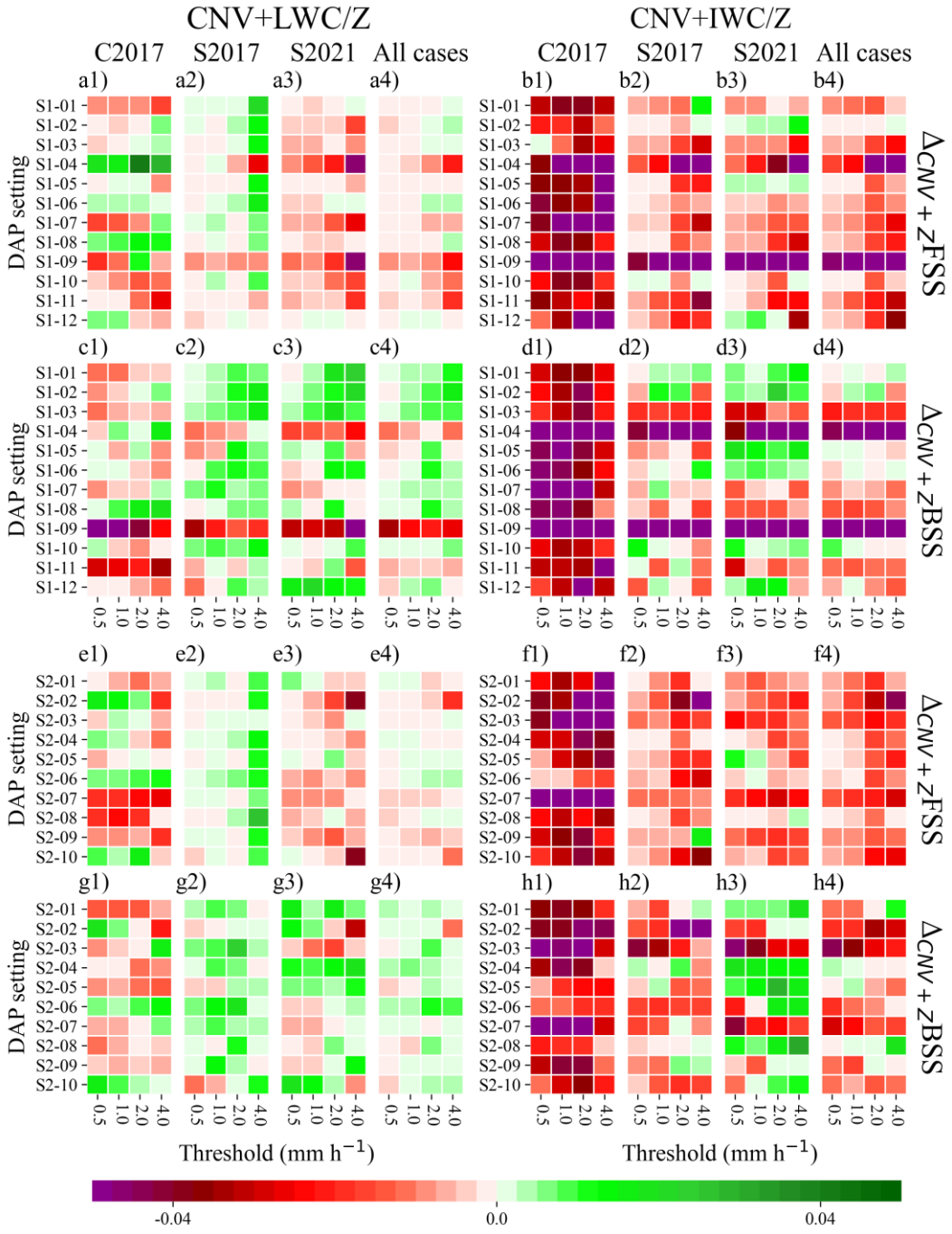

FIGURE 5.4: Weighted medians of differences in first-guess deterministic FSS (first and third panel rows) and BSS (second and fourth panel rows) between the CNV+LWC/Z (left block) or CNV+IWC/Z (right block) configurations with the near-random sampled DAP settings (S1-01 to S1-12 and S2-01 to S2-10 in Table 5.2) and the CNV+Z configuration for the precipitation accumulation thresholds 0.5, 1.0, 2.0, and 4.0 mm h^{-1} and the 2017 convective (C2017; left most columns within the two blocks), 2017 stratiform (S2017; second column within each block), and 2021 stratiform (S2021; third columns within each block) precipitation periods considered. The right most column in each block depicts the weighted median over all considered precipitation cases. The weights are determined by threshold exceedances in the RADOLAN data (see Fig. 5.3). Green colors indicate improvements in first-guesses with respect to the CNV+Z configuration, red colors deteriorations.

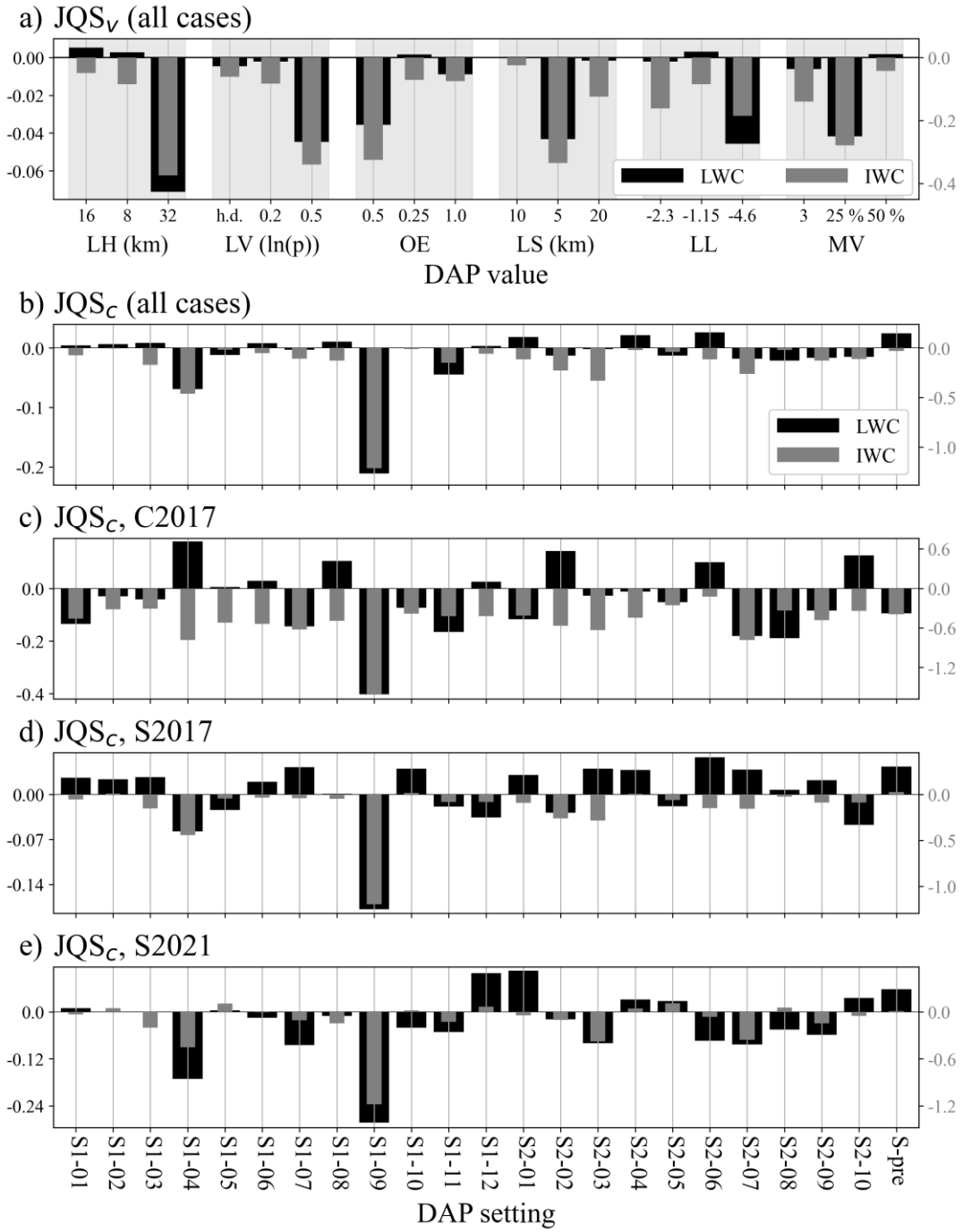

FIGURE 5.5: a) Comparison of the tested values for the DAPs LH, LV, OE, LS, LL, and MV in Table 5.1 using the univariate measure JQS_v defined in Eq. (5.10) for the LWC (black bars) and IWC (grey bars) assimilation in the CNV+LWC/Z and CNV+IWC/Z assimilation configurations with the DAP settings from the first DAP setting sample (S1-01 to S1-12 in Table 5.2). In b), all 22 sampled DAP settings (first and second samples S1-01 to S1-12 and S2-01 to S2-10 in Table 5.2) plus the pre-selected DAP setting (setting S-pre in Table 5.1) are compared with each other in terms of the univariate measure JQS_c for the LWC (black bars) and IWC (grey bars) assimilation considering all rainfall cases C2017, S2017, and S2021 together. Panels c), d), and e) are like panel b), but with the univariate measure JQS_c calculated for the individual rainfall cases C2017, S2017, and S2021, respectively.

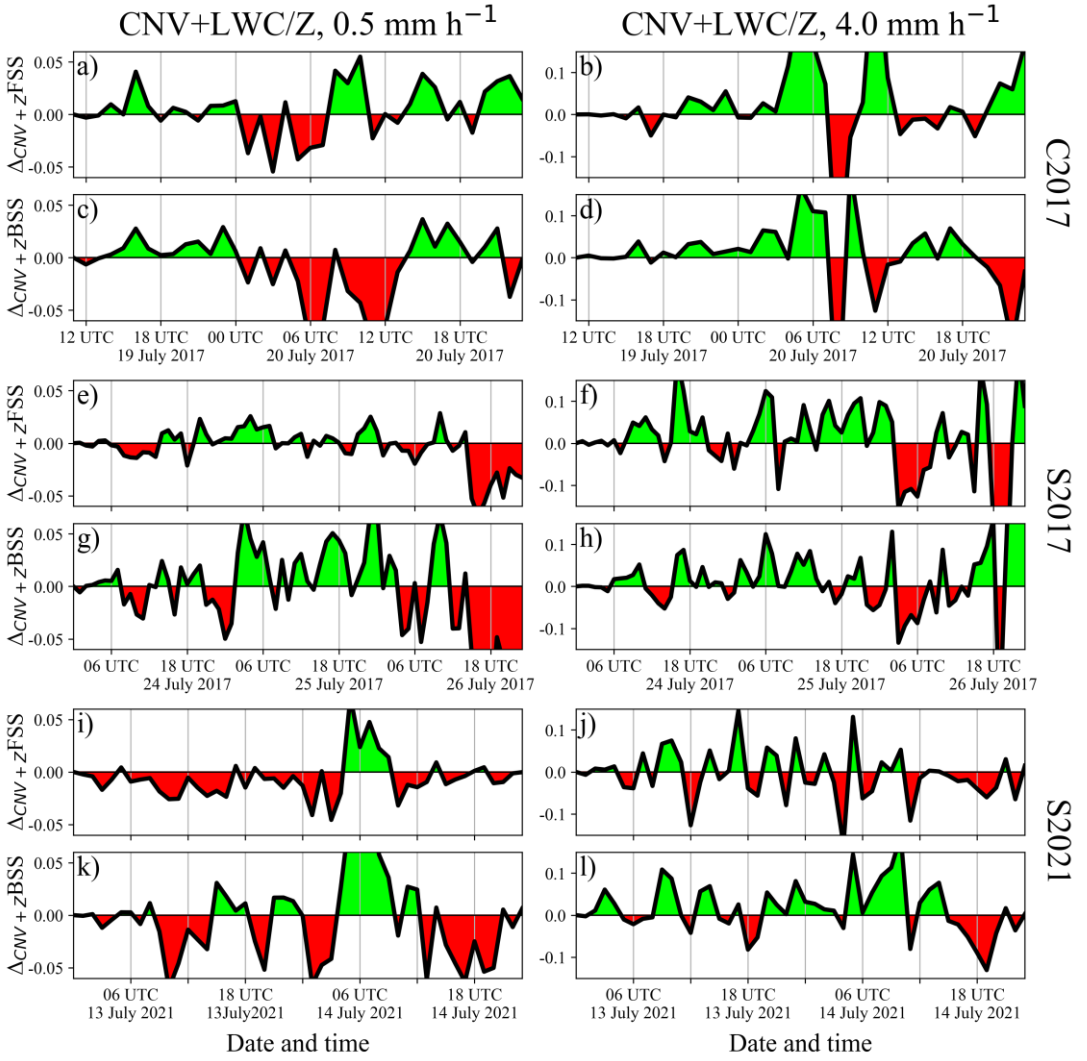

FIGURE 5.6: Time series of the difference in first-guess deterministic FSS (first rows for each case, i.e., panels a), b), e), f), i), and j)) and BSS (second rows for each case, i.e., panels c), d), g), h), k), and l)) values for precipitation accumulation thresholds of 0.5 (left column) and 4.0 mm h^{-1} (right column) between the CNV+LWC/Z and CNV+Z configurations with the found best-performing DAP settings for LWC (S2-06, see Table 5.2) for the a)-d) 2017 convective case (C2017), e)-h) 2017 stratiform case (S2017), and i)-l) 2021 stratiform case (S2021). Green shading indicate improvements using the CNV+LWC/Z configuration over the CNV+Z configuration, red colors indicate deteriorations.

LWC assimilation (Fig. 5.4e,g) and mostly limited to the stratiform S2021 case for the IWC assimilation (Fig. 5.4f3,h3). However, the new DAP sets (S2-01 through S2-10 in Table 5.2; Fig. 5.4e-h) do not perform significantly better compared to the first sample (S1-01 through S1-12 in Table 5.2; Fig. 5.4a-d) on average, except that strong negative outliers do not exist anymore.

The 22 DAP settings in Table 5.2 are compared to each other for the LWC and IWC assimilations in terms of their impact on first-guess deterministic and ensemble QPF quality by using the univariate measure JQS$_c$ defined in Eq. (5.10). Several DAP

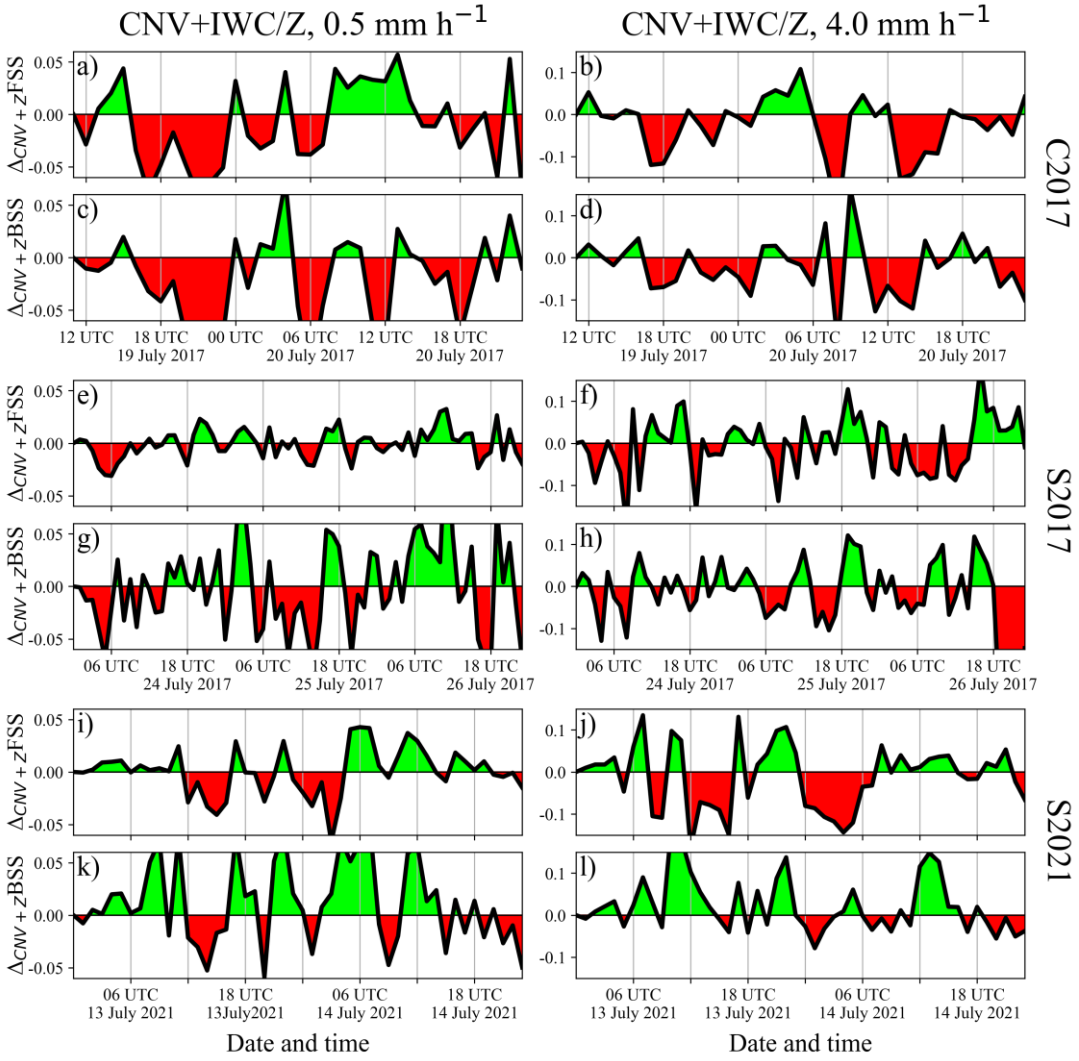

FIGURE 5.7: As Fig. 5.6, but for the IWC assimilation with the CNV+IWC/Z configuration using the corresponding found best DAP setting (S1-02, see Table 5.2).

settings (e.g., S2-01, S2-04, or S2-06) yield positive JQS$_c$ values for the LWC assimilation (black bars in Fig. 5.5b) and thus improved first-guess FSS and BSS values compared to the assimilation of Z_H data alone (CNV+Z). In contrast, for the IWC assimilation, positive JQS$_c$ values are visible for only a few DAP settings for the stratiform S2021 case (grey bars in Fig. 5.5e). Among all 22 tested settings, the setting S2-06 (LH of 8 km, LV of 0.2 ln(p), OE of 0.25, LS of 20 km, LL of -1.15, and MV of 3; see Table 5.2) results in the best JQS$_c$ value for the LWC assimilation considering all cases (black bars in Fig. 5.5b). For IWC, the DAP setting S1-02 (LH of 8 km, LV of 0.5 ln(p), OE of 0.25, LS of 10 km, LL of -1.15, and MV of 50 %; see Table 5.2) yield the best (but around zero) overall JQS$_c$ (grey bars in Fig. 5.5b). The identified best-performing DAP settings S2-06 and S1-02 are hereafter used to assimilate the LWC and IWC estimates, respectively, in this study.

The assimilation of the LWC estimates in the CNV+LWC/Z configuration with the respective best DAP set improves first-guesses for the 2017 precipitation cases

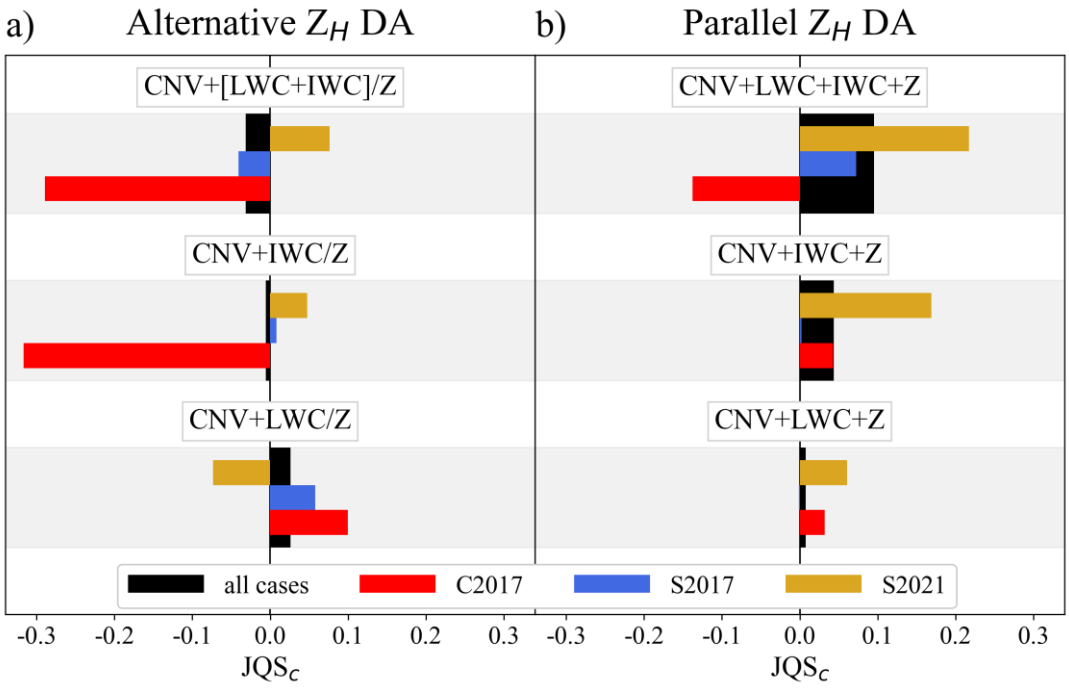

FIGURE 5.8: Comparison of different radar data set configurations in terms of the univariate measure JQS_c defined in Eq. (5.10). Configurations assimilating LWC and/or IWC with respective best DAP sets (S2-06 and S1-02 in Table 5.2) a) instead of Z_H data, where possible ("alternative Z_H DA"), in the CNV+LWC/Z, CNV+IWC/Z, and CNV+[LWC+IWC]/Z configurations (lower, middle, and upper bars), and b) together with Z_H data ("parallel Z_H DA") at the same superobbing points in the CNV+LWC+Z, CNV+IWC+Z, and CNV+LWC+IWC+Z configurations (lower, middle, and upper bars) are compared. Black bars indicate the JQS_c values calculated over all three precipitation cases considered, and red, blue, and golden bars indicate the JQS_c values for individual cases C2017, S2017, and S2021.

(Fig. 5.4e1,e2,g1,g2 and black bars in Fig. 5.5c,d) compared to the CNV+Z configuration, but mostly degrades the first-guess QPF quality for the 2021 stratiform case (Fig. 5.4e3,g3 and black bars in Fig. 5.5e). As expected, the time series of the first-guess FSS and BSS values for an accumulation threshold of 0.5 mm h^{-1} show slight, systematic improvements for the 2017 precipitation cases over the configuration assimilating Z data alone (CNV+Z) in some time periods (green colors in Fig. 5.6a,c,e,g), but more pronounced degradations for the 2021 case (red colors in Fig. 5.6i,k). Improvements can also be found for the highest investigated threshold of 4.0 mm h^{-1} for the 2017 cases (see Fig. 5.6b,d,f,h), especially for the BSS and the first about 18 first guesses of the C2017 case (Fig. 5.6d), while for the 2021 case the result is rather neutral compared to the CNV+Z configuration (see Fig. 5.6j,l). The assimilation of IWC (CNV+IWC/Z) with the best-performing DAP set yields improved first guess QPF compared to the CNV+Z configuration particularly for the stratiform S2021 case (Fig. 5.4b3,d3 and grey bars in Fig. 5.5e), but clear quality decreases for the convective C2017 case (Fig. 5.4b1,d1 and grey bars in Fig. 5.5c). Time series of first-guess FSS and BSS values at a threshold of 0.5 mm h^{-1} underscore

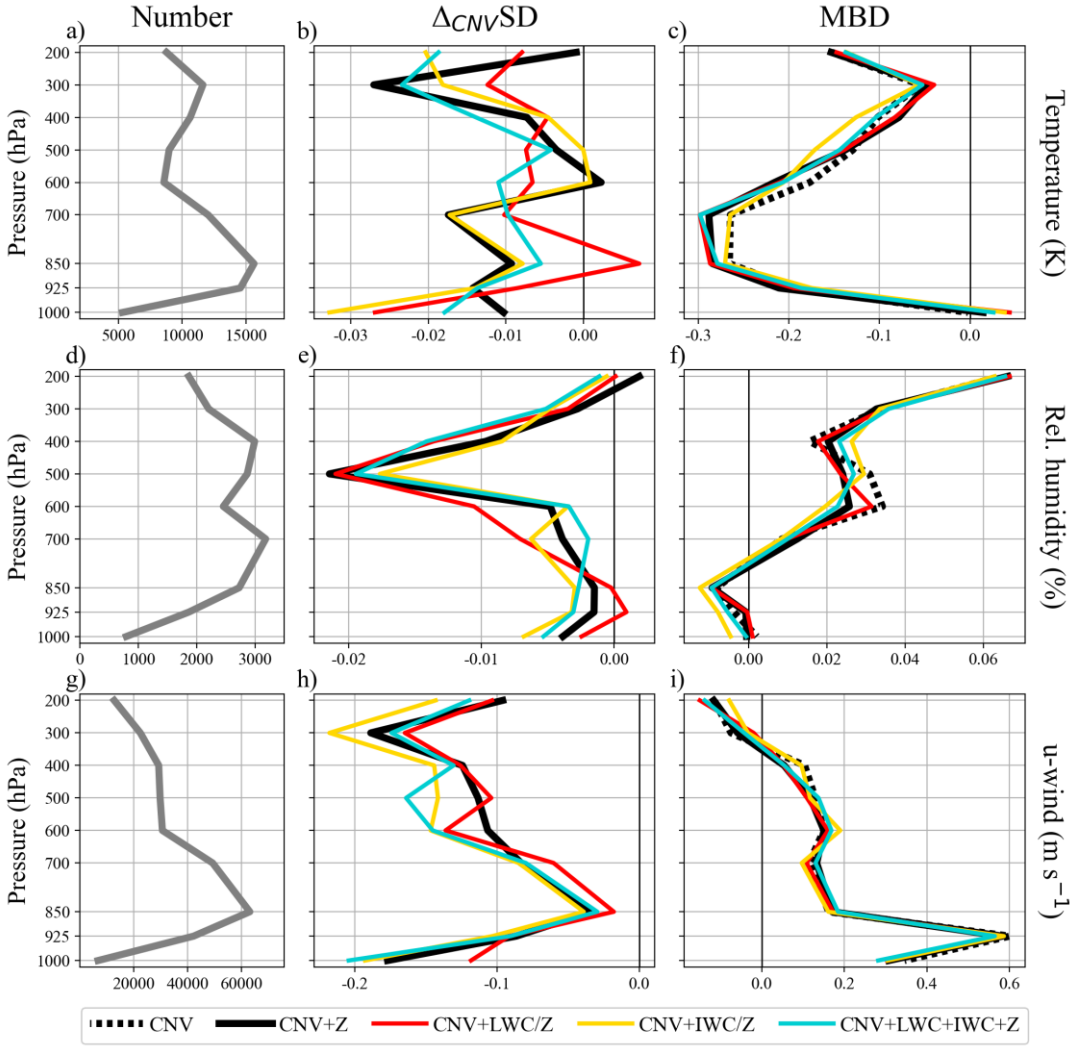

FIGURE 5.9: Vertical profiles of differences in standard deviations (SD; middle column) with respect to the CNV configuration and of mean-bias deviations (MBD; right column) of first-guess forecasts obtained from hourly assimilation cycles with the CNV (black dotted curves), CNV+Z (black solid curves), CNV+LWC/Z (red curves), CNV+IWC/Z (yellow curves), and CNV+LWC+IWC+Z (blue curves) assimilation configurations of temperature (upper row), relative humidity (middle row), and u-wind (lower row) from conventional measurements over Germany. The respective numbers of observations contributing to the SD and MBD calculations are shown in the left column (grey curves). All rainfall cases are considered together and the best-performing DAP settings for LWC and IWC (S2-06 and S1-02 in Table 5.2) are used in the LWC and/or IWC assimilating configurations.

this finding: slight, systematic improvements are evident for the 2021 case in some situations (Fig. 5.7i,k), while clear first-guess quality degradations are evident for the 2017 convective case (Fig. 5.7a,c). A very similar picture is obtained for the highest investigated threshold of 4.0 mm h^{-1} (right panel column in Fig. 5.7).

The better performance of the IWC assimilation for the 2021 stratiform case may be due to the higher radial resolution of the more recent radar data of DWD (recall that the resolution was increased from 1 to 0.25 km in spring 2021), which results in

better K_{DP} estimates, because many more consecutive radar bins are considered for the 9 km window used for the K_{DP} estimation in this thesis. The same window length for the lower-resolution data for the 2017 cases contains only one quarter of the data compared to the high-resolution 2021 case and thus may pose difficulties for proper K_{DP} estimation in certain situations. E.g., estimating K_{DP} from only nine consecutive values may favor negative K_{DP} estimates resulting in negative IWC estimates, which are set to the lower limit (LL) prior to superobbing and are thus treated as "no-precipitation". Replacing such negative K_{DP} values with zero or with the IWC(Z_H) relation proposed by Atlas et al. (1995) resulted in some improvements, but the first-guess QPF quality achieved with these two approaches was still below that of the CNV+Z configuration (not shown).

The parallel assimilation of LWC estimates and Z_H data at the same superobbing points (CNV+LWC+Z) overall results in a reduction in the JQS$_c$ compared to the alternative assimilation approach used before (CNV+LWC/Z), but is still better than the assimilation of Z_H data alone (CNV+Z; lower black bars in Fig. 5.8). In contrast, the parallel assimilation of IWC estimates with Z data (CNV+IWC+Z) leads to an improvement in the JQS$_c$ compared to the alternative assimilation strategy (CNV+IWC/Z; middle black bars in Fig. 5.8) above the CNV+Z quality. Assimilation of all radar data sets together (CNV+LWC+IWC+Z) gives the best JQS$_c$ value among the tested configurations (upper black bar in Fig. 5.8b).

The effect of assimilating the 3D microphysical LWC and IWC estimates on first-guesses of temperature, relative humidity, and u-wind speed is investigated by means of conventional observations (e.g., from commercial airplanes or radio soundings) over Germany. The assimilation of radar information (i.e., Z_H, LWC, and IWC) generally reduces respective standard deviations (SD) compared to the assimilation of conventional observations alone (differences of CNV+Z, CNV+LWC/Z, CNV+IWC/Z, and CNV+LWC+IWC+Z configurations with respect to the CNV configuration drawn as black solid, red, yellow, and blue curves in Fig. 5.9b,e,h), while the impact on the bias (MBD) is less clear overall (CNV, CNV+Z, CNV+LWC/Z, CNV+IWC/Z, and CNV+LWC+IWC+Z configurations shown as black dotted, black solid, red, yellow, and blue lines in Fig. 5.9c,f,i). The assimilation of LWC or/and IWC estimates in the CNV+LWC/Z, CNV+IWC/Z, and CNV+LWC+IWC+Z configurations show SD and MBD values similar to the assimilation of Z_H data alone (CNV+Z), but slightly, systematically improved SD values in the u-wind speed with the assimilation of IWC estimates as alternatives to Z_H data (CNV+IWC/Z; compare yellow with black curve in Fig. 5.9h) are evident.

5.3.2 Experiment Part B: Nine-Hour Forecasts

From the analyses produced in hourly assimilation cycles with the different assimilation configurations tested (with the best-performing DAP settings used for the LWC and IWC assimilations), nine-hour forecasts with the ICON-D2 model are produced. Assimilating Z_H observations (CNV+Z) clearly improves the deterministic

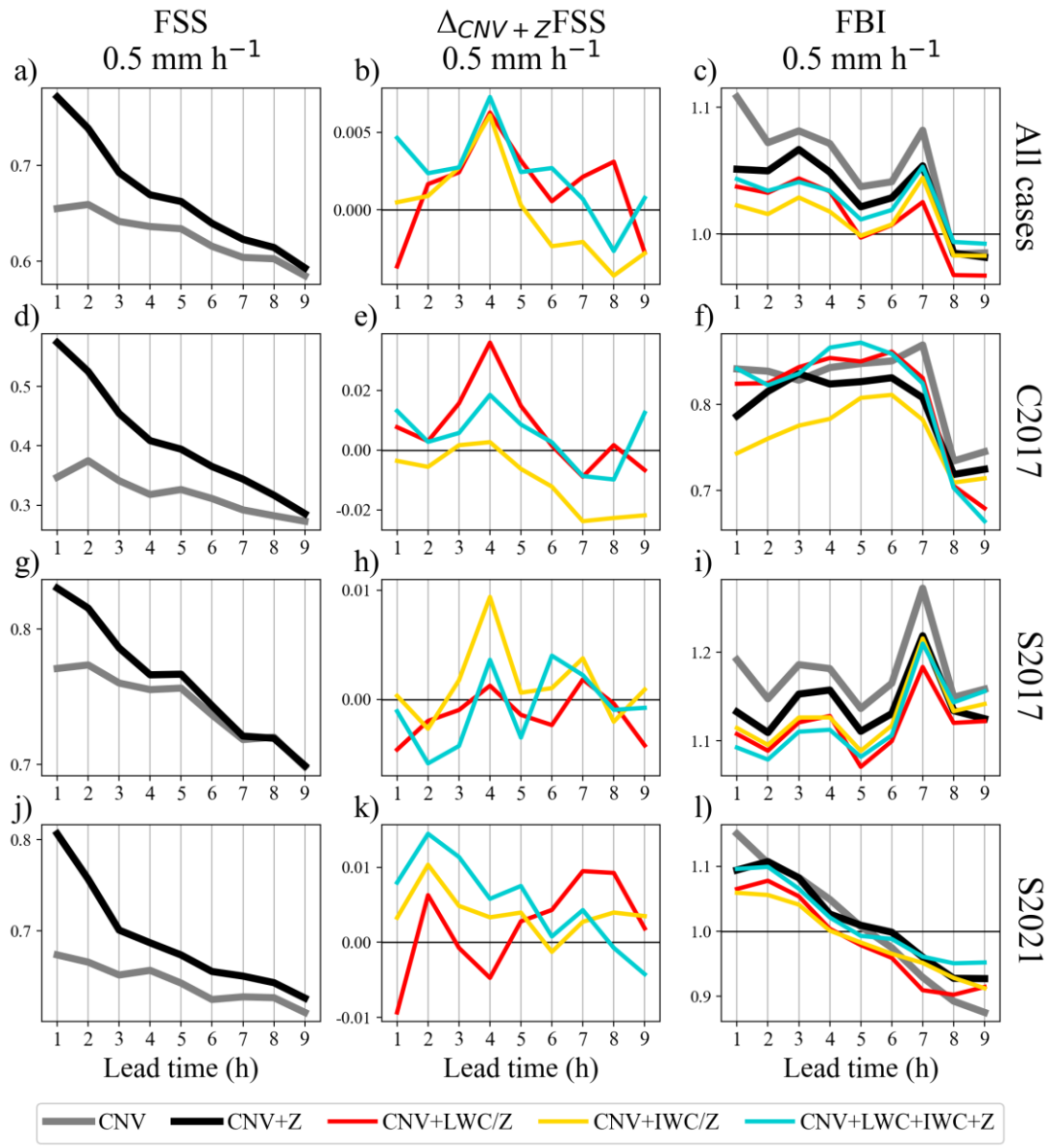

FIGURE 5.10: Left panel column: time series of the deterministic FSS for a 0.5 mm h^{-1} threshold of nine-hour forecasts initiated every third hour from hourly assimilation cycles with the CNV and CNV+Z configurations (grey and black curves) as means over all precipitation cases considered (upper row), over the 2017 convective case C2017 only (second row), over the 2017 stratiform case S2017 only (third row), and over the 2021 stratiform case S2021 only (lower row). Middle column: corresponding deviations in mean deterministic FSS from the CNV+Z configuration of the CNV+LWC/Z (red curves), CNV+IWC/Z (yellow curves), and CNV+LWC+IWC+Z (blue curves) configurations using the best-performing DAP settings found for LWC and IWC (S2-06 and S1-01 in Table 5.2). Right column: corresponding mean deterministic FBI values.

FSS for a threshold of 0.5 mm h^{-1} for all forecast hours compared to the assimilation of no radar information (CNV) on average over all cases and over each individual case (compare black with grey curves in Fig. 5.10a,d,g,j). The same qualitative result is obtained with the deterministic FBI on mean over all cases (black curve closer to

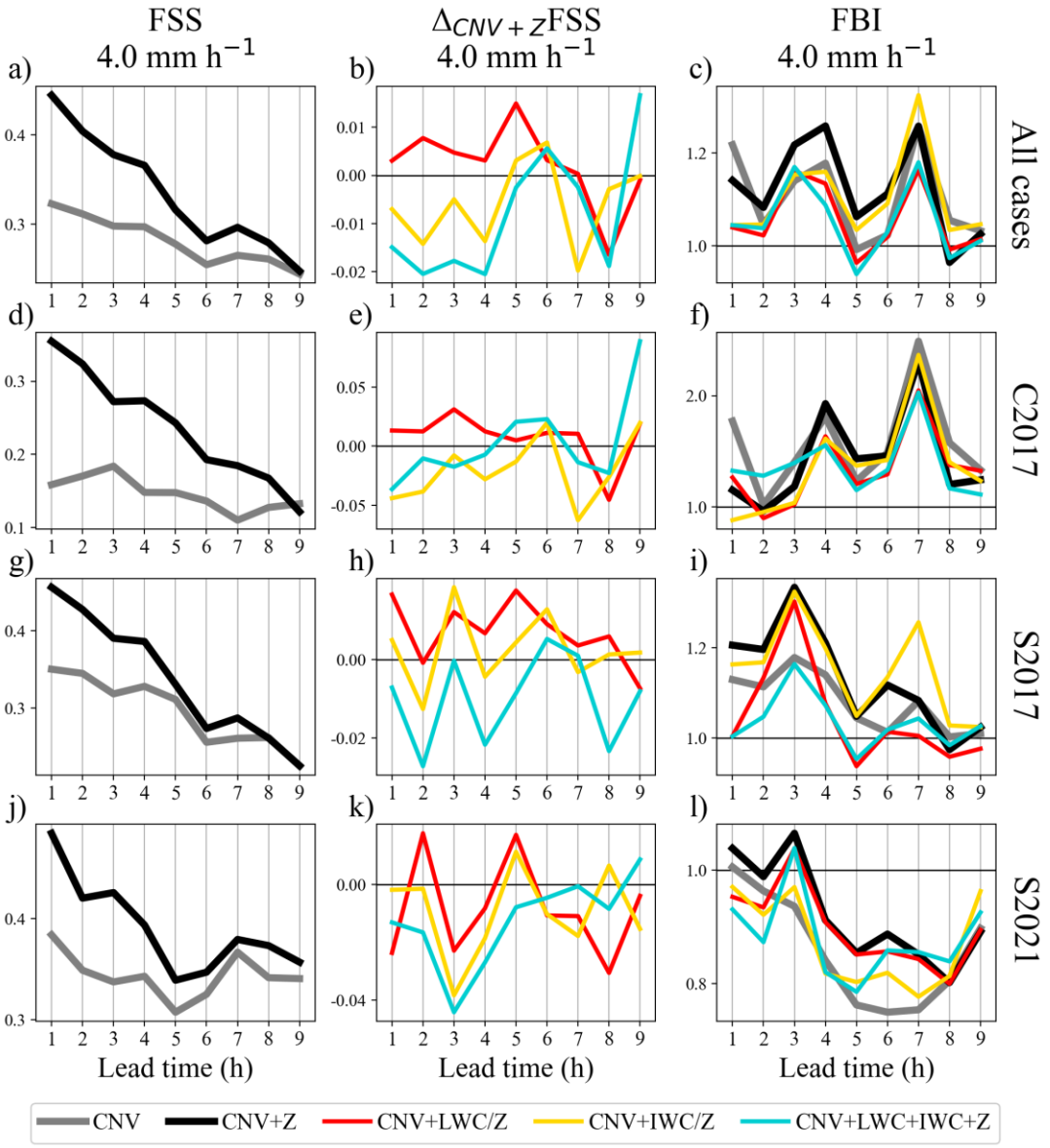

FIGURE 5.11: As Fig. 5.10, but for an accumulation threshold of 4.0 mm h^{-1}.

the zero line than the grey curve in Fig. 5.10c) and for the stratiform S2017 and S2021 cases (Fig. 5.10i,l), while for the convective C2017 case the underforecasting is enhanced by the Z_H assimilation compared to CNV (compare black with grey curve in Fig. 5.10f). For the highest threshold of 4.0 mm h^{-1}, similar results for FSS are obtained (compare black with grey curves in Fig. 5.11a,d,g,j), while overforecasting quantified by FBI is enhanced by the Z_H assimilation on average (Fig. 5.11c).

Assimilating LWC estimates instead of Z_H data where possible (CNV+LWC/Z) further improves the FSS on average slightly over all cases for most of the forecast time (red curve mostly above zero line in Fig. 5.10b). This improvement arises from improvements over the CNV+Z configuration for the first 6 h of the convective C2017 case (red curve in Fig. 5.10e) and the forecast hours five to nine of the 2021 stratiform case (Fig. 5.10k). FBI improvements over the CNV+Z configuration are

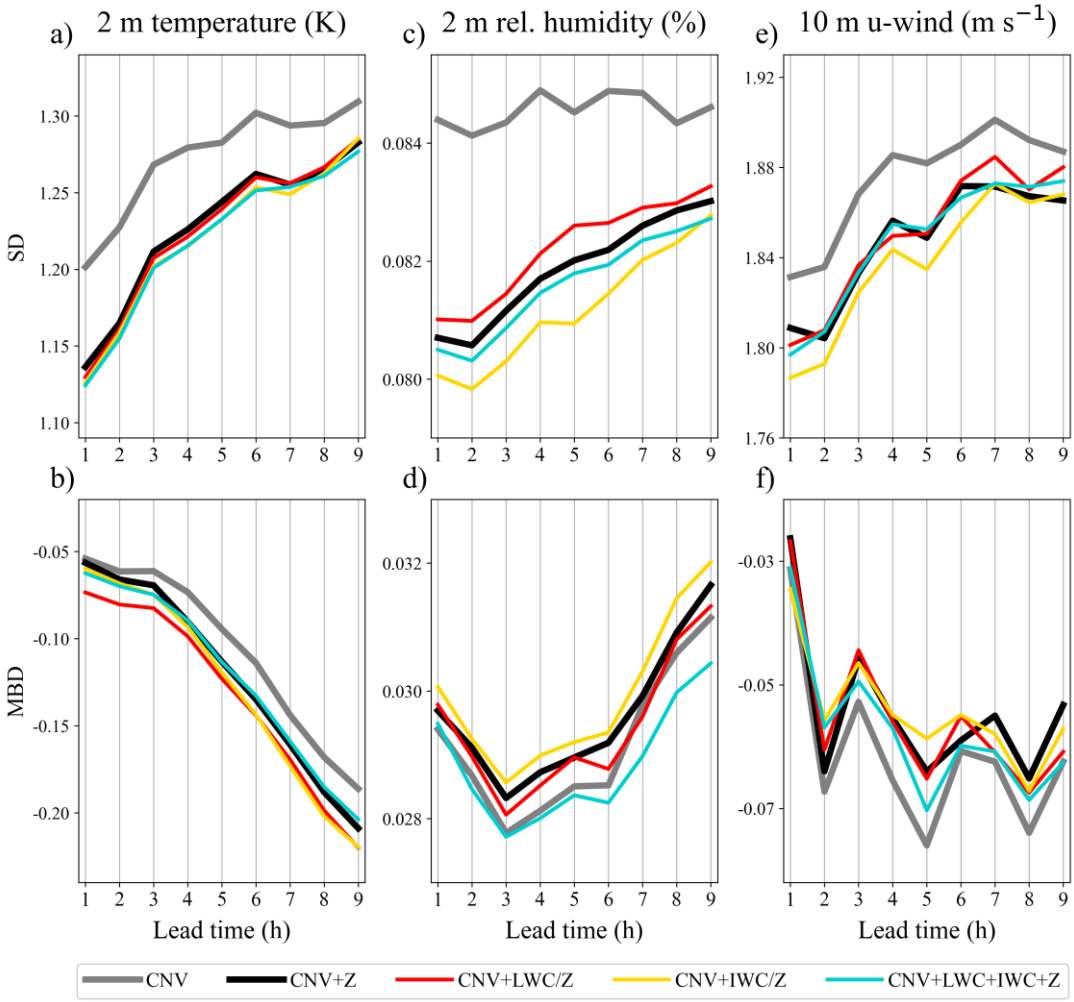

FIGURE 5.12: Mean standard deviations (SD; upper panel row) and mean bias deviations (MBD; lower panel row) of model forecasted 2 m temperature (left panel column), 2 m relative humidity (middle panel column), and 10 m u-wind (right panel column) from conventional near-surface observations in Germany as functions of forecast lead time. Means are calculated over nine-hour forecasts initiated every third hour from hourly assimilation cycles with assimilation configurations CNV (grey curves), CNV+Z (black curves), CNV+LWC/Z (red curves), CNV+IWC/Z (yellow curves), and CNV+LWC+IWC+Z (blue curves), using the best DAP settings for LWC and IWC (S2-06 and S1-02 in Table 5.2), and taking all precipitation cases C2017, S2017, and S2021 into account.

also achieved due to the LWC assimilation for up to seven hours lead time on average over all cases (compare red with black curve in Fig. 5.10c) and at least for the first four forecast hours for the individual cases (Fig. 5.10f,i,l). Similarly, the CNV+LWC/Z configuration slightly improves the FSS for the highest investigated threshold of 4.0 mm h^{-1} for the first 7 h lead time on mean over all cases as well (red curve in Fig. 5.11b). In contrast to the assimilation of Z_H data alone (CNV+Z), the assimilation of LWC instead of Z_H where possible (CNV+LWC/Z) improves the FBI compared to the assimilation of no radar information (CNV) on mean over all cases for the 4.0 mm h^{-1} threshold (compare red, black, and grey curves in Fig. 5.11c). Note

that the much smaller data set the investigation for the 4.0 mm h^{-1} threshold is based on makes the respective results more prone to sampling errors and thus less reliable compared to the respective results of 0.5 mm h^{-1} threshold evaluation (compare golden with black curve in Fig. 5.3).

Assimilation of IWC estimates as alternatives to Z_H, where possible (CNV+IWC/Z), also slightly improves the FSS for a threshold of 0.5 mm h^{-1} on average over all cases for the first five forecast hours (yellow curve in Fig. 5.10b). As expected from the first-guess analysis, the mean FSS for the 2017 convective case is degraded for most forecast hours compared to the CNV+Z configuration (yellow curve below zero line in Fig. 5.10e), and the stratiform cases, especially the 2021 case, show improvements (yellow curves in Fig. 5.10h,k). The FBI is improved on mean over all cases for the first 7 h lead time and is best among all tested configurations for the first 5 h (compare yellow with remaining lines in Fig. 5.10c). As for FSS, the mean FBI deteriorates compared to the CNV+Z configuration for the convective 2017 case, while improvements are achieved for the stratiform cases (Fig. 5.10i,l). However, mean FSS is below the assimilation of Z_H data alone (CNV+Z) for the highest 4.0 mm h^{-1} threshold considered (yellow curve in Fig. 5.11b), where improvements are still visible for the mean FBI (Fig. 5.11c).

The on average best-performing FSS for the low 0.5 mm h^{-1} threshold for the first 6 h lead time is obtained when all radar data sets are assimilated together (CNV+LWC+IWC+Z; blue curve in Fig. 5.10b). However, the good FBI results of the CNV+IWC/Z configuration are not achieved, but the FBI is still improved with respect to the CNV+Z configuration for the first six forecast hours (compare blue, yellow, and black curves in Fig. 5.10c). For the highest 4.0 mm h^{-1} threshold, the CNV+LWC+IWC+Z configuration yields the worst FSS on average for the first 5 h lead time (blue curve in Fig. 5.11b), while the average FBI values are still improved compared to CNV+Z (compared blue and black curves in Fig. 5.11c).

As expected, the SDs of 2 m temperature, 2 m relative humidity, and 10 m u-wind generally increase as functions of the forecast lead time in all DA configurations (CNV, CNV+Z, CNV+LWC/Z, CNV+IWC/Z, and CNV+LWC+IWC+Z drawn as grey, black, red, yellow, and blue curves in Fig. 5.12a,c,e). The assimilation of radar observations always reduces the SDs compared to the assimilation of conventional measurements only (CNV; compare grey with the other curves in Fig. 5.12a,c,e). The assimilation of IWC estimates instead of Z_H data, where possible (CNV+IWC/Z), yields the best SDs for the near-surface relative humidity and u-wind (yellow curves in Fig. 5.12a,c) among all tested configurations and is only marginally outperformed by the assimilation of all radar data sets together (CNV+LWC+IWC+Z) for the 2 m temperature (compare blue with yellow curve in Fig. 5.12a). Assimilation of radar data generally only reduces MBDs for the 10 m u-wind compared to the configuration without radar DA (CNV; compare grey with other curves in Fig. 5.12b,d,f), except for the CNV+LWC+IWC+Z configuration, which yields the lowest bias for the 2 m relative humidity among all tested DA configurations (blue curve in Fig. 5.12d).

5.4 Summary and Conclusions

In this chapter, polarimetric observations from the German C-band radar network were assimilated in Germany in DWD's convective-scale KENDA-ICON-D2 system for the first time. The polarimetric information was assimilated indirectly using microphysical retrievals of LWC and IWC below and above the melting layer, respectively, and their impact on short-term QPF was evaluated. The LWC estimator used was the one developed in Chapter 3 of this thesis, while for the IWC estimation a state-of-the-art hybrid estimator proposed in the literature was used. In a first part, the impact of the microphysical retrieval assimilation on first-guess (hourly) QPF was investigated with different data assimilation parameter (DAP) settings and radar data set configurations. Then, nine-hour forecasts initiated from hourly assimilation cycles with the most successful assimilation settings were evaluated.

Four data set configurations were considered to identify the best-performing DAP settings for LWC and IWC: only conventional observations (CNV), conventional plus 3D Z_H observations (CNV+Z), conventional observations plus LWC estimates replacing Z_H observations, where available (CNV+LWC/Z), and conventional data plus IWC estimates replacing Z_H data, where possible (CNV+IWC/Z). For the two intense stratiform precipitation cases in the summers of 2017 and 2021 and the intense convective case in the summer of 2017 considered, a rather small horizontal observation localization length-scale of 8 km and a lower limit of -1.15 in log(LWC) and log(IWC) yielded the best first-guess. This suggests that first-guess QPF benefits from a rather small influence of the microphysical estimates on the model state, most likely due to discrepancies between the model and true microphysics. Moreover, a relatively small observation error standard deviation of 0.25 in log(LWC) and log(IWC) yielded the best first-guess results. The best values for the remaining DAPs considered differed for LWC and IWC: the vertical localization length-scales were 0.2 in logarithm of pressure for LWC and 0.5 in logarithm of pressure for IWC; the best superobbing window sizes were 20 km for LWC and 10 km for IWC; the minimum required number of valid values in the superobbing window for superobbing were three observations for LWC and 50 % valid observations of the full number of radar pixels in the superobbing window required for IWC.

The assimilation of the LWC estimates (CNV+LWC/Z) with the respective best-performing DAP setting improved the first-guess for most precipitation cases and accumulation thresholds compared to the assimilation of Z_H data alone (CNV+Z). In contrast, the best DAP set for IWC mostly degraded the first guess, especially for the 2017 convective case, except for the 2021 stratiform period, which showed improvements over the CNV+Z configuration. The latter may be due to the much higher radial resolution of the more recent data after the volume scan resolution was increased at DWD from 1 to 0.25 km in spring 2021. The higher resolution improves the K_{DP} estimation because for a given estimation window four times more radar bins contribute to the K_{DP} estimate compared to the 2017 data, which leads to more stable K_{DP} estimates and less noise. The same effect might be less visible for LWC because

the hybrid LWC retrieval uses K_{DP} only for high-intensity precipitation (Z_H > 45 dBZ; see Chapter 3). One reason for the poor performance of the IWC assimilation especially for the 2017 convective case, besides possible inadequacies in the model's ice module, may be the fact that the IWC retrieval is based on assumptions valid for snowfall, but not for hail or graupel, like the assumed inversely proportional relationship assumed between the density and size of hydrometeors. However, hail and/or graupel likely is present in intense summer convective precipitation in Germany, which may be at least in part a reason for the worse performance of the IWC assimilation for convective precipitation. Interestingly, the LWC assimilation for the same case led to clearly improved first-guess results, despite the fact that the LWC retrieval was not adapted to hail and/or graupel as well (see Chapter 3). The utilization of a higher ρ_{HV} threshold below the melting layer for filtering of the radar data potentially also masked out radar bins contaminated by hail and/or graupel, which thus may serve as an explanation for the better results achieved.

Overall, the best first-guess QPF was yielded when all radar data sets considered (i.e., Z_H, LWC, and IWC) were assimilated together (CNV+LWC+IWC+Z).

Deterministic nine-hour QPF initiated with radar observations (i.e., CNV+Z, CNV+LWC/Z, CNV+IWC/Z, or CNV+LWC+IWC+Z, with LWC and IWC assimilated with the respective best DAP sets) in general clearly outperformed those forecasts initiated with conventional data only (CNV) in terms of Fraction Skill Score (FSS) and Frequency Bias (FBI). Forecasts initiated from the assimilation of LWC estimates (CNV+LWC/Z) using the respective best-performing DAP setting slightly outperformed the ones produced with the assimilation of Z_H data alone (CNV+Z) in terms of deterministic FSS on average over all cases and for most forecast lead times; best results were obtained for the 2017 convective case overall. The same applies to the assimilation of IWC (CNV+IWC/Z) with the respective best DAP set, however, the mean FSS mostly deteriorated for the 2017 convective case compared to the CNV+Z configuration, but was slightly, systematically improved for the high-resolution 2021 stratiform case for a 0.5 mm h^{-1} threshold. Forecasts initiated with the assimilation of all radar data sets considered together (CNV+LWC+IWC+Z) gave the best FSS for a 0.5 mm h^{-1} threshold on average for the first 6 h lead time. Finally, the assimilation of LWC and/or IWC in general mostly improved the average FBI over all cases compared to the assimilation of Z_H data alone (CNV+Z).

Chapter 6

Conclusions and Outlook

Accurate quantitative precipitation forecasts (QPF) by numerical weather prediction (NWP) models are and remain of high societal interest, especially in times of global warming, which leads to increasing frequency and intensity of heavy precipitation events across the earth (IPCC, 2021). The assimilation of horizontal radar reflectivity Z_H and radar radial wind observations in convective-scale NWP systems has been shown to be highly beneficial for improving QPF (e.g., Bick et al., 2016). Polarimetric radar observations contain additional independent information on cloud-precipitation microphysics compared to Z_H alone and thus have the potential to further improve QPF through data assimilation. However, the assimilation of polarimetric measurements in NWP models is still in its infancy.

This study made a first step in assimilating polarimetric information from the German national C-band weather radar network into the operational convective-scale NWP system of the German meteorological service (DWD, Deutscher Wetterdienst). The system uses the ICON-D2 model, a limited-area setup of the Icosahedral Nonhydrostatic (ICON; Zängl et al., 2015) model over Germany, and the KENDA (Kilometre-scale Ensemble Data Assimilation; Schraff et al., 2016) data assimilation system, which includes the LETKF (Local Ensemble Transform Kalman Filter; Hunt et al., 2007) scheme. Polarimetry-based microphysical retrievals of liquid and ice water content (LWC and IWC) below and above the melting layer, respectively, were assimilated and the impact on short-term QPF compared to the assimilation of Z_H observations alone was evaluated. To this goal, a new polarimetric LWC estimator was developed for C-band. Here, the central research questions formulated in Chapter 1 are revisited in view of the findings presented in the former chapters.

Q1: What is the best-performing polarimetric LWC retrieval for application to the German C-band radar network?

Based on a large German pure-rain disdrometer data set and T-matrix scattering calculations at C-band, a set of LWC retrievals based on reflectivity Z_H, the combination of Z_H and differential reflectivity Z_{DR}, specific horizontal attenuation A_H, and specific differential phase K_{DP} was developed. For the LWC(Z_H), LWC(Z_H, Z_{DR}), LWC(A_H), and LWC(K_{DP}) estimators, a quadratic, a bivariate linear, a quadratic, and a linear relation (on the logarithmic scale), respectively, yielded the best results and outperformed existing retrievals from the scientific literature, when

applied to simulated radar observations. Their application to four stratiform and five convective summer precipitation events monitored with the German C-band radar network yielded overall satisfactory results in terms of low biases. However, the new polarimetric LWC(Z_H, Z_{DR}) and LWC(A_H) retrievals resulted in less pronounced improvements compared to the new LWC(Z_H) estimator than expected from the simulations. In addition, the new LWC(K_{DP}) estimator resulted in an even worse performance. In general, improvements achieved above existing LWC estimators were also smaller than expected from the simulations. This may partly be attributed to errors introduced by the comparison of in-situ with remotely sensed observations, and partly to additional uncertainties arising from low signal-to-noise ratios of the radar data, especially of the total differential phase in weak precipitation, spatial degradation of K_{DP}, and radar calibration problems.

A hybrid LWC estimator was used for the assimilation of polarimetric information below the melting layer. In weak rain (total differential phase shift < 5 deg) the new LWC(Z_H, Z_{DR}) retrieval is used because phase-based variables (A_H and K_{DP}) may suffer from low signal-to-noise ratios while the impact of (differential) attenuation on Z_H and Z_{DR} is small. In stronger rain (total phase shift > 5 deg), where estimates of A_H and K_{DP} are more reliable, the new LWC(A_H) retrieval is applied where Z_H < 45 dBZ, and the new LWC(K_{DP}) retrieval is used elsewhere. This hybrid LWC retrieval resulted in low biases and gave better correlations than all non-hybrid estimators, when applied to C-band observations over Germany.

Q2: Does the assimilation of polarimetric microphysical retrievals into the KENDA-ICON-D2 system of DWD improve short-term QPF compared to the assimilation of Z_H observations alone?

Polarimetric LWC and IWC retrievals from the German national C-band radar network were assimilated in the KENDA-ICON-D2 system. The hybrid LWC estimator (see above and published in Reimann et al., 2021) was used for polarimetric information below the melting layer and the hybrid IWC estimator proposed by Carlin et al. (2021) and evaluated with in-situ observations by Blanke et al. (2023) for observations above the melting layer. The results of the assimilation were analyzed for two stratiform precipitation cases in the summers of 2017 and 2021 and one convective precipitation case in the summer of 2017.

The first-guess (hourly) QPF quality was used to identify optimal data assimilation settings (e.g., observation localization length scales and errors) for LWC and IWC. With the optimal settings, the LWC assimilation mostly improved first-guess QPF quality compared to the assimilation of Z_H data alone while the IWC assimilation mostly degraded the first-guess except for the 2021 stratiform case. The latter most probably profited from an increase in radial resolution of the observations from 1 to 0.25 km and thus better K_{DP} estimates. Since the IWC retrieval was developed based on assumptions valid for snowfall but not for graupel and/or hail, such as the inversely

proportional relationship assumed between hydrometeor density and size, the potential presence of graupel and/or hail in convection likely in intense convective summertime precipitation in Germany may at least be partly responsible for the especially bad performance for the 2017 convective case. The best first-guess QPF quality was obtained when Z_H, LWC, and IWC were assimilated together.

Based on the analyses produced with the optimal data assimilation settings, nine-hour forecast runs were performed and evaluated. The LWC assimilation slightly improved the deterministic Fraction Skill Score (FSS) values compared to the assimilation of Z_H alone for most forecast hours with best results for the 2017 convective case. Systematic improvements were also found for the mean deterministic Frequency Bias (FBI). The IWC assimilation slightly improved the mean FSS values only in the first five forecast hours over the assimilation of Z_H observations alone. As expected from the first-guess evaluation, best results were obtained for the 2021 stratiform case, but clear FSS degradations were found for the 2017 convective case. The FBI improved on average, but was degraded for convective precipitation as well. The best FSS values on average for the first six forecast hours were obtained when Z_H, LWC, and IWC were assimilated together. Overall, the assimilation of polarimetric microphysical retrievals from the German C-band radar network in the KENDA-ICON-D2 system at DWD could slightly improve short-term QPF compared to the assimilation of Z_H observations alone. The IWC assimilation alone was only successful in stratiform precipitation when the radar data have a high radial resolution but degraded QPF quality for convective precipitation.

The assimilation experiment conducted in this thesis (and submitted for publication, Reimann et al., 2023) was based on the operational standard configuration of KENDA, which produces analysis increments only for the microphysical variables cloud water mixing ratio and specific humidity in the LETKF analysis step besides for temperature, pressure, and horizontal wind. The other hydrometeor species in the single-moment microphysical scheme are not simultaneously updated due to assimilation impact considerations made for the Z_H assimilation at DWD. Thus, they are only indirectly updated via analysis increments in the other updated model variables in the ensuing model forecast. The choice of simultaneously updated microphysical variables can, however, impact the microphysical state of the model; thus, additional investigations should be performed for final conclusions (personal communication Klaus Stephan, DWD). E.g., it should be explored if QPF improves when LWC estimates also update (via cross-correlations in the first-guess ensemble) rain mixing ratios in the analysis step, or when IWC estimates also update ice species such as cloud ice and snow mixing ratios.

This research is a first step towards an operational assimilation of polarimetric radar observations in Germany in the future. The results suggest that the radial resolution of the polarimetric C-band radar data plays an important role especially for the IWC estimation and its subsequent assimilation via better K_{DP} estimates. Since the present analysis is based to a major extent on data with only 1 km radial

resolution, the optimal data assimilation settings and configurations should also be revised with high-resolution data prior to a potential operationalization. The study did also not investigate the sensitivity of the nine-hour QPF quality to modifications in the data assimilation settings due to limited data storage and computing time, which may be worthwhile, because first-guess quality does not automatically translate to similar improvements in QPF with longer lead times.

This thesis gave first insights into the benefits of assimilating state-of-the-art 3D polarimetric microphysical LWC and IWC retrievals into a convective-scale Ensemble-Kalman-Filter-based NWP system in Germany. It demonstrated that the assimilation of the IWC retrievals above the melting layer posed problems particularly for convective precipitation, potentially due to the presence of hail and/or graupel in these situations. Accordingly, the development of more appropriate IWC retrieval algorithms for convective precipitation cores represents one of the next steps to further improve the exploitation of polarimetric ice microphysical retrievals for radar data assimilation in Germany in the future. Besides estimators of LWC and IWC, the assimilation of other polarimetric microphysical retrievals such as retrievals of the mean-volume diameter or the total number concentration of particles per unit volume remains to be explored. However, a double moment microphysical scheme, which simulates particle number concentrations besides hydrometeor mixing ratios, would be necessary for these experiments. To what extent such higher moment schemes would favor the assimilation of the polarimetric information contained in the microphysical LWC and IWC estimates remains to be investigated as well, because double moment schemes are more able to reproduce polarimetric signatures than single moment schemes (e.g., Jung et al., 2010a).

The direct assimilation of polarimetric radar observations using the polarimetric version of the EMVORADO (Efficient Modular Volume-scanning Radar Forward Operator; Zeng et al., 2016) radar simulator implemented in the KENDA data assimilation system remains another target of future research in radar data assimilation in Germany. However, the reproduction of realistic polarimetric moments above the melting layer with the EMVORADO simulator for data assimilation is challenging due to the T-matrix scattering method being largely inappropriate in the ice phase (e.g., Shrestha et al., 2022). Currently, steps are undertaken to solve this problem by coupling scattering data bases to the EMVORADO radar simulator within the research project PROM (Polarimetric Radar Observations meet Atmospheric Modelling) funded by DFG (Deutsche Forschungsgemeinschaft). Besides the ongoing refinement of the polarimetric EMVORADO forward operator for the ice phase, near-future research may explore, as a first step, the direct assimilation of polarimetric radar moments in the liquid phase below the melting layer, for which the T-matrix method is more appropriate than for applications above the melting layer.

List of Names and Abbreviations

3DVar	**3D Var**iational DA scheme
4DVar	**4D Var**iational DA scheme
ACI	**A**dditive **C**ovariance **I**nflation
ADAS	**A**RPS' **D**ata **A**ssimilation **S**ystem
AR6 IPCC	Sixth **A**ssessment **R**eport of the **I**ntergovernmental **P**anel on **C**limate **C**hange
ARPS	**A**dvanced **R**egional **P**rediction **S**ystem
ASB	DWD radar on Borkum
BOO	DWD radar in **BOO**stedt
C2017	**C**onvective precipitation DA case from 19 to 20 July **2017**
CNV	Assimilation of **C**o**NV**entional data only
CNV+IWC+Z	Like **CNV plus** 3D **IWC** estimates **plus** 3D $\boldsymbol{Z_H}$ data
CNV+IWC/Z	Like **CNV plus** 3D **IWC** estimates **instead** of $\boldsymbol{Z_H}$ data where possible
CNV+LWC+IWC+Z	Like **CNV plus** 3D **LWC** estimates **plus** 3D **IWC** estimates **plus** 3D $\boldsymbol{Z_H}$ data
CNV+LWC+Z	Like **CNV plus** 3D **LWC** estimates **plus** 3D $\boldsymbol{Z_H}$ data
CNV+LWC/Z	Like **CNV plus** 3D **LWC** estimates **instead** of $\boldsymbol{Z_H}$ data where possible
CNV+Z	Like **CNV plus** 3D $\boldsymbol{Z}$ data
CNV+[LWC+IWC]/Z	Like **CNV plus** 3D **LWC** and **IWC** estimates **instead** of $\boldsymbol{Z_H}$ data where possible
COMET	***C**entro **O**perativo per la **MET**eorologia* (Italian operational center for meteorology)
COSMO	**CO**nsortium for **S**mall-scale **MO**deling model
COSMO-DE/2I	Limited-area convection-allowing version of the COSMO model over Germany/Italy
CRPP	**C**ovariance **R**elaxation to **P**rior **P**erturbations
CRPS	**C**ovariance **R**elaxation to **P**rior **S**pread
DA	**D**ata **A**ssimilation
DAP	**D**ata **A**ssimilation **P**arameter
DFG	***D**eutsche **F**orschungs**G**emeinschaft* (German research community)
DRS	DWD radar in **DR**e**S**den
DSD	**D**rop **S**ize **D**istribution
DWD	***D**eutscher **W**etter**D**ienst* (German national meteorological service)

EAKF	Ensemble adjustment Kalman filter
ECMWF	**E**uropean **C**entre for **M**edium-Range **W**eather **F**orecasts
EIS	DWD radar on **EIS**berg
EKF	**E**xtended **K**alman **F**ilter
EMD	DWD radar in **EMD**en
EMVORADO	**E**fficient **M**odular **VO**lume scanning **RAD**ar forward **O**perator
EnKF	**En**semble **K**alman **F**ilter
EnSRF	**En**semble **S**quare-**R**oot **F**ilter
EnVar	Hybrid **En**semble-**Var**iational DA scheme
ESS	DWD radar in **ESS**en
ETKF	**E**nsemble **T**ransform **K**alman **F**ilter
FBG	DWD radar on **F**eld**B**er**G**
FLD	DWD radar in **FL**echt**D**orf
GSI	**G**ridpoint **S**tatistical **I**nterpolation
HNR	DWD radar in **H**a**N**nove**R**
ICON	**ICO**sahedral **N**onhydrostatic model
ICON-D2	Limited-area setup of the ICON model over Germany
ICON-EU	Nesting setup of the ICON model over Europe
ISN	DWD radar in **IS**e**N**
JMA	**J**apan **M**eteorological **A**gency
KENDA	**K**ilometre-scale **EN**semble **D**ata **A**ssimilation
KF	**K**alman **F**ilter
LAPS	**L**ocal **A**nalysis and **P**rediction **S**ystem
LEKF	**L**ocal **E**nsemble **K**alman **F**ilter
LETKF	**L**ocal **E**nsemble **T**ransform **K**alman **F**ilter
LHN	**L**atent **H**eat **N**udging
LHS	**L**atin **H**ypercube **S**ampling
MCI	**M**ultiplicative **C**ovariance **I**nflation
MEM	DWD radar in **MEM**mingen
MM5	Fifth-Generation Pennsylvania State University–National Center for Atmospheric Research **M**esoscale **M**odel
NEU	DWD radar in **NEU**haus
NHB	DWD radar in **N**eu**H**eilen**B**ach
NMC-method	**N**ational **M**eteorological **C**enter method to derive the background error covariance matrix statistically
NWP	**N**umerical **W**eather **P**rediction
OFT	DWD radar in **OF**fen**T**hal
OSSE	**O**bserving **S**ystem **S**imulation **E**xperiment
PPI	**P**lan **P**osition **I**ndicator
PRO	DWD radar in **PRO**etzel

QPE	**Q**uantitative **P**recipitation **E**stimation
QPF	**Q**uantitative **P**recipitation **F**orecast
QVP	**Q**uasi **V**ertical **P**rofile
RADOLAN	**RAD**ar **O**n**L**ine **AN**eichung (DWD's QPE product)
RealPEP	Near-**Real**time Quantitative **P**recipitation **E**stimation and **P**rediction (name of DFG-funded project)
ROS	DWD radar in **ROS**tock
S2017	**S**tratiform precipitation DA case from 24 to 26 July **2017**
S2021	**S**tratiform precipitation DA case from 13 to 14 July **2021**
SCM	**S**uccessive **C**orrections **M**ethod
SHV-mode	Scan mode of **S**imultaneous transmission/reception in **H**orizontal and **V**ertical polarization channels
TUR	DWD radar in **TU**e**R**kheim
UMD	DWD radar in **UM**men**D**orf
VDRAS	4D**V**ar **D**oppler **R**adar **A**nalysis **S**ystem
WRF	**W**eather **R**esearch and **F**orecasting model
ZPHI-method	Method to derive specific attenuation

List of Symbols

$a_{(q_{th})}$	Total number of points that exceed q_{th} in P_O and P_M
$\boldsymbol{A}$	Linear operator $\boldsymbol{A} = \boldsymbol{I} - \widetilde{\boldsymbol{K}}\boldsymbol{H}$ in the ETKF scheme
$A_{H/V}$	Horizontal/vertical specific attenuation (dB/km)
A_{Thies}	Detection area of the Thies-disdrometers (m^2)
$\arg(c)$	Argument of a complex number c
$b_{(q_{th})}$	Total number of points where q_{th} is exceeded in P_M but not in P_O
b_{ZPHI}	Exponent of an empirical power law relationship between (unattenuated) z_H and A_H
$\boldsymbol{B}$	$N \times N$ background error covariance matrix
$\boldsymbol{B}_0$	$\boldsymbol{B}$ at the initial time of the 4DVar assimilation window
BS	Brier score
BSS	Brier skill score
$c_{(q_{th})}$	Total number of points where q_{th} is not exceeded in P_M but in P_O
c^*	Complex conjugate of a complex number c
$d_{A/B}$	Degrees of freedom of retrieval A/B
$\vec{d}$	Observation increment or innovation vector of dimension O
$\dot{\vec{d}}_i$	Negative observation increment vector of dimension O
D	Particle diameter (mm)
D_m	Mean volume diameter of raindrops (mm)
DCW	Width of diameter classes of Thies-disdrometers (mm)
$\mathrm{E}[x]$	Expected value of a random variable x
$E_{H/V}$	Magnitude of $\vec{E}_{H/V}$ (V m^{-1})
$E^0_{H/V}$	Maximum magnitude of $\vec{E}_{H/V}$ (V m^{-1})
$E_{i/s/t/r}$	Magnitude of incident/scattered/transmitted/radar-received electric field vector (V m^{-1})
$\vec{E}$	Electric field vector (V m^{-1})
$\vec{E}_{H/V}$	Horizontal/vertical electric field vector component (V m^{-1})
$\vec{E}_{i/s/t/r}$	Incident/scattered/transmitted/radar-received electric field vector (V m^{-1})
f	Wave frequency (Hz)
$F_{O/M}$	Fields of fractions obtained from $I_{O/M}$

F_{test}	F-test statistic
FBI	Frequency bias
FSS	Fractions skill score
$\boldsymbol{H}$	Linearized observation operator
$\boldsymbol{H}^T$	Adjoint of $\boldsymbol{H}$
$\boldsymbol{H}_i$	$\boldsymbol{H}$ at the ith time in the 4DVar assimilation window
$\boldsymbol{H}_i^T$	Adjoint of $\boldsymbol{H}_i$
$\mathcal{H}$	(Non-linear) Observation operator
$\boldsymbol{I}$	Identity matrix
$I_{O/M}$	Binary fields obtained from $P_{O/M}$
$\mathrm{Im}(c)$	Imaginary part of a complex number c
IWC	Ice water content (g m^{-3})
j	Complex solution to the equation $j^2 = -1$
J	3DVar/4DVar Cost function
$J_{b/o/c}$	Background/observation/penalty term of J
$\tilde{J}$	Cost function on subspace $\tilde{\mathcal{S}}$
$\tilde{J}^*$	Cost function $\tilde{J}$ with linearized observation operator
JQS	Joint quality score
k	Wave number (m^{-1})
$\vec{k}_{i/k}$	Unit vectors in the propagation direction of the incident/scattered waves
$\boldsymbol{K}$	Kalman gain obtained from ensemble
$\widetilde{\boldsymbol{K}}$	Kalman gain for updating the deviations from the ensemble mean
K_{DP}	Specific differential phase (deg km^{-1})
$K_{H/V}$	Effective propagation constants at horizontal/vertical polarization (m^{-1})
$\lvert K_w \rvert$	Function of ε_w, $\lvert K_w \rvert = \frac{\varepsilon_w - 1}{\varepsilon_w + 2}$
$\boldsymbol{L}^T$	Adjoint of linear tangent forecast model operator
$\boldsymbol{L}_{i-1}^T$	$\boldsymbol{L}^T$ in the vicinity of $\vec{x}_i$
LC	Resolution of Cartesian grid (km)
LH	Horizontal observation localization length-scale (km)
LL	Lower limit of data for superobbing
$\log(x)$	Decadic logarithm of a number x
LS	Superobbing window size (km)
LV	Vertical observation localization length-scale (ln(p))
LWC	Liquid water content (g m^{-3})

M	Ensemble size
$\mathcal{M}$	(Nonlinear) Forward model operator
M_i	ith angular moment of the canting angle distribution
$\boldsymbol{M}_{DSD}$	2D matrix of counts in Thies-disdrometer diameter (mm) and velocity (m s^{-1}) classes
$\boldsymbol{M}_{DSD,d}$	Sum of $\boldsymbol{M}_{DSD}$ over all velocity classes (mm)
MBD	Mean-bias deviation
MSD	Mean squared deviation
MV	Minimum number of valid values for superobbing
$n_{A/B}$	Sample size for retrievals A/B for F-test
n_{FSS}	Window size for fractions in FSS calculation
n_w	Refractive index of water
N	Dimension of model state vector
$\mathcal{N}$	Normal distribution
$N(D)$	Particle size distribution (m^{-3}mm^{-1})
N_{0s}	y-axis intercept of an exponential particle size distribution (m^{-3}mm^{-1})
N_w	Normalized number concentration of raindrops (m^{-3}mm^{-1})
O	Dimension of the observation vector
OE	Observation error standard deviation
p_{ens}	Fraction of ensemble members
$P(\mathrm{A})$	Probability of an event A
$P(\mathrm{A}\|\mathrm{B})$	Probability of an event A given that an event B occurred
$P_{O/M}$	Projected fields of RADOLAN/model data
$\boldsymbol{P}_{a/b/f}$	$N \times N$ analysis/background/forecast error covariance matrix obtained from ensemble
$\widetilde{\boldsymbol{P}}_a$	$N \times N$ analysis error covariance matrix from ensemble in subspace $\tilde{S}$
PCC	Pearson correlation coefficient
$\mathrm{PCC}_{A/B}$	PCC yielded by retrieval A/B
PIA	Two-way path-integrated attenuation (dB)
$q_{r/c/s/g/i}$	Rain/cloud water/snow/graupel/cloud ice mixing ratios (g m^{-3})
q_{th}	Accumulation threshold (mm h^{-1})
$\vec{q}^m$	mth subgrid-scale noise process ensemble member of dimension N
$\boldsymbol{Q}$	Covariance matrix of a zero-mean noise process representing subgrid-scale processes not resolved by the forecast model of dimension $N \times N$
r_0	Range of center bin for superobbing (km)
$\vec{r}^m$	Observation perturbation for the mth ensemble member following $\boldsymbol{R}$

r_ψ	Function of σ_ψ, $r_\psi = \exp[-2\sigma_\psi^2]$ ($\exp[\text{radians}^2]$)
$\boldsymbol{R}$	$O \times O$ observation error covariance matrix
$\boldsymbol{R}_i$	$\boldsymbol{R}$ at the i^{th} time in the 4DVar assimilation window
R_{scm}	Maximum radius of observation influence in SCM
$\mathrm{Re}(c)$	Real part of a complex number c
RMSD	Root mean square deviation
RR	Near-surface rain rate (mm h^{-1})
RR_{mod}	Simulated rain rate in LHN approach (mm h^{-1})
RR_{obs}	Observed rain rate in LHN approach (mm h^{-1})
$s_{a/b}$	Complex scattering amplitude along a spheroid's axis a/b
s_{HH}, s_{HV}, s_{VV}, s_{VH}	Complex (back)scattering amplitudes; the first index denotes the polarization channel that transmits, the second index denotes the polarization channel that receives; H/V denote the horizontal/vertical polarization channels
$s_{HH}^{(0)}$, $s_{VV}^{(0)}$	Complex forward scattering amplitudes; the first index denotes the polarization channel that transmits, the second index denotes the polarization channel that receives; H/V denote the horizontal/vertical polarization channels
$\boldsymbol{S}$	(Back)Scattering Matrix
$\mathcal{S}$	Subspace spanned by the ensemble perturbation vectors in the LETKF of dimension M
$\tilde{\mathcal{S}}$	Subspace from which the perturbation matrix $\boldsymbol{X}_b$ transforms an M-dimensional vector $\vec{w}$ into the M-dimensional subspace $\mathcal{S}$
$\boldsymbol{S}'$	Transmission-included scattering matrix
SD	Standard deviation
SNR	Signal-to-noise ratio (dB)
$\boldsymbol{T}$	Transmission matrix
T_{HH}, T_{HV}, T_{VV}, T_{VH}	Elements of the transmission matrix $\boldsymbol{T}$; the first index denotes the polarization channel that transmits, the second index denotes the polarization channel that receives; H/V denote the horizontal/vertical polarization channels
ΔT_{LHN}	Incremental temperature profile in LHN approach (K)
$\Delta T_{LH,mod}$	Vertical profile of modelled temperature change by latent heating in LHN approach (K)
$\mathcal{T}$	Number of observations in the 4DVar assimilation window
v_t	Terminal fall velocity of particles (m s^{-1})
$\vec{v}^T$	Transpose of a vector $\vec{v}$

V	Number of verification grid points for FSS, BSS, and FBI
V_r	Doppler radial wind (m s^{-1})
$\vec{w}_a^m$	Weighting vector for mth ensemble member in LETKF of dimension M
$\overline{\vec{w}_a}$	Ensemble mean of $\vec{w}_a^m$
$\boldsymbol{W}_a$	$M \times M$ matrix of weights in the LETKF
$\boldsymbol{W}_a^m$	mth column of $\boldsymbol{W}_a$
$\vec{x}$	Variable model state vector of dimension N
$\vec{x}_{a/b}$	Analysis/background state vector of dimension N
$\vec{x}_f$	Forecast model state of dimension N
$\vec{x}_i$	Model state integrated to the ith observation time in the 4DVar window
$\vec{x}_t$	True state of the atmosphere on the model grid of dimension N
$\vec{x}_{a/b}^{det}$	Deterministic analysis/background state vector of dimension N
$\vec{x}_{b/a}^m$	mth background/analysis ensemble member of dimension N
$\overline{\vec{x}_{b/a}}$	Background/analysis ensemble mean of dimension N
$\overline{\vec{x}_{f/a}}$	Ensemble mean $\vec{x}_{f/a}$ of dimension N
$\vec{x}_{f/a}^m$	mth forecast/analysis state ensemble member of dimension N
$\vec{x}_{f/a}^{m\prime}$	Deviation of $\vec{x}_{f/a}^m$ from $\overline{\vec{x}_{f/a}}$ of dimension N
$\boldsymbol{X}_{b/a}$	$N \times M$ matrix of ensemble perturbations from $\overline{\vec{x}_{b/a}}$
$\vec{y}_o$	Observation vector of dimension O
$\vec{y}_b^m$	mth background ensemble member in observation space of dimension O
$\overline{\vec{y}_b}$	Ensemble mean of $\vec{y}_b^m$ of dimension O
$\overline{\vec{y}_o}$	Ensemble mean observation vector of dimension O
$\vec{y}_o^{m\prime}$	mth observation perturbation from $\overline{\vec{y}_o}$ of dimension O
$\boldsymbol{Y}_b$	$O \times M$ matrix of ensemble perturbations from $\overline{\vec{y}_b}$
z_{DR}	Linear differential reflectivity
$z_{H/V}$	Linear horizontal/vertical reflectivity factor (mm^6 m^{-3})
$Z_{H/V}$	Logarithmic horizontal/vertical reflectivity factor (dBZ)
$Z_{H,att}$	Attenuated (measured) Z_H (dBZ)
$z_{H,att}$	Attenuated (measured) z_H (mm^6 m^{-3})
Z_{DP}	Reflectivity difference (mm^6 m^{-3})
Z_{DR}	Differential reflectivity (dB)
$Z_{DR,att}$	Attenuated (measured) Z_{DR} (dB)
ΔZ_H	Reduction in Z_H along a ray by attenuation (dBZ)
α	Attenuation parameter (dB deg^{-1})

α_{LHN}	Ratio between RR_{obs} and RR_{mod} in LHN approach
β	Differential attenuation parameter (dB deg^{-1})
γ_{scm}	Factor for R_{scm} in Barnes (1964) SCM approach
δ	Backscatter differential phase (deg)
ε_w	Dielectric constant of water
$\vec{\varepsilon}_b$	Background error vector with dimension N
$\vec{\varepsilon}_o$	Observation error vector with dimension O
κ	Factor related to the degree of riming
λ	Radar wavelength (mm)
ρ_{HV}	Co-polar cross-correlation coefficient
ρ_{tot}	Total air density (kg m^{-3})
ρ_w	Density of water (g m^{-3})
$\sigma_{\chi/\psi}$	Standard deviations of χ/ψ with $\sigma_\chi = \sigma_\psi / sin(\psi)$ (radians)
$\Delta\tau_{DSD}$	Time interval for single drop size distributions (s)
$\varphi_{H/V}$	Start phases of $\vec{E}_{H/V}$ (deg)
φ_{DP}	Propagation differential phase (deg)
φ_{DP}^{sys}	Differential phase from the radar system (deg)
$\Delta\varphi$	Difference between φ_H and φ_V (deg)
Φ_{DP}	Total differential phase (deg)
$\Delta\Phi_{DP}$	Total increment in Φ_{DP} along a ray below the melting layer (deg)
χ	Angle between the spheroid axis a and the vertical direction in the polarization plane (deg)
ψ	Angle between the spheroid axis a and the direction of wave propagation (deg)
∇	Gradient
$\langle \ldots \rangle$	Integral over $N(D)$

List of Figures

List of Tables

Bibliography

Aksoy, A., D. C. Dowell, and C. Snyder, 2009: A multicase comparative assessment of the ensemble Kalman filter for assimilation of radar observations. Part I: storm-scale analyses. *Monthly Weather Review*, 137 (6), 1805-1824, DOI: 10.1175/2008MWR2691.1.

Aksoy, A., D. C. Dowell, and C. Snyder, 2010: A multicase comparative assessment of the ensemble Kalman filter for assimilation of radar observations. Part II: short-range ensemble forecasts. *Monthly Weather Review*, 138 (4), 1273-1292, DOI: 10.1175/2009MWR3086.1.

Albers, S. C., 1995: The LAPS wind analysis. *Weather and Forecasting*, 10 (2), 342-352, DOI: 10.1175/1520-0434(1995)010<0342:TLWA>2.0.CO;2.

Albers, S. C., J. A. McGinley, D. L. Birkenheuer, and J. R. Smart, 1996: The local analysis and prediction system (LAPS): analyses of clouds, precipitation, and temperature. *Weather and Forecasting*, 11 (3), 273-287, DOI: 10.1175/1520-0434(1996)011<0273:TLAAPS>2.0.CO;2.

Alpert, J. C., and V. K. Kumar, 2007: Radial wind super-obs from the WSR-88D radars in the NCEP operational assimilation system. *Monthly Weather Review*, 135 (3), 1090–1109, DOI:10.1175/MWR3324.1.

Anderson, J. L., 2001: An ensemble adjustment Kalman filter for data assimilation. *Monthly Weather Review*, 129 (12), 2884-2903, DOI: 10.1175/1520-0493(2001)129<2884:AEAKFF>2.0.CO;2.

Anderson, J. L., and S. L. Anderson, 1999: A Monte Carlo implementation of the nonlinear filtering problem to produce ensemble assimilations and forecasts. *Monthly Weather Review*, 127 (12), 2741-2758, DOI: 10.1175/1520-0493(1999)127<2741:AMCIOT>2.0.CO;2.

Atlas, D., S. Y. Matrosov, A. J. Heymsfield, M.-D. Chou, and D. B. Wolff, 1995: Radar and radiation properties of ice clouds. *Journal of Applied Meteorology and Climatology*, 34 (11), 2329-2345, DOI: 10.1175/1520-0450(1995)034<2329: RARPOI>2.0.CO;2.

Balakrishnan, N., and D. S. Zrnic, 1990: Estimation of rain and hail rates in mixed-phase precipitation. *Journal of the Atmospheric Sciences*, 47 (5), 565-583, DOI: 10.1175/1520-0469(1990)047<0565:EORAHR>2.0.CO;2.

Baldauf, M., A. Seifert, J. Förstner, D. Majewski, M. Raschendorfer, and T. Reinhardt, 2011: Operational convective-scale numerical weather prediction with the COSMO model: description and sensitivities. *Monthly Weather Review*, 139 (12), 3887-3905, DOI: 10.1175/MWR-D-10-05013.1.

Bannister, R. N., 2017: A review of operational methods of variational and ensemble-variational data assimilation. *Quarterly Journal of the Royal Meteorological Society*, 143 (703), 607-633, DOI: 10.1002/qj.2982.

Barnes, S. L., 1964: A technique for maximizing details in numerical weather map analysis. *Journal of Applied Meteorology and Climatology*, 3 (4), 396-409, DOI: 10.1175/1520-0450(1964)003<0396:ATFMDI>2.0.CO;2.

Battaglia, A., E. Rustemeier, A. Tokay, U. Blahak, and C. Simmer, 2010: PARSIVEL snow observations: a critical assessment. *Journal of Atmospheric and Oceanic Technology*, 27 (2), 333-344, DOI: 10.1175/2009JTECHA1332.1.

Bergthörsson, P., and B. R. Döös, 1955: Numerical weather map analysis. *Tellus*, 7 (3), 329-340, DOI: 10.3402/tellusa.v7i3.8902.

Bick, T., C. Simmer, S. Trömel, K. Wapler, H.-J. Hendricks Franssen, K. Stephan, U. Blahak, C. Schraff, and coauthors, 2016: Assimilation of 3D radar reflectivities with an ensemble Kalman filter on the convective scale. *Quarterly Journal of the Royal Meteorological Society*, 142 (696), 1490-1504, DOI: 10.1002/qj.2751.

Bishop, C. H., B. J. Etherton, and S. J. Majumdar, 2001: Adaptive sampling with the ensemble transform Kalman filter. Part I: theoretical aspects. *Monthly Weather Review*, 129 (3), 420-436, DOI: 10.1175/1520-0493(2001)129<0420:ASWTET>2.0.CO;2.

Blanke, A., A. J. Heymsfield, M. Moser, and S. Trömel, 2023: Evaluation of polarimetric ice microphysical retrievals with OLYMPEX campaign data. *EGUsphere*, 2023, 1-27, DOI: 10.5194/egusphere-2022-1488.

Bodine, D. J., M. R. Kumjian, R. D. Palmer, P. L. Heinselman, and A. V. Ryzhkov, 2013: Tornado damage estimation using polarimetric radar. *Weather and Forecasting*, 28 (1), 139-158, DOI: 10.1175/WAF-D-11-00158.1.

Bonavita, M., L. Torrisi, and F. Marcucci, 2010: Ensemble data assimilation with the CNMCA regional forecasting system. *Quarterly Journal of the Royal Meteorological Society*, 136 (646), 132-145, DOI: 10.1002/qj.553.

Brandes, E. A., G. Zhang, and J. Vivekanandan, 2002: Experiments in rainfall estimation with a polarimetric radar in a subtropical environment. *Journal of Applied Meteorology and Climatology*, 41 (6), 674-685, DOI: 10.1175/1520-0450(2002)041<0674:EIREWA>2.0.CO;2.

Bratseth, A. M., 1986: Statistical interpolation by means of successive corrections. *Tellus A: Dynamic Meteorology and Oceanography*, 38 (5), 439-447, DOI: 10.3402/tellusa.v38i5.11730.

Brewster, K., 1996: Application of a Bratseth analysis scheme including Doppler radar. *15th Conference on Weather Analysis and Forecasting*, AMS, 19-23 August 1996, Norfolk, Virginia, USA.

Bringi, V. N., and V. Chandrasekar, 2001: *Polarimetric Doppler weather radar: principles and applications*. Cambridge University Press.

Bringi, V. N., V. Chandrasekar, N. Balakrishnan, and D. S. Zrnic, 1990: An examination of propagation effects in rainfall on radar measurements at microwave frequencies. *Journal of Atmospheric and Oceanic Technology*, 7 (6), 829-840, DOI: 10.1175/1520-0426(1990)007<0829:AEOPEI>2.0.CO;2.

Bringi, V. N., T. D. Keenan, and V. Chandrasekar, 2001: Correcting C-band radar reflectivity and differential reflectivity data for rain attenuation: a self-consistent method with constraints. *IEEE Transactions on Geoscience and Remote* Sensing, 39 (9), 1906-1915, DOI: 10.1109/36.951081.

Buehner, M., 2005: Ensemble-derived stationary and flow-dependent background-error covariances: Evaluation in a quasi-operational NWP setting. *Quarterly Journal of the Royal Meteorological Society*, 131 (607), 1013-1043, DOI: 10.1256/qj.04.15.

Bukovcic, P., A. V. Ryzhkov, and D. S. Zrnic, 2020: Polarimetric relations for snow estimation – radar verification. *Journal of Applied Meteorology and Climatology*, 59 (5), 991-1009, DOI: 10.1175/JAMC-D-19-0140.1.

Bukovcic, P., A. V. Ryzhkov, D. S. Zrnic, and G. Zhang, 2018: Polarimetric radar relations for quantification of snow based on disdrometer data. *Journal of Applied Meteorology and Climatology*, 57 (1), 103-120, DOI: 10.1175/JAMC-D-17-0090.1.

Burgers, G., P. J. van Leeuwen, and G. Evensen, 1998: Analysis scheme in the ensemble Kalman filter. *Monthly Weather Review*, 126 (6), 1719-1724. DOI: 10.1175/1520-0493(1998)126<1719:ASITEK>2.0.CO;2.

Carlin, J. T., J. Gao, J. C. Snyder, and A. V. Ryzhkov, 2017: Assimilation of ZDR columns for improving the spinup and forecast of convective storms in storm-scale models: proof-of-concept experiments. *Monthly Weather Review*, 145 (12), 5033-5057, DOI: 10.1175/MWR-D-17-0103.1.

Carlin, J. T., H. D. Reeves, and A. V. Ryzhkov, 2021: Polarimetric observations and simulations of sublimating snow: implications for nowcasting. *Journal of Applied Meteorology and Climatology*, 60 (8), 1035-1054, DOI: 10.1175/JAMC-D-21-0038.1.

Carlin, J. T., A. V. Ryzhkov, J. C. Snyder, and A. Khain, 2016: Hydrometeor Mixing Ratio Retrievals for Storm-Scale Radar Data Assimilation: Utility of Current Relations and Potential Benefits of Polarimetry. In Monthly Weather Review 144 (8), pp. 2981–3001. DOI: 10.1175/MWR-D-15-0423.1.

Caya, A., J. Sun, and C. Snyder, 2005: A comparison between the 4DVAR and the ensemble Kalman filter techniques for radar data assimilation. *Monthly Weather Review*, 133 (11), 3081-3094, DOI: 10.1175/MWR3021.1.

Chang, S.-F., J. Sun, Y.-C. Liou, S.-L. Tai, and C.-Y. Yang, 2014: The influence of erroneous background, beam-blocking and microphysical non-linearity on the application of a four-dimensional variational Doppler radar data assimilation

system for quantitative precipitation forecasts. *Meteorological Applications*, 21 (2), 444-458, DOI: 10.1002/met.1439.

Chen, J.-Y., S. Trömel, A. V. Ryzhkov, and C. Simmer, 2021: Assessing the benefits of specific attenuation for quantitative precipitation estimation with a C-Band radar network. *Journal of Hydrometeorology*, 22 (10), 2617-2631, DOI: 10.1175/JHM-D-20-0299.1.

Courtier, P., E. Andersson, W. Heckley, D. Vasiljevic, M. Hamrud, A. Hollingsworth, F. Rabier, M. Fisher, and coauthors, 1998: The ECMWF implementation of three-dimensional variational assimilation (3D-Var). I: formulation. *Quarterly Journal of the Royal Meteorological Society*, 124 (550), 1783-1807, DOI: 10.1002/qj.49712455002.

Cressman, G. P., 1959: An operational objective analysis system. *Monthly Weather Review*, 87 (10), 367-374, DOI: 10.1175/1520-0493(1959)087<0367:AOOAS>2.0.CO;2.

Delanoe, J. M. E., A. J. Heymsfield, A. Protat, A. Bansemer, and R. J. Hogan, 2014: Normalized particle size distribution for remote sensing application. *Journal of Geophysical Research: Atmospheres*, 119 (7), 4204-4227, DOI: 10.1002/2013JD020700.

Desroziers, G., L. Berre, B. Chapnik, and P. Poli, 2005: Diagnosis of observation, background and analysis-error statistics in observation space. *Quarterly Journal of the Royal Meteorological Society*, 131 (613), 3385-3396, DOI: 10.1256/qj.05.108.

Diederich, M., A. V. Ryzhkov, C. Simmer, P. Zhang, and S. Trömel, 2015: Use of specific attenuation for rainfall measurement at X-Band radar wavelengths. Part II: rainfall estimates and comparison with rain gauges. *Journal of Hydrometeorology*, 16 (2), 503-516, DOI: 10.1175/JHM-D-14-0067.1.

Ding, Z., K. Zhao, K. Zhu, Y. Feng, H. Huang, and Z. Yang, 2022: Assimilation of polarimetric radar observation with GSI cloud analysis for the prediction of a squall line. *Geophysical Research Letters*, 49 (16), e2022GL098253, DOI: 10.1029/2022GL098253.

Dolan, B., S. A. Rutledge, S. Lim, V. Chandrasekar, and M. Thurai, 2013: A robust C-band hydrometeor identification algorithm and application to a long-term polarimetric radar dataset. *Journal of Applied Meteorology and Climatology*, 52 (9), 2162-2186, DOI: 10.1175/JAMC-D-12-0275.1.

Dong, J., and M. Xue, 2012: Assimilation of radial velocity and reflectivity data from coastal WSR-88D radars using an ensemble Kalman filter for the analysis and forecast of landfalling hurricane Ike (2008). *Quarterly Journal of the Royal Meteorological Society*, 139 (671), 467-487, DOI: 10.1002/qj.1970.

Doviak, R. J., and D. S. Zrnic, 2006: *Doppler radar and weather observations*. Courier Corporation.

Dowell, D. C., and L. J. Wicker, 2009: Additive noise for storm-scale ensemble data assimilation. *Journal of Atmospheric and Oceanic Technology*, 26 (5), 911-927, DOI: 10.1175/2008JTECHA1156.1.

Dowell, D. C., L. J. Wicker, and C. Snyder, 2011: Ensemble Kalman filter assimilation of radar observations of the 8 May 2003 Oklahoma City supercell: influences of reflectivity observations on storm-scale analyses. *Monthly Weather Review*, 139 (1), 272-294, DOI: 10.1175/2010MWR3438.1.

Dowell, D. C., F. Zhang, L. J. Wicker, C. Snyder, and N. A. Crook, 2004: Wind and temperature retrievals in the 17 May 1981 Arcadia, Oklahoma, supercell: ensemble Kalman filter experiments. *Monthly Weather Review*, 132 (8), 1982-2005, DOI: 10.1175/1520-0493(2004)132<1982:WATRIT>2.0.CO;2.

Du, M., J. Gao, G. Zhang, Y. Wang, P. L. Heiselman, and C. Cui, 2021: Assimilation of polarimetric radar data in simulation of a supercell storm with a variational approach and the WRF model. *Remote Sensing*, 13 (16), 3060, DOI: 10.3390/rs13163060.

Duda, J. D., X. Wang, Y. Wang, and J. R. Carley, 2019: Comparing the assimilation of radar reflectivity using the direct GSI-based ensemble–variational (EnVar) and indirect cloud analysis methods in convection-allowing forecasts over the continental United States. *Monthly Weather Review*, 147 (5), 1655-1678, DOI: 10.1175/MWR-D-18-0171.1.

Evensen, G., 1994: Sequential data assimilation with a nonlinear quasi-geostrophic model using Monte Carlo methods to forecast error statistics. *Journal of Geophysical Research: Oceans*, 99 (C5), 10143-10162, DOI: 10.1029/94JC00572.

Evensen, G., 2003: The ensemble Kalman filter: theoretical formulation and practical implementation. *Ocean Dynamics*, 53, 343-367, DOI: 10.1007/s10236-003-0036-9.

Gal-Chen, T., 1978: A method for the initialization of the anelastic equations: implications for matching models with observations. *Monthly Weather Review*, 106 (5), 587-606, DOI: 10.1175/1520-0493(1978)106<0587:AMFTIO>2.0.CO;2.

Gao, J., and D. J. Stensrud, 2012: Assimilation of reflectivity data in a convective-scale, cycled 3DVAR framework with hydrometeor classification. *Journal of the Atmospheric Sciences*, 69 (3), 1054-1065, DOI: 10.1175/JAS-D-11-0162.1.

Gao, J., and M. Xue, 2008: An efficient dual-resolution approach for ensemble data assimilation and tests with simulated Doppler radar data. *Monthly Weather Review*, 136 (3), 945-963, DOI: 10.1175/2007MWR2120.1.

Gao, J., M. Xue, K. Brewster, and K. K. Droegemeier, 2004: A three-dimensional variational data analysis method with recursive filter for Doppler radars. *Journal of Atmospheric and Oceanic Technology*, 21 (3), 457-469, DOI: 10.1175/1520-0426(2004)021<0457:ATVDAM>2.0.CO;2.

Gao, J., M. Xue, D. J. Stensrud, and K. Zhao, 2013: The development of a hybrid EnKF-3DVAR algorithm for storm-scale data assimilation. *Advances in Meteorology*, 2013, 512656, DOI: 10.1155/2013/512656.

Gao, S., and J. Min, 2018: Analysis and prediction of a mesoscale convective system over East China with an ensemble square root filter radar data assimilation approach. *Atmospheric Science Letters*, 19 (2), e806, DOI: 10.1002/asl.806.

Gaspari, G., and S. E. Cohn, 1999: Construction of correlation functions in two and three dimensions. *Quarterly Journal of the Royal Meteorological Society*, 125 (554), 723-757, DOI: 10.1002/qj.49712555417.

Gastaldo, T., V. Poli, C. Marsigli, P. P. Alberoni, and T. Paccagnella, 2018: Data assimilation of radar reflectivity volumes in a LETKF scheme. *Nonlinear Processes in Geophysics*, 25 (4), 747-764, DOI: 10.5194/npg-25-747-2018.

Gastaldo, T., V. Poli, C. Marsigli, D. Cesari, P. P. Alberoni, and T. Paccagnella, 2021: Assimilation of radar reflectivity volumes in a pre-operational framework. *Quarterly Journal of the Royal Meteorological Society*, 147 (735), 1031-1054, DOI: 10.1002/qj.3957.

Ge, G., J. Gao, and M. Xue, 2012: Diagnostic pressure equation as a weak constraint in a storm-scale three-dimensional variational radar data assimilation system. *Journal of Atmospheric and Oceanic Technology*, 29 (8), 1075-1092, DOI: 10.1175/JTECH-D-11-00201.1.

Giangrande, S. E., and A. V. Ryzhkov, 2008: Estimation of rainfall based on the results of polarimetric echo classification. *Journal of Applied Meteorology and Climatology*, 47 (9), 2445-2462, DOI: 10.1175/2008JAMC1753.1.

Gosset, M., 2004: Effect of nonuniform beam filling on the propagation of radar signals at X-band frequencies. Part II: examination of differential phase shift. *Journal of Atmospheric and Oceanic Technology*, 21 (2), 358-367, DOI: 10.1175/1520-0426(2004)021<0358:EONBFO>2.0.CO;2.

Greene, D. R., and R. A. Clark, 1972: Vertically integrated liquid water – a new analysis tool. *Monthly Weather Review*, 100 (7), 548-552, DOI: 10.1175/1520-0493(1972)100<0548:VILWNA>2.3.CO;2.

Gustafsson, N., T. Janjic, C. Schraff, D. Leuenberger, M. Weissmann, H. Reich, P. Brousseau, T. Montmerle, and coauthors, 2018: Survey of data assimilation methods for convective-scale numerical weather prediction at operational centres. *Quarterly Journal of the Royal Meteorological Society*, 144 (713), 1218-1256, DOI: 10.1002/qj.3179.

Hamill, T. M., and C. Snyder, 2000: A hybrid ensemble Kalman filter–3D variational analysis scheme. *Monthly Weather Review*, 128 (8), 2905-2919, DOI: 10.1175/1520-0493(2000)128<2905:AHEKFV>2.0.CO;2.

Hamill, T. M., J. S. Whitaker, and C. Snyder, 2001: Distance-dependent filtering of background error covariance estimates in an ensemble Kalman filter. *Monthly*

Weather Review, 129 (11), 2776-2790, DOI: 10.1175/1520-0493(2001)129<2776:DDFOBE>2.0.CO;2.

Hamrud, M., M. Bonavita, and L. Isaksen, 2015: EnKF and hybrid gain ensemble data assimilation. Part I: EnKF implementation. *Monthly Weather Review*, 143 (12), 4847-4864, DOI: 10.1175/MWR-D-14-00333.1.

Hane, C. E., and P. S. Ray, 1985: Pressure and buoyancy fields derived from Doppler radar data in a tornadic thunderstorm. Journal of the Atmospheric Sciences, 42 (1), 18-35, DOI: 10.1175/1520-0469(1985)042<0018:PABFDF>2.0.CO;2.

Hawkness-Smith, L. D., and D. Simonin, 2021: Radar reflectivity assimilation using hourly cycling 4D-Var in the Met Office Unified Model. *Quarterly Journal of the Royal Meteorological Society*, 147 (736), 1516-1538, DOI: 10.1002/qj.3977.

Helmert, K., P. Tracksdorf, J. Steinter, M. Werner, M. Frech, N. Rathmann, T. Hengstebeck, M. Mott, and coauthors, 2014: DWDs new radar network and post-processing algorithm chain. *8th European Conference on Radar in Meteorology and Hydrology*, 1-5 September 2014, Garmisch-Partenkirchen, Germany.

Heymsfield, A. J., S. Y. Matrosov, and N. B. Wood, 2016: Toward improving ice water content and snow-rate retrievals from radars. Part I. X and W bands, emphasizing CloudSat. *Journal of Applied Meteorology and Climatology*, 55 (9), 2063-2090, DOI: 10.1175/JAMC-D-15-0290.1.

Hogan, R. J., M. P. Mittermaier, and A. J. Illingworth, 2006: The retrieval of ice water content from radar reflectivity factor and temperature and its use in evaluating a mesoscale model. *Journal of Applied Meteorology and Climatology*, 45 (2), 301-317, DOI: 10.1175/JAM2340.1.

Hoke, J. E., and R. A. Anthes, 1976: The initialization of numerical models by a dynamic-initialization technique. *Monthly Weather Review*, 104 (12), 1551-1556, DOI: 10.1175/1520-0493(1976)104<1551:TIONMB>2.0.CO;2.

Holt, A. R., and J. W. Shepherd, 1979: Electromagnetic scattering by dielectric spheroids in the forward and backward directions. *Journal of Physics A: Mathematical and General*, 12 (1), 159, DOI: 10.1088/0305-4470/12/1/029.

Houtekamer, P. L., and H. L. Mitchell, 1998: Data assimilation using an ensemble Kalman filter technique. *Monthly Weather Review*, 126 (3), 796-811, DOI: 10.1175/1520-0493(1998)126<0796:DAUAEK>2.0.CO;2.

Houtekamer, P. L., and H. L. Mitchell, 2001: A sequential ensemble Kalman filter for atmospheric data assimilation. *Monthly Weather Review*, 129 (1), 123-137, DOI: 10.1175/1520-0493(2001)129<0123:ASEKFF>2.0.CO;2.

Houtekamer, P. L., and H. L. Mitchell, 2005: Ensemble Kalman filtering. *Quarterly Journal of the Royal Meteorological Society*, 131 (613), 3269-3289, DOI: 10.1256/qj.05.135.

Houtekamer, P. L., H. L. Mitchell, G. Pellerin, M. Buehner, M. Charron, L. Spacek, and B. Hansen, 2005: Atmospheric data assimilation with an ensemble Kalman

filter: results with real observations. *Monthly Weather Review*, 133 (3), 604-620, DOI: 10.1175/MWR-2864.1.

Hu, M., and M. Xue, 2007: Impact of configurations of rapid intermittent assimilation of WSR-88D radar data for the 8 May 2003 Oklahoma City tornadic thunderstorm case. *Monthly Weather Review*, 135 (2), 507-525, DOI: 10.1175/MWR3313.1.

Hu, M., M. Xue, and K. Brewster, 2006a: 3DVAR and cloud analysis with WSR-88D Level-II data for the prediction of the Fort Worth, Texas, tornadic thunderstorms. Part I: cloud analysis and its impact. *Monthly Weather Review*, 134 (2), 675-698, DOI: 10.1175/MWR3092.1.

Hu, M., M. Xue, J. Gao, and K. Brewster, 2006b: 3DVAR and cloud analysis with WSR-88D Level-II data for the prediction of the Fort Worth, Texas, tornadic thunderstorms. Part II: impact of radial velocity analysis via 3DVAR. *Monthly Weather Review*, 134 (2), 699-721, DOI: 10.1175/MWR3093.1.

Hunt, B. R., E. J. Kostelich, and I. Szunyogh, 2007: Efficient data assimilation for spatiotemporal chaos: a local ensemble transform Kalman filter. *Physica D: Nonlinear Phenomena*, 230 (1-2), 112-126, DOI: 10.1016/j.physd.2006.11.008.

Ide, K., P. Courtier, M. Ghil, and A. C. Lorenc, 1997: Unified notation for data assimilation: operational, sequential and variational. *Journal of the Meteorological Society of Japan. Ser. II*, 75 (1B), 181-189, DOI: 10.2151/jmsj1965.75.1B_181.

Illingworth, A. J., and R. J. Thompson, 2005: The estimation of moderate rain rates with operational polarization radar. *32nd Conference on Radar Meteorology*, AMS, 24-28 October, Albuquerque, New Mexico, USA, P9R.1.

IPCC, 2021: Summary for Policymakers. In: *Climate Change 2021: The Physical Science Basis. Contribution of Working Group I to the Sixth Assessment Report of the Intergovernmental Panel on Climate Change*. [Masson-Delmotte, V., P. Zhai, A. Pirani, S.L. Connors, C. Péan, S. Berger, N. Caud, Y. Chen, L. Goldfarb, M.I. Gomis, M. Huang, K. Leitzell, E. Lonnoy, J.B.R. Matthews, T.K. Maycock, T. Waterfield, O. Yelekçi, R. Yu, and B. Zhou (eds.)]. Cambridge University Press, Cambridge, United Kingdom and New York, New York, USA, 3-32, DOI: 10.1017/9781009157896.001.

Jacques, D., and D. Michelson, 2022: Latent heat nudging in the Canadian high-resolution (2.5 km) regional deterministic prediction system. *Monthly Weather Review*, 150 (9), 2299-2315, DOI: 10.1175/MWR-D-22-0028.1.

Jacques, D., D. Michelson, J.-F. Caron, and L. Fillion, 2018: Latent heat nudging in the Canadian regional deterministic prediction system. *Monthly Weather Review*, 146 (12), 3995-4014, DOI: 10.1175/MWR-D-18-0118.1.

Jameson, A. R., and E. A. Mueller, 1985: Estimation of propagation-differential phase shift from sequential orthogonal linear polarization radar measurements. *Journal of Atmospheric and Oceanic Technology*, 2 (2), 133-137, DOI: 10.1175/1520-0426(1985)002<0133:EOPDPS>2.0.CO;2.

Johnson, A., X. Wang, J. R. Carley, L. J. Wicker, and C. Karstens, 2015: A comparison of multiscale GSI-based EnKF and 3DVar data assimilation using radar and conventional observations for midlatitude convective-scale precipitation forecasts. *Monthly Weather Review*, 143 (8), 3087-3108, DOI: 10.1175/MWR-D-14-00345.1.

Jones, C. D., and B. Macpherson, 1997: A latent heat nudging scheme for the assimilation of precipitation data into an operational mesoscale model. *Meteorological Applications*, 4 (3), 269-277. DOI: 10.1017/S1350482 797000522.

Jung, Y., M. Xue, and M. Tong, 2012: Ensemble Kalman filter analyses of the 29–30 May 2004 Oklahoma tornadic thunderstorm using one- and two-moment bulk microphysics schemes, with verification against polarimetric radar data. *Monthly Weather Review*, 140 (5), 1457-1475, DOI: 10.1175/MWR-D-11-00032.1.

Jung, Y., M. Xue, and G. Zhang, 2010a: Simulations of polarimetric radar signatures of a supercell storm using a two-moment bulk microphysics scheme. *Journal of Applied Meteorology and Climatology*, 49 (1), 146-163, DOI: 10.11 75/2009JAMC2178.1.

Jung, Y., M. Xue, and G. Zhang, 2010b: Simultaneous estimation of microphysical parameters and the atmospheric state using simulated polarimetric radar data and an ensemble Kalman filter in the presence of an observation operator error. *Monthly Weather Review*, 138 (2), 539-562, DOI: 10.1175/2009MWR2748.1.

Jung, Y., M. Xue, G. Zhang, and J. M. Straka, 2008b: Assimilation of simulated polarimetric radar data for a convective storm using the ensemble Kalman filter. Part II: impact of polarimetric data on storm analysis. *Monthly Weather Review*, 136 (6), 2246-2260, DOI: 10.1175/2007MWR2288.1.

Jung, Y., G. Zhang, and M. Xue, 2008a: Assimilation of simulated polarimetric radar data for a convective storm using the ensemble Kalman filter. Part I: observation operators for reflectivity and polarimetric variables. *Monthly Weather Review*, 136 (6), 2228-2245, DOI: 10.1175/2007MWR2083.1.

Kalman, R. E., 1960: A new approach to linear filtering and prediction problems. *Journal of Basic Engineering*, 82 (1), 35-45, DOI: 10.1115/1.3662552.

Kalman, R. E., and R. S. Bucy, 1961: New results in linear filtering and prediction theory. *Journal of Basic Engineering*, 83 (1), 95-108, DOI: 10.1115/1.3658902.

Kalnay, E., 2003: *Atmospheric modeling, data assimilation and predictability*. Cambridge University Press.

Kapitza, H., 1991: Numerical experiments with the adjoint of a nonhydrostatic mesoscale model. *Monthly Weather Review*, 119 (12), 2993-3011, DOI: 10.1175 /1520-0493(1991)119<2993:NEWTAO>2.0.CO;2.

Kawabata, T., T. Kuroda, H. Seko, and K. Saito, 2011: A cloud-resolving 4DVAR assimilation experiment for a local heavy rainfall event in the Tokyo metropolitan

area. *Monthly Weather Review*, 139 (6), 1911-1931, DOI: 10.1175/2011MWR 3428.1.

Kennedy, P. C., and S. A. Rutledge, 2011: S-band dual-polarization radar observations of winter storms. *Journal of Applied Meteorology and Climatology*, 50 (4), 844-858, DOI: 10.1175/2010JAMC2558.1.

Kumjian, M. R., 2013a: Principles and applications of dual-polarization weather radar. Part I: description of the polarimetric radar variables. *Journal of Operational Meteorology*, 1 (19), 226-242, DOI: 10.15191/nwajom.2013.0119.

Kumjian, M. R., 2013b: Principles and applications of dual-polarization weather radar. Part III: artifacts. *Journal of Operational Meteorology*, 1 (21), 265-274, DOI: 10.15191/nwajom.2013.0121.

Kumjian, M. R., A. P. Khain, N. Benmoshe, E. Ilotoviz, A. V. Ryzhkov, and V. T. J. Phillips, 2014: The anatomy and physics of ZDR columns: investigating a polarimetric radar signature with a spectral bin microphysical model. *Journal of Applied Meteorology and Climatology*, 53 (7), 1820-1843, DOI: 10.11 75/JAMC-D-13-0354.1.

Kumjian, M. R., and A. V. Ryzhkov, 2008: Polarimetric signatures in supercell thunderstorms. *Journal of Applied Meteorology and Climatology*, 47 (7), 1940-1961, DOI: 10.1175/2007JAMC1874.1.

Lange, H., and G. C. Craig, 2014: The impact of data assimilation length scales on analysis and prediction of convective storms. *Monthly Weather Review*, 142 (10), 3781-3808, DOI: 10.1175/MWR-D-13-00304.1.

Le Dimet, F.-X., and O. Talagrand, 1986: Variational algorithms for analysis and assimilation of meteorological observations: theoretical aspects. *Tellus A*, 38A (2), 97-110, DOI: 10.1111/j.1600-0870.1986.tb00459.x.

Leinonen, J., 2014: High-level interface to T-matrix scattering calculations: architecture, capabilities and limitations. *Optics Express*, 22 (2), 1655-1660, DOI: 10.1364/OE.22.001655.

Leuenberger, D., and A. Rossa, 2007: Revisiting the latent heat nudging scheme for the rainfall assimilation of a simulated convective storm. *Meteorology and Atmospheric Physics*, 98, 195-215, DOI: 10.1007/s00703-007-0260-9.

Lewis, J. M., and J. C. Derber, 1985: The use of adjoint equations to solve a variational adjustment problem with advective constraints. *Tellus A*, 37A (4), 309-322, DOI: 10.1111/j.1600-0870.1985.tb00430.x.

Li, X., and J. R. Mecikalski, 2010: Assimilation of the dual-polarization Doppler radar data for a convective storm with a warm-rain radar forward operator. *Journal of Geophysical Research: Atmospheres*, 115 (D16), DOI: 10.1029/2009JD 013666.

Li, X., and J. R. Mecikalski, 2012: Impact of the dual-polarization Doppler radar data on two convective storms with a warm-rain radar forward operator. *Monthly Weather Review*, 140 (7), 2147-2167, DOI: 10.1175/MWR-D-11-00090.1.

Li, X., and J. R. Mecikalski, 2013: Evaluation of the sensitivity of the dual-polarization Doppler warm-rain radar data assimilation to radar forward operators for a convective storm. *Journal of the Meteorological Society of Japan. Ser. II*, 91(3), 287-304, DOI: 10.2151/jmsj.2013-304.

Li, X., J. R. Mecikalski, and D. Posselt, 2017: An ice-phase microphysics forward model and preliminary results of polarimetric radar data assimilation. *Monthly Weather Review*, 145 (2), 683-708, DOI: 10.1175/MWR-D-16-0035.1.

Li, Y., X. Wang, and M. Xue, 2012: Assimilation of radar radial velocity data with the WRF hybrid ensemble–3DVAR system for the prediction of hurricane Ike (2008). *Monthly Weather Review*, 140 (11), 3507-3524, DOI: 10.1175/MWR-D-12-00043.1.

Lin, Y., P. S. Ray, and K. W. Johnson, 1993: Initialization of a modeled convective storm using Doppler radar derived fields. *Monthly Weather Review*, 121 (10), 2757-2775, DOI: 10.1175/1520-0493(1993)121<2757:IOAMCS>2.0.CO;2.

Liu, C.-L., and A. J. Illingworth, 2000: Toward more accurate retrievals of ice water content from radar measurements of clouds. *Journal of Applied Meteorology and Climatology*, 39 (7), 1130-1146, DOI: 10.1175/1520-0450(2000)039<1130:TMAROI>2.0.CO;2.

Liu, Z.-Q., and F. Rabier, 2002: The interaction between model resolution, observation resolution and observation density in data assimilation: a one-dimensional study. *Quarterly Journal of the Royal Meteorological Society*, 128 (582), 1367-1386, DOI: 10.1256/003590002320373337.

Lorenc, A. C., 1986: Analysis methods for numerical weather prediction. *Quarterly Journal of the Royal Meteorological Society*, 112 (474), 1177-1194, DOI: 10.1002/qj.49711247414.

Lorenc, A. C., 2003: The potential of the ensemble Kalman filter for NWP – a comparison with 4D-Var. *Quarterly Journal of the Royal Meteorological Society*, 129 (595), 3183-3203, DOI: 10.1256/qj.02.132.

Lorenz, E. N., 1965: A study of the predictability of a 28-variable atmospheric model. *Tellus*, 17 (3), 321-333, DOI: 10.1111/j.2153-3490.1965.tb01424.x.

Macpherson, B., 2001: Operational experience with assimilation of rainfall data in the Met Office Mesoscale model. *Meteorology and Atmospheric Physics*, 76, 3-8, DOI: 10.1007/s007030170035.

Marshall, J. S., and W. Mc K. Palmer, 1948: The distribution of raindrops with size. *Journal of the Atmospheric Sciences*, 5 (4), 165-166, DOI: 10.1175/1520-0469(1948)005<0165:TDORWS>2.0.CO;2.

Matsui, T., B. Dolan, S. A. Rutledge, W.-K. Tao, T. Iguchi, J. Barnum, and S. E. Lang, 2019: POLARRIS: a polarimetric radar retrieval and instrument simulator. *Journal of Geophysical Research: Atmospheres*, 124 (8), 4634-4657, DOI: 10.1029/2018JD028317.

Meng, Z., and F. Zhang, 2011: Limited-area ensemble-based data assimilation. *Monthly Weather Review*, 139 (7), 2025-2045, DOI: 10.1175/2011MWR3418.1.

Milan, M., V. Venema, D. Schüttemeyer, and C. Simmer, 2008: Assimilation of radar and satellite data in mesoscale models: a physical initialization scheme. *Meteorologische Zeitschrift*, 17 (6), 887-902, DOI: 10.1127/0941-2948/2008/0340.

Miller, R. N., M. Ghil, and F. Gauthiez, 1994: Advanced data assimilation in strongly nonlinear dynamical systems. *Journal of the Atmospheric Sciences*, 51 (8), 1037-1056, DOI: 10.1175/1520-0469(1994)051<1037:ADAISN>2.0.CO;2.

Mitchell, H. L., P. L. Houtekamer, and G. Pellerin, 2002: Ensemble size, balance, and model-error representation in an ensemble Kalman filter. *Monthly Weather Review*, 130 (11), 2791-2808, DOI: 10.1175/1520-0493(2002)130<2791:ESBAME>2.0.CO;2.

Miyoshi, T., Y. Sato, and T. Kadowaki, 2010: Ensemble Kalman filter and 4D-Var intercomparison with the Japanese operational global analysis and prediction system. *Monthly Weather Review*, 138 (7), 2846-2866, DOI: 10.1175/2010MWR3209.1.

Navon, I. M., and D. M. Legler, 1987: Conjugate-gradient methods for large-scale minimization in meteorology. *Monthly Weather Review*, 115 (8), 1479-1502, DOI: 10.1175/1520-0493(1987)115<1479:CGMFLS>2.0.CO;2.

Olson, D. A., N. W. Junker, and B. Korty, 1995: Evaluation of 33 years of quantitative precipitation forecasting at the NMC. *Weather and Forecasting*, 10 (3), 498-511, DOI: 10.1175/1520-0434(1995)010<0498:EOYOQP>2.0.CO;2.

Ott, E., B. R. Hunt, I. Szunyogh, A. V. Zimin, E. J. Kostelich, M. Corazza, E. Kalnay, D. J. Patil, and coauthors, 2004: A local ensemble Kalman filter for atmospheric data assimilation. *Tellus A: Dynamic Meteorology and Oceanography*, 56 (5), 415-428, DOI: 10.3402/tellusa.v56i5.14462.

Park, H. S., A. V. Ryzhkov, D. S. Zrnic, and K.-E. Kim, 2009: The hydrometeor classification algorithm for the polarimetric WSR-88D: description and application to an MCS. *Weather and Forecasting*, 24 (3), 730-748, DOI: 10.1175/2008WAF2222205.1.

Parrish, D. F., and J. C. Derber, 1992: The National Meteorological Center's spectral statistical-interpolation analysis system. *Monthly Weather Review*, 120 (8), 1747-1763, DOI: 10.1175/1520-0493(1992)120<1747:TNMCSS>2.0.CO;2.

Pfeifer, M., G. C. Craig, M. Hagen, and C. Keil, 2008: A polarimetric radar forward operator for model evaluation. *Journal of Applied Meteorology and Climatology*, 47 (12), 3202-3220, DOI: 10.1175/2008JAMC1793.1.

Poterjoy, J., 2016: A localized particle filter for high-dimensional nonlinear systems. *Monthly Weather Review*, 144 (1), 59-76, DOI: 10.1175/MWR-D-15-0163.1.

Poterjoy, J., R. A. Sobash, and J. L. Anderson, 2017: Convective-scale data assimilation for the Weather Research and Forecasting Model using the local

particle filter. *Monthly Weather Review*, 145 (5), 1897-1918, DOI: 10.1175/MWR-D-16-0298.1.

Praz, C., Y.-A. Roulet, and A. Berne, 2017: Solid hydrometeor classification and riming degree estimation from pictures collected with a multi-angle snowflake camera. *Atmospheric Measurement Techniques*, 10 (4), 1335-1357, DOI: 10.5194/amt-10-1335-2017.

Prill, F., D. Reinert, D. Rieger, and G. Zängl, 2020: ICON tutorial November 2020: working with the ICON model. *German national weather service (DWD)*, https://www.dwd.de/DE/leistungen/nwv_icon_tutorial/pdf_einzelbaende/icon_tutorial2020.html.

Putnam, B. J., Y. Jung, N. Yussouf, D. Stratman, T. A. Supinie, M. Xue, C. Kuster, and J. Labriola, 2021: The impact of assimilating ZDR observations on storm-scale ensemble forecasts of the 31 May 2013 Oklahoma storm event. *Monthly Weather Review*, 149 (6), 1919-1942, DOI: 10.1175/MWR-D-20-0261.1.

Putnam, B. J., M. Xue, Y. Jung, N. A. Snook, and G. Zhang, 2014: The analysis and prediction of microphysical states and polarimetric radar variables in a mesoscale convective system using double-moment microphysics, multinetwork radar data, and the ensemble Kalman filter. *Monthly Weather Review*, 142 (1), 141-162, DOI: 10.1175/MWR-D-13-00042.1.

Putnam, B. J., M. Xue, Y. Jung, N. A. Snook, and G. Zhang, 2017: Ensemble probabilistic prediction of a mesoscale convective system and associated polarimetric radar variables using single-moment and double-moment microphysics schemes and EnKF radar data assimilation. *Monthly Weather Review*, 145 (6), 2257-2279, DOI: 10.1175/MWR-D-16-0162.1.

Putnam, B. J., M. Xue, Y. Jung, N. A. Snook, and G. Zhang, 2019: Ensemble Kalman filter assimilation of polarimetric radar observations for the 20 May 2013 Oklahoma tornadic supercell case. *Monthly Weather Review*, 147 (7), 2511-2533, DOI: 10.1175/MWR-D-18-0251.1.

Qiu, C.-J., and Q. Xu, 1992: A simple adjoint method of wind analysis for single-Doppler data. *Journal of Atmospheric and Oceanic Technology*, 9 (5), 588-598, DOI: 10.1175/1520-0426(1992)009<0588:ASAMOW>2.0.CO;2.

Rabier, F., H. Järvinen, E. Klinker, J.-F. Mahfouf, and A. Simmons, 2000: The ECMWF operational implementation of four-dimensional variational assimilation. I: Experimental results with simplified physics. *Quarterly Journal of the Royal Meteorological Society*, 126 (564), 1143-1170, DOI: 10.1002/qj.49712656415.

Reimann, L., C. Simmer, and S. Trömel, 2021: Dual-polarimetric radar estimators of liquid water content over Germany. *Meteorologische Zeitschrift*, 30 (3), 237-249, DOI: 10.1127/metz/2021/1072.

Reimann, L., C. Simmer, and S. Trömel, 2023: Assimilation of 3D polarimetric microphysical retrievals in a convective-scale NWP system. Submitted to

Atmospheric Chemistry and Physics, EGUsphere [preprint], DOI: 10.5194/egusphere-2023-1132.

Roberts, N. M., and H. W. Lean, 2008: Scale-selective verification of rainfall accumulations from high-resolution forecasts of convective events. *Monthly Weather Review*, 136 (1), 78–97, DOI: 10.1175/2007MWR2123.1.

Routray, A., U. C. Mohanty, S. R. H. Rizvi, D. Niyogi, K. K. Osuri, and D. Pradhan, 2010: Impact of Doppler weather radar data on numerical forecast of Indian monsoon depressions. *Quarterly Journal of the Royal Meteorological Society*, 136 (652), 1836-1850, DOI: 10.1002/qj.678.

Roux, F., 1985: Retrieval of thermodynamic fields from multiple-Doppler radar data using the equations of motion and the thermodynamic equation. *Monthly Weather Review*, 113 (12), 2142-2157, DOI: 10.1175/1520-0493(1985)113<2142:ROTFFM>2.0.CO;2.

Ryzhkov, A. V., M. Diederich, P. Zhang, and C. Simmer, 2014: Potential utilization of specific attenuation for rainfall estimation, mitigation of partial beam blockage, and radar networking. *Journal of Atmospheric and Oceanic Technology*, 31 (3), 599-619, DOI: 10.1175/JTECH-D-13-00038.1.

Ryzhkov, A. V., S. E. Giangrande, and T. J. Schuur, 2005a: Rainfall estimation with a polarimetric prototype of WSR-88D. *Journal of Applied Meteorology and Climatology*, 44 (4), 502-515, DOI: 10.1175/JAM2213.1.

Ryzhkov, A. V., M. R. Kumjian, S. M. Ganson, and P. Zhang, 2013: Polarimetric radar characteristics of melting hail. Part II: practical implications. *Journal of Applied Meteorology and Climatology*, 52 (12), 2871-2886, DOI: 10.1175/JAMC-D-13-074.1.

Ryzhkov, A. V., M. Pinsky, A. Pokrovsky, and A. Khain, 2011: Polarimetric radar observation operator for a cloud model with spectral microphysics. *Journal of Applied Meteorology and Climatology*, 50 (4), 873-894, DOI: 10.1175/2010JAMC2363.1.

Ryzhkov, A. V., T. J. Schuur, D. W. Burgess, and D. S. Zrnic, 2005b: Polarimetric tornado detection. *Journal of Applied Meteorology and Climatology*, 44 (5), 557-570, DOI: 10.1175/JAM2235.1.

Ryzhkov, A. V., P. Zhang, H. Reeves, M. R. Kumjian, T. Tschallener, S. Trömel, and C. Simmer, 2016: Quasi-vertical profiles – a new way to look at polarimetric radar data. *Journal of Atmospheric and Oceanic Technology*, 33 (3), 551-562, DOI: 10.1175/JTECH-D-15-0020.1.

Ryzhkov, A. V., and D. S. Zrnic, 1998: Beamwidth effects on the differential phase measurements of rain. *Journal of Atmospheric and Oceanic Technology*, 15 (3), 624-634, DOI: 10.1175/1520-0426(1998)015<0624:BEOTDP>2.0.CO;2.

Ryzhkov, A. V., D. S. Zrnic, and B. A. Gordon, 1998: Polarimetric method for ice water content determination. *Journal of Applied Meteorology and Climatology*, 37 (2), 125-134, DOI: 10.1175/1520-0450(1998)037<0125:PMFIWC>2.0.CO;2.

Ryzhkov, A. V., and D. S. Zrnic, 2019: *Radar polarimetry for weather observations*. Springer Nature Switzerland AG 2019, DOI: 10.1007/978-3-030-05093-1.

Sachidananda, M., and D. S. Zrnic, 1985: ZDR measurement considerations for a fast scan capability radar. *Radio Science*, 20 (4), 907-922, DOI: 10.1029/RS020i004p00907.

Sachidananda, M., and D. S. Zrnic, 1986: Differential propagation phase shift and rainfall rate estimation. *Radio Science*, 21 (2), 235-247, DOI: 10.1029/RS021i002p00235.

Sasaki, Y., 1970: Some basic formalisms in numerical variational analysis. *Monthly Weather Review*, 98 (12), 875-883, DOI: 10.1175/1520-0493(1970)098<0875:SBFINV>2.3.CO;2.

Sassen, K., 1987: Ice cloud content from radar reflectivity. *Journal of Applied Meteorology and Climatology*, 26 (8), 1050-1053, DOI: 10.1175/1520-0450(1987)026<1050:ICCFRR>2.0.CO;2.

Sassen, K., and T. Chen, 1995: The lidar dark band: an oddity of the radar bright band analogy. *Geophysical Research Letters*, 22 (24), 3505-3508, DOI: 10.1029/95GL03367.

Schenkman, A. D., M. Xue, A. Shapiro, K. Brewster, and J. Gao, 2011b: Impact of CASA radar and Oklahoma Mesonet data assimilation on the analysis and prediction of tornadic mesovortices in an MCS. *Monthly Weather Review*, 139 (11), 3422-3445, DOI: 10.1175/MWR-D-10-05051.1.

Schenkman, A. D., M. Xue, A. Shapiro, K. Brewster, and J. Gao, 2011a: The analysis and prediction of the 8–9 May 2007 Oklahoma tornadic mesoscale convective system by assimilating WSR-88D and CASA radar data using 3DVAR. *Monthly Weather Review*, 139 (1), 224-246, DOI: 10.1175/2010MWR3336.1.

Schinagl, K., P. Friederichs, S. Trömel, and C. Simmer, 2019: Gamma drop size distribution assumptions in bulk model parameterizations and radar polarimetry and their impact on polarimetric radar moments. *Journal of Applied Meteorology and Climatology*, 58 (3), 467-478, DOI: 10.1175/JAMC-D-18-0178.1.

Schraff, C., H. Reich, A. Rhodin, A. Schomburg, K. Stephan, A. Perianez, and R. Potthast, 2016: Kilometre-scale ensemble data assimilation for the COSMO model (KENDA). *Quarterly Journal of the Royal Meteorological Society*, 142 (696), 1453-1472, DOI: 10.1002/qj.2748.

Sekhon, R. S., and R. C. Srivastava, 1970: Snow size spectra and radar reflectivity. *Journal of the Atmospheric Sciences*, 27 (2), 299-307, DOI: 10.1175/1520-0469(1970)027<0299:SSSARR>2.0.CO;2.

Seliga, T. A., and V. N. Bringi, 1976: Potential use of radar differential reflectivity measurements at orthogonal polarizations for measuring precipitation. *Journal of Applied Meteorology and Climatology*, 15 (1), 69-76, DOI: 10.1175/1520-0450(1976)015<0069:PUORDR>2.0.CO;2.

Seliga, T. A., and V. N. Bringi, 1978: Differential reflectivity and differential phase shift: applications in radar meteorology. *Radio Science*, 13 (2), 271-275, DOI: 10.1029/RS013i002p00271.

Shapiro, A., S. Ellis, and J. Shaw, 1995: Single-Doppler velocity retrievals with Phoenix II data: clear air and microburst wind retrievals in the planetary boundary layer. *Journal of the Atmospheric Sciences*, 52 (9), 1265-1287, DOI: 10.1175/1520-0469(1995)052<1265:SDVRWP>2.0.CO;2.

Shrestha, P., S. Trömel, R. Evaristo, and C. Simmer, 2022: Evaluation of modelled summertime convective storms using polarimetric radar observations. *Atmospheric Chemistry and Physics*, 22 (11), 7593-7618, DOI: 10.5194/acp-22-7593-2022.

Simonin, D., S. P. Ballard, and Z. Li, 2014: Doppler radar radial wind assimilation using an hourly cycling 3D-Var with a 1.5 km resolution version of the Met Office Unified Model for nowcasting. *Quarterly Journal of the Royal Meteorological Society*, 140 (684), 2298-2314, DOI: 10.1002/qj.2298.

Snook, N. A., M. Xue, and Y. Jung, 2011: Analysis of a tornadic mesoscale convective vortex based on ensemble Kalman filter assimilation of CASA X-band and WSR-88D radar data. *Monthly Weather Review*, 139 (11), 3446-3468, DOI: 10.1175/MWR-D-10-05053.1.

Snook, N. A., M. Xue, and Y. Jung, 2015: Multiscale EnKF assimilation of radar and conventional observations and ensemble forecasting for a tornadic mesoscale convective system. *Monthly Weather Review*, 143 (4), 1035-1057, DOI: 10.1175/MWR-D-13-00262.1.

Snyder, J. C., H. B. Bluestein, G. Zhang, and S. J. Frasier, 2010: Attenuation correction and hydrometeor classification of high-resolution, X-band, dual-polarized mobile radar measurements in severe convective storms. *Journal of Atmospheric and Oceanic Technology*, 27 (12), 1979-2001, DOI: 10.1175/2010JTECHA1356.1.

Snyder, C., and F. Zhang, 2003: Assimilation of simulated Doppler radar observations with an ensemble Kalman filter. *Monthly Weather Review*, 131 (8), 1663-1677, DOI: 10.1175//2555.1.

Sobash, R. A., and D. J. Stensrud, 2013: The impact of covariance localization for radar data on EnKF analyses of a developing MCS: observing system simulation experiments. *Monthly Weather Review*, 141 (11), 3691-3709, DOI: 10.1175/MWR-D-12-00203.1.

Souto, M. J., C. F. Balseiro, V. Perez-Munuzuri, M. Xue, and K. Brewster, 2003: Impact of cloud analysis on numerical weather prediction in the Galician region of Spain. *Journal of Applied Meteorology and Climatology*, 42 (1), 129-140, DOI: 10.1175/1520-0450(2003)042<0129:IOCAON>2.0.CO;2.

Stephan, K., S. Klink, and C. Schraff, 2008: Assimilation of radar-derived rain rates into the convective-scale model COSMO-DE at DWD. *Quarterly Journal of the Royal Meteorological Society*, 134 (634), 1315-1326, DOI: 10.1002/qj.269.

Sugimoto, S., N. A. Crook, J. Sun, Q. Xiao, and D. M. Barker, 2009: An examination of WRF 3DVAR radar data assimilation on its capability in retrieving unobserved variables and forecasting precipitation through observing system simulation experiments. *Monthly Weather Review*, 137 (11), 4011-4029, DOI: 10.1175/2009MWR2839.1.

Sun, J., 2005a: Initialization and numerical forecasting of a supercell storm observed during STEPS. *Monthly Weather Review*, 133 (4), 793-813, DOI: 10.1175/MWR2887.1.

Sun, J., 2005b: Convective-scale assimilation of radar data: progress and challenges. *Quarterly Journal of the Royal Meteorological Society*, 131 (613), 3439-3463, DOI: 10.1256/qj.05.149.

Sun, J., M. Chen, and Y. Wang, 2010: A frequent-updating analysis system based on radar, surface, and mesoscale model data for the Beijing 2008 forecast demonstration project. *Weather and Forecasting*, 25 (6), 1715-1735, DOI: 10.1175/2010WAF2222336.1.

Sun, J., and N. A. Crook, 1997: Dynamical and microphysical retrieval from Doppler radar observations using a cloud model and its adjoint. Part I: model development and simulated data experiments. *Journal of the Atmospheric Sciences*, 54 (12), 1642-1661, DOI: 10.1175/1520-0469(1997)054<1642:DAMRFD>2.0.CO;2.

Sun, J., and N. A. Crook, 1998: Dynamical and microphysical retrieval from Doppler radar observations using a cloud model and its adjoint. Part II: retrieval experiments of an observed Florida convective storm. *Journal of the Atmospheric Sciences*, 55 (5), 835-852, DOI: 10.1175/1520-0469(1998)055<0835:DAMRFD>2.0.CO;2.

Sun, J., D. W. Flicker, and D. K. Lilly, 1991: Recovery of three-dimensional wind and temperature fields from simulated single-Doppler radar data. *Journal of the Atmospheric Sciences*, 48 (6), 876-890, DOI: 10.1175/1520-0469(1991)048<0876:ROTDWA>2.0.CO;2.

Sun, J., and Y. Zhang, 2008: Analysis and prediction of a squall line observed during IHOP using multiple WSR-88D observations. *Monthly Weather Review*, 136 (7), 2364-2388, DOI: 10.1175/2007MWR2205.1.

Tabary, P., A.-A. Boumahmoud, H. Andrieu, R. J. Thompson, A. J. Illingworth, E. Le Bouar, and J. Testud, 2011: Evaluation of two “integrated” polarimetric quantitative precipitation estimation (QPE) algorithms at C-band. *Journal of Hydrology*, 405 (3-4), 248-260, DOI: 10.1016/j.jhydrol.2011.05.021.

Talagrand, O., 1997: Assimilation of observations, an introduction. *Journal of the Meteorological Society of Japan. Ser. II*, 75 (1B), 191–209, DOI: 10.2151/jmsj1965.75.1B_191.

Talagrand, O., and P. Courtier, 1987: Variational assimilation of meteorological observations with the adjoint vorticity equation. I: theory. *Quarterly Journal of the Royal Meteorological Society*, 113 (478), 1311-1328, DOI: 10.1002/qj.49711347812.

Tanamachi, R. L., L. J. Wicker, D. C. Dowell, H. B. Bluestein, D. T. Dawson, and M. Xue, 2013: EnKF assimilation of high-resolution, mobile Doppler radar data of the 4 May 2007 Greensburg, Kansas, supercell into a numerical cloud model. *Monthly Weather Review*, 141 (2), 625-648, DOI: 10.1175/MWR-D-12-00099.1.

Testud, J., E. Le Bouar, E. Obligis, and M. Ali-Mehenni, 2000: The rain profiling algorithm applied to polarimetric weather radar. *Journal of Atmospheric and Oceanic Technology*, 17 (3), 332-356, DOI: 10.1175/1520-0426(2000)017<0332:TRPAAT>2.0.CO;2.

Testud, J., S. Oury, R. A. Black, P. Amayenc, and X. Dou, 2001: The concept of "normalized" distribution to describe raindrop spectra: a tool for cloud physics and cloud remote sensing. *Journal of Applied Meteorology and Climatology*, 40 (6), 1118-1140, DOI: 10.1175/1520-0450(2001)040<1118:TCONDT>2.0.CO;2.

Tippett, M. K., J. L. Anderson, C. H. Bishop, T. M. Hamill, and J. S. Whitaker, 2003: Ensemble square root filters. *Monthly Weather Review*, 131 (7), 1485-1490, DOI: 10.1175/1520-0493(2003)131<1485:ESRF>2.0.CO;2.

Tong, M., and M. Xue, 2005: Ensemble Kalman filter assimilation of Doppler radar data with a compressible nonhydrostatic model: OSS experiments. *Monthly Weather Review*, 133 (7), 1789-1807, DOI: 10.1175/MWR2898.1.

Tong, W., G. Li, J. Sun, X. Tang, and Y. Zhang, 2016: Design strategies of an hourly update 3DVAR data assimilation system for improved convective forecasting. *Weather and Forecasting*, 31 (5), 1673-1695, DOI: 10.1175/WAF-D-16-0041.1.

Trömel, S., A. V. Ryzhkov, P. Zhang, and C. Simmer, 2014: Investigations of backscatter differential phase in the melting layer. *Journal of Applied Meteorology and Climatology*, 53 (10), 2344-2359, DOI: 10.1175/JAMC-D-14-0050.1.

van Leeuwen, P. J., 2009: Particle filtering in geophysical systems. *Monthly Weather Review*, 137 (12), 4089-4114, DOI: 10.1175/2009MWR2835.1.

Vendrasco, E. P., J. Sun, D. L. Herdies, and C. F. de Angelis, 2016: Constraining a 3DVAR radar data assimilation system with large-scale analysis to improve short-range precipitation forecasts. *Journal of Applied Meteorology and Climatology*, 55 (3), 673-690, DOI: 10.1175/JAMC-D-15-0010.1.

Vivekanandan, J., V. N. Bringi, M. Hagen, and P. Meischner, 1994: Polarimetric radar studies of atmospheric ice particles. *IEEE Transactions on Geoscience and Remote Sensing*, 32 (1), 1-10, DOI: 10.1109/36.285183.

Vobig, K., K. Stephan, U. Blahak, K. Khosravian, and R. Potthast, 2021: Targeted covariance inflation for 3D-volume RADAR reflectivity assimilation with the LETKF. *Quarterly Journal of the Royal Meteorological Society*, 147 (740), 3789-3805, DOI: 10.1002/qj.4157.

Vulpiani, G., M. Montopoli, L. D. Passeri, A. G. Gioia, P. Giordano, and F. S. Marzano, 2012: On the use of dual-polarized C-band radar for operational rainfall retrieval in mountainous areas. *Journal of Applied Meteorology and Climatology*, 51 (2), 405-425, DOI: 10.1175/JAMC-D-10-05024.1.

Wang, X., 2010: Incorporating ensemble covariance in the Gridpoint Statistical Interpolation variational minimization: a mathematical framework. *Monthly Weather Review*, 138 (7), 2990-2995, DOI: 10.1175/2010MWR3245.1.

Wang, X., D. M. Barker, C. Snyder, and T. M. Hamill, 2008: A hybrid ETKF–3DVAR data assimilation scheme for the WRF model. Part I: observing system simulation experiment. *Monthly Weather Review*, 136 (12), 5116-5131, DOI: 10.1175/2008MWR2444.1.

Wang, X., C. Snyder, and T. M. Hamill, 2007: On the theoretical equivalence of differently proposed ensemble–3DVAR hybrid analysis schemes. *Monthly Weather Review*, 135 (1), 222-227, DOI: 10.1175/MWR3282.1.

Wang, H., J. Sun, S. Fan, and X.-Y. Huang, 2013a: Indirect assimilation of radar reflectivity with WRF 3D-Var and its impact on prediction of four summertime convective events. *Journal of Applied Meteorology and Climatology*, 52 (4), 889-902, DOI: 10.1175/JAMC-D-12-0120.1.

Wang, H., J. Sun, X. Zhang, X.-Y. Huang, and T. Auligne, 2013b: Radar data assimilation with WRF 4D-Var. Part I: system development and preliminary testing. *Monthly Weather Review*, 141 (7), 2224-2244, DOI: 10.1175/MWR-D-12-00168.1.

Wang, W., and T. T. Warner, 1988: Use of four-dimensional data assimilation by newtonian relaxation and latent-heat forcing to improve a mesoscale-model precipitation forecast: a case study. *Monthly Weather Review*, 116 (12), 2593-2613, DOI: 10.1175/1520-0493(1988)116<2593:UOFDDA>2.0.CO;2.

Wang, Y., and X. Wang, 2017: Direct assimilation of radar reflectivity without tangent linear and adjoint of the nonlinear observation operator in the GSI-based EnVar system: methodology and experiment with the 8 May 2003 Oklahoma City tornadic supercell. *Monthly Weather Review*, 145 (4), 1447-1471, DOI: 10.1175 /MWR-D-16-0231.1.

Weygandt, S. S., A. Shapiro, and K. K. Droegemeier, 2002: Retrieval of model initial fields from single-Doppler observations of a supercell thunderstorm. Part II: thermodynamic retrieval and numerical prediction. *Monthly Weather Review*, 130 (3), 454-476, DOI: 10.1175/1520-0493(2002)130<0454:ROMIFF>2.0.CO;2.

Wheatley, D. M., K. H. Knopfmeier, T. A. Jones, and G. J. Creager, 2015: Storm-scale data assimilation and ensemble forecasting with the NSSL experimental warn-on-forecast system. Part I: radar data experiments. *Weather and Forecasting*, 30 (6), 1795-1817, DOI: 10.1175/WAF-D-15-0043.1.

Whitaker, J. S., and T. M. Hamill, 2002: Ensemble data assimilation without perturbed observations. *Monthly Weather Review*, 130 (7), 1913-1924, DOI: 10.1175/1520-0493(2002)130<1913:EDAWPO>2.0.CO;2.

Whitaker, J. S., and T. M. Hamill, 2012: Evaluating methods to account for system errors in ensemble data assimilation. *Monthly Weather Review*, 140 (9), 3078-3089, DOI: 10.1175/MWR-D-11-00276.1.

Wilks, D. S., 2019: Statistical methods in the atmospheric sciences. Elsevier.

Wu, W.-S., R. J. Purser, and D. F. Parrish, 2002: Three-dimensional variational analysis with spatially inhomogeneous covariances. *Monthly Weather Review*, 130 (12), 2905-2916, DOI: 10.1175/1520-0493(2002)130<2905:TDVAWS>2.0.CO;2.

Wu, B., J. Verlinde, and J. Sun, 2000: Dynamical and microphysical retrievals from Doppler radar observations of a deep convective cloud. *Journal of the Atmospheric Sciences*, 57 (2), 262-283, DOI: 10.1175/1520-0469(2000)057<0262:DAMRFD>2.0.CO;2.

Xiao, Q., Y.-H. Kuo, J. Sun, W.-C. Lee, D. M. Barker, and E. Lim, 2007: An approach of radar reflectivity data assimilation and its assessment with the inland QPF of typhoon Rusa (2002) at landfall. *Journal of Applied Meteorology and Climatology*, 46 (1), 14-22, DOI: 10.1175/JAM2439.1.

Xiao, Q., Y.-H. Kuo, J. Sun, W.-C. Lee, E. Lim, Y.-R. Guo, and D. M. Barker, 2005: Assimilation of Doppler radar observations with a regional 3DVAR system: impact of Doppler velocities on forecasts of a heavy rainfall case. *Journal of Applied Meteorology and Climatology*, 44 (6), 768-788, DOI: 10.1175/JAM2248.1.

Xu, M., N. A. Crook, Y. Liu, and R. Rasmussen, 2004: Real-time analysis and short term forecasting of snowbands using a mesoscale model. *11th Conference on Aviation, Range and Aerospace meteorology*, AMS, 4–8 October 2004, Hyannis, Massachusetts, P9.3.

Xu, Q., and C.-J. Qiu, 1994: Simple adjoint methods for single-Doppler wind analysis with a strong constraint of mass conservation. *Journal of Atmospheric and Oceanic Technology*, 11 (2), 289-298, DOI: 10.1175/1520-0426(1994)011<0289:SAMFSD>2.0.CO;2.

Xue, M., M. Tong, and K. K. Droegemeier, 2006: An OSSE framework based on the ensemble square root Kalman filter for evaluating the impact of data from radar networks on thunderstorm analysis and forecasting. *Journal of Atmospheric and Oceanic Technology*, 23 (1), 46-66, DOI: 10.1175/JTECH1835.1.

Xue, M., D. Wang, J. Gao, K. Brewster, and K. K. Droegemeier, 2003: The Advanced Regional Prediction System (ARPS), storm-scale numerical weather prediction and data assimilation. *Meteorology and Atmospheric Physics*, 82, 139-170, DOI: 10.1007/s00703-001-0595-6.

Yang, S.-C., E. Kalnay, B. R. Hunt, and N. E. Bowler, 2009: Weight interpolation for efficient data assimilation with the Local Ensemble Transform Kalman Filter. *Quarterly Journal of the Royal Meteorological Society*, 135 (638), 251-262, DOI: 10.1002/qj.353.

Yokota, S., H. Seko, M. Kunii, H. Yamauchi, and H. Niino, 2016: The tornadic supercell on the Kanto plain on 6 May 2012: polarimetric radar and surface data assimilation with EnKF and ensemble-based sensitivity analysis. *Monthly Weather Review*, 144 (9), 3133-3157, DOI: 10.1175/MWR-D-15-0365.1.

Zängl, G., D. Reinert, P. Ripodas, and M. Baldauf, 2015: The ICON (ICOsahedral Non-hydrostatic) modelling framework of DWD and MPI-M: description of the non-hydrostatic dynamical core. *Quarterly Journal of the Royal Meteorological Society*, 141 (687), 563-579, DOI: 10.1002/qj.2378.

Zeng, Y., U. Blahak, and D. Jerger, 2016: An efficient modular volume-scanning radar forward operator for NWP models: description and coupling to the COSMO model. *Quarterly Journal of the Royal Meteorological Society*, 142 (701), 3234-3256, DOI: 10.1002/qj.2904.

Zhang, G., 2016: *Weather radar polarimetry*. CRC Press.

Zhang, J., F. Carr, and K. Brewster, 1998: ADAS cloud analysis. Preprints *12th Conference on Numerical Weather Prediction*, AMS, Phoenix, Arizona, USA, 185-188.

Zhang, G., J. Gao, and M. Du, 2021: Parameterized forward operators for simulation and assimilation of polarimetric radar data with numerical weather predictions. *Advances in Atmospheric Sciences*, 38 (5), 737-754, DOI: 10.1007/s00376-021-0289-6.

Zhang, G., V. N. Mahale, B. J. Putnam, Y. Qi, Q. Cao, A. D. Byrd, P. Bukovcic, D. S. Zrnic, and coauthors, 2019: Current status and future challenges of weather radar polarimetry: bridging the gap between radar meteorology/hydrology/engineering and numerical weather prediction. *Advances in Atmospheric Sciences*, 36 (6), 571-588, DOI: 10.1007/s00376-019-8172-4.

Zhang, F., C. Snyder, and J. Sun, 2004: Impacts of initial estimate and observation availability on convective-scale data assimilation with an ensemble Kalman filter. *Monthly Weather Review*, 132 (5), 1238-1253, DOI: 10.1175/1520-0493(2004)132<1238:IOIEAO>2.0.CO;2.

Zhang, G., J. Vivekanandan, and E. Brandes, 2001: A method for estimating rain rate and drop size distribution from polarimetric radar measurements. *IEEE Transactions on Geoscience and Remote Sensing*, 39 (4), 830-841, DOI: 10.1109/36.917906.

Zhang, F., Y. Weng, J. A. Sippel, Z. Meng, and C. H. Bishop, 2009: Cloud-resolving hurricane initialization and prediction through assimilation of Doppler radar observations with an ensemble Kalman filter. *Monthly Weather Review*, 137 (7), 2105-2125, DOI: 10.1175/2009MWR2645.1.

Zhu, K., M. Xue, K. Ouyang, and Y. Jung, 2020: Assimilating polarimetric radar data with an ensemble Kalman filter: OSSEs with a tornadic supercell storm simulated with a two-moment microphysics scheme. *Quarterly Journal of the Royal Meteorological Society*, 146 (729), 1880-1900, DOI: 10.1002/qj.3772.

Ziegler, C. L., 1985: Retrieval of thermal and microphysical variables in observed convective storms. Part 1: model development and preliminary testing. *Journal of the Atmospheric Sciences*, 42 (14), 1487-1509, DOI: 10.1175/1520-0469(1985)042<1487:ROTAMV>2.0.CO;2.

Zrnic, D. S., and A. V. Ryzhkov, 1996: Advantages of rain measurements using specific differential phase. *Journal of Atmospheric and Oceanic Technology*, 13 (2), 454-464, DOI: 10.1175/1520-0426(1996)013<0454:AORMUS>2.0.CO;2.

Zrnic, D. S., and A. V. Ryzhkov, 1999: Polarimetry for weather surveillance radars. *Bulletin of the American Meteorological Society*, 80 (3), 389-406, DOI: 10.1175/1520-0477(1999)080<0389:PFWSR>2.0.CO;2.